Master of Science Thesis

Modelling of a Gas Generator Powered Mortar Parachute Deployment Device

Simulation Tool

Charles Gueudet

Faculty of Aerospace Engineering · Delft University of Technology

TU Delft Delft University of Technology

Mortar & Gas Generator Parachute Deployment Device

Simulation Tool

MASTER OF SCIENCE THESIS

For obtaining the degree of Master of Science in Aerospace Engineering at Delft University of Technology

Charles Gueudet

20/02/2025

Faculty of Aerospace Engineering · Delft University of Technology

The work in this thesis was supported by Aerospace Propulsion Products B.V. Their cooperation is gratefully acknowledged.

DELFT UNIVERSITY OF TECHNOLOGY
FACULTY OF AEROSPACE
ENGINEERING

DEPARTMENT OF AEROSPACE STRUCTURES AND MATERIALS

GRADUATION COMMITTEE

Dated: 07/03/2025

Chair holder:

_____
Ir. I. Uriol Balbin

Committee members:

_____
Dr.ir. E. Mooij

_____
Dr.ir. S.R. Turteltaub

_____
Ir. A. Groot

Abstract

This thesis was conducted within Aerospace Propulsion Products, a company specialized in rocket engine igniters and Parachute Deployment Devices (PDDs) for space applications. The objective of this research was to develop a high-fidelity numerical model in Python capable of accurately predicting the performance of a PDD system. Given input parameters such as component geometry, propellant load, material properties, and environmental conditions, the model serves as a predictive tool to assist engineers in designing and optimizing PDDs for future planetary exploration missions.

To achieve this, an extensive study of parachute ejection mechanisms was first conducted, analysing the physical principles governing gas generator combustion, gas flow dynamics, structural interactions, and aerodynamic forces. A numerical model was then formulated using fundamental principles of combustion, ballistics, physics, and thermodynamics, incorporating detailed representations of the gas generator, plenum, and parachute pack. Once developed, the model was calibrated using experimental data and systematically verified and validated against deployment tests to assess its accuracy in predicting key performance metrics such as pressure profiles, reaction forces, and ejection velocity.

The validated model was then subjected to a sensitivity analysis to identify the most influential parameters affecting system performance. The results demonstrated that parameters such as the discharge coefficient, chamber volumes, plenum dimensions, and propellant loading significantly impact the pressure buildup, deployment timing, and ejection dynamics. Additionally, variations observed in experimental repeatability highlighted the inherent uncertainties in physical testing, further emphasizing the value of numerical modelling in PDD development.

By providing a robust and accurate simulation framework, this research contributes to the advancement of next-generation PDD systems. The model developed in this study offers engineers a powerful tool for optimizing PDD designs, ensuring reliable deployment performance across various mission scenarios. Future work will focus on further refining the model by incorporating additional experimental data and extending its applicability to a wider range of deployment conditions.

Table of Contents

List of Figures

List of Tables

Preface

This thesis represents the final part of my engineering studies, which began at the University of Queensland in Australia as a mechanical engineering student and is now concluding at Delft University of Technology with a master's degree in aerospace engineering. Over the course of these studies, I have developed a strong foundation in both mechanical and aerospace engineering principles, which has culminated in this research project.

The thesis was conducted in collaboration with Aerospace Propulsion Products, a company specializing in the development of Parachute Deployment Devices (PDDs) as well as rocket engine ignition systems for space exploration missions. My work focused on developing a numerical model capable of accurately predicting the performance of PDD systems under various operational conditions. This model was intended to assist engineers in designing future products that will be used in planetary entry, descent, and landing missions.

Throughout this research, I explored the complex dynamics of parachute ejection mechanisms, applying principles from combustion, thermodynamics, and aerodynamics to develop a mathematical model in Python. The validation and sensitivity analysis of the model, carried out with experimental data, were crucial steps in ensuring the model's reliability and providing deeper insights into the key parameters that govern PDD performance.

This work concludes my studies in aerospace engineering and marks an important step in my professional journey. I look forward to continuing my career in this field, applying the knowledge gained during my academic and professional experiences.

Acknowledgments

I would like to express my sincere gratitude to Dr. Sergio Turteltaub, my supervisor at Delft University of Technology, for his invaluable guidance and assistance throughout the development and writing of this thesis. His expertise and thoughtful feedback have been essential to the success of this research. I would also like to thank Ashwyn Groot, my supervisor at Aerospace Propulsion Products, whose support, patience, and inspiration were crucial during the course of this project.

Additionally, I would like to extend my appreciation to Bernd Brauers, the COO of Aerospace Propulsion Products, for placing his trust in me to carry out this project. His confidence in my abilities provided me with the opportunity to work on a meaningful and challenging problem.

Finally, I would like to thank my friends and family for their unwavering support and encouragement throughout this entire journey. Their belief in me has been a constant source of motivation.

Delft, University of Technology

Charles Gueudet, 7th of March 2025

Chapter 1

Introduction

Planetary exploration requires a well-coordinated Entry, Descent, and Landing (EDL) sequence to enable safe spacecraft landings on distant surfaces. Parachute systems play a pivotal role within this process, contributing to controlled deceleration, stabilization, and precision in landing. This chapter introduces the critical concepts surrounding parachute systems, focusing on their design, deployment mechanics, and performance within EDL frameworks. The complex dynamics of parachute deployment, particularly within the context of planetary entry, necessitate a detailed exploration of the components, operational methods, and considerations involved.

Understanding parachute deployment devices (PDDs) is essential, as they represent the mechanisms responsible for initiating and controlling the deployment sequence of the parachute canopy. The study of PDDs encompasses a range of technologies and engineering principles that ensure safe, efficient, and reliable deployments in varying planetary atmospheres. This chapter outlines the fundamentals of EDL parachute systems and PDDs, addressing the challenges, requirements, and historical insights drawn from significant planetary missions. From mechanical drogue guns to advanced pyrotechnic mortars, each deployment device's design offers unique solutions that enhance the performance and reliability of EDL systems in extreme environments.

Through a review of core deployment devices and methodologies, this chapter establishes the foundation for a technical discussion on the engineering considerations critical to parachute deployment success. Subsequent sections will delve into the specific components, mechanics, and systems that define modern PDD technology, drawing on key examples from Mars, Titan, and Earth re-entry missions to illustrate effective design principles and deployment strategies.

1.1 Parachute for Planetary Entry Descent and Landing (EDL)

Parachute systems, as illustrated in Figure 1, play a crucial role in the success of Entry, Descent, and Landing (EDL) operations by enabling controlled deceleration and precise landing of spacecraft. These systems typically consist of various components, including the parachute canopy, risers, deployment mechanism, reefing systems, and control devices (Knacke, 1991). Each component has a specific

function and contributes to the overall effectiveness and reliability of the system. The parachute canopy, often the most prominent component, generates aerodynamic drag to slow down the spacecraft during descent. It is carefully designed to provide sufficient surface area while being lightweight and durable. The deployment device is responsible for the precise and timely release of the parachute canopy during entry, descent, and landing. A reliable and efficient deployment mechanism ensures the successful inflation and deployment of the parachute, enabling the deceleration and stabilization of the spacecraft for a safe and controlled descent.

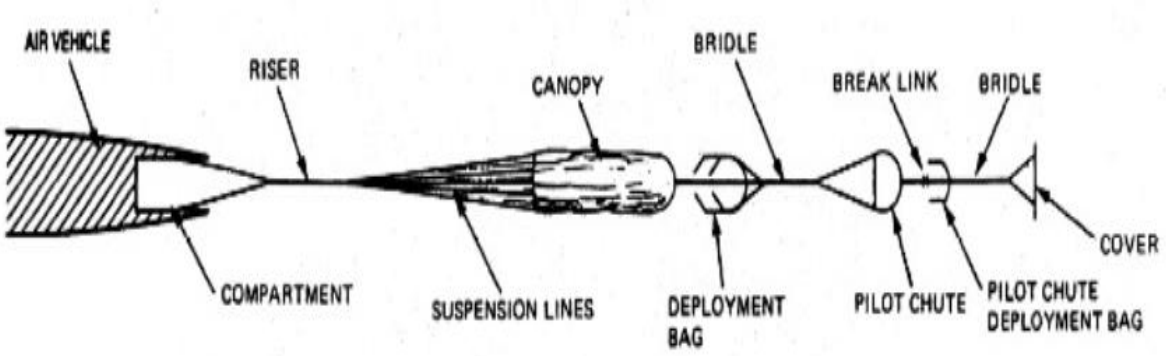

Figure 1: Parachute Assembly (Knacke, 1991)

The reliability of the parachute EDL system is of utmost importance and has been extensively proven. However, in the case of complex systems, it is crucial to thoroughly analyse and review all aspects and components of the entire system cycle. Failure to properly integrate the system can result in mishaps, such as the one experienced by Space Shuttle flight 7 in 1983, where an incorrect sensor signal led to premature parachute disconnect and the loss of solid-fuel boosters (Knacke, 1991).

Considerations of weight and volume play a significant role in the design process. For lightweight vehicles, parachute assemblies typically account for around 5% of the total vehicle weight, while vehicles weighing several thousand pounds allocate 3 to 4% for these assemblies (Knacke, 1991). A complete recovery system, including flotation, location, and retrieval assemblies, generally weighs around 10 ± 2% of the total vehicle weight. For instance, the 254kg Apollo parachute assembly, essential for landing during the journey around the moon and back to Earth, posed a significant weight expense. Consequently, great efforts were made to reduce overall spacecraft weight by eliminating even small amounts of weight.

In the context of aerial targets, the parachute system serves to retrieve the target in the final minutes of the mission. Any weight savings in the system directly contribute to improving the target's performance, such as payload capacity. The selection process for parachutes often begins with considering the stability requirement. Parachutes used for aircraft deceleration, first-stage drogue chutes, and most ordnance-retardation parachutes demand a high level of stability, automatically ruling out many high-drag parachutes. For the final descent parachute, which is typically the heaviest component of a recovery system, preference is usually given to high-drag, solid textile parachutes. These parachutes offer smaller diameters, resulting in lower weights and volumes. To mitigate parachute oscillation, which should ideally be limited to 0 to 10 degrees (Knacke, 1991), cluster parachutes may be employed.

Parachutes must be ejected from the vehicle to avoid the wake effect, which can prevent correct inflation and reduce the drag of the parachute. This necessity arises because the wake created by the forebody (the spacecraft) can significantly interfere with the parachute's performance. Each forebody produces a wake that affects the parachute, depending on the ratio of the inflated parachute diameter to the forebody diameter and the distance between the end of the forebody and the leading edge of the inflated parachute canopy. The wake effect can cause substantial drag loss, reducing the effectiveness of the parachute. To mitigate this, parachutes are often ejected at relatively high velocities from the spacecraft to ensure they enter a region of cleaner air, well clear of the forebody wake. Tests conducted in NASA and Wright

Field vertical wind tunnels determined that for vertical descending bodies, the parachute should be ejected to a distance equivalent to more than four times, and preferably six times, the forebody diameter, into good airflow behind the forebody (Knacke, 1991).

Deploying a small parachute in the wake of a large forebody can cause considerable loss in parachute drag and may affect the stability of the parachute. Drag losses of up to 25% have been experienced in wind-tunnel and free-flight tests. Successful inflation with shorter distances should be proven in tests of the most unfavourable—not the most favourable—deployment conditions. Figure 2 presents parachute drag losses caused by forebody wake measured in wind-tunnel and free-flight tests. These data emphasize the importance of adequately distancing the parachute from the wake to ensure optimal performance and reliability. Superimposed on wind-tunnel data, free-flight test results obtained on the reefed Apollo command module drogue chute further validate these findings. This knowledge underscores the importance of proper ejection techniques to avoid the detrimental effects of the forebody wake on parachute performance.

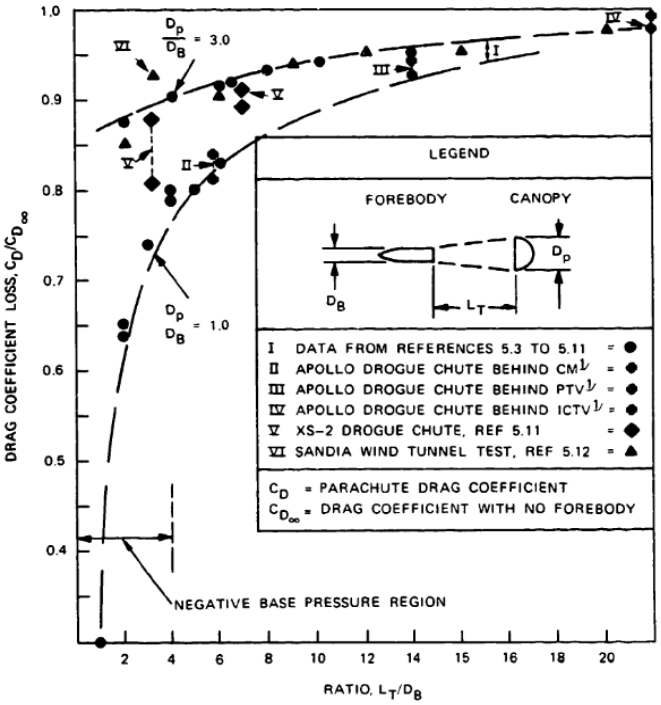

Figure 2: Parachute Drag Loss Caused by Forebody Wake (Knacke, 1991)

Given these complexities in parachute deployment, it is evident that the deployment mechanism itself is a crucial component that determines the success of the EDL process. Parachute deployment denotes the sequence of events that begins with the opening of a parachute compartment or parachute pack attached to the body to be recovered. Deployment continues with the extraction of the parachute until the canopy and suspension lines are stretched behind the body and the parachute canopy is ready to start the inflation process. This deployment is associated with a mass shock (snatch force) created by the acceleration of the mass of the parachute to the velocity of the body to be recovered. The task of a good deployment system is to limit the mass shock to an acceptable level. Shock limitation is accomplished by controlling the parachute deployment process and providing means for progressive incremental acceleration of all parts of the parachute to the velocity of the forebody. A high snatch force is usually the result of a poor deployment system. The need for a controlled progressive parachute deployment increases with parachute size and deployment velocity, and with the number of parachutes in the assembly. An uncontrolled high acceleration of the canopy skirt may also cause reefing cutters to rip away from their anchor points and damage the reefing installation.

The controlled parachute deployment method, shown in conceptual form in Figure 1, is the basic deployment method for all parachute assemblies used for the recovery and retardation of air and space vehicles, ordnance items, and high-speed payloads. This method is also recommended, in an appropriate form, for other parachute assemblies, including personnel and aircrew emergency parachute systems. Controlled parachute deployment starts with the forced ejection of a parachute compartment cover or a drogue gun slug that, in turn, pulls a pilot chute or first-stage drogue chute away from the air vehicle and into good airflow behind the vehicle. Mortar ejection or rocket extraction may also be used for forced deployment of pilot or drogue chutes.

Figure 1 shows a controlled deployment of a parachute assembly that starts with the ejection of the compartment cover, which extracts the pilot chute stored in a small bag. Important in the deployment of the parachute assembly is the sequence: riser, suspension lines, and canopy. This type of sequence is

called line-first deployment. The deployment bag of the main parachute contains two compartments, one for riser and suspension lines, and another for the canopy. All assembly components are retained in their respective compartments, using stow loops and tie cords. This arrangement ensures a controlled deployment with tension on all parts of the parachute assembly. Figure 1 shows the pilot chute permanently attached to the main parachute canopy, an arrangement that has proven beneficial to all large reefed parachutes. Mortar ejection or rocket extraction deploy the pilot or drogue chute directly. These two methods are described later.

Understanding and optimizing these deployment systems is paramount. In the following sections, various parachute deployment devices will be explored, examining their design, functionality, and application in ensuring effective EDL operations. Notable EDL missions such as the Mars Pathfinder, Phoenix Mars Lander, Mars Science Laboratory (Curiosity rover), and the Perseverance rover have all relied on meticulously designed parachute deployment systems to achieve successful landings on Mars. The Huygens probe's descent onto Titan and the Genesis and Stardust missions' sample returns to Earth further exemplify the critical role of effective parachute deployment mechanisms in a wide range of planetary exploration missions.

1.2 Parachute Deployments Devices (PDD)

Parachute deployment involves a sequence of events beginning with the opening of a parachute compartment or pack attached to the landing body. This deployment process includes the extraction of the parachute until the canopy and suspension lines are fully extended behind the body, ready for inflation. For successful inflation, the parachute must be expelled at a specific distance from the vehicle to counteract the "wake" effect. The wake effect can interfere with proper inflation by creating turbulent air behind the vehicle. The successful deployment of a parachute depends on minimizing the mass shock, or snatch force, resulting from the rapid acceleration of the parachute to the vehicle's speed. An effective deployment system controls and reduces the mass shock to acceptable levels. High snatch forces typically indicate a poorly designed deployment system. The need for controlled and reliable parachute deployment is more critical with larger parachutes, higher deployment velocities, and an increased number of parachutes in the assembly. A well-controlled and successful parachute deployment requires a positive extraction method, such as a mechanically or pyrotechnically ejected parachute.

1.2.1 Drogue Gun

The drogue gun deployment device, commonly known as a drogue gun, is a mechanism used in aviation and aerospace applications to deploy a drogue parachute or drogue chute. The primary function of a drogue parachute is to stabilize or decelerate an aircraft or spacecraft, facilitating controlled descent or reduced speed during various operational scenarios. Typically, a drogue gun deployment device comprises several components, including a pressurized gas system, a firing mechanism, and a canister or housing where the drogue chute is stored. When activated, the firing mechanism releases a burst of pressurized gas, propelling the drogue parachute out of the canister and enabling its deployment. The design of the deployment device ensures the rapid and reliable deployment of the drogue chute in a controlled manner.

The operation of a drogue gun is similar to that of a pistol. The gun body is attached to the main aircraft or spacecraft. Upon receiving the deployment command, a piston, analogous to a pistol shell, known as a drogue gun slug, is fired away from the vehicle into the airflow behind it. The drogue gun slug, attached to a bridle, serves the purpose of either directly extracting the pilot chute or extracting a small deployment bag containing the pilot chute. It is important to note that drogue gun slugs are limited in weight to approximately 900 grams (Knacke, 1991), making them suitable for lightweight pilot chutes only. Due to their low reaction force, drogue guns can be conveniently stowed at various locations on the main aircraft or spacecraft.

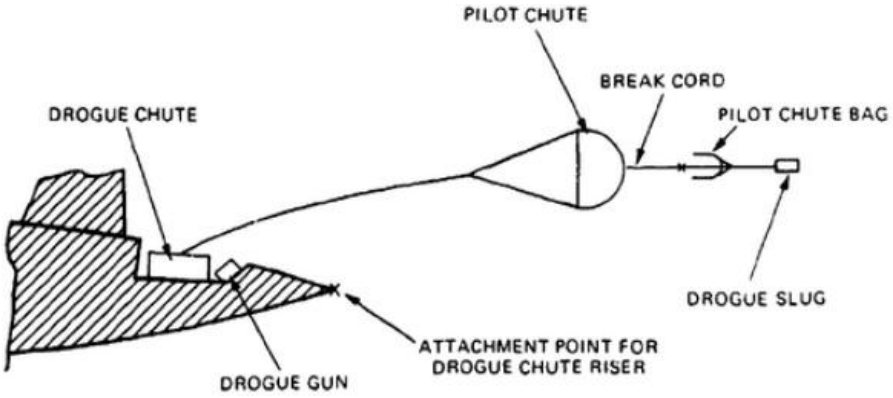

Figure 3: Drogue Gun Deployment (Knacke, 1991)

Figure 3 illustrates the configuration where the drogue gun slug remains permanently attached to the pilot chute bag, with both the slug and bag separating after deployment is completed. This design is preferred as it prevents the drogue gun slug from becoming entangled with the pilot chute, thereby minimizing the risk of damage.

Overall, the utilization of a drogue gun deployment device provides a reliable and efficient means of deploying drogue parachutes. Its controlled deployment process plays a crucial role in ensuring the stabilization and deceleration of aircraft or spacecraft during critical operations.

1.2.2 Tractor Rocket

Tractor rocket systems are a common method used in parachute deployment to extract the parachute from its housing and ensure proper deployment. Figure 4 illustrates two typical methods of rocket extraction in parachute deployment. In the first version, the rocket is stored alongside the parachute assembly, while in the second version, the rocket is positioned within the deployment bag, which has a doughnut-shaped design. Both configurations have demonstrated successful deployment outcomes.

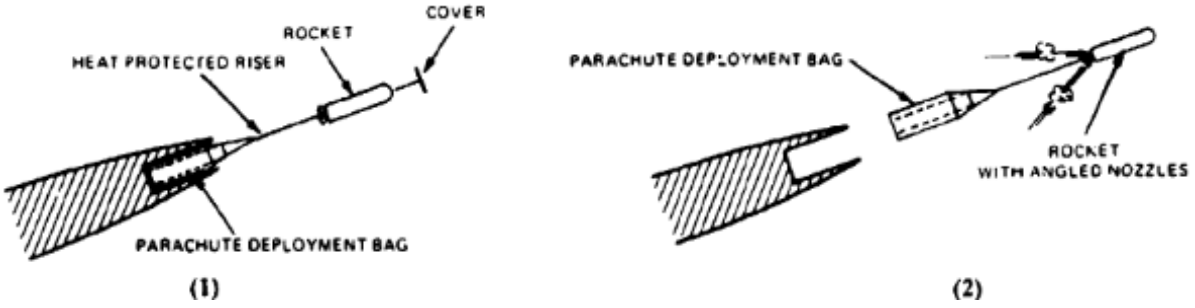

Figure 4: Two Typical Rocket-Extraction Methods (Knacke, 1991)

Rocket extraction offers favourable deployment characteristics by exerting a pulling force on the parachute bag from the top, facilitating a sequence where the lines are deployed first. One notable advantage of rocket extraction is that it does not generate reaction forces that need to be absorbed by the vehicle. This aspect simplifies the structural requirements and integration of the deployment system with the vehicle. Additionally, protection against the short-duration rocket blast has generally not presented a significant concern (Knacke, 1991).

Using rocket extraction in parachute deployment for re-entry vehicles offers several advantages, including efficient deployment and minimal reaction forces on the vehicle. However, this method introduces complexity and additional weight to the system. There are also potential environmental risks associated with using rockets, such as debris and contamination, which can increase costs and limit

redundancy. Therefore, a careful mission-specific evaluation is essential to determine the suitability of rocket extraction for each application.

The design of tractor rocket systems must consider various factors, including the thrust profile, burn duration, and aerodynamic stability, to ensure reliable and effective deployment. By fine-tuning these parameters, the deployment system can achieve precise control over the timing and force of the parachute ejection, making it suitable for a wide range of applications, from high-speed re-entry vehicles to complex aerial payload deliveries.

Understanding and optimizing these deployment systems is paramount. In the following sections, additional parachute deployment devices will be explored, examining their design, functionality, and application in ensuring effective EDL operations.

1.2.3 Pneumatic Mortar

Pneumatic mortar systems have been extensively employed in aerospace recovery operations, providing reliable and repeatable parachute deployment. Mortar-launched parachute systems have a significant history of use, notably in the Gemini and Apollo programs, where they facilitated the deployment of drogue parachutes into free airflow with high reliability. This design heritage continues with the Orion program, which utilizes two Variable Porosity Conical Ribbon Drogue Parachutes connected to the Orion capsule using wire rope risers to ensure system integrity during off-angle deployments (Koster, Wells, & Sinclair, 2011).

Unlike the Gemini and Apollo programs, which conducted numerous mortar-based drogue deployment tests, the Orion program faced challenges due to development schedules and other constraints. To address these challenges, Airborne Systems North America proposed using a pneumatic mortar system. This system employs compressed nitrogen as the propulsive force for deploying the drogue parachute, offering an alternative to traditional explosive mortars.

The trigger system for the pneumatic mortar utilizes a series of rupture discs placed in sequence, employing commercially available disc fixtures commonly used in industrial fluid and gas delivery systems. The design goal for the pneumatic mortar system was to maintain portability, allowing it to be transported to remote testing sites. Figure 6 illustrates a pneumatic mortar assembly, which comprises the tank, rupture disc assembly, and mortar body, all secured as a unit by twelve 19mm diameter studs.

Mortar-launched parachute systems, with a legacy of reliability from programs like Gemini and Apollo, offer proven and repeatable parachute deployment. They ensure the integrity of parachute systems during off-angle deployments, as seen in the Orion program. However, challenges in extensive testing and the introduction of a pneumatic system with rupture discs add complexity and potential cost considerations. Nevertheless, the portability of the pneumatic system enhances testing flexibility, making it a valuable option for modern aerospace recovery operations.

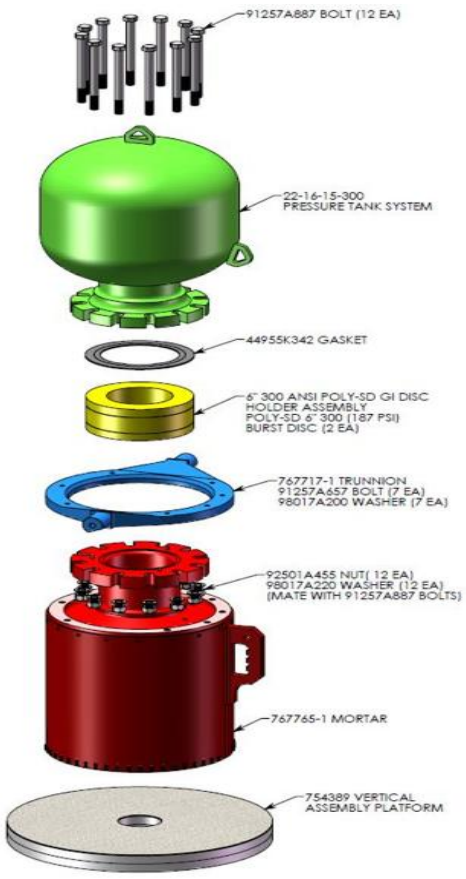

Figure 5: Pneumatic Mortar Assembly (Koster, Wells, & Sinclair, 2011)

1.2.4 Pyrotechnic Mortar (Gas Generator)

Pyrotechnic mortars serve as an effective means of deploying parachute assemblies by utilizing mechanisms similar to the firing of shells from cannons. This deployment method is particularly advantageous for propelling parachutes away from spinning or tumbling vehicles, ensuring they enter stable airflow. Unlike other deployment methods that rely on manual triggers, mortar deployment employs the pressure produced by the quasi-instantaneous burning of propellant to eject the parachute assembly.

One significant advantage of mortar deployment is its ability to rapidly position parachute assemblies in favourable airflow behind the vehicle. This rapid deployment ensures the parachute enters stable airflow quickly, which is crucial for effective deceleration and stabilization of the vehicle. However, this method also presents certain disadvantages. The substantial recoil force generated by the mortar requires careful design considerations to manage the resulting loads. Additionally, mortar deployment necessitates a relatively large mortar body and relies on the inertia forces of ejection to achieve successful canopy deployment, bag strip off, and line and canopy stretching.

The assembly of the parachute deployment device (PDD) is illustrated in Figure 6. The primary components of the PDD include the gas generator (GG), the sabot, and the mortar tube. The assembly also includes miscellaneous fasteners, O-rings, and parachute attachment hardware. The sabot is inserted at the bottom of the mortar tube, providing a base for the parachute pack. It functions as a freely moving piston within the mortar tube and is equipped with an O-ring seal to confine the gas generated by the GG.

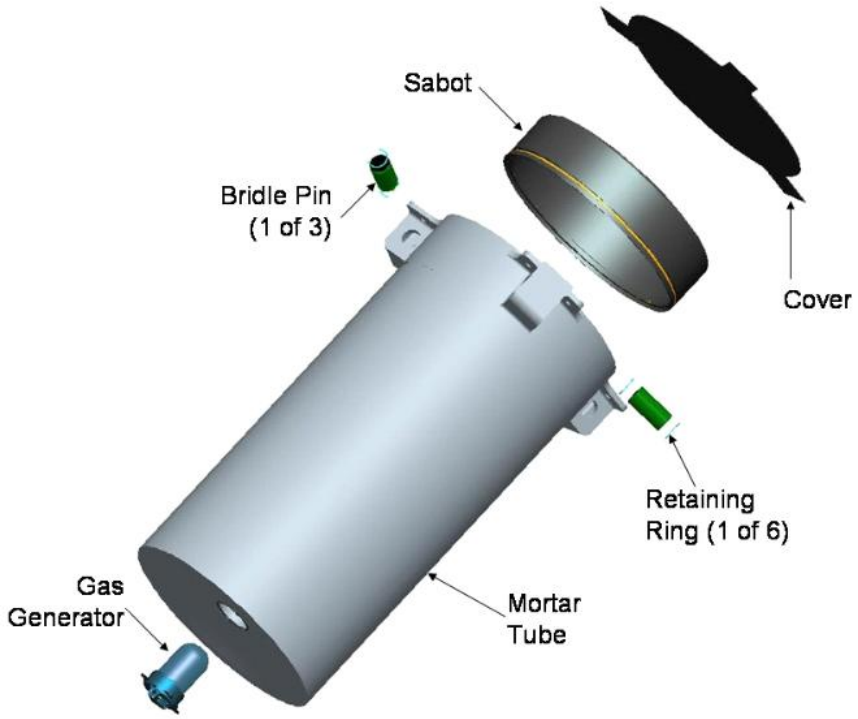

Figure 6: Mortar and Gas Generator Assembly (Rowan, Moran, & S. Adams, 2009)

The Gas Generator is positioned at the base of the mortar tube, directly beneath the sabot. When the solid propellant in the GG combusts, it rapidly generates gas within the ullage volume beneath the sabot. Acting as a piston, the sabot propels the parachute out of the mortar tube, breaking the retention ties by applying pressure on the cover. The parachute pack continues its movement until it reaches its maximum line stretch, at which point the canopy is deployed and initiates the inflation process (Rowan, Moran, & S. Adams, 2009).

Several mission-specific applications of mortar-based parachute deployment highlight the versatility and complexity of these systems:

Mars Science Laboratory (MSL): The parachute of the MSL was deployed using a 95-gram charge of General Dynamics Ordnance and Tactical Systems St. Marks Ball Powder® propellant. This propellant produced an operating pressure of 16,000 psi and a temperature of approximately 2,649°C, ensuring effective parachute deployment in the Martian atmosphere (Rowan, Moran, & S. Adams, 2009).

Galileo Jupiter Probe: The parachute deployment system utilized a combination of HMX and BKNO3 propellants due to their low outgassing properties. The propellant mix for this mission included 0.3 grams of BKNO3 and 0.6 grams of 8028 propellant. BKNO3 burned to create a high-pressure environment, facilitating the combustion of the 8028 discs. This mixture resulted in an impetus of 284,050 J/kg for BKNO3 and 1,091,350 J/kg for 8028 (Whalley & Churchill, 2003). The choice of these propellants proved successful, allowing for adjustments in the propellant mix and weights throughout the program.

Mars Exploration Rover (MER): For the MER, a 16.8-gram charge of Winchester ball powder was determined optimal for the GG in its Mortar Deployer System (MDS). The combustion of this propellant occurred within less than 2 milliseconds, allowing for rapid and effective parachute deployment (E. Vasas & Styner, 2003).

Viking Mars Lander: The parachute mortar of the Viking mission included a cartridge assembly with a volume of 5.71 cubic inches and 0.125 pounds of propellant. The propellant consisted of two charges: a 0.045-pound booster charge of PL6670 granulated propellant and a 0.080-pound main charge of wafer-shaped PL6670 propellant. This configuration achieved a working pressure of 13,250 psi, ensuring the successful deployment of the parachute (Brecht, Pleasants, & Mehring, 1973).

Mortar deployment, while effective and rapid, requires careful design to handle the high recoil forces and ensure successful parachute deployment. The inclusion of components such as the GG, sabot, and mortar tube are critical to the function of the PDD, ensuring the reliable deployment of parachute assemblies in various aerospace applications.

1.3 Mortar & Gas Parachute Deployment Device

This section delves into the mortar and gas generator parachute deployment device, a critical system designed for reliable and efficient parachute deployment in aerospace applications. By combining solid propellant combustion and mechanical propulsion, this device ensures precise and controlled deployment of parachutes, which is essential for the stability and deceleration of spacecraft or payloads during critical flight phases. This part will detail the primary components of the device and their specific functions, emphasizing the technical intricacies and engineering considerations that underpin its design and operations.

1.3.1 Gas Generator

The Gas Generator (GG) is integral to the mortar and gas parachute deployment device, delivering a powerful and rapid burst of hot gas to create the necessary pressure for propelling the sabot and parachute pack to the required ejection speed. Essentially functioning as a miniature rocket motor, the GG achieves high-pressure combustion of nitrocellulose propellant. To ensure the propellant ignites reliably, the gas generator is hermetically sealed, enabling the buildup of high pressure and temperature for stable, continuous combustion. This back pressure is crucial for consistent and dependable propellant ignition. **Error! Reference source not found.** illustrates the components of a typical gas generator system.

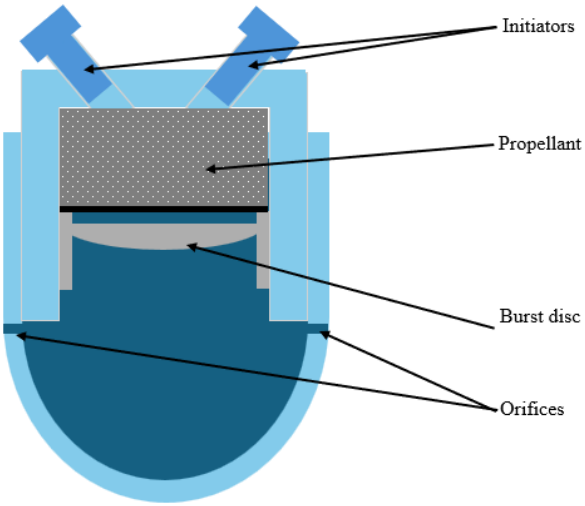

Figure 7: Gas Generator Assembly

Activation of the gas generator system is achieved through electrically energized initiators that ignite the propellant. When ignited, the initiators add both pressure and energy to the system, initiating the combustion process. The propellant then combusts, generating high-temperature gas that pressurizes the internal volume of the unit. As the combustion process continues, the burning propellant particles produce hot gases, leading to a buildup of pressure within the fixed volume. This increased gas pressure exerts force on the surrounding mechanical components.

A vital component of the GG is the burst disk, a thin membrane designed to rupture at a specific pressure threshold. The burst disk initially reduces the size of the combustion chamber, allowing the pressure to rise more quickly and ensuring good ignition and combustion of the propellant. Once the predetermined pressure limit is reached, the burst disk breaks, allowing the hot gases and burning propellant particles to escape through the orifices. These orifices are specifically designed to control the mass flow from the upstream volume to the downstream volume. As a result, a steady pressure rise inside the plenum volume of the mortar tube, ensuring a controlled and stable deployment. Different gas generator systems use various propellant types and operate at different pressures, depending on the specific requirements of the deployment device (Rowan, Moran, & S. Adams, 2009).

1.3.1.1 Initiators

The development of initiators has been a critical aspect of ensuring reliable ignition within gas generators used in aerospace applications. The technology has evolved significantly over time, transitioning from the dual bridgewire Apollo Standard Initiator (ASI) to the Single Bridgewire Apollo Standard Initiator (SBASI), and later to the Viking Standard Initiator (VSI). Each iteration has improved upon the reliability and performance necessary for successful missions.

In 1966, the NASA Standard Initiator (NSI) was developed and qualified to meet the rigorous demands of the Apollo lunar missions. This design later became a standard component across various NASA programs, including the Space Shuttle system and its payloads (Hohmann, Tipton, & Dutton, 2000). The NSI features a thin metal bridge wire surrounded by a pyrotechnic charge composed of finely powdered zirconium metal mixed with finely powdered potassium perchlorate, all held together by a Viton-B rubber binder (as shown in Figure 8).

The NSI operates by electrically heating the bridge wire, which ignites the surrounding pyrotechnic charge. This ignition produces a small detonation and generates high pressures. The primary role of the NSI is to convert an electrical signal into a pyrotechnic reaction, often referred to as a "first fire." This reaction creates a flame and hot particles that can ignite other propellants and generate a pressure impulse (Varghese, 1988). The ability to reliably and quickly initiate combustion is critical for the effective operation of the gas generator and the overall parachute deployment system.

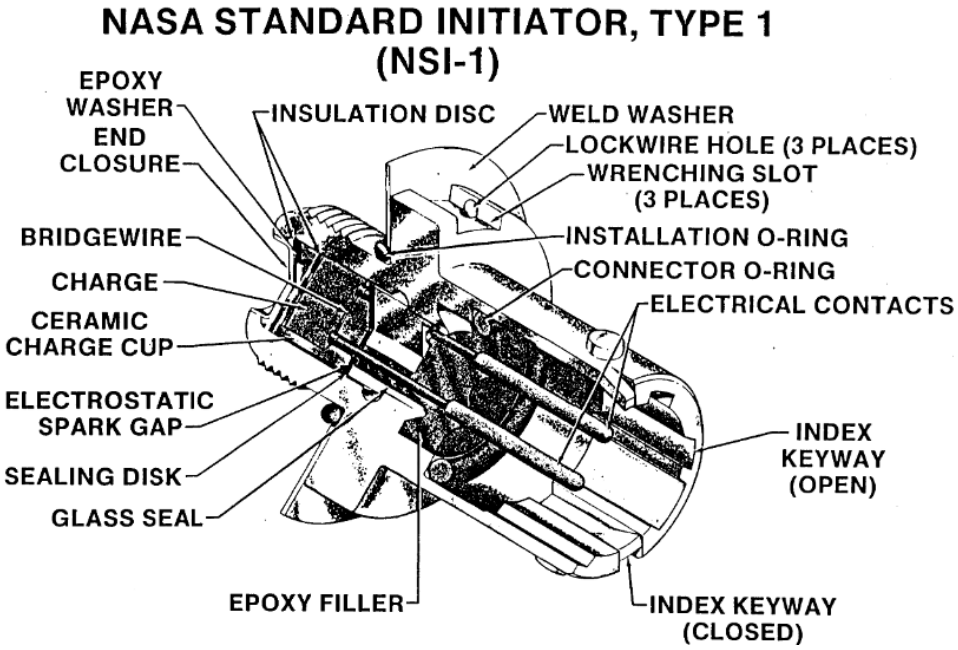

Figure 8: NASA Standard Initiator (Varghese, 1988)

In this project, the initiators used are almost identical to the NSI. The electrical heating of the bridge wire initiates the combustion process, leading to the production of high-temperature gas that pressurizes the internal volume of the gas generator.

1.3.1.2 Solid Propellant

The term "solid propellant" refers to a variety of materials used to generate high-temperature gases for propulsion and other applications. Solid propellants can be categorized into several types, each designed for specific purposes, such as space launch boosters, tactical missiles, or gas generators. These propellants vary in their chemical compositions, burning rates, physical properties, and performance characteristics.

Solid propellants are generally classified into two main categories: double-base (DB) propellants and composite propellants.

Double-Base Propellants: Double-base propellants are composed of a homogeneous mixture of nitrocellulose (NC) and nitro-glycerine (NG), often with minor additives to enhance performance. Both NC and NG serve as the fuel and oxidizer, providing the necessary energy for combustion. Nitrocellulose, an ester derived from the nitration of cellulose in nitric acid, serves as the fundamental constituent of this type of propellant. Nitrocellulose can undergo gelatinization when exposed to various solvents, with nitro-glycerine being the most commonly employed solvent. As homogeneous propellants most often comprise these two primary components, they are often referred to as double-base propellants or ballistites. These propellants are also known as smokeless propellants, having replaced black powder towards the end of the nineteenth century. Variants such as extruded double-base (EDB) and cast double-base (CDB) have been developed to improve performance. Enhancements include the addition of crystalline nitramines (HMX or RDX) to form cast-modified double-base propellants, and incorporating elastomeric binders like cross-linked polybutadiene, resulting in elastomeric-modified cast double-base (EMCDB) propellants. These propellants are known for producing minimal smoke exhaust (Novozhilov & Novozhilov, 2021) & (Sutton & Biblarz, 2001).

Composite Propellants: Composite propellants consist of a heterogeneous mixture where oxidizer crystals, such as ammonium perchlorate (AP), and powdered fuel, typically aluminium, are embedded in a matrix of synthetic rubber or plastic binder, like hydroxyl-terminated polybutadiene (HTPB). The

fuel and oxidizer in composite propellants are not chemically fused at the molecular level; instead, they remain separate, making them heterogeneous propellants. These propellants are cast from a combination of solid and liquid ingredients, which are then cured to form a solid, rigid grain. Composite propellants are widely used in modern rocket motors due to their high performance and versatility. The components of a composite propellant consist of microscopic particles that range in size from a few micrometres to fractions of a millimetre, sometimes dispersed within the matrix of the other component (Novozhilov & Novozhilov, 2021) & (Sutton & Biblarz, 2001).

For gas generator applications, propellants are designed to produce high-temperature gases without generating thrust. These gas generator propellants typically operate at lower combustion temperatures, ranging from 800 to 1600 K, compared to rocket motor propellants that exceed 2400 K. The lower temperature combustion gases are ideal for generating large volumes of gas at high pressure without requiring significant insulation for the container (Sutton & Biblarz, 2001)

In this project, the focus is on nitrocellulose, a type of double-base propellant, due to its effectiveness and reliability. Nitrocellulose is derived from cellulose treated with nitric acid, creating a highly flammable compound. When ignited, nitrocellulose undergoes rapid combustion, producing high-temperature gases that pressurize the gas generator and drive the parachute deployment process. Its high burn rate and substantial energy output make nitrocellulose an excellent choice for applications requiring rapid and intense energy release, ensuring consistent performance in critical aerospace missions.

The performance of solid propellants, including nitrocellulose, depends on various factors such as combustion characteristics, burning rate, surface area, and grain geometry. These aspects are studied under the field of solid combustion theory, which will be further explored in Chapter 2.

1.3.1.3 Burst Disk

The burst disk is a critical component in the gas generator, serving multiple essential functions to ensure both the protection and performance of the propellant.

Firstly, this sealing prevents the propellant from deteriorating over time, maintaining its stability and effectiveness for reliable ignition and operation. Additionally, it protects against the outgassing of the propellant in space, ensuring that the integrity of the propellant is maintained in the vacuum of space .

Secondly, during operation, the burst disk enables the rapid accumulation of pressure within the gas generator. This rapid pressure build-up is crucial for complete ignition and swiftly achieving choked flow through the orifices. The choked flow condition ensures that the gas exits the generator at maximum velocity, providing the necessary force to propel the sabot and parachute pack from the mortar tube (Pawlikowski, 1986).

1.3.1.4 Orifices

Orifices in the gas generator are meticulously designed to regulate the mass flow rate of the exhaust gases, ensuring that the mortar tube pressure and parachute ejection velocities reach optimal levels. These precisely dimensioned orifices play a critical role in achieving the desired performance characteristics of the deployment system (Rowan, Moran, & S. Adams, 2009).

The primary function of the orifices is to control the rate at which gas is expelled from the gas generator. By regulating this flow, the orifices ensure that the pressure within the mortar tube builds up to the required level, enabling the parachute to be ejected at the correct velocity. This precise control is essential for the stable and effective deployment of the parachute.

Furthermore, the orifices maintain a high enough pressure inside the gas generator to ensure complete combustion of the propellant. This controlled combustion is vital for generating a steady and reliable

flow of hot gases. The balance achieved by the orifices between internal gas pressure and the rate of gas expulsion ensures that the propellant burns efficiently and the gas generator operates within its designed parameters.

1.3.2 Mortar Assembly

The mortar assembly, as shown in Figure 9, consists of several key components, including the mortar tube, bridle attachment, and gas generator. The components ejected from the mortar during deployment include the sabot, parachute pack and mortar cover. These ejected components are securely held in place within the mortar by shear pins until the gas generator is initiated.

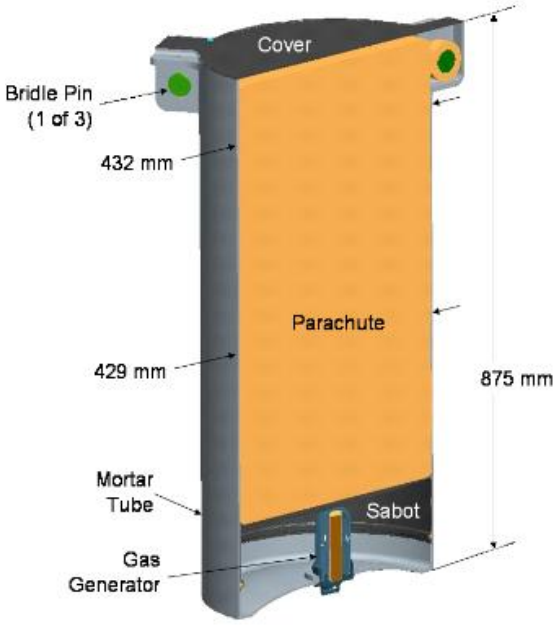

Figure 9: Mars Exploration Rover Mortar Assembly (E. Vasas & Styner, 2003)

1.3.2.1 Mortar Tube

The primary element of the Parachute Deployment Device (PDD) system is the mortar tube, typically crafted from aluminium due to its favourable strength-to-weight ratio. Initially, the Viking generation utilized a construction method involving the assembly of various components (Brecht, Pleasants, & Mehring, 1973). However, later generations such as the Mars Exploration Rover (MER) and Mars Science Laboratory (MSL) adopted a more efficient approach, employing weight-optimized structures machined from a single billet (Rowan, Moran, & S. Adams, 2009) & (E. Vasas & Styner, 2003).

Figure 10: Mortar Tube

The design of the mortar tube is intricate, featuring a bore with tight tolerances and external features that require complex milling operations. These external features are crucial for the seamless integration of the mortar tube with other components within the PDD system. The precisely machined bore ensures accurate and reliable performance during the deployment process. This precision is vital for maintaining the structural integrity of the mortar tube under the high pressures generated during the deployment sequence, ensuring the effective expulsion of the parachute pack and associated components.

1.3.2.2 Sabot

As shown in Figure 9, the sabot, also referred to as the piston, is positioned at the bottom of the mortar tube and serves as the base for the parachute pack. The sabot is engineered to function as a free-running piston within the mortar tube, featuring O-ring seals that effectively contain the gas generated by the gas generator (E. Vasas & Styner, 2003). These seals ensure that the pressure build-up within the mortar tube is directed efficiently towards propelling the parachute pack. The sabot is designed to achieve ejection velocities typically exceeding 40 meters per second (Rowan, Moran, & S. Adams, 2009).

Figure 11: Sabot Assembly

1.3.2.3 Parachute Pack

The parachute pack is a complex and dynamic elastic system composed of several key components: the canopy, suspension lines, and risers, all of which are carefully folded and tightly packed into a deployment bag. This bag is placed on a support structure, often referred to as the sabot, and secured within the canister by a riveted or mechanical lid. The configuration of the parachute pack within the mortar canister is designed to ensure a controlled and reliable ejection upon activation. Figure 12 provides a cross-sectional view of the typical layout, illustrating the arrangement of the parachute pack and the placement of the sabot within the mortar canister (Pawlikowski, 1986).

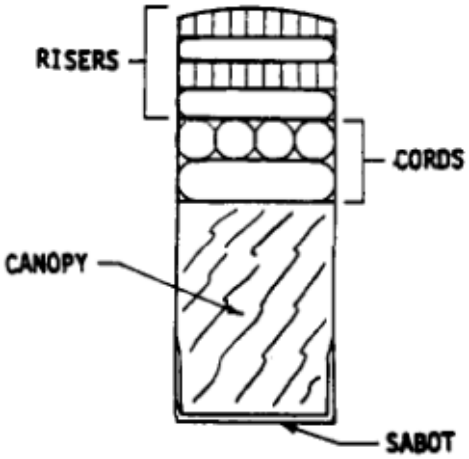

Figure 12: Parachute Pack Cross-Sectional View (Pawlikowski, 1986)

Before insertion into the mortar tube, the parachute undergoes a meticulous folding and packing process to fit into the parachute bag. The packing density is a critical factor that affects the performance of the entire system. Parachutes with insufficient packing density may lead to excessive compressibility, which can result in reduced deployment force and a shorter effective stroke of the piston or ejection mechanism. This reduced stroke can lead to incomplete or delayed deployment, compromising the system's overall effectiveness. On the other hand, a higher packing density provides greater resistance

to compressibility, ensuring that the necessary force is maintained during deployment.

Achieving the correct packing density typically requires mechanical assistance, with hydraulic presses often employed to compress the parachute pack to the required levels. While certain densities may be ideal for performance, the process of reaching these packing levels presents challenges. As the parachute material approaches its solid density, both the compressive force and the time needed to achieve the desired packing increase significantly. This balance between packing force and time is a key consideration during the preparation of the parachute pack. (Pleasants, 1974)

During the deployment process, the mortar system is activated, causing the gas generator to ignite and build pressure within the canister. This pressure propels the parachute pack out of the mortar tube. As the pack is expelled, retention ties or other securing mechanisms are severed, allowing the pack to displace the cover or cap at the top of the mortar tube. Depending on the specific system design, the pack may or may not include additional components such as a sabot capture bag, which is used in some systems to ensure that the sabot remains contained within the mortar after the parachute pack is deployed. In systems where this is implemented, the capture bag inverts during deployment to contain the sabot, preventing any unintended interference during the parachute inflation phase.

Once the parachute pack has been expelled from the mortar tube, it continues to unfold as the suspension lines stretch out to their full length. At this stage, the parachute canopy begins to inflate, catching the air and creating the necessary drag to decelerate the vehicle or object to which it is attached. The smooth transition from the mortar ejection to full canopy inflation is crucial for ensuring a stable and controlled deployment, minimizing the risk of tangling or malfunction (E. Vasas & Styner, 2003).

1.3.2.4 Lid & Shear Pins

The lid is a crucial component of the parachute deployment system, serving as the cap that seals the top of the mortar tube. It ensures that the parachute remains securely packed and protected within the canister during all phases of the mission until deployment. The lid, typically constructed from lightweight and robust materials like aluminium, is attached to the top of the mortar tube using **shear** pins. These shear pins are designed to withstand the forces acting on the system during handling and flight but are calibrated to break under specific conditions during the deployment sequence.

During parachute deployment, the gas generator ignites, producing high-pressure gas that drives a piston (or sabot) upwards inside the mortar tube. This piston compresses the parachute pack against the lid. The pressure behind the piston builds rapidly, and the shear pins are designed to break when the pressure reaches a precise threshold. This pressure is carefully calculated to ensure that once the pins break, the piston has generated enough force to propel the parachute pack with the correct acceleration, ultimately achieving the desired exit velocity**.** (Pleasants, 1974).

Figure 13: Lid & Shear Pins Assembly

The shear pins act as critical control points in this process. Rather than simply holding the lid in place, they serve a dual purpose: (1) maintaining the lid securely during all phases before deployment, and (2) ensuring that the parachute is ejected at the correct speed. The pins are engineered to break at a specific pressure, which is determined by the forces required to accelerate the parachute pack to its target exit velocity. This velocity is key to the successful deployment of the parachute, as it influences how effectively the parachute unfurls and inflates during descent.

The shear strength of the pins is calculated based on the necessary force to eject the parachute at the optimal speed, factoring in the mass of the parachute pack and the dynamics of the expanding gas. The

breaking pressure of the shear pins is also carefully chosen to balance the force applied to the parachute pack, avoiding excessive compression that could damage the canopy while still delivering enough force for effective ejection.

The lid itself features an external lip that ensures precise alignment with the top of the mortar tube, aiding in the assembly process. This lip also helps secure the lid in place during pre-deployment, preventing any unwanted movement or misalignment.

Additionally, the clearance between the lid and the mortar tube plays a role in the performance of the shear pins. An increase in this clearance can shift the mechanical failure mode of the pins from pure shear to a combination of shear and bending. This change affects the force required to break the pins and, consequently, the timing of the parachute's release. Furthermore, the fit between the shear pins and their holes can influence the shear load experienced by the pins, which is another critical factor in ensuring a controlled and precise deployment. (Pleasants, 1974).

1.4 Research Objective and Research Question

The objective of this research is to develop and validate a high-fidelity simulation framework for modelling the dynamics of a parachute deployment device used in planetary entry, descent, and landing systems. The study aims to accurately capture the physical processes involved in parachute deployment, including gas generator combustion, plenum pressurization, parachute pack compression, and ejection dynamics. By integrating experimental data and numerical simulations, this research seeks to enhance the predictive capabilities of PDD modelling, enabling better design optimization and improved reliability in future planetary missions.

To achieve this objective, the study focuses on developing a comprehensive numerical model capable of simulating the full deployment sequence. The research question and sub-questions outlined below provide a structured approach to investigating and addressing key challenges in PDD modelling.

1.4.1 Research Question

How can a high-fidelity numerical model be developed to accurately simulate the dynamics of a Parachute Deployment Device for planetary Entry, Descent, and Landing applications?

To answer the main research question, three key sub-questions are formulated to address specific aspects of the PDD modelling process:

- What are the key physical and operational parameters influencing PDD performance, and how can they be integrated into the model?
- How can experimental data be used to validate the numerical model and improve its predictive accuracy?
- What optimization strategies can be applied to enhance the reliability and efficiency of PDD systems for planetary exploration missions?

These sub-questions provide a structured approach to addressing the main research question, guiding the study toward a comprehensive understanding of PDD modelling and performance optimization.

Chapter 2

Solid Combustion & Dynamics

This chapter introduces the core theoretical frameworks essential to understanding the physical processes governing the Parachute Deployment Device (PDD) system. The focus of this chapter is divided into two major areas: solid combustion and the dynamics of both the gas and solid bodies within the system.

The chapter begins with an exploration of solid combustion theory, which forms the foundation of gas generation within the PDD system. Understanding how solid propellants burn, the ignition mechanisms, and the models that describe the burning surface and rate are critical to simulating the behaviour of the gas generator. This section delves into the intricacies of ignition models, surface regression, and the burning rates of propellants, highlighting the importance of accurately modelling these processes to predict gas output and system performance.

Following this, the discussion transitions into energy losses, which affect the efficiency of the gas generator and the dynamics of the deployment system. The chapter examines the heat losses, both convective and radiative, and the frictional losses arising from the interaction of the sabot and parachute pack within the PDD system. Additionally, the impact of gravity and drag losses, particularly during ground tests, is considered in this section.

The latter part of the chapter shifts to fluid dynamics, focusing on the behaviour of the gases generated by the combustion process. It covers the properties of gases under high pressure and temperature, the flow through the orifices, and the conservation laws governing mass, momentum, and energy within the system. These principles are crucial for modelling the gas flow and predicting the forces acting on the solid components of the system.

Finally, the chapter presents the solid body dynamics governing the motion and interaction of the piston, parachute pack, and other components in the PDD system. This section covers the compression characteristics of the parachute pack, the spring and damping models used to describe its behaviour, and the translational motion of both the piston and parachute pack. Understanding these dynamics is essential for predicting the system's overall performance, from gas generation to parachute ejection.

2.1 Solid Combustion

Solid combustion is a fundamental process in the operation of gas generators used in parachute deployment devices. Understanding the mechanisms of ignition, the behaviour of the burning surface, and the burning rate are essential for designing reliable and efficient systems. This chapter delves into the various models that describe these processes. To develop an accurate simulation model for our gas generator system, we must thoroughly understand and define these aspects of solid combustion.

Solid-propellant combustion models can be categorized into two main types: purely one-dimensional models and non-one-dimensional models. The purely one-dimensional models encompass classical and phenomenological models, often incorporating various generalizations of the Zel'dovich approach. Non-one-dimensional models include those with local non-one-dimensionality, which is inevitably accompanied by local unsteadiness. This unsteadiness can be mitigated through the process of averaging.

Unsteady solid-propellant combustion models, like their steady-state counterparts, face a fundamental challenge due to the lack of detailed information regarding the chemical and physical processes occurring in the condensed phase (Gusachenko & Zarko, 2008). It is important to note the limitations of extending the purely one-dimensional approach to regions of instability. Future advancements in unsteady (and quasi-steady-state) solid-propellant combustion models for homogeneous compositions could involve incorporating local non-one-dimensionality and accounting for the unsteadiness arising from the instability of the subsurface reaction zone. Additionally, verifying the potential existence of chemical instability capable of inducing similar non-one-dimensionality and unsteadiness could provide further avenues for development.

2.1.1 Ignition Model

Accurately reproducing ignition phenomena is essential for interior ballistic modelling, especially in the context of gas generators used in parachute deployment devices. Australia's Defence Science and Technology Organisation (DSTO) employs the Casbar code for modelling gun interior ballistics, solving the governing equations for the transient flow of chemically reacting gas and particulates within a finite volume discretization of the computational domain. Currently, Casbar models propellant ignition using a simple go/no-go condition, where ignition occurs if the gas surrounding the propellant exceeds a defined ignition temperature.

Solid propellant ignition and the transition to self-sustained combustion is a complex physicochemical process. This process is crucial for the performance of gas generators in parachute deployment systems. Ignition is typically initiated by an external energy source, such as a pyrotechnic igniter, emitting heat energy and hot particles into the propellant bed. The ignition process involves multiple simultaneous energy sources, including convection of hot gases, conduction from impinging hot particles, radiation from igniter gases and particles, and heat from atom recombination and vapor condensation.

Gun and rocket propellants traditionally consist of several chemical ingredients combined either heterogeneously or homogeneously. Homogeneous propellants, such as single-base nitrocellulose or double-base nitrocellulose and nitro-glycerine, are common in gun applications, while heterogeneous propellants, such as those containing AP, HMX, or RDX, are more common in solid rocket applications. Composite propellants are increasingly used in gun applications, but AP-based propellants are avoided due to the corrosive hydrogen chloride produced during combustion.

The ignition process involves several complex stages, transitioning from the initial application of heat to steady-state combustion, where solid propellants are converted to gas products through oxidation at extremely high pressures and temperatures. This occurs over a fraction of a second, creating a highly hostile environment that remains not fully understood despite decades of research. Significant condensed phase reactions, coupled with numerous gas phase reactions, complicate the formation of a

suitable model of solid propellant ignition and combustion.

When a propellant is subjected to sufficient heat energy to achieve self-sustained combustion, three significant reaction regions develop, defined by the thermal state of the propellants or their constituents:

Solid Phase Region: This region consists of the propellant in its initial solid state. Upon the application of heat, the surface temperature increases, conducting heat into the solid core until a phase change occurs. Solid-phase exothermic reactions may lead to thermal degradation, though these are often negligible.

Transition Region: This region consists of either a two-phase mixture of melted liquid propellant and evaporated gas or a sublimation interface. Propellants may exhibit melting behaviour, forming a melt layer, or transition through pyrolysis mechanisms. This layer, often referred to as the foam layer, is characterized by complex reactions such as vaporization, condensation, decomposition, and oxidation.

Gas Phase Region: In this final region, evaporated species react and decompose into other species. The gas layer exhibits pressure-dependent behaviour with sub-layers like the fizz zone and dark zone. In the flame zone, oxidation reactions release significant energy, sustaining combustion through heat feedback in the form of radiation, convection, and conduction.

The gas layer itself exhibits transient, pressure-dependent behaviour, with multiple sub-layers. At low burning pressures (below approximately 1 MPa), no visible flame exists above the burning propellant surface. As pressure increases, a weak flame may become visible, eventually appearing attached to the surface at higher pressures. The region between the burning surface and visible flame can consist of the fizz zone and the dark zone, where rapid reactions and slower oxidation processes occur, respectively. The flame zone releases significant energy, approaching the adiabatic flame temperature, sustaining the combustion process until the propellant is consumed.

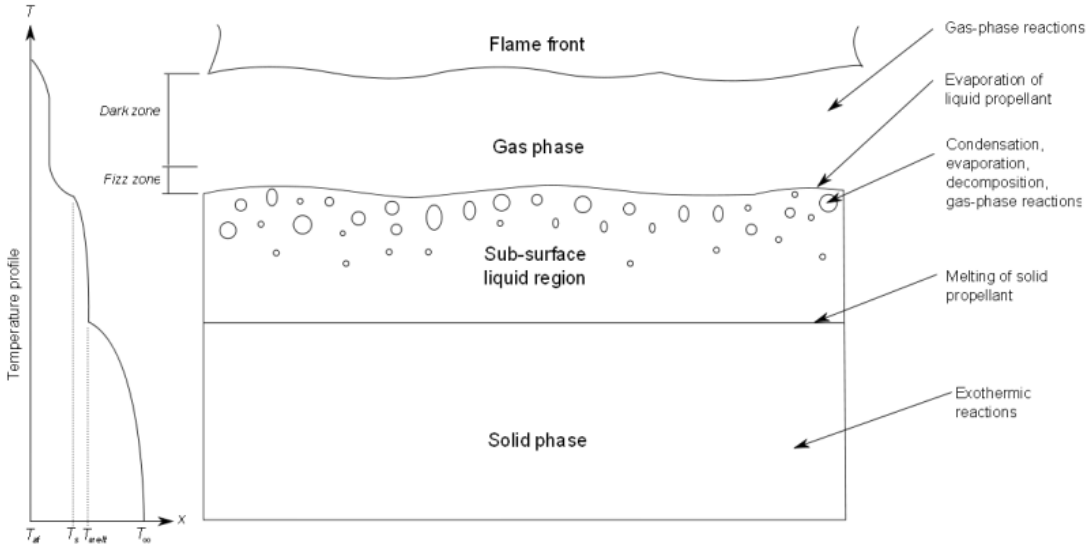

Figure 14: Solid Propellant Combustion Schematic (Harrland & Johnston, 2012)

Figure 14 illustrates the three significant reaction regions and the transition from solid to gas phase during combustion. (Harrland & Johnston, 2012).

Gas-Phase Reaction Ignition Models

The model used in our simulation tool is based on the Gas-phase reaction ignition models, which consider a comprehensive range of physical mechanisms occurring during propellant combustion, thereby forming a complete mathematical description of the process (Beckstead, Puduppakkam, Thakre, & Yang, 2007).

In the gas-phase reaction model, the solid phase region is modelled by considering the conservation of energy. For propellant mixtures, properties are averaged based on the mass fraction of the constituents. Solid-phase exothermic reactions are typically neglected as they do not significantly contribute to the ignition transient.

External to the solid phase is the two-phase subsurface region, consisting of melted liquid propellant and evaporated propellant gas. This region involves numerous complex physicochemical processes, such as thermal decomposition, evaporation, bubble formation, gas-phase reactions within bubbles, and transport of mass and energy between phases. A spatial averaging technique is used to simplify these interactions. A fractional-voidage Φ_f is used to define the cross-sectional areas assumed by the gas and condensed phases, with the gas bubbles occupying a fractional area $A_g = \Phi_f A$, where A is the cross-sectional area of the propellant sample. The conservation equations are then combined using this fractional voidage.

In the subsurface region, both evaporation and condensation occur simultaneously. The net difference between these rates is determined empirically. The mass conversion rate due to evaporation is then found by multiplying the net mass conversion rate by the specific surface area.

The following gas-phase analysis (Beckstead, Puduppakkam, Thakre, & Yang, 2007) focuses on the conservation of mass, energy, and species transport for a multi-component chemically reacting system. The system of equations accommodates finite-rate chemical kinetics and variable thermophysical properties. Mass diffusion velocity V_i of an individual species arises from both concentration and temperature gradients, where D_{T_i} is the thermodiffusion coefficient [K^{-1}], D_i is the diffusion coefficient [m^2/s], T and T_g are the temperature and the gas phase temperature respectively [K] and x the spatial coordinates [m]:

$$V_i = -D_i \frac{1}{X_i}\frac{\partial X_i}{\partial x} + D_i \frac{D_{T_i}}{X_i}\frac{1}{T}\frac{\partial T_g}{\partial x} \tag{2.1}$$

The ideal gas law for a multi-component system and suitable boundary conditions close the system of equations. Given its comprehensive nature, the gas-phase reaction model includes both solid and gas phases. The solid phase conservation of energy equation considers surface regression:

$$\rho_s c_s \frac{\partial T_s}{\partial t} + \rho_s \dot{r} c_s \frac{\partial T_s}{\partial x} = k_s \frac{\partial^2 T_s}{\partial x^2} \tag{2.2}$$

Here, the subscript s defines the solid phase, ρ is the density [kg/m^3], $\dot{r}$ is the linear regression rate [m/s] and k the thermal conductivity [W/mK].

The boundary condition at the propellant surface includes the energy associated with the phase change from solid to gas at $x = 0$:

$$-k_s \frac{\partial T_s}{\partial x} = \dot{q}(t) + \rho_s \dot{r} \dot{q}_{l-g} \tag{2.3}$$

Where $\dot{q}_{l-g}$ is the heat associated with phase change and $\dot{q}$ is the rate of heat flux [W/m^2]. The

subsurface region is assumed to be infinitely thin and occurs only at the interface between the solid and gas regions.

Mass conservation within the solid phase (assuming a single-component system) is expressed as:

$$\dot{m}_s = \rho_s \dot{r} \tag{2.4}$$

indicating that the rate of mass change within the solid phase is due to the regression of the propellant surface, multiplied by the density. A mass balance between the solid and gas phases yields the conservation of mass equation for the gas phase:

$$\dot{m}_g = \rho_g u_g = \dot{m}_s = \rho_s \dot{r}_s \tag{2.5}$$

Here, the subscript g defines the gas parameters and u is the velocity [m/s].

Thus, the rate of mass addition to the gas phase equals the mass loss from the solid phase due to evaporation or sublimation. At the propellant surface, the phase change process determines the rate of regression r_s. Various models approximate the mass transfer between phases, with the decomposition of the solid often modelled through a pressure-dependent surface regression:

$$\dot{r} = \begin{cases} Ap^n e^{\left(-E_A/R\left(\frac{1}{T_{ign}} - \frac{1}{T_{surf}}\right)\right)}; & T_{surf} < T_{ign} \\ Ap^n; & T_{surf} = T_{ign} \end{cases} \tag{2.6}$$

Where E_A is the activation energy for the pyrolysis equation, T_{surf} is the surface temperature [K], T_{ign} is the ignition temperature which is a parameter of the propellant specie [K], R is the Universal gas constant [J/mol·K], A is the surface area [m²], p is the pressure [Pa] and n the burning rate law exponent. This model allows a smooth transition from non-combusting decomposition to steady-state burning.

The conservation of energy equation for the gas phase is:

$$\rho_g c_g \frac{\partial T_g}{\partial t} + \rho_s \dot{r} c_g \frac{\partial T_g}{\partial x} = k_g \frac{\partial^2 T_g}{\partial x^2} + \dot{q}_g \dot{w}_g(x) \tag{2.7}$$

where $\dot{q}_g$ represents the heat released, and $\dot{w}_g$ is the mass of reactant produced by the gas chemical reactions. Casbar includes provisions for multi-component gas-phase reactions, allowing complex gas kinetics of propellant combustion to be modelled using Arrhenius rate equations for intermediate reaction steps. The boundary condition applied to the gas region is:

$$T_{x=0} = T_{surf} \tag{2.8}$$

where T_{surf} is the propellant surface temperature. In this model, ignition is assumed to occur when the heat feedback to the propellant surface sustains combustion without external influence, although this ignition point is somewhat arbitrary (Harrland & Johnston, 2012).

Defining the Point of Ignition

Establishing deflagration within solid propellant is challenging, making the specification of the point of ignition somewhat vague. Ignition can be considered to have occurred when, upon the removal of the ignition stimuli, the propellant achieves self-sustained combustion with no further application of energy. For gas-phase reaction models, defining an ignition point is somewhat arbitrary, as they can model the transition from a solid propellant at ambient conditions to steady-state combustion.

In experimental investigations, ignition is often established by light emission, pressure and/or temperature rise, behaviour of the propellant after the removal of ignition stimuli, or examination of the propellant grain after quenching. In mathematical investigations, ignition is typically defined to have occurred when a certain surface temperature has been reached (the ignition temperature), the rate of temperature rise is above a specified value, the rate of heat generation is greater than the rate of heat loss to the surroundings, or by observing the behaviour of the mathematical model after the artificial ignition stimuli has been removed. Selecting an ignition criterion relevant to the process being modelled and the ignition model itself is crucial (Harrland & Johnston, 2012).

2.1.2 Burning Surface Model

Optimizing the gasification rate for a propulsion charge and designing granulations to achieve desired performance requires a quantitative formulation of the total propulsion charge form-function. This formulation expresses the fraction of charge burnt (z) at any time (t) as a function of grain geometry and surface regression distance (r) (Stals, 1975):

$$z_i = \sum_{i=1}^{j} a_i r^i \quad , \qquad i = 1, 2, \ldots, j \tag{2.9}$$

where the grain geometric coefficients a_i are explicitly defined based on grain dimensions. This model maintains physical relevance across all grain shapes and is adaptable to account for radial chemical gradients within grains, such as those resulting from deterrents and inhibitors. The regression distance can be measured experimentally once the grain flame is extinguished, and its time derivative (dr/dt) provides the grain surface regression rate. Additionally, sliver burn can be explicitly formulated in terms of r.

Using explicit geometric constants (a_i) allows for comprehensive parametric studies on the impact of grain geometry on propulsion charge performance. This method offers several advantages, including versatility, as it is applicable to all grain shapes and capable of incorporating complex geometrical and chemical characteristics. The regression distance can be empirically validated through experimental measurement, providing a reliable foundation for modelling. Furthermore, it facilitates detailed parametric studies and optimization of grain geometry for enhanced performance.

Given that a cubic polynomial in r adequately defines most grain geometries, the following equation is employed as the foundational form-function:

$$z = a_1 r + a_2 r^2 + a_3 r^3 \tag{2.10}$$

The geometric constants a_1, a_2 and a_3 are derived for cylindrical multiperforated grains later in this section. This formulation significantly enhances the ability to predict and optimize propulsion charge performance by providing a robust model that incorporates essential geometric and chemical characteristics (Stals, 1975).

Historically, the burning of solid propellant grains has been assumed to occur under the following idealized conditions:

a. **Homogeneity**: Each grain is chemically and physically homogeneous in all directions, with no cracking or mechanical degradation during ignition and combustion processes.

b. **Uniformity**: The segment of the total charge consists of chemically and geometrically identical grains that ignite simultaneously and uniformly within the entire segment.

c. **Instantaneous Ignition**: Each grain is ignited instantaneously over all its uninhibited external surfaces, with the speed of igniter flame spread being much greater than the initial propellant

burning rate (P. Vieille, 1893).

d. **Parallel Layer Burning**: The uninhibited grain surface burns in parallel layers and perpendicular to the surface, with the same surface regression rate across the entire burning surface (G. Piobert, 1839).

However, these assumptions are often violated to varying degrees. Ideal propellant production conditions rarely achieve perfect homogeneity and uniformity, leading to variations and inconsistencies in grain production. While Vieille's assumption holds for porous propellant beds such as artillery charges, it may not apply to compact, high-density small arms charges where non-isochronous ignition can occur. Additionally, Piobert's law is only semi-quantitative, particularly within the perforations of multiperforated grains, and is highly dependent on the specific conditions. These violations cannot be easily quantified or statistically reproduced between different lots of the same propellant. Therefore, assumptions (a) to (d) are retained to provide geometric form functions that, while semi-quantitative, are useful in propellant grain design, controlling propellant mass burning rates, and subsequent computations on interior ballistics and closed chamber performance (Stals, 1975).

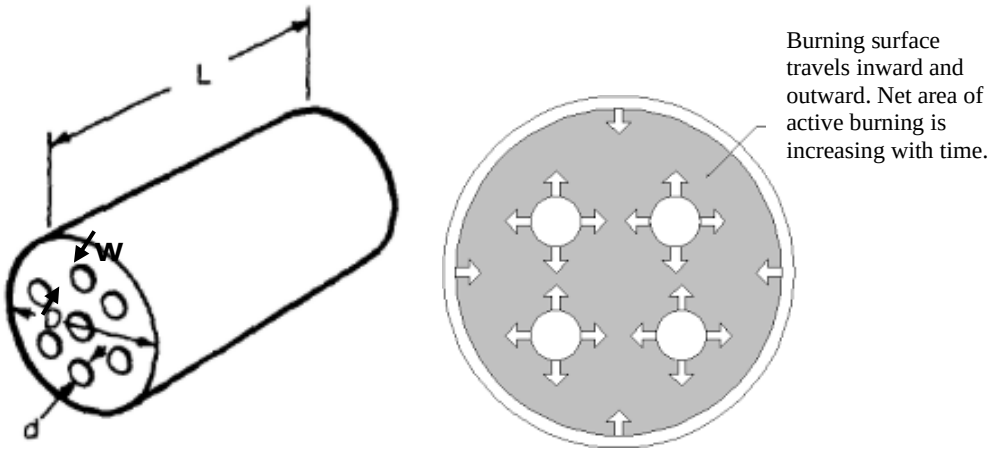

Figure 15: Multi-Perforated Grain

2.1.2.1 Calculation of the Burning Surface Area

Prior to Web Burnthrough

For the multiperforated grains with $N = 7$ perforations as seen on Figure 15, symmetrical perforated grains, and equal webs, the burning surface area and the fraction of charge burnt before web burnthrough can be calculated using the following formulae:

Given:

- S_0 is the initial surface area of the grain
- V_0 is the initial volume of the grain
- D is the outer diameter of the grain
- N is the number of perforations
- d is the diameter of each perforation
- L is the length of the grain
- r is the grain surface regression distance
- u is defined as $2r$

The initial surface area S_0 is given by:

$$S_0 = \pi L(D + Nd) + 0.5\pi(D^2 - Nd^2) \quad (2.11)$$

The initial volume V_0 is given by:

$$V_0 = 0.25\pi L(D^2 - Nd^2) \quad (2.12)$$

The burning surface area S at any burn distance u is given by:

$$S = \pi(L - u)[D - u + N(d + u)] + 0.5\pi[(D - u)^2 - N(d + u)^2] \quad (2.13)$$

Where the geometric coefficients $a_1, , a_2$ and a_3 are:

$$a_1 = 2[2L(D + Nd) + D^2 - Nd^2]/L(D^2 - Nd^2) \quad (2.15)$$

$$a_2 = -4[2(D + Nd) - L(N - 1)]/L(D^2 - Nd^2) \quad (2.15)$$

$$a_3 = -8(N - 1)/L(D^2 - Nd^2) \quad (2.16)$$

During Sliver Burn

Sliver burn refers to the combustion process that occurs after the primary web of a multiperforated grain has been consumed. In multiperforated propellant grains, the initial burning phase involves the regression of the web until it burns through. Once the web is burned through, the remaining sections of the grain, known as slivers, continue to burn.

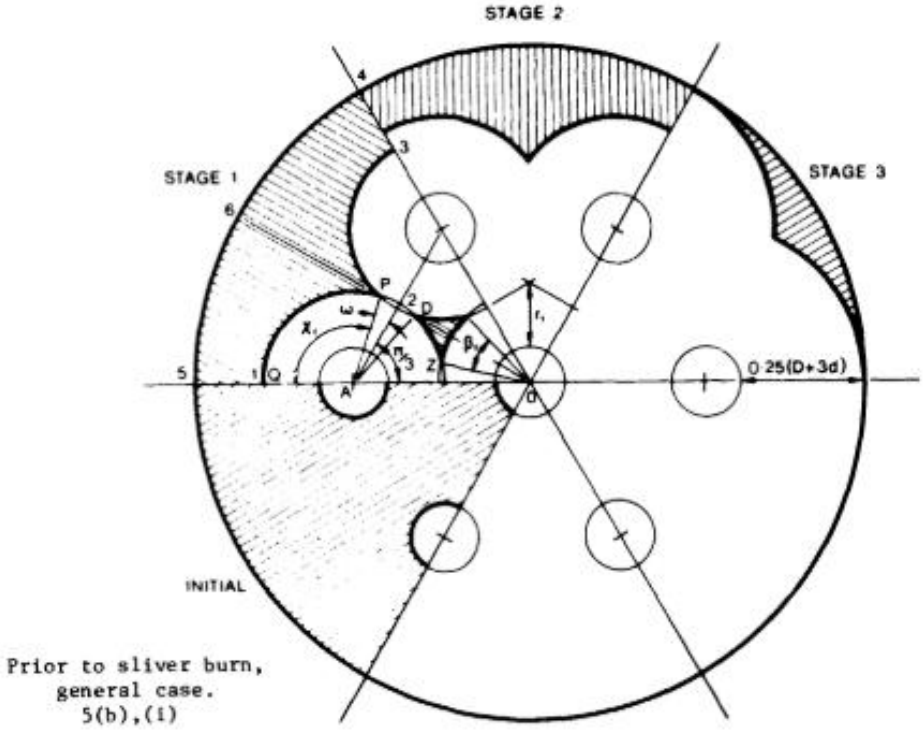

Figure 16: Propellant Grain Burning Stages (Stals, 1975)

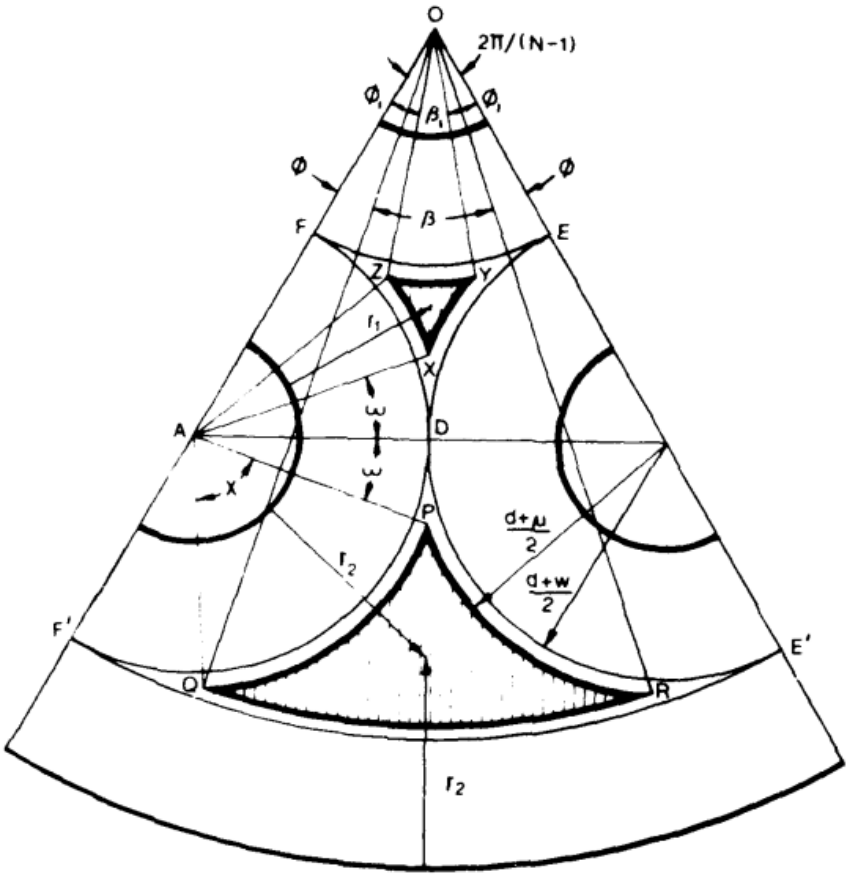

Figure 17: Geometry for Sliver Burn Process (Stals, 1975)

Geometric Considerations

Assume six symmetric perforations arranged on a circle of radius $0.25(D+d)$. Key geometric parameters include (Figure 17):

$$\mathrm{OA} = 0.25(\mathrm{D} + \mathrm{d})$$

$$\mathrm{AD} = \mathrm{OA}\sin(\pi/(\mathrm{N}-1)) = 0.5\mathrm{OA}$$

$$\mathrm{OZ} = \mathrm{AQ} = \mathrm{AZ} = 0.5(\mathrm{d} + \mathrm{u})$$

$$\mathrm{OQ} = 0.5(D - u)$$

$$\omega = \arccos(\mathrm{AD}/\mathrm{AQ}) \qquad (2.21)$$

$$\mathrm{OAQ} = \arccos[(OA^2 + AQ^2 - OQ^2)/2OA.\ \ AQ] \qquad (2.22)$$

$$\chi = \mathrm{OAQ} - \omega - \pi(0.5 - 1/(\mathrm{N}-1)) \qquad (2.23)$$

$$\Phi = \arccos[(OA^2 + OQ^2 - AQ^2)/2OA.\ \ AQ] \qquad (2.24)$$

$$\beta = 2(\pi/(\mathrm{N}-1) - \Phi) \qquad (2.25)$$

$$\Phi_1 = arcos(OA/2.\ OZ) \qquad (2.26)$$

$$\beta_1 = 2\pi/(N-1) - 2\Phi_1 \qquad (2.27)$$

Surface Areas

The areas of lateral surfaces, end surfaces, and total sliver surfaces are calculated as follows:

- Lateral surfaces of large slivers, for any regression distance $w > u > u_2$:

$$S_L = (N-1)(L-u)(\beta.OQ + 2\chi.AQ) \quad (2.28)$$

- Lateral surfaces of small slivers, for $w > u > u_1$:

$$S_l = (N-1)(L-u)(3\ OZ.\beta_1) \quad (2.29)$$

- End surfaces of large slivers, for $w > u > u_2$:

$$S_E = 2(\mathrm{N}-1)\{\mathrm{OQ}\sin(0.5\beta)\,[(2\mathrm{AQ}\sin(0.5\chi))^2 - (\mathrm{OQ}\sin(0.5\beta))^2]^{\frac{1}{2}} + 0.5OQ^2(\beta - \sin(\beta)) - AQ^2(\chi - \sin(\chi))\} \quad (2.30)$$

- End surfaces of small slivers, for $w > u > u_1$:

$$S_e = 2(\mathrm{N}-1)OZ^2\{sin^2(0.5\beta_1)\ 1.73206 - 1.5[\beta_1 - \sin(\beta_1)]\} \quad (2.31)$$

Total Area

The total area of sliver surfaces is therefore:

$$\mathrm{S} = S_L + S_l + S_E + S_e \quad (2.32)$$

In summary, the burning surface area calculations for multiperforated propellant grains, both prior to web burnthrough and during sliver burn, are crucial for optimizing the performance of propulsion charges. This method, based on the model developed by (Stals, 1975), accounts for the complex geometric configurations and surface regression dynamics, providing accurate predictions of burn fraction and gas generation rates. Utilizing these calculations allows for the enhancement of propellant charge design and performance.

2.1.3 Burning Rate Model

The Burning Rate Model describes the relationship between pressure, temperature, and the burn rate of the solid propellant. It captures how the propellant's combustion progresses under different conditions.

Burning rate:

$$\begin{cases} r = \beta\left(\frac{P}{P_{ref}}\right)^{\alpha} e^{\left(-\frac{Ea}{R}\times\left(\frac{1}{T_{ig}}-\frac{1}{T}\right)\right)} & \text{if } T < T_{ig} \quad (2.33) \\ r = \beta\left(\frac{P}{P_{ref}}\right)^{\alpha} & if\ T > T_{ig} \quad (2.34) \end{cases}$$

Where:

$\beta = \beta_0\left(1 + \sigma(T_{env} - T_0)\right)$	# Burn law coefficient [mm s-1]
P_{ref} = 1E6 Pa	# Reference pressure of 1MPa
β_0 = 0.0023	# Burn law coefficient (at 21°C) [m/s]
σ = 0.0015	# Temperature sensitivity burn law coefficient [K^-1]
α = 0.78	# Burn law exponent
T_0 = 273.15 + 21	# Constant reference temperature [K]
T_{ig} = 273.15 + 190	# Auto-ignition temperature [K]
Ea = 197	# Activation energy [J/mol]

2.2 Energy Losses

In the PDD system, accurately modelling energy losses is essential for predicting overall performance. The primary energy losses in the system are heat losses and friction losses. Heat losses occur both within the gas generator and the plenum, impacting the efficiency of gas expansion and pressure buildup. Additionally, friction losses involve the friction experienced by the sabot and the parachute pack, affecting the deployment velocity of the parachute. Understanding these energy losses is vital for optimizing the performance of the PDD system. By accurately modelling these losses, we can better predict the system's behaviour under various conditions and enhance its design and operation. This section delves into the different types of energy losses and their respective models.

2.2.1 Heat Losses

According to (Arpad & Channon, 1979), the mode of heat loss in the parachute deployment device (PDD) system varies as the propellant burns. Initially, when the propellant is first ignited, convection predominates as the primary mode of heat loss. As the burning continues, radiative heat loss becomes more significant. Therefore, heat loss is analysed into its convective and radiative components. During the combustion of the propellant, gas generation leads to convective heat transfer to the chamber walls, accompanied by radiative heat losses. Once the propellant is fully consumed, convective heat loss becomes negligible compared to radiative heat loss. This section will explore the mechanisms of convective and radiative heat losses and their contributions to the overall energy losses in the PDD system (Price & Juhasz, 1977).

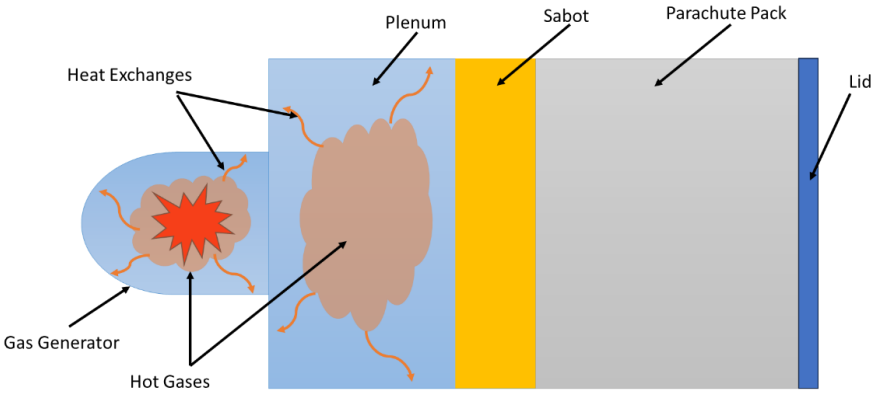

Figure 18: PDD Heat Losses Diagram

2.2.1.1 Convective Heat Losses

To compute the convection heat loss rate ($\dot{Q}_c$) at any given point in the analysis, the following equation is used:

$$\dot{Q}_c = h_c A(T_g - T_w) \tag{2.35}$$

where:

- $\dot{Q}_c$ is the convective heat loss rate,
- h_c is the convective heat loss coefficient, which will be calibrated,
- A is the total wall surface area,
- T_g is the temperature of the gas,
- T_w is the temperature of the wall.

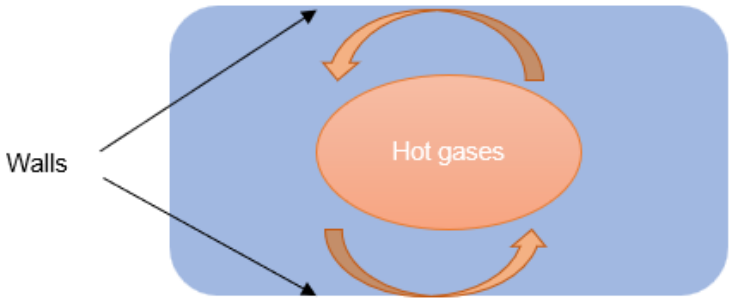

Figure 19: Convective Heat Losses

This equation accounts for the heat transferred from the hot gases generated by the burning propellant to the chamber walls through convection. The convective heat loss coefficient h_c will be determined through calibration to accurately model the heat transfer dynamics in the system.

2.2.1.2 Radiative Heat Losses

To compute the radiative heat loss rate ($\dot{Q}_r$) at any given point in the analysis, the following equation is used:

$$\dot{Q}_r = \varepsilon_g \varepsilon_w A \sigma \left(T_g^{\,4} - T_w^{\,4} \right) \qquad (2.36)$$

where:

- $\dot{Q}_r$ represents the rate of heat transfer due to radiation (W),
- ε_g is the emissivity of the gases,
- ε_w is the emissivity of the mortar wall,
- A represents the total surface area of the canister exposed to radiation (m^2),
- σ is the Stefan-Boltzmann constant, approximately equal to 5.67×10E−8 $W/(m^2 \cdot K^4)$,
- T_g represents the temperature of the gases (K),
- T_w represents the temperature of the mortar wall (K).

This equation accounts for the heat transferred from the hot gases to the canister walls through radiation. The emissivity values (ε_g and ε_w) and the surface area (A) are crucial parameters in determining the radiative heat loss. The Stefan-Boltzmann constant (σ) provides a standard measure for the intensity of thermal radiation emitted by a black body in thermal equilibrium.

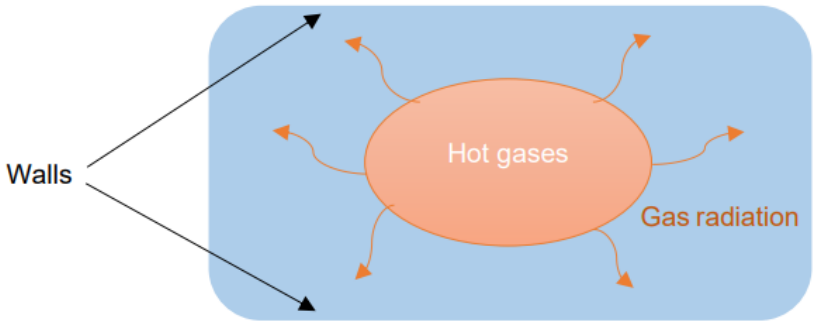

Figure 20: Radiative Heat Losses

2.2.2 Friction Losses

Friction losses play a significant role in the overall performance and efficiency of propulsion systems. In the context of PDD, two primary sources of friction losses are considered: the friction associated with the sabot and the friction encountered by the parachute pack. Understanding and accurately modelling these friction losses are essential for predicting the system's behaviour and optimizing its performance.

2.2.2.1 Sabot's Friction Model

In analysing the friction losses associated with the piston within the PDD system, it is assumed that the friction is primarily generated by the two O-rings. These O-rings are compressed between the walls of the mortar tube and the grooves of the piston. By knowing the squeeze percentage and the Young's modulus of the O-ring material, we can determine the normal force exerted by each O-ring.

To calculate the normal compression force (F_n) exerted by each O-ring, the following equation is used:

$$F_n = E \cdot \frac{\delta}{d_2} \cdot A \tag{2.37}$$

Here, E represents the elastic modulus of the O-ring material, A is the radial deformation, d_2 is the cross-section diameter of the O-ring, and A is the contact surface area between the O-ring and the tube wall. This calculation provides the normal force exerted by the compressed O-ring.

Once the normal force is determined, the frictional force (F_s) can be calculated using:

$$F_s = \mu_s \cdot F_n \tag{2.38}$$

In this equation, μ_s is the coefficient of friction, and F_n is the normal force. This model effectively describes the frictional losses due to the O-rings in the PDD system, allowing for a more accurate prediction of the system's performance and the impact of frictional forces.

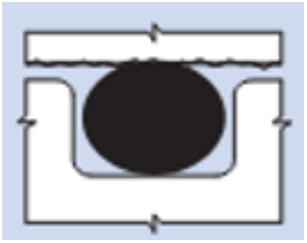

Figure 21: O-Ring Bed

2.2.2.2 Parachute Pack Friction Model

Before Shear Pins Break

During the operation of the PDD system, we assume that friction is generated primarily by the interaction between the parachute pack and the mortar tube walls. When the piston compresses the parachute pack against the lid, it induces radial expansion of the pack. This expansion is constrained by the walls of the mortar tube, creating normal stress. As the parachute material moves within the mortar tube, this normal stress results in friction.

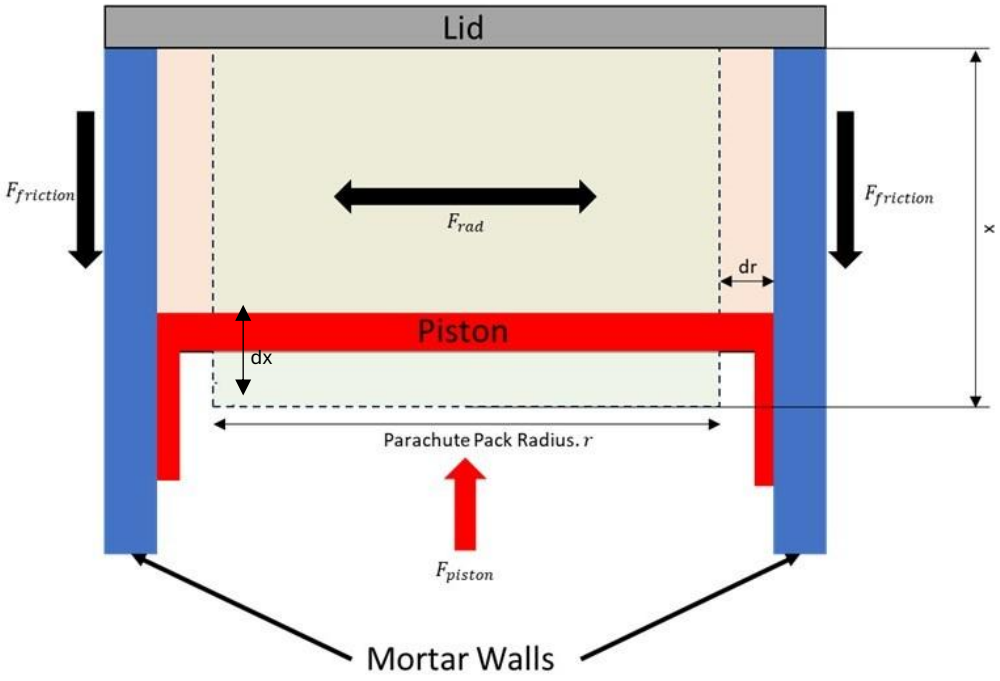

Figure 22: Parachute Pack Compression Diagram

The frictional force (F_μ) is defined as the product of the radial force (F_{rad}) and the friction coefficient (μ):

$$F_\mu = F_{rad} \times \mu \tag{2.39}$$

To determine F_{rad}, we start by examining the strains and stresses within the parachute pack. The axial strain (ϵ_{axi}) and radial strain (ϵ_{rad}) are given by:

$$\epsilon_{axi} = \frac{dx}{x} \tag{2.40}$$

$$\epsilon_{rad} = \frac{dr}{r} \tag{2.41}$$

Poisson's ratio (ϑ_{pack}), which relates the radial strain to the axial strain, is:

$$\vartheta_{pack} = \frac{\epsilon_{rad}}{\epsilon_{axi}} = \frac{dr \cdot x}{dx \cdot r} \tag{2.42}$$

The radial force (F_{rad}) can then be expressed using Hooke's Law, which links stress and strain for the material:

$$F_{rad} = E \times A_{rad} \times \frac{dr}{r} \tag{2.42}$$

Where:

E is the Young's modulus of the parachute material (MPa), A_{rad} is the area of the interface between the wall of the mortar and the parachute material, defined by $A_{rad} = 2\pi lr$, where l is the length of the mortar tube (m), and r is the radius of the parachute pack (m).

The relation between the axial strain and the force applied in the axial direction (F_{piston}) is:

$$F_{piston} = E \times A_{axi} \times \frac{dx}{x} \tag{2.43}$$

Where:

A_{axi} is the cross-sectional area of the mortar tube, defined by $A_{axi} = \pi r^2$.

By dividing the expressions for F_{rad} and F_{piston}, we obtain:

$$F_{rad} = \frac{2l}{r} \times \vartheta_{pack} \times F_{piston} \tag{2.44}$$

Thus, the general form for the frictional force is:

$$F_f = \mu_{pack} \times \frac{2l}{r} \times \vartheta_{pack} \times F_{piston} \tag{2.45}$$

These equations and relationships form the basis for modelling the frictional forces within the PDD, ensuring a comprehensive understanding of the energy losses due to friction during operation.

After Shear Pins Break

After the shear pins break, the parachute pack experiences a vertical force applied by the piston, which is given by the equation

$$F_{piston} = P_{gas} \times A_{piston} \tag{2.46}$$

In this equation, P_{gas} represents the gas pressure, and A_{piston} is the area of the piston. This force initiates the decompression of the parachute pack against the cylinder walls.

The normal force due to this decompression changes as the parachute pack moves upward. This can be expressed as

$$F_n = F_{n_{initial}} \left(1 - \frac{x}{L}\right) \tag{2.47}$$

where $F_{n_{initial}}$ is the initial normal force immediately after the shear pins break, L is the initial length of the parachute pack in contact with the cylinder walls, and x represents the vertical displacement of the parachute pack. The initial normal force $F_{n_{initial}}$ is related to the initial vertical compression force through the Poisson's ratio ϑ_{pack} by the equation

$$F_{n_{initial}} = F_{piston} \times \vartheta_{pack} \tag{2.48}$$

As the parachute pack moves upward, the contact surface area $A_{contact}$ between the parachute pack and the cylinder walls changes. This contact area is calculated using the equation:

$$A_{contact} = P_{pack} \times (L - x) \tag{2.49}$$

where P_{pack} is the perimeter of the parachute pack. The friction force $F_{friction}$ acting on the parachute pack can then be defined as:

$$F_{friction} = \mu_{pack} \times F_{n_{initial}} \left(1 - \frac{x}{L}\right) \tag{2.50}$$

Where μ_{pack} is the friction coefficient.

By substituting the expression for $F_{n_{initial}}$ into the friction force equation, we obtain:

$$F_{friction} = \mu_{pack} \times \vartheta_{pack} \times P_{gas} \times A_{piston} \times \left(1 - \frac{x}{L}\right) \quad (2.51)$$

This equation provides a comprehensive model for the friction force acting on the parachute pack after the shear pins break, incorporating factors such as the gas pressure, piston area, Poisson's ratio, and the changing contact surface area as the pack moves.

2.2.3 Gravity & Drag Losses

In addition to heat and friction losses, gravity and drag also contribute to the overall energy losses in the PDD system, especially during ground testing. These factors are crucial for accurately comparing the system simulation with deployment tests, although in the operational environment of the PDD, gravity and air resistance are minimal.

Gravity Losses

The force of gravity acts on the components of the PDD system during testing, influencing their motion. Specifically, the gravitational force F_g on the parachute pack is calculated as:

$$F_g = m \cdot g \quad (2.52)$$

Where m is the mass of the parachute pack and g is the acceleration due to gravity. Gravity impacts the trajectory and velocity of the parachute pack during test conditions.

Drag Losses

Drag losses are particularly relevant for the parachute pack during its deployment in atmospheric conditions. The aerodynamic drag force F_d opposing the motion of the parachute pack is given by:

$$F_d = \frac{1}{2} \cdot C_d \cdot \rho \cdot A \cdot v^2 \quad (2.53)$$

Where C_d is the drag coefficient, ρ is the air density, A is the cross-sectional area of the parachute pack, and v is its velocity. These drag losses are significant during deployment tests conducted in atmospheric conditions.

By incorporating gravity and drag forces into the energy loss calculations, we can achieve a more accurate and realistic comparison of the PDD system's performance during testing versus its operational environment. This ensures the model's predictive capability is aligned with observed behaviours under test conditions, even though gravity and drag are negligible in the actual operational environment of the PDD.

2.3 Dynamics

2.3.1 Fluid Dynamics

2.3.1.1 Gas Properties – Noble Abel Equation of State

Accurate modelling of gas generators using interior ballistics enhances design efficiency and performance optimization. Simulating flow fields within a gas generator requires a precise description of the thermodynamic behavior of the propellant gas. The Noble-Abel equation offers a straightforward and reasonably accurate equation of state for propellant gases under the high densities and temperatures typical in gas generators. However, most models need additional thermodynamic functions derived from this equation of state. This section details the derivation of such thermodynamic functions for Noble-Abel gases.

The ability to model gas generators accurately using interior ballistics enables quicker and more cost-effective design and optimization. Modelling can predict and evaluate a gas generator's performance characteristics before construction, testing, or modification. While targeted experiments can partially achieve this predictive capability, modelling provides additional advantages. The extreme conditions of the interior ballistic environment complicate experimental instrumentation and measurement, but modelling allows for determining all physical quantities throughout the simulation domain. The flexibility to include or exclude different physical phenomena enables models to assess the relative effects of various ballistic processes. Moreover, modelling supports automated optimization, such as minimizing charge weight by optimizing propellant grain geometry while ensuring that muzzle velocity and maximum pressure constraints are met (Johnston, 2005).

One of the simplest classes of interior ballistics models are lumped parameter models, where the dynamic firing process is represented by mean (lumped) state variables. These models assume a particular pressure gradient between different sections of the GG and apply this to calculate pressure and resulting acceleration. Two-phase, multi-dimensional computational fluid dynamics (CFD) solvers provide higher-fidelity simulations but are computationally expensive. These tools can model physical phenomena such as inter-phase drag, axial and radial flame spreading within the propellant bed, boundary layer formation, and pressure waves. Intermediate complexity codes combine a one-dimensional flow solver with a lumped-parameter model.

Regardless of the approach used, all models require an accurate description of the thermodynamics of the propellant gas. Consider the Euler equations, which can be thought of as a simplified version of the Reynolds-averaged Navier-Stokes equations used by CFD solvers to describe the ballistic flow. Assuming no source terms, for a control volume V, the Euler equations can be written in integral form as:

$$\frac{\partial}{\partial t}\int_V \boldsymbol{U}\, dV + \int_S \boldsymbol{F}\, dS = 0 \tag{2.54}$$

Where $\boldsymbol{U}$ is a vector representing conserved flow quantities at points within the control volume, $\boldsymbol{F}$ is a vector of fluxes across the surface of the control volume, and t is the time variable. For a single-species, single-phase flow, the vectors $\boldsymbol{U}$ and $\boldsymbol{F}$ may be expressed as:

$$U = \begin{bmatrix} \rho \\ \rho \boldsymbol{u} \\ \rho E \end{bmatrix}, \ \ and \ \boldsymbol{F} = \begin{bmatrix} \rho(\boldsymbol{u}\cdot\hat{\boldsymbol{n}}) \\ \rho \boldsymbol{u}(\boldsymbol{u}\cdot\hat{\boldsymbol{n}}) + P\hat{\boldsymbol{n}} \\ \rho E(\boldsymbol{u}\cdot\hat{\boldsymbol{n}}) + \boldsymbol{P}(\boldsymbol{u}\cdot\hat{\boldsymbol{n}}) \end{bmatrix} \tag{2.55}$$

Here, $\boldsymbol{u}$ is the fluid velocity vector, and $\hat{\boldsymbol{n}}$ is a unit normal to the control volume surface. The primitive variables ρ, P, and E represent density, absolute static pressure, and intensive total energy, respectively. Total energy can be expressed in terms of internal energy and kinetic energy as:

$$E = e + \frac{1}{2}|\boldsymbol{u}|^2, \tag{2.56}$$

Internal energy can be calculated by integrating the constant-volume specific heat with respect to temperature:

$$e = \int_{T_{ref}}^{T} c_v dT \tag{2.57}$$

Equations (*2.54*) to (*2.57*) contain six variables but provide only five relations. To solve the system, an additional equation relating the state variables of the fluid must be provided. For gases at moderate to low density, the ideal gas equation of state:

$$P = \rho RT \tag{2.58}$$

where R is the specific gas constant, can be used to close the system. The ideal gas equation of state is accurate provided that the average intermolecular spacing or mean free path of the gas is very large compared to the size of the gas molecules, and intermolecular forces are weak. However, the high gas densities occurring in a GG during combustion render the ideal gas equation of state inaccurate. Solid loading densities for GG propellants are typically of the order of 500–1,000 kg/m³. Peak gas densities produced during the ballistic cycle may also approach this magnitude since most of the propellant is burnt before significant expansion.

While still an approximation, the van der Waals equation of state provides an improvement in accuracy for high-density gases. It is of the form:

$$(P + \alpha/v^2)(v - b) = RT \tag{2.59}$$

where the gas specific volume $v \equiv 1\rho$. The co-volume b compensates for the finite volume occupied by the gas molecules, while the term α/v^2 accounts for intermolecular attraction forces. Note that in the case $\alpha = b = 0$, equation (*2.59*) reverts to the ideal gas equation of state. In GG applications, the high propellant gas temperature means that intermolecular attraction energy is small compared to molecular kinetic energy (Powell, Wilmot, Haar, & Klein, 1979). Thus, the attraction term can be removed without significant loss of accuracy, resulting in the so-called Noble-Abel equation of state:

$$P(v - b) = RT \tag{2.60}$$

Equation (*2.60*) can describe the propellant gas with sufficient accuracy for both lumped parameter and CFD models. For lumped parameter modelling, nothing further is required.

Specific Heats

In our model, the specific heat at constant pressure as a function of density and temperature is required. For completeness, both specific heats will be considered in this subsection. They are defined as:

$$c_p \equiv \left(\frac{\partial h}{\partial T}\right)_p \; and \; c_v \equiv \left(\frac{\partial e}{\partial T}\right)_v \tag{2.61}$$

From (Anderson, 1999), the gradient of c_p with respect to pressure at constant temperature can be related to the equation of state via:

$$\left(\frac{\partial c_p}{\partial P}\right)_T = -T\left(\frac{\partial^2 v}{\partial T^2}\right)_P \tag{2.62}$$

Evaluating the right-hand side for the Noble-Abel equation of state yields:

$$\left(\frac{\partial c_p}{\partial P}\right)_T = -\frac{T\partial^2}{\partial T^2}\left(\frac{RT}{P} + b\right)_P = 0 \tag{2.63}$$

This also proves that:

$$\left(\frac{\partial c_p}{\partial \rho}\right)_T = 0 \tag{2.64}$$

and hence:

$$c_p(\rho, T) = c_p(T) \tag{2.65}$$

for a Noble-Abel gas. A similar proof is possible for specific heat at constant volume:

$$\left(\frac{\partial c_v}{\partial v}\right)_T = T\left(\frac{\partial^2 P}{\partial T^2}\right)_v = T\frac{\partial^2}{\partial T^2}\left(\frac{RT}{v-b}\right)_v = 0 \tag{2.66}$$

and thus:

$$c_v(\rho, T) = c_v(T) \tag{2.67}$$

These results show that, for a Noble-Abel gas, the specific heat functions can be conveniently implemented in computer code as a curve fit or look-up table in terms of temperature only. As an alternative to providing the specific heats as a function of temperature, the calorifically perfect approximation could also be made:

$$c_p = constant \; and \; c_v = constant$$

Specific Gas Constant

The previous section showed that both c_p and c_v could be expressed as functions of temperature only. We now proceed to show that these quantities can be related, such that if one specific heat is known, the other may be calculated easily. This eliminates the need to provide two separate tables (or curve fits). From (Anderson, 1999):

$$c_p - c_v = -T\left(\frac{\partial^2 v}{\partial T^2}\right)_P^2 \left(\frac{\partial P}{\partial v}\right)_T \tag{2.68}$$

Evaluating the partial derivatives from the Noble-Abel equation of state yields:

$$c_p - c_v = T\left(\frac{R}{P}\right)^2 \frac{RT}{(v-b)^2} \tag{2.69}$$

Upon simplifying, we get the convenient relationship:

$$c_p - c_v = R \tag{2.70}$$

which is the same as that for ideal gases.

2.3.1.2 Mass Flow Through the Orifices

To determine the flow rate of gas from the gas generator to the mortar tube through the orifices, we begin by assessing whether the flow is choked or not. This is determined by calculating the critical pressure ratio:

Critical Pressure Ratio

$$\frac{P_{cr}}{P_u} = \left(\frac{2}{k+1}\right)^{\frac{k}{k-1}} \tag{2.71}$$

If $\frac{P_d}{P_u} < \frac{P_{cr}}{P_u}$, the flow is choked. Otherwise, the flow is non-choked.

Non-Choked Flow

Initially, the flow of gas through the orifice is non-choked, meaning $\frac{P_{cr}}{P_u} < \frac{P_d}{P_u} \leq 1$, so the mass flow rate is given by:

$$\dot{m} = \frac{P_u A_{eff}}{\sqrt{T_u}} \sqrt{\frac{2\gamma}{R(\gamma-1)}} \left[\left(\frac{P_d}{P_u}\right)^{\frac{2}{k}} - \left(\frac{P_d}{P_u}\right)^{\frac{k+1}{k}} \right] \tag{2.72}$$

Here:

- $\dot{m}$ is the mass flow rate.
- P_u and T_u are the upstream stagnation conditions (inside the GG).
- P_d is the downstream pressure (inside the mortar tube).
- A_{eff} is the effective flow area of the orifice.
- γ is the specific heat ratio of the gas.
- R is the gas constant.

The effective flow area A_{eff} is defined as:

$$A_{eff} = C_d A_o \tag{2.73}$$

Where:

- C_d is the flow coefficient, accounting for the discharge characteristics of the orifice.
- A_o is the geometric area of the of the orifice.

Choked Flow

As the simulation progresses and $\frac{P_d}{P_u} < \frac{P_{cr}}{P_u}$, the flow becomes choked. This means the flow rate reaches its maximum limit, which can be calculated by:

$$\dot{m} = \dot{m}_{max} = \frac{P_u A_{eff}}{\sqrt{T_u}} \sqrt{\frac{\gamma}{R}} \left(\frac{2}{k+1}\right)^{\frac{k+1}{2(k-1)}} \tag{2.74}$$

Here:

- $\dot{m}$ is the maximum mass flow rate.
- The other variables retain their previously defined meanings.

2.3.1.3 Conservation Laws

Parachute deployment gas generator models rely on fundamental conservation laws to operate effectively. These generators produce gas through chemical reactions or the release of pressurized gas, following the principles of mass, momentum, and energy conservation. According to the law of conservation of mass, the total mass of gas remains constant throughout the gas generator's operation. The law of conservation of momentum states that the momentum of the gas generated propels the system, enabling the gas to exert a force on the surroundings. Lastly, the law of conservation of energy dictates that the energy stored in the gas generator is converted into kinetic energy and thermal energy as the gas expands.

2.3.1.3.1 Conservation of Mass

The rate of change of fluid mass inside a control volume must be equal to the net rate of fluid flow into the volume. Physically, this statement requires that mass is neither created nor destroyed in the control volume and can be translated into the integral form of the continuity equation:

$$\frac{\partial}{\partial t}\iiint_V \rho \, dV = -\oiint_S \rho \boldsymbol{u} \cdot d\boldsymbol{S} \tag{2.75}$$

In the context of the gas generator, the mass balance of gases is determined by the amount of gas generated through propellant combustion and the gas outflow through the orifice(s). The mass of the gases produced is approximately equal to the mass of the propellant burned, with any negligible propellant residue accounted for. As a result, an expression for the mass of the gas in the generator at any given time can be represented by the equation:

$$M = m_{in} - m_{out} \tag{2.76}$$

And then, the change in mass is expressed as:

$$\frac{dM}{dt} = \frac{d(\rho V)}{dt} = \dot{m}_{in} - \dot{m}_{out} \tag{2.77}$$

$$\frac{d\rho}{dt} = -\frac{\rho}{V}\frac{dV}{dt} + \frac{1}{V}(\dot{m}_{in} - \dot{m}_{out}) \tag{2.78}$$

Where M is the mass, ρ is the density, and V is the volume.

2.3.1.3.2 Conservation of Momentum

Newton's second law of motion applied to a control volume states that any change in momentum of the fluid within that control volume will be due to the net flow of momentum into the volume and the action of external forces acting on the fluid within the volume. The integral form is:

$$\frac{\partial}{\partial t}\iiint_V \rho \boldsymbol{u} \, dV = -\oiint_S (\rho \boldsymbol{u} \cdot d\boldsymbol{S})\boldsymbol{u} - \oiint_S p d\boldsymbol{S} + \iiint_V \rho \boldsymbol{f}_{body} dV + \boldsymbol{F}_{surf} \tag{2.79}$$

At the initial state, the mortar and the parachute pack inside it are stationary, implying that the initial total momentum of this system is zero. Upon initiating the mortar, it propels the parachute pack forward, generating a recoil in the opposite direction. Both the parachute pack and the mortar possess equal magnitudes of momentum but in opposing directions. Due to the mortar being fixed, the velocity of the parachute pack is much higher than that of the mortar's recoil velocity. The conservation of momentum is described by the equation:

$$m_1 \cdot v_1 + m_2 \cdot v_2 = m_1' \cdot v_1' + m_2' \cdot v_2' \tag{2.80}$$

where:

- m_1 and m_2 are the initial masses of the objects.
- v_1 and v_2 are the initial velocities of the objects.
- m_1' and m_2' are the final masses of the objects.
- v_1' and v_2' are the final velocities of the objects.

This equation states that the total momentum before the ignition of the propellant is equal to the total momentum after the event, assuming no external forces are acting on the system.

2.3.1.3.3 Conservation of Energy

The conservation of energy states that while energy can change forms, the total energy within a closed system remains constant. The integral form is:

$$\rho \frac{Dh}{Dt} = \frac{Dp}{Dt} + \nabla \cdot (k\nabla T) + \Phi \tag{2.81}$$

In the context of the mortar system deploying a parachute pack, the conservation of energy principle is essential. This principle asserts that the total energy within an isolated system remains constant, regardless of interactions or transformations. For this specific system, various forms of energy come into play, including internal energy (C_v), heat (Q), and work (W), and temperature (T). The energy balance can be represented as:

$$\frac{dE}{dt} = \frac{d(\rho V C_v T)}{dt} = \dot{m}_{in} e_{in} - \dot{m}_{out} e_{out} - \dot{Q} - \dot{W} \tag{2.82}$$

Here, E is the total energy, e is the specific energy, and $\dot{m}$ represents mass flow rates.

These conservation laws are fundamental to accurately simulating the fluid dynamics within the gas generator and the mortar tube system, ensuring that mass, momentum, and energy are conserved throughout the process.

2.3.2 Solid Body Dynamics

This section delves into the dynamic behaviour of the solid components within the mortar tube, with a primary focus on the parachute pack and piston (sabot). We will first present the compression characteristics of the parachute pack, utilizing both spring and damper models to accurately describe its behaviour under compression. Following this, we will explore the translational motion of the piston and parachute pack within the mortar tube, examining their interactions and movements during the deployment process. Finally, we will discuss the dynamics of the parachute pack after ejection.

2.3.2.1 Parachute Pack Compression

To accurately model the behavior of the parachute pack during the deployment process, it is essential to understand its compression characteristics. The parachute pack experiences significant compression forces as it is pushed by the piston within the mortar tube. Two primary models are employed to describe this compression: the Spring Model and the Damping Model. These models allow us to simulate the physical response of the parachute pack under different conditions.

2.3.2.1.1 Spring Model

To model the compression behaviour of the parachute pack, compression tests were conducted. These tests revealed that the relationship between force (F) and displacement (Δx) of the parachute pack

follows an exponential behaviour, differing from the linear relationship described by Hooke's Law. The exponential relationship can be represented by the equation:

$$F = Ce^{k\Delta x} \tag{2.83}$$

In this equation:

- F is the applied force.
- Δx is the displacement.
- C and k are constants specific to the characteristics of the parachute pack.

To find the constants C and k, the equation can be linearized by taking the natural logarithm of both sides, yielding:

$$\ln(F) = \ln(C) + k\Delta x \tag{2.84}$$

By performing linear regression on the measured data points for F and Δx, the constants can be estimated. The regression process involves plotting $\ln(F)$ against Δx and determining the best fitting values for $\ln(F)$ and k.

Given the experimental data points, the constants were found to be:

- $k \approx 73.56$ (units are m^{-1} since displacement is in meters).
- $C \approx 34.66$ (units are Newtons).

The coefficient of determination, R^2, was approximately 0.997, indicating a very good fit of the exponential model to the data. The updated relationship between the force and displacement for the parachute pack is now:

$$F = 34.66e^{73.56\Delta x} \tag{2.85}$$

This formula accurately represents the behaviour of the parachute pack's compression over the measured displacement range. The corresponding plot of force vs. displacement validates the exponential model, showing the measured data points and the fitted curve. This modelling approach provides a precise description of the parachute pack's compression characteristics, which is essential for predicting its behaviour in the deployment system.

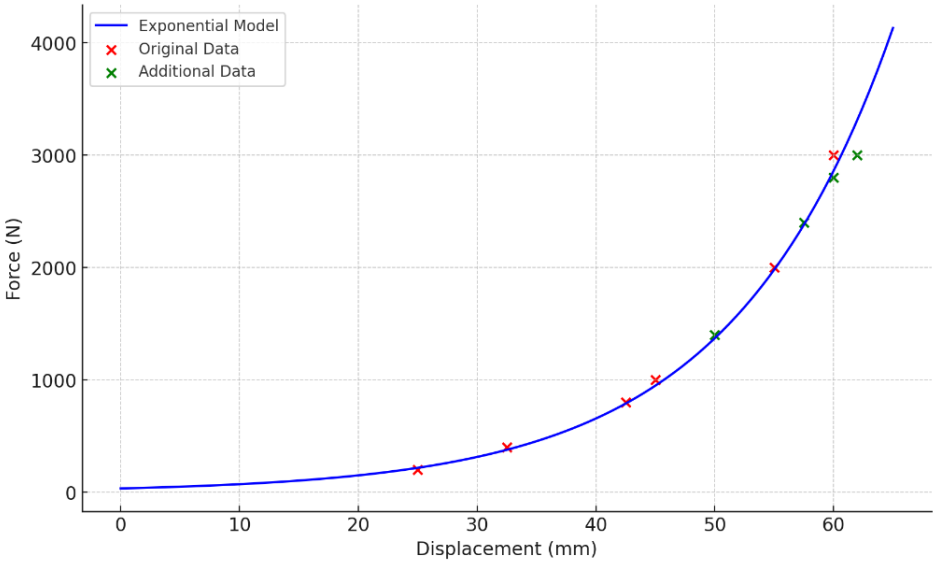

Figure 23: Force Vs. Displacement Spring

2.3.2.1.2 Damping Model

To model the damping behaviour of the parachute pack, we consider the resistance offered by the pack to motion due to its material properties. This resistance is characterized by a damping force, which opposes the motion and is typically proportional to the velocity of compression or expansion.

The damping force (F_d) can be described by the equation:

$$F_d = -c\frac{dx}{dt} \tag{2.86}$$

where:

- F_d is the damping force.
- c is the damping coefficient.
- $\frac{dx}{dt}$ is the velocity of displacement (rate of change of displacement).

This simple model assumes that the damping force is directly proportional to the velocity of the parachute pack's motion. The damping coefficient c will be determined from calibration using the deployment tests, allowing us to accurately capture the resistance behaviour of the parachute pack during its compression and expansion phases.

2.3.2.2 Sabot & Parachute Pack Motion

2.3.2.2.1 Before Shear Pins Break

Before the shear pins break, the motion of the piston and the parachute pack within the mortar tube is governed by various forces. The primary force accelerating the piston is the gas force generated by the gas generator. This force is denoted as F_{gas} and is given by:

$$F_{gas} = \mathrm{Ab}_{\mathrm{piston}} \cdot (\mathrm{P2} - \mathrm{P}_{\mathrm{env}}) \tag{2.90}$$

Where $\mathrm{Ab}_{\mathrm{piston}}$ is the base area of the piston, $\mathrm{P2}$ is the pressure under the piston, and $\mathrm{P}_{\mathrm{env}}$ is the environmental pressure.

Opposing the gas force, we have several other forces:

The Compression Force (F_{Comp}) is the force exerted by the compressed parachute pack, modelled as a spring force, given by:

$$F_{Comp} = C_{pack} \cdot exp\,(x1 \cdot k_{pack}) \tag{2.91}$$

Where C_{pack} is the spring constant, $x1$ is the compression distance, and k_{pack} is the exponential constant related to the compression characteristics.

The Frictional Force on the Piston ($F_{Friction_{piston}}$) accounts for the friction between the piston and the mortar tube walls. It is given by:

$$F_{Friction_{piston}} = \left(F_{n_{seal}} \cdot \mu_{seal}\right) \cdot 2 \tag{2.92}$$

Where $F_{n_{seal}}$ is the normal force due to the O-Ring seals, and μ_{seal} is the coefficient of friction of the O-Ring seals.

The Frictional Force on the Parachute Pack ($F_{Friction_{pack}}$) accounts for the friction between the parachute pack and the mortar tube. This force is given by:

$$F_{Friction_{pack}} = (\mu_{pack} \cdot \nu_{pack} \cdot P2 \cdot Ab_{pack} \cdot (L_{pack} - x2)/L_{pack}) \quad (2.93)$$

Where μ_{pack} is the coefficient of friction of the pack, ν_{pack} is a parameter related to the pack material, $P2$ is the pressure on the pack, Ab_{pack} is the base area of the pack, L_{pack} is the initial length of the pack, and $x2$ is the displacement of the parachute pack.

The Damping Force (F_{Damper}) accounts for the damping effect of the parachute pack and is given by:

$$F_{Damper} = c_{pack} \cdot u1 \quad (2.94)$$

Where c_{pack} is the damping coefficient, and $u1$ is the velocity of the piston.

Additionally, the Gravitational Force accounts for the combined weight of the parachute pack ($m1$), piston ($m2$), and lid ($m3$). This force is given by:

$$(m1 + m2 + m3) \cdot g \quad (2.95)$$

Where g is the acceleration due to gravity.

The net acceleration of the piston and the parachute pack is then given by:

$$a_{piston} = a_{pack} = \frac{F_{gas} - F_{Comp} - F_{Friction_{pack}} - F_{Friction_{piston}} - F_{Damper} - (M1+M2+M3) \cdot g}{m1+m2+m3} \quad (2.96)$$

2.3.2.2.2 After Shear Pins Break

After the shear pins break, the motion of the piston and the parachute pack is influenced by different forces compared to before the shear pins break. The main forces to consider are the gas force, frictional forces on the piston and parachute pack, gravitational force, and aerodynamic forces coupled to the motion.

The net acceleration of the piston (a_{piston}) and the parachute pack (a_{pack}) is determined by the following equations:

The net acceleration of the piston, considering the various forces acting on it after the shear pins break, is given by:

$$a_{piston} = \frac{F_{gas} - F_{Friction_{pack}} - F_{Friction_{piston}} - (M1+M2+M3) \cdot g - F_{aero_{coupled}}}{m1+m2+m3} \quad (2.97)$$

Here, $F_{aero_{coupled}}$ is the aerodynamic force of both the parachute pack and the piston.

The net acceleration of the parachute pack, considering the various forces acting on it after the shear pins break, is given by:

$$a_{pack} = \frac{F_{gas} - F_{Friction_{pack}} - F_{Friction_{piston}} - (M1+M2+M3) \cdot g - F_{aero_{coupled}} - F_{Damper} + F_{Comp}}{m1+m2+m3} \quad (2.98)$$

Here, F_{Comp} is the compression force exerted by the parachute pack. This force is zero until the pack starts to decompress after the pins break.

After the shear pins break, the compression force on the parachute pack is considered differently:

If the piston has not moved beyond the mortar tube stroke length (Sm), the compression force (F_{Comp})

and damping force (F_{Damper}) are both zero.

When the piston starts decompressing, the compression force and damping force are given by:

$$F_{Comp} = C_{pack} \cdot exp\,(decomp_{displ} \cdot k_{pack}) \quad (2.99)$$

$$F_{Damper} = c_{pack} \cdot decomp_{rate} \quad (2.100)$$

Where $decomp_{displ}$ is the decompression displacement and $decomp_{rate}$ is the decompression rate.

The frictional forces vary depending on the position of the piston:

If the piston is within the stroke length (Sm) and not beyond the position of the top O-ring ($l2$):

$$F_{Friction_{piston}} = \left(F_{n_{seal}} \cdot \mu_{seal}\right) \cdot 2 \quad (2.101)$$

$$F_{Friction_{pack}} = \left(\mu_{pack} \cdot \nu_{pack} \cdot P2 \cdot Ab_{pack} \cdot \frac{L_{pack} - x2}{L_{pack}}\right) \quad (2.102)$$

If the piston moves beyond $l2$, only one O-ring is in contact with the mortar tube walls, and the parachute pack is out of the mortar tube, then:

$$F_{Friction_{piston}} = \left(F_{n_{seal}} \cdot \mu_{seal}\right) \quad (2.103)$$

$$F_{Friction_{pack}} = 0 \quad (2.104)$$

When the piston is completely outside the cylinder:

Both $F_{Friction_{piston}}$ and $F_{Friction_{pack}}$ are zero.

Chapter 3

Program Development

This chapter details the development and structure of the simulation program engineered to model the complex dynamics of a Parachute Deployment Device (PDD). The program is built on a modular framework, with each module dedicated to specific system components and operational dynamics. Key modules include those for input data, defining properties such as gas generator parameters, parachute pack specifications, and environmental settings. The main simulation module orchestrates core computations, while submodules handle event triggers, mass flows, force calculations, and dynamic interactions, such as compression and damping, encountered during deployment.

The modular architecture promotes scalability, ease of maintenance, and adaptability, facilitating future program enhancements and adjustments to suit diverse deployment scenarios. The final section of this chapter covers the post-processing and visualization of simulation outcomes, presenting key performance metrics—such as pressures, forces, and displacements—through comprehensive graphs and data outputs. This structured approach enables an in-depth assessment of the PDD's performance under varying conditions, establishing a robust foundation for evaluating system behavior and refining design parameters.

3.1 Overview

The program aims to simulate the dynamics of a Parachute Deployment Device using principles of interior ballistics, fluid dynamics, and solid body dynamics. It predicts the behaviour of the gas generator, the motion of the piston and parachute pack, and the forces involved in the deployment process. The program includes features to model mass and energy flows, simulate the compression and damping behaviour of the parachute pack, and account for various frictional forces within the system.

The architecture of the program is divided into several interconnected modules, each handling a specific aspect of the simulation:

Input Modules:

- **Gas Generator Inputs (MDT_GG_input)**: Defines the parameters of the combustion chamber, post-combustion chamber, orifices, wall thermal properties, and details about the nitrocellulose propellant. Outputs a structured set of all the above parameters.

- **Mortar Inputs (MDT_MRTR_input)**: Defines the plenum's dimensions and thermal properties, provides details about the parachute pack, and outputs a structured array containing all the mentioned parameters.

- **Environment Inputs (MDT_ENV_input)**: Specifies gas constants and environmental conditions, defines operating conditions, and outputs structured environmental data for use in further simulations.

Main Module:

- **Mortar Dynamic Tool (MDT_Dynamics_Tool)**: Primary run file for mortar simulation, handling initialization, input files, simulation settings, core simulation execution, and post-processing and plotting results.

Subroutines:

- **Simulation Core (MDT_Simcore)**: Integration algorithms, state vector management, differential equations solving, pressure and reaction force calculations, and final results compilation.

- **Dynamics (MDT_Dynamics)**: Contains differential equations, initial gas and propellant variables, initiators model, mass and heat flow, and pack forces.

- **Events (MDT_Events)**: Triggers events based on various conditions like pressure differences and distance travelled.

- **Nitrocellulose Grain Surface (MDT_NTC_Surface)**: Calculates the burning surface area of nitrocellulose grains.

- **Nozzle Mass Flow (MDT_NozzleFlow)**: Computes mass flow through the GG orifices for both choked and un-choked flow.

- **Volume Flux After Burstdisk Failure (MDT_Burstdisk)**: Simulates a burst event over a specified time interval.

- **Pack Compression Forces (MDT_Compression)**: Calculates spring, damping, and friction forces for the parachute pack.

Output Module:

- **Post Processing (MDT_Basic_Figures)**: Plots basic performance parameters, including gas densities, pressures, temperatures, sabot and lid velocities, displacements, and reaction force visualization.

This architecture ensures modularity, scalability, and ease of maintenance, allowing for the inclusion of additional features and enhancements in the future. The program facilitates faster and more cost-effective design and optimization of gas generators, enabling the prediction and assessment of system performance characteristics before physical prototypes are built or tests are conducted.

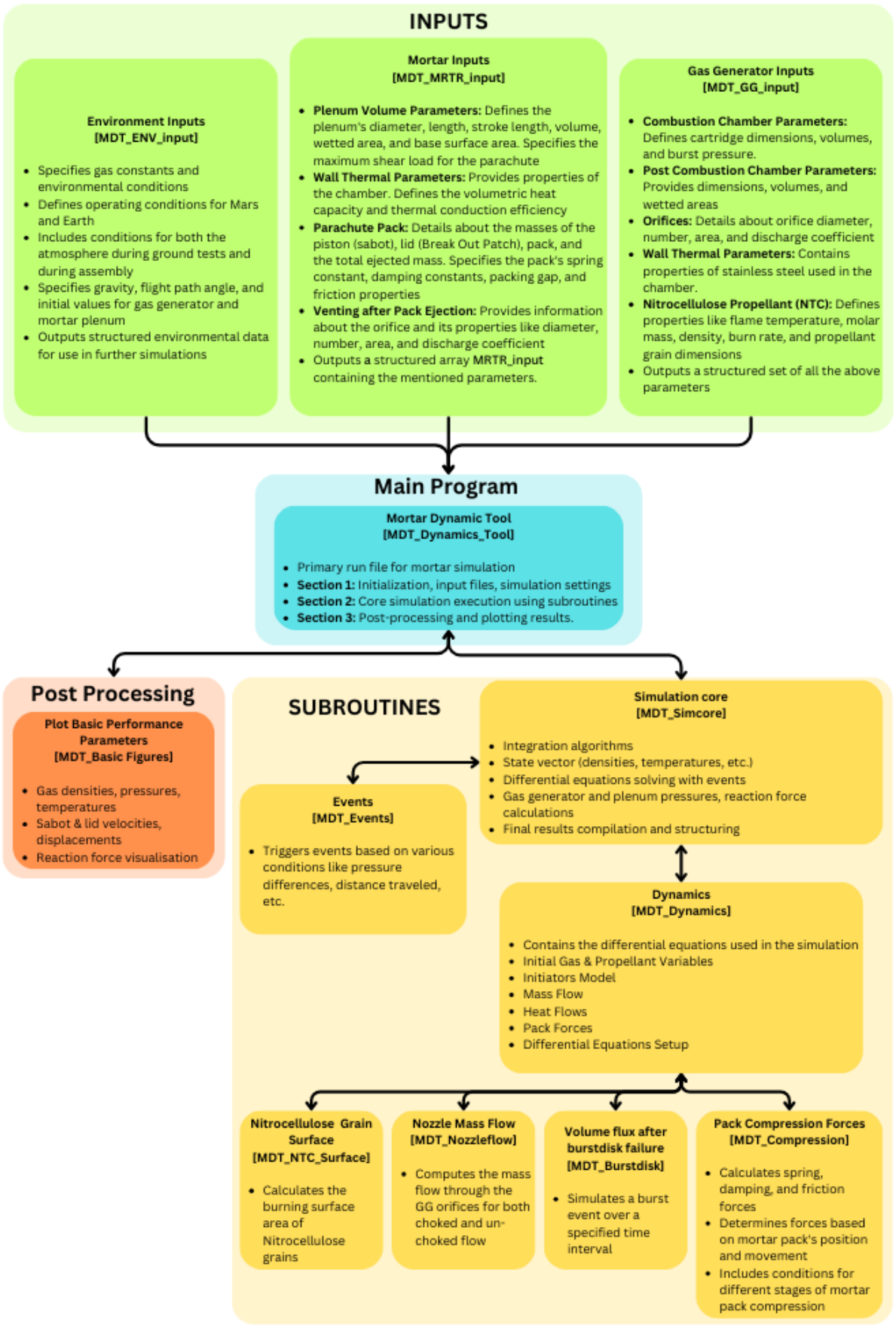

Figure 24: Program Structure

3.2 Input Modules

3.2.1 Gas Generator Inputs

The `PDD_GG_input` module organizes and defines the input parameters for the gas generator used in the Parachute Deployment Device (PDD) simulation. This module captures various aspects of the gas generator, including initiators, combustion chamber characteristics, post-combustion chamber parameters, orifice details, thermal properties, and propellant specifics. The parameters are systematically stored in dictionaries to facilitate structured access and manipulation within the simulation.

The module begins by defining the properties and performance characteristics of the initiators. These include details such as the number of initiators, function time, nominal output pressure, mass of propellant, energy output, and the required burn rate. These parameters are encapsulated within the dictionary `INIT`.

Parameter	Variable	Description
Number of initiators	n_init	Number of initiators used
Function time	t_init	Time duration for the initiators' function
Nominal output pressure	P_init	Pressure output by the initiators
Mass of propellant	m_zpp	Mass of propellant within the initiators
Energy output	h_init	Energy produced by the initiators
Required burn rate	r_init	Burn rate necessary for the initiators

Table 1: Initiators Input Parameters

Next, the combustion chamber characteristics are defined, encompassing actual volume, wall surface area, and burst pressure of the burst disk. These parameters are stored in the dictionary `Vcomb`.

Parameter	Variable	Description
Actual volume	Va	Volume of the combustion chamber
Wall surface area	Aa	Surface area of the combustion chamber walls
Burst pressure	Pb	Pressure at which the main burst disk ruptures

Table 2: Combustion Chamber Input Parameters

The post-combustion chamber parameters capture the volume and wall surface area of the post-combustion chamber, stored in the dictionary `Vpost`.

Parameter	Variable	Description
Volume	Va	Volume of the post-combustion chamber
Wall surface area	Aa	Surface area of the post-combustion chamber walls

Table 3: Post-Combustion Chamber Input Parameters

Orifice details are defined, including orifice diameter, number of orifices, orifice area, and discharge coefficient. These parameters are stored in the dictionary `orifices`.

Parameter	Variable	Description
Orifice diameter	Do	Diameter of the orifices
Number of orifices	no	Total number of orifices
Orifice area	Ao	Area of the orifices
Discharge coefficient	Cd	Coefficient describing flow efficiency through orifices

Table 4: Orifices Input Parameters

The thermal properties of the combustion chamber walls include density, thermal conductivity, thermal capacity, wall thickness, and emissivity. These parameters are stored in the dictionary `thermal`.

Parameter	Variable	Description
Density	rho	Density of the chamber wall material
Thermal conductivity	lbd	Thermal conductivity of the chamber walls
Thermal capacity	cp	Heat capacity of the chamber wall material
Wall thickness	s	Average thickness of the chamber walls
Emissivity	ε	Emissivity of the chamber wall material

Table 5: GG Thermal Properties Input Parameters

Lastly, the module defines the properties of the propellant, such as gas constant, adiabatic flame temperature, molar mass, ratio of specific heats, specific gas constant, specific heat at constant pressure, co-volume of reaction products, bulk density, burn law coefficients, rate constant reference temperature, auto-ignition temperature, activation energy, loaded propellant mass, and grain dimensions. These parameters are stored in the dictionaries `NTC` and `NTC_dim`.

Parameter	Variable	Description
Gas constant	Ri	Universal gas constant
Adiabatic flame temperature	T	Flame temperature under adiabatic conditions
Molar mass	M	Molar mass of the propellant gas
Ratio of specific heats	Gam	Ratio of specific heats for the propellant gas
Specific gas constant	R	Gas constant specific to the propellant gas
Specific heat at constant pressure	Cp	Specific heat capacity at constant pressure
Co-volume of reaction products	b	Co-volume of reaction products
Bulk density	rho	Density of the propellant in bulk form
Burn law coefficient	beta_0	Coefficient for the propellant burn rate law
Burn law exponent	a	Exponent in the burn rate law
Auto-ignition temperature	Tig	Temperature at which the propellant auto-ignites
Activation energy	Ea	Energy required to initiate the propellant burn
Loaded propellant mass	PL	Mass of the propellant loaded into the generator
Propellant grain length	L	Length of the individual propellant grains
Grain outer diameter	Do	Diameter of the propellant grains
Grain perforation diameter	Di	Diameter of perforations in the propellant grains
Number of perforations	p	Number of perforations per propellant grain
Initial volume of grains	V	Volume of individual propellant grains

Table 6: NTC Propellant Input Parameters

The final output of the module is a comprehensive dictionary `GG` that consolidates all these components, providing a structured and accessible set of parameters for the simulation.

3.2.2 Mortar Tube Inputs

The `PDD_MRTR_input` module organizes and defines the input parameters for the mortar tube used in the Parachute Deployment Device (PDD) simulation. This module captures various aspects of the mortar tube, including plenum dimensions, thermal properties, piston characteristics, lid properties, and parachute pack specifics. The parameters are systematically stored in dictionaries to facilitate structured access and manipulation within the simulation.

The module begins by defining the dimensions and properties of the plenum. These include the plenum diameter, length, stroke length, volume, wetted area, base surface area, maximum shear load per pin, number of pins, and compression force during integration. These parameters are encapsulated within the dictionary `plenum`.

Parameter	Variable	Description
Plenum diameter	Dm	Diameter of the plenum
Plenum length	Lm	Length of the plenum
Stroke length	Sm	Stroke length of the mortar tube
Plenum volume	Vm	Volume of the plenum
Plenum wetted area	Am	Wetted area of the plenum
Mortar base surface area	Ab	Base surface area of the mortar
Max shear load per pin	Fburst	Maximum shear load per pin for the lid
Number of pins	N	Number of pins
Compression force during integration	Fpreload	Compression force during integration of the parachute pack

Table 7: Mortar Tube Input Parameters

Next, the thermal properties of the mortar tube walls are defined. These include density, thermal conductivity, thermal capacity, wall thickness, and emissivity. These parameters are stored in the dictionary `thermal`.

Parameter	Variable	Description
Density	rho	Density of the mortar tube wall material
Thermal conductivity	lbd	Thermal conductivity of the wall material
Thermal capacity	cp	Heat capacity of the wall material
Wall thickness	s	Average thickness of the mortar tube walls
Emissivity	ε	Emissivity of the mortar tube wall material

Table 8: Mortar Tube Thermal Input Parameters

The piston characteristics are then defined, capturing the mass, elastic modulus of O-rings, radial deformation of O-rings, cross-section diameter of O-rings, contact surface area between O-rings and walls, coefficient of dynamic friction, normal compression force, travel distances of O-rings, piston diameter, top surface area, drag coefficient, and piston lateral skirt. These parameters are stored in the dictionary `piston`.

Parameter	Variable	Description
Piston mass	M_piston	Mass of the piston
Elastic modulus of O-rings	E_seal	Elastic modulus of the O-rings
Radial deformation of O-rings	δ_seal	Radial deformation of the O-rings
Cross-section diameter of O-rings	d_seal	Cross-section diameter of the O-rings
Contact surface area of O-rings	A_seal	Contact surface area between O-rings and walls
Coefficient of dynamic friction	μ_seal	Coefficient of dynamic friction with grease
O-rings normal compression force	Fn_seal	Normal compression force of the O-rings
Travel distance of O-ring 1	l_1	Travel distance of the first O-ring
Travel distance of O-ring 2	l_2	Travel distance of the second O-ring
Piston diameter	Dm_piston	Diameter of the piston
Piston top surface area	Ab_piston	Top surface area of the piston
Drag coefficient	Cd	Drag coefficient
Piston lateral skirt	skirt	Lateral skirt of the piston

Table 9: Piston Input Parameters

The module also defines the properties of the lid, including its mass, top surface diameter, top surface area, and drag coefficient. These parameters are stored in the dictionary `lid`.

Parameter	Variable	Description
Lid mass	M_lid	Mass of the lid
Lid top surface diameter	Dm_lid	Diameter of the lid's top surface
Lid top surface area	Ab_lid	Surface area of the lid's top surface
Drag coefficient	Cd	Drag coefficient

Table 10: Lid Input Parameters

Finally, the module defines the properties of the parachute pack, including its mass, coefficient of dynamic friction, Poisson's ratio, diameter, length, base surface area, spring constant, drag coefficient, and damping coefficient. These parameters are stored in the dictionary `pack`.

Parameter	Variable	Description
Parachute pack mass	M_pack	Mass of the parachute pack
Coefficient of dynamic friction	μ_pack	Coefficient of dynamic friction of parachute pack
Poisson's ratio	ν_pack	Poisson's ratio of the parachute pack
Parachute pack diameter	Dm_pack	Diameter of the parachute pack
Parachute pack length	L_pack	Length of the parachute pack
Parachute pack base surface area	Ab_pack	Base surface area of the parachute pack
Parachute spring constant	k_pack	Spring constant of the parachute pack
Parachute spring force	C_pack	Force constant of the parachute pack
Drag coefficient	Cd	Drag coefficient of the parachute pack
Damping coefficient	c_pack	Damping coefficient of the parachute pack

Table 11: Parachute Pack Input Parameters

3.2.3 Environment Inputs

The `PDD_ENV_input` module organizes and defines the input parameters for the environmental conditions affecting the Parachute Deployment Device (PDD) simulation. This module captures various aspects of the environment, including atmospheric conditions during assembly and operation, and initial conditions for the gas generator and mortar plenum. The parameters are systematically stored in dictionaries to facilitate structured access and manipulation within the simulation. The module begins by defining the gas constant, which is used throughout the simulation for various calculations. It then defines the atmospheric conditions during operation and assembly. These include pressure, adiabatic index, molar mass, specific gas constant, and temperature. These parameters are encapsulated within the dictionaries `Opp` (for operational conditions) and `Assy` (for assembly conditions).

Parameter	Variable	Description
Pressure during operation	Pop	Atmospheric pressure during operation
Adiabatic index	Gop	Adiabatic index during operation
Molar mass	Mop	Molar mass of atmospheric gas during operation
Specific gas constant	Rop	Specific gas constant during operation
Temperature during operation	Top	Atmospheric temperature during operation

Table 12: Operational Conditions Input Parameters

During assembly, the atmospheric conditions might differ from those during operational tests. Therefore, it's essential to define separate parameters to accurately represent the assembly environment. These parameters include the atmospheric pressure, temperature, adiabatic index, molar mass of the atmospheric gas, and the specific gas constant during the assembly phase.

Parameter	Variable	Description
Pressure during assembly	Pas	Atmospheric pressure during assembly
Adiabatic index	Gas	Adiabatic index during assembly
Molar mass	Mas	Molar mass of atmospheric gas during assembly
Specific gas constant	Ras	Specific gas constant during assembly
Temperature during assembly	Tas	Atmospheric temperature during assembly

Table 13: Assembly Conditions Input Parameters

The module also defines the initial values for the gas generator and mortar plenum. These include initial pressure and density in both the gas generator and mortar plenum. These parameters are crucial for setting the initial state of the simulation and are stored within the dictionary `Opp`.

Parameter	Variable	Description
Initial pressure in gas generator	Pgg_t0	= Pas * (Top / Tas)
Initial density in gas generator	rgg_t0	= Pas / (Ras * Tas)
Initial pressure in mortar plenum	Ppl_t0	= Pop
Initial density in mortar plenum	rpl_t0	= Pop / (Rop * Top)
Local acceleration due to gravity	g	Gravitational acceleration
Flight path angle	af	Flight path angle during operation

Table 14: Initial Value Parameters

The parameters are systematically stored in dictionaries `Opp` and `Assy` for operational and assembly conditions respectively and combined into the final dictionary `ENV` for structured and accessible use within the simulation.

3.3 Main Module & Submodules

3.3.1 Mortar Dynamic Tool

The main module, named the Mortar Dynamics Tool (MDT), orchestrates the entire simulation process of the parachute deployment device by integrating inputs from various submodules and executing the necessary computations. It manages the flow of the simulation, beginning with gathering user inputs, processing the inputs through submodules, executing the core simulation, and finally post-processing the results to provide comprehensive output data.

The simulation process starts with the MDT prompting the user to enter key parameters such as the temperature during the ground test, the assembly temperature, and the mass of the propellant. These inputs are critical as they influence the simulation settings and outcomes.

After collecting user inputs, the MDT loads input parameters from three dedicated submodules: Gas Generator (GG), Mortar Tube (MRTR), and Environmental Conditions (ENV). Each submodule organizes and defines necessary parameters for the simulation, ensuring that all relevant aspects are considered. The GG input module includes parameters such as initiator characteristics, combustion chamber properties, and propellant details. The MRTR input module specifies dimensions, thermal properties, piston characteristics, and other mortar tube-related parameters. The ENV input module describes environmental conditions during ground tests and assembly, including atmospheric pressure, temperature, and gravity.

Once the inputs are loaded, the MDT sets the integration and simulation parameters. These include integration tolerances, the total duration of the simulation, the time step for output data, the maximum trajectory distance, and a specific time reference for the simulation. These settings ensure that the simulation runs efficiently and accurately, capturing all necessary dynamics of the PDD.

The core of the simulation is executed by a dedicated subroutine that integrates the dynamic equations governing the PDD. This subroutine processes the input parameters and simulation settings, performs the necessary computations, and returns the simulation results. The MDT coordinates this process, ensuring that all variables are correctly passed to the subroutine and that the resulting data is appropriately captured.

After the core simulation is complete, the MDT handles post-processing tasks. This phase involves calculating additional values, such as shear loads, and generating visual representations of the simulation results. The post-processing subroutine provides valuable insights into the behaviour and efficiency of the PDD by plotting figures and analysing performance data.

3.3.2 Subroutines

The subroutines form the backbone of the Mortar Dynamics Tool, each performing specific tasks to simulate various aspects of the Parachute Deployment Device. These subroutines are modular, allowing for easy updates and maintenance. Below is a detailed explanation of each subroutine and its function within the MDT.

3.3.2.1 Simcore

The Simcore subroutine serves as the core computational engine of the Mortar Dynamics Tool. It integrates dynamic equations to simulate the behaviour of the parachute deployment device. This subroutine handles initial conditions, solving differential equations, event management, and compiling results into structured output.

3.3.2.1.1 Initial Conditions

The Simcore subroutine begins by setting up the initial conditions for the simulation. These initial conditions are crucial for accurately modelling the behaviour of the parachute deployment device. The state vector `s` is initialized with 18 elements, each representing a specific parameter within the system.

The parameters include regressed length of nitrocellulose, gas properties in both the gas generator and the plenum, initial volumes, densities, temperatures, speeds, and displacements of the piston and parachute pack, as well as the initial mass of propellant in the initiators. These values are derived from the environmental input and other configuration files loaded into the simulation. The state vector `s` is organized as follows:

Parameter	Description	Variable	Initial Value
s[0]	Regressed length Nitrocellulose	r_{ntc}	0 m
s[1]	Gamma in GG	γ_{GG}	`ENV['Assy']['G']`
s[2]	Specific gas constant in GG	R_{GG}	`ENV['Assy']['R']`
s[3]	Gas generator initial volume	V_{GG}	`GG['Vcomb']['Va'] - GG['NTC']['PL'] / GG['NTC']['rho']`
s[4]	Density gas in GG	ρ_{GG}	`ENV['Opp']['rgg_t0']`
s[5]	Temperature gas in GG	T_{GG}	`ENV['Opp']['T']`
s[6]	Temperature wall in GG	$T_{w_{GG}}$	`ENV['Opp']['T']`
s[7]	Gamma in plenum	γ_{PL}	`ENV['Opp']['G']`
s[8]	Specific gas constant plenum	R_{PL}	`ENV['Opp']['R']`
s[9]	Plenum Volume	V_{PL}	`MRTR['plenum']['Vm']`
s[10]	Plenum gas density	ρ_{PL}	`ENV['Opp']['rpl_t0']`
s[11]	Initial piston speed	v_{piston}	0 m/s
s[12]	Initial piston displacement	x_{piston}	0 m
s[13]	Initial parachute pack speed	v_{pack}	0 m/s
s[14]	Initial parachute pack displacement	x_{pack}	0 m
s[15]	Temperature gas plenum	T_{PL}	`ENV['Opp']['T']`
s[16]	Temperature wall plenum	$T_{w_{PL}}$	`ENV['Opp']['T']`
s[17]	Propellant in initiators	m_{init}	`GG['INIT']['m_zpp']*GG['INIT']['n_init']`

Table 15: Initial Conditions Vector

3.3.2.1.2 Result Vectors

In this section, the result vectors are preallocated to ensure efficient data storage and retrieval during the simulation process. This preparation involves setting up time vectors, state vectors, and event-related vectors that will be used throughout the simulation.

Time Vectors

The simulation time span is defined using the provided time range and time step. This vector encompasses the entire duration of the simulation, divided into discrete time steps. The `tspan` variable is used to store this range, while `tout` is initialized to keep track of the output time vector starting from the initial time.

State Vectors

The state vectors store the dynamic state of the system at each time step. The initial state vector is duplicated to create the output state vector, which will be populated as the simulation progresses. The `S` vector is initialized with the initial state, while `teout`, `Seout`, and `ieout` are initialized to capture the times, states, and indices of events, respectively.

Event Vectors

The event vectors manage the occurrence and handling of specific events during the simulation. These events might include milestones like the bursting of a disk, the release of shear pins, or other significant occurrences that affect the system's behaviour. The `state` vector tracks the state of events, and `testate` records the times of these events. Initial conditions for events are set, and a list of event functions is created. A mapping from events to their indices is also established to facilitate event handling during the simulation.

These vectors are critical in the simulation for checking various conditions and ensuring that the simulation progresses correctly. They allow the simulation to capture the dynamic behaviour of the system, respond to specific events, and maintain an accurate timeline of the system's state changes.

3.3.2.1.3 ODE System, Solver & Events Handling

The MDT_Simcore module is the core of the PDD simulation, responsible for solving the system of ordinary differential equations (ODEs) that govern the dynamics of the Parachute Deployment Device. Using the solve_ivp function from the SciPy library, the module handles numerical integration over a specified time range. It sets up initial conditions, manages input parameters from other modules, and processes the results. This module controls the simulation's overall flow, ensuring that the dynamic processes are accurately captured.

The detailed system of ODEs is implemented within the MDT_Dynamics module, which models key physical phenomena, such as the combustion of Nitrocellulose (NC) propellant, mass and energy flows, and mechanical forces acting on the piston and parachute pack. These equations describe how the system's state variables evolve over time, capturing the interactions between gas generation, mechanical movement, and heat transfer.

- Regressed length of propellant grains: $\frac{ds_0}{dt} = r_{ntc}$ *(3.1)*
- Ratio of specific heat of gas in GG: $\frac{ds_1}{dt} = \frac{M_{ntc}(\Gamma_{ntc} - s_1)}{s_3 \cdot s_4}$ *(3.2)*
- Specific gas constant in GG: $\frac{ds_2}{dt} = \frac{M_{ntc}(\mathrm{R}_{GG} - s_2)}{s_3 \cdot s_4}$ *(3.3)*

- GG volume: $\frac{ds_3}{dt} = A_{ntc} r_{ntc} + V_{postcomb} \cdot MDT\_Burstdisk()$ *(3.4)*
- Density of gas in GG: $\frac{ds_4}{dt} = -\frac{s_4}{s_3}\frac{ds_3}{dt} + \frac{M_{ntc} M_{noz}}{s_3}$ *(3.5)*
- Gas temperature in GG: $\frac{ds_5}{dt} = -\frac{s_5}{s_4}\frac{ds_4}{dt} - \frac{s_5}{s_3}\frac{ds_3}{dt} + \frac{s_{19} + H_{ntc} - M_{noz} \cdot C_{p_1} \cdot s_5 - Q_{GG}}{C_{v_1} \cdot s_3 \cdot s_4}$ *(3.6)*
- GG walls temperature: $\frac{ds_6}{dt} = \frac{Q_{GG}}{C_{GG}}$ *(3.7)*
- Ratio of specific heats of gas in PL: $\frac{ds_7}{dt} = M_{noz} \cdot \frac{s_1 - s_7}{s_9 \cdot s_{10}}$ *(3.8)*
- Specific gas constant in PL: $\frac{ds_8}{dt} = M_{noz} \cdot \frac{s_2 - s_8}{s_9 \cdot s_{10}}$ *(3.9)*
- PL volume: $\frac{ds_9}{dt} = A_{piston} \cdot s_{11}$ *(3.10)*
- Gas density in PL: $\frac{ds_{10}}{dt} = -\frac{s_{10}}{s_9}\frac{ds_9}{dt} + \frac{M_{noz} - M_{vent}}{s_9}$ *(3.11)*
- Parachute pack velocity: $\frac{ds_{11}}{dt} = a_{piston}$ *(3.12)*
- Parachute pack displacement: $\frac{ds_{12}}{dt} = s_{11}$ *(3.13)*
- Piston velocity: $\frac{ds_{13}}{dt} = a_{pack}$ *(3.14)*
- Piston displacement: $\frac{ds_{14}}{dt} = s_{13}$ *(3.15)*
- Gas temperature in PL: $\frac{ds_{15}}{dt} = -s_{15} \cdot \left(\frac{1}{s_9}\frac{ds_9}{dt} + \frac{1}{s_{10}}\frac{ds_{10}}{dt}\right) + \frac{H_m - Q_{PL}}{C_{v_2} \cdot s_9 \cdot s_{10}}$, $H_m = M_{noz} \cdot C_{p_1} \cdot s_5 - M_{vent} \cdot C_{p_2} \cdot s_{15}$ *(3.16)*
- If vent starts: $\frac{ds_{15}}{dt} = \frac{H_m - Q_{PL}}{C_{v_2} \cdot s_9 \cdot s_{10}}$ *(3.17)*
- PL walls temperature: $\frac{ds_{16}}{dt} = \frac{Q_{PL}}{C_{PL}}$ *(3.18)*
- Initiators propellant amount: $\frac{ds_{17}}{dt} = -r_{init} \cdot n_{init}$ *(3.19)*
- Initiators pressure output: $\frac{ds_{18}}{dt} = P_{init}$ *(3.20)*
- Initiators energy output: $\frac{ds_{19}}{dt} = H_{init}$ *(3.21)*

Solving Methods: Explicit vs. Implicit

Numerical methods for solving ODEs can be divided into explicit and implicit approaches. In explicit methods, the new value of the dependent variable at the next time step is computed directly from the known values at the current step. Although explicit methods, like the Euler method, are simpler and computationally efficient per step, they tend to be conditionally stable. This means that they require small time steps to maintain accuracy and stability, especially when dealing with stiff systems.

An explicit method like the Euler method can be written as:

$$y_{n+1} = y_n + h \cdot f(t_n, y_n) \quad (3.22)$$

Where h is the step size, y_n is the current value, and $f(t_n, y_n)$ is the function describing the derivative at time t_n.

On the other hand, implicit methods solve for the new value of the dependent variable by solving an equation involving both current and future states. This makes them particularly useful for stiff equations, as they allow for larger time steps without risking instability. A common implicit method is the Backward Euler method:

$$y_{n+1} = y_n + h \cdot f(t_n, y_{n+1}) \quad (3.23)$$

In this method, y_{n+1} is on both sides of the equation, and its calculation generally involves solving a system of equations iteratively. Implicit methods are preferred for stiff systems because they are unconditionally stable and can handle the sharp changes typical of such systems.

Why the Radau Method?

The Radau method, an implicit Runge-Kutta method, is well-suited for stiff ODEs, making it an ideal choice for the PDD simulation. It uses stiffly accurate collocation points to maintain stability while solving equations that exhibit rapid changes, such as gas generation, mechanical motion, and thermal processes. This method enables the simulation to use larger time steps without compromising accuracy, which is critical for capturing both the fast dynamics (e.g., pressure spikes) and the slower processes (e.g., heat transfer) involved in the PDD.

Solver

The solver iteratively integrates the system's equations over the specified time range. The initial conditions set the starting point, and the solver progresses through the time steps defined by `tspan2`. The `solve_ivp` function is configured with various parameters, including the method ('Radau'), the initial state vector, and additional arguments representing the simulation variables, gas generator parameters, mortar parameters, and environmental conditions. The solver also handles the occurrence of events by including event detection functions.

Events Handling

vent handling in the simulation is managed by the MDT_Events module, which defines the key milestones that alter the behaviour of the system. These events include critical moments like the bursting of the disk or the ejection of the piston. Events are defined as functions that return zero when a specific condition is met, such as when the pressure difference exceeds a preset limit or when the piston reaches the end of its stroke. The solve_ivp function continuously monitors these conditions and triggers events accordingly.

When an event is detected, several actions occur: the time and state of the system at the event are recorded, and the system's state is updated based on the event outcome. The event processing then modifies the necessary variables, such as updating the pressure after the disk burst, and adjusts the simulation parameters to reflect the new conditions. This ensures the system transitions smoothly through phases such as venting or parachute deployment. The simulation continues with the adjusted state, and the results are accumulated for further analysis, capturing both pre- and post-event dynamics.

The event-driven approach ensures that the PDD simulation is not only time-stepped but also reacts appropriately to physical triggers, capturing key transitions in the deployment process. This mechanism ensures the fidelity of the simulation, allowing it to accurately model the critical events that drive the system's behaviour throughout the entire sequence.

3.3.2.1.4 Finalising Results

In the final stage of the simulation, we consolidate and process the computed results. This involves calculating key physical quantities such as pressures and forces, which are crucial for analysing the behaviour of the parachute deployment device.

Calculating Pressures

To determine the pressures inside the gas generator and the mortar tube, we initialize a pressure matrix PPP with zeros. This matrix has dimensions corresponding to the length of the state vector SSS and includes two columns for the pressures in GG and MRTR, respectively.

- **Pressure inside the GG:** The pressure inside the GG is computed using the specific gas constant, temperature, and density values from the state vector, along with the co-volume of the reaction products. The pressure is then converted to megapascals (MPa).

- **Pressure inside the MRTR:** The pressure inside the MRTR is calculated in two stages: before and after the event of venting completion (event 4).
  Before event 4: We determine the index corresponding to the time of event 4. If event 4 has occurred, we use its index; otherwise, we use the last index of the state vector. Using this index, we compute the pressure inside the MRTR up to the time of event 4 based on the specific gas constant, temperature, and density values.

  After event 4: After event 4, the pressure inside the MRTR is set equal to the outside environmental pressure.

Calculating Forces

The forces acting on the piston and the parachute pack are calculated using the differences in their respective velocities and the known masses of the components.

Reaction forces: The reaction forces on the piston and the parachute pack are computed by considering the changes in their velocities over time. These forces are combined to obtain the total force acting on the system. After event 4, the force is set to zero when the force is negative, indicating that the pack has vented and external forces no longer contribute to its motion.

Combining Results

Finally, the computed pressures and forces are combined with the state vector to form the final state matrix. This augmented state vector ensures that all necessary data is captured for further analysis. The time vector is also finalized to correspond to the entire simulation duration.

The consolidated results, including the state matrix, time vector, and events, provide a comprehensive view of the PDD's dynamic behaviour. This detailed set of simulation results facilitates further analysis and validation, ensuring that the simulation accurately captures the PDD's performance under various conditions.

3.3.2.2 Events

The Events module in the parachute deployment device simulation is designed to handle specific conditions that occur during the simulation. These conditions, or events, are critical for accurately modelling the dynamic behaviour of the system. Each event is defined as a function that returns zero when a particular condition is met, signalling the occurrence of the event. The events are managed using the `solve_ivp` function from the SciPy library, which integrates the system of ordinary differential equations (ODEs) and checks for these events.

Event 1: Burst Disk Opening

The first event checks the pressure difference between the gas generator and the plenum to determine when the burst disk opens. This event is triggered when the pressure difference exceeds the burst pressure of the disk.

$$event\_1 = (P_{GG} - P_{PL}) - P_{burst} \tag{3.24}$$

Where P_{GG} is the pressure in the gas generator and P_{PL} is the pressure in the plenum and P_{burst} is the burst pressure of the burstdisk. The event is terminal, meaning the solver will stop integrating once this event is detected, and it is direction-sensitive, triggering only when the pressure difference is increasing.

Event 2: Shear Pins Opening

The second event checks the force exerted by the gas pressure on the piston against the shear pins holding it in place. This event is triggered when the spring compression force exceeds the maximum shear load of the pins.

$$event\_2 = F_{Comp} - (N \cdot F_{burst} - F_{preload}) \tag{3.25}$$

Where F_{Comp} is the spring compression force, N is the number of shear pins that hold the lid, F_{burst} is the maximum shear load per pin, and $F_{preload}$ is the preload force during integration of the parachute pack. This event is terminal and direction-sensitive, triggering only when the force is increasing.

Event 3: Piston Skirt Reaches End of Stroke

The third event checks the position of the piston to determine when it reaches the end of its stroke length, including the skirt length. This event is triggered when the piston displacement exceeds the stroke length.

$$event\_3 = x_{piston} - (Sm + skirt) \tag{3.26}$$

Where x_{piston} is the piston displacement, Sm is the mortar stroke length, and $skirt$ is the length of the piston skirt. This event is terminal and direction-sensitive, triggering only when the piston displacement is increasing.

Event 4: Venting Completed

The fourth event checks the pressure in the plenum to determine when venting is completed. This event is triggered when the plenum pressure drops to the environmental pressure.

$$event\_4 = P_{PL} - P_{env} \tag{3.27}$$

where P_{PL} is the pressure in the plenum and P_{env} is the environmental pressure. This event is terminal and direction-sensitive, triggering only when the pressure is decreasing.

Event 5: Maximum Distance Reached

The fifth event checks the displacement of the parachute pack to determine when it reaches the maximum distance allowed in the simulation.

$$event\_5 = x_{piston} - x_{max} \tag{3.28}$$

where x_{max} is the maximum displacement. This event is terminal and direction-sensitive, triggering only when the displacement is increasing.

Event 6: Pack Falls to Ground

The sixth event checks the displacement of the parachute pack to determine when it falls to the ground. This event is triggered when the parachute pack displacement exceeds 1.5 meters.

$$event\_6 = x_{pack} - 1.5 \tag{3.29}$$

This event is terminal and direction-sensitive, triggering only when the displacement is decreasing.

3.3.2.3 Dynamics

The `MDT_Dynamics` module is a key component of the Parachute Deployment Device (PDD) simulation, responsible for calculating the derivatives of the state variables over time. This module integrates various submodules that handle specific aspects of the simulation, such as burn rates, nozzle flows, and compression dynamics.

3.3.2.3.1 Initiators Model

The initiators setup in the MDT_Dynamics module defines the initial configuration and subsequent behaviour of the initiators used in the gas generator. These initiators play a critical role in initiating the propellant combustion process by providing the necessary pressure and enthalpy.

The burn rate of the initiator propellant, denoted as r_{init}, is specified in kilograms per second (kg/s). It is calculated based on the initial mass of the propellant and the total burn time. The burn time t_{init} represents the total duration over which the initiators burn, measured in seconds (s). Based on results from the testing campaign, it was found that the initiators burn for approximately 3 milliseconds (ms) on average. The total number of initiators n_{init} used in the gas generator is also specified.

For each initiator, the pressure output P_{init} and the enthalpy output H_{init} are defined. The pressure output is the total pressure generated by each initiator when fully burned, measured in Pascals (Pa). The enthalpy output is calculated as the product of the specific enthalpy and the mass of the propellant, measured in Joules (J):

$$H_{output} = h_{init} \times m_{zpp} \tag{3.30}$$

The pressure increase rate and heat increase rate are then computed. The pressure increase rate and the enthalpy increase rate per second per initiator are defined by:

$$\dot{p} = \frac{P_{output}}{t_{init}} \tag{3.31}$$

$$\dot{h} = \frac{H_{output}}{t_{init}} \tag{3.32}$$

During the simulation, the module determines the added pressure and enthalpy from the initiators based on the elapsed time t and the number of initiators n_{init}. If the initiators are still burning (i.e., if there is remaining propellant and the current time is less than or equal to the burn time), the pressure and enthalpy contributions are calculated:

$$P_{init} = \dot{p} \times t \times n_{init} \tag{3.33}$$

$$H_{init} = \dot{h} \times t \times n_{init} \tag{3.34}$$

After the burn time has elapsed, the initiators no longer contribute additional pressure or enthalpy to the system, and these values are set to zero:

$$P_{init} = 0$$

$$H_{init} = 0$$

The model for the initiators is simplified and is based on known parameters, including the mass of propellant in each initiator, burning duration, pressure, and enthalpy output. This ensures that the initial thrust and energy contributions are accurately represented in the simulation, providing a realistic depiction of the gas generator's behaviour during the early stages of the PDD's operation.

3.3.2.3.2 Gas Variables

The calculation of gas variables within the MDT_Dynamics module is crucial for accurately modelling the thermodynamic properties and behaviour of the gases involved in the Parachute Deployment Device (PDD) simulation. This section explains the key calculations performed for determining gas pressures, specific heat capacities, and other related variables.

To begin with, the pressures in both the gas generator and the plenum are calculated using the Noble-Abel equation of state, which accounts for the non-ideal behaviour of gases at high pressures and densities. For the gas generator, the pressure $P1$ is determined using the formula:

$$P_{GG} = s[0] + s[2] \cdot s[5] \cdot \frac{s[4]}{1 - s[4] \cdot GG[\mathrm{NTC}][\mathrm{b}]} + P_{init} \quad (3.35)$$

where:

- $s[0] = r_{ntc}$ is the regressed length of Nitrocellulose
- $s[2] = R_{GG}$ is the specific gas constant in the gas generator
- $s[5] = T_{GG}$ is the temperature of the gas in the gas generator
- $s[4] = \rho_{GG}$ is the density of the gas in the gas generator
- $GG[\mathrm{NTC}][\mathrm{b}]$ is the co-volume of reaction products
- $P_{init}$is the pressure contribution from the initiators.

Similarly, the pressure $P2$ in the plenum is calculated as:

$$P_{PL} = \mathrm{s}[8] \cdot \mathrm{s}[15] \cdot \frac{\mathrm{s}[10]}{1 - \mathrm{s}[10] \cdot \mathrm{GG}[\mathrm{NTC}][\mathrm{b}]} \quad (3.36)$$

where:

- $\mathrm{s}[8] = R_{PL}$ is the specific gas constant in the plenum,
- $s[15] = T_{PL}$ is the temperature of the gas in the plenum,
- $s[10] = \rho_{PL}$ is the density of the gas in the plenum.

Next, the specific heat capacities at constant pressure (Cp) and constant volume (Cv) are derived. These capacities are essential for energy calculations and are derived from the specific gas constants and the ratios of specific heats. For the gas generator, the specific heat capacity at constant pressure Cp_1 and at constant volume Cv_1 are given by:

$$Cp_1 = \frac{s[2] \cdot s[1]}{s[1] - 1} \quad (3.37)$$

$$Cv_1 = \frac{s[2]}{s[1] - 1} \tag{3.38}$$

Where $s[1] = \gamma_{GG}$ is the ratio of specific heats in the gas generator.

For the plenum, the specific heat capacity at constant pressure Cp_2 and at constant volume Cv_2 are calculated as:

$$Cp_2 = \frac{s[8] \cdot s[7]}{s[7] - 1} \tag{3.39}$$

$$Cv_2 = \frac{s[8]}{s[7] - 1} \tag{3.40}$$

Where $s[7] = \gamma_{PL}$ is the ratio of specific heats in the plenum.

These calculations provide the necessary thermodynamic properties to accurately simulate the behaviour of the gases within the PDD system, ensuring that energy transfers and pressure dynamics are properly modelled.

3.3.2.3.3 Propellant

The propellant dynamics involve calculating the regression rate and the burning surface area of Nitrocellulose (NC). The regression rate, r_{ntc}, is computed using the `MDT_Burnrate` module, which considers the pressure and temperature within the gas generator. The burning surface area, A_{ntc}, is determined using the `MDT_NTC_Surface` module, based on the current regressed length and the geometric dimensions of the Nitrocellulose grains. These modules will be presented in detail later.

3.3.2.3.4 Mass Flows

The mass flow rates within the system are essential for understanding the dynamics of gas movement through various sections of the Parachute Deployment Device (PDD). The mass flow calculations take into account different stages and components such as the propellant, nozzles, and vents.

The propellant mass flow rate, M_{ntc}, is calculated based on the density of Nitrocellulose (ρ_{ntc}), the burning surface area (A_{ntc}), and the regression rate (r_{ntc}). This is crucial for determining the amount of gas generated over time.

$$M_{ntc} = \rho_{ntc} \times A_{ntc} \times r_{ntc} \tag{3.41}$$

For the nozzles, the mass flow rate, M_{noz} is calculated using the `MDT_Nozzleflow` module. This calculation considers the pressure difference between the gas generator and the plenum, the specific gas constant, and the temperature of the gas. The state variable ensures that this mass flow is only considered when appropriate.

$$M_{noz} = MDT_{NozzleFlow}(P_{GG}, P_{PL}, \gamma_{GG}, T_{GG}, GG[\text{orifices}], GG[\text{NTC}][\text{b}]) * state[0]) \tag{3.42}$$

Here, $state[0]$ is 0 if the burstdisk has not broke and 1 if it has. It is the condition for the gas to be able to escape from the gas generator to the plenum volume of the mortar tube.

Additionally, the mass flow rate M_{vent}, which represent the vent of the plenum volume after the piston has been ejected, is determined after the vent event is triggered ($state[2] = 1$). This mass flow is calculated similarly to the nozzle flow but considers the environmental pressure.

$$M_{vent} = state[2] \times MDT_{Nozzleflow}(P_{PL}, P_{env}, \gamma_{PL}, R_{PL}, T_{PL}, MRTR["orifices"], GG[\text{NTC}][\text{b}]) \tag{3.43}$$

Where:

- $P_{env} = ENV["Opp"]["P"]$ is the environment pressure during operation.
- $MRTR[\text{orifices}]$ is the gap between the skirt of the piston and the walls of the mortar tube during venting.

When certain conditions are met (e.g., state [3] is 1), the mass flow through the vents equals the nozzle mass flow rate, indicating a direct flow without additional resistance.

These mass flow calculations are integrated into the system dynamics to update the state variables accurately, reflecting the changes in mass distribution within the PDD over time.

3.3.2.3.5 Heat Flows

The heat flows within the system consider both convective and radiative heat transfer, as well as the enthalpy flow from the propellant combustion.

Convective Heat Losses

Convective heat transfer occurs between the gas and the walls of the GG and PL. The heat transfer coefficients (hc_{GG} and hc_{PL}) are used to calculate the convective heat loss based on the temperature difference between the gas and the wall.

$$Q_{GG_{conv}} = hc_{GG} \cdot (A_{GG_{comb}} + A_{GG_{postcomb}} \cdot state[0]) \cdot (T_{GG} - T_{w_{GG}}) \quad (3.44)$$

$$Q_{PL_{conv}} = hc_{PL} \cdot (A_{PL} + \pi \cdot D_{PL} \cdot x_{piston}) \cdot (T_{PL} - T_{w_{PL}}) \quad (3.45)$$

Radiative Heat Losses

Radiative heat transfer is calculated using the Stefan-Boltzmann law. The thermal emissivity (ϵ) and the Stefan-Boltzmann constant (σ) are used to determine the radiative heat loss based on the difference in the fourth power of the temperatures.

$$Q_{GG_{rad}} = \epsilon_{GG} \cdot \epsilon_{gas} \cdot \sigma \cdot (A_{GG_{comb}} + A_{GG_{postcomb}} \cdot state[0]) \cdot ({T_{GG}}^4 - {T_{w_{GG}}}^4) \quad (3.46)$$

$$Q_{PL_{rad}} = \epsilon_{PL} \cdot \epsilon_{gas} \cdot \sigma \cdot (A_{PL} + \pi \cdot D_{PL} \cdot x_{piston}) \cdot ({T_{PL}}^4 - {T_{w_{PL}}}^4) \quad (3.47)$$

The total heat loss for the GG and PL is the sum of the convective and radiative losses:

$$Q_{GG} = Q_{GG_{conv}} + Q_{GG_{rad}} \quad (3.48)$$

$$Q_{PL} = Q_{PL_{conv}} + Q_{PL_{rad}} \quad (3.49)$$

Enthalpy Flow from Propellant

The enthalpy flow from the combustion of the Nitrocellulose (NTC) propellant is calculated using the mass flow rate (M_{ntc}), specific heat capacity at constant pressure (Cp), and the adiabatic flame temperature (T_{ad}):

$$H_{ntc} = M_{ntc} \cdot Cp_{ntc} \cdot T_{\text{ad}} \quad (3.50)$$

3.3.2.3.6 Pack Forces

The forces acting on the parachute pack and piston within the mortar tube are critical to understanding the dynamics of the Parachute Deployment Device (PDD). These forces include the spring force,

damper force, friction forces, gas pressure force, gravity force, and air resistance. These forces are combined to calculate the accelerations of the piston and the parachute pack.

Masses Definition

The masses involved in the simulation are defined as follows:

$M1$: Mass of the parachute pack.

$M2$: Mass of the piston.

$M3$: Mass of the lid.

Spring, Damper, and Friction Forces

The spring force (F_{Comp}), damper force (F_{Damper}), friction force on the piston ($F_{Friction_{piston}}$), and friction force on the parachute pack ($F_{Friction_{pack}}$) are computed using the `MDT_Compression` submodule. These forces depend on the current state of the system, including the positions and velocities of the piston and parachute pack, the pressure in the plenum, and the time elapsed.

Gravity Force

The gravitational force component acting along the flight path angle is calculated as:

$$G = g \cdot cos\,(\alpha) \tag{3.51}$$

where g is the local acceleration due to gravity and α\alphaα is the flight path angle.

Gas Pressure Force

The force exerted by the gas pressure on the piston is calculated using the pressure difference across the piston:

$$\begin{cases} A_{b_{piston}} \cdot (P_{PL} - P_{env}) & if\ P2 > P_{env} \\ 0 & otherwise \end{cases} \tag{3.52}$$

where $A_{b_{piston}}$ is the base area of the piston, P_{PL} is the pressure in the plenum, and P_{env} is the environmental pressure.

Air Resistance

The air resistance acting on the lid is calculated as:

$$F_{Aero_{coupled}} = Cd \cdot A_{b_{lid}} \cdot \frac{P_{env}}{2 \cdot R_{PL} \cdot T_{PL}} \cdot {u_{pack}}^2 \tag{3.53}$$

Where Cd is the drag coefficient, $A_{b_{lid}}$ is the base area of the lid, R_{PL} is the specific gas constant in the plenum, T_{PL} is the temperature of the gas in the plenum, and u_{pack} is the velocity of the parachute pack.

Calculation of Accelerations

The accelerations of the piston and the parachute pack are calculated based on the state of the system:

Before Shear Pins Break:

$$a_{piston} = a_{pack} = \frac{F_{gas} - F_{Comp} - F_{Friction_{pack}} - F_{Friction_{piston}} - F_{Damper} - (M1 + M2 + M3) \cdot G}{M1 + M2 + M3}$$

(3.54)

After Shear Pins Break and Before Venting:

$$a_{piston} = \frac{F_{gas} - F_{Friction_{pack}} - F_{Friction_{piston}} - (M1 + M2 + M3) \cdot G}{M1 + M2 + M3} \quad (3.55)$$

$$a_{pack} = \frac{F_{gas} - F_{Friction_{pack}} - F_{Friction_{piston}} - (M1+M2+M3) \cdot G - F_{Aero_{coupled}} - F_{Damper} + F_{Comp}}{M1+M2+M3} \quad (3.56)$$

After Venting:

$$a_{piston} = -M2 \cdot G - F_{Aero_{coupled}} \quad (3.57)$$

$$a_{pack} = -M1 \cdot G - F_{Aero_{coupled}} \quad (3.58)$$

These accelerations are used to update the velocities and displacements of the piston and parachute pack in the differential equations, ensuring accurate modelling of their motion throughout the simulation.

3.3.2.4 Burnrate

The `MDT_Burnrate` module calculates the burn rate based on the pressure and temperature conditions within the gas generator, as well as the characteristics of the propellant. This module implements the burn rate law, which takes into account both the pressure dependence and the temperature sensitivity of the propellant burn rate.

The burn rate is calculated using the following steps:

Burn Law Coefficient: The burn law coefficient, β, is adjusted based on the environmental temperature:

$$\beta = \beta_0 \cdot (1 + \sigma \cdot (T_{env} - T_0)) \quad (3.59)$$

where:

- β_0 is the base burn law coefficient.
- σ is the temperature sensitivity coefficient.
- T_{env} is the environmental temperature.
- T_0 is the reference temperature.

Burn Rate Calculation: The burn rate, r, is computed differently based on the temperature of the propellant:

If the temperature T_{GG} is below the ignition temperature T_{ig}:

$$r = \beta \cdot \left(\frac{P_{GG}}{P_{ref}}\right)^a \cdot exp\left(-\frac{E_a}{R_{GG}}\left(\frac{1}{T_{ig}} - \frac{1}{T_{GG}}\right)\right) \quad (3.60)$$

Where:

- P_{GG} is the pressure.
- a is the pressure exponent in the burn rate law.
- E_a is the activation energy.
- R_{GG} is the specific gas constant for the propellant.

- T_{ig} is the ignition temperature.
- P_{ref} is the reference pressure, typically 1 MPa.

If the temperature T_{GG} is at or above the ignition temperature T_{ig}:

$$r = \beta \cdot \left(\frac{P_{GG}}{P_{ref}}\right)^{a} \tag{3.61}$$

The burn rate law captures the propellant's response to pressure and temperature, ensuring that the simulation accurately reflects the physical behaviour of the gas generator. This allows for precise modelling of the propellant's combustion process, which is crucial for predicting the system's performance under various conditions.

3.3.2.5 Burning Surface

The `MDT_NTC_Surface` module calculates the burning surface area of the Nitrocellulose (NTC) propellant grains, which is critical for determining the burn rate and gas generation rate in the parachute deployment device simulation. The module considers the regression of the grain surface due to combustion and computes the resulting surface area based on the grain's geometric parameters. The calculation process starts with determining the initial surface area based on the grain's outer and inner dimensions. Intermediate values and angles are computed to define the grain's geometry. As the grain burns and regresses, the surface area is updated accordingly. The final burning surface area is determined by summing the linear and exponential components, adjusting for regression, and considering the number of grains.

Geometric Parameters

The calculation begins by defining several geometric parameters that describe the physical dimensions and structure of the propellant grains. These parameters include:

- L: Length of the grain.
- D: Outer diameter of the grain.
- d: Diameter of the perforations within the grain.
- N: Number of perforations in the grain.
- w: Web thickness of the grain.
- u: Regression distance, defined as $2r$.
- n: Number of grains.

These parameters are essential for defining the initial shape and volume of the grain. The length L and outer diameter D give the overall dimensions of the grain, while the inner perforations, characterized by d and N, affect the burning surface area as the grain regresses.

Intermediate Geometric Calculations

Several intermediate geometric values are computed to assist in calculating the burning surface area:

- $OA = 0.25(D + d)$: The average of the outer and inner radii of the grain.
- $AD = \frac{1}{2}OA$: Half of the average diameter.

- $OZ = AQ = \frac{1}{2}(d + u)$: Inner dimensions affected by the regression distance.
- $OQ = \frac{1}{2}(D - u)$: Outer dimension affected by the regression distance.

Using these intermediate values, several angles are calculated:

- $\omega = arcos(AD/AQ)$ *(3.62)*
- $OAQ = arcos\left(\frac{OA^2+AQ^2-OQ^2}{2 \cdot OA \cdot AQ}\right)$ *(3.63)*
- $\chi = OAQ - \omega - \pi\left(0.5 - \frac{1}{N-1}\right)$ *(3.64)*
- $\Phi = \arccos\left(\frac{OA^2+OQ^2-AQ^2}{2 \cdot OA \cdot OQ}\right)$ *(3.65)*
- $\beta = 2(\pi/(N-1) - \Phi)$ *(3.66)*
- $\Phi_1 = arcos(OA/2 \cdot OZ)$ *(3.67)*
- $\beta_1 = 2\pi(N-1) - 2\Phi_1$ *(3.68)*

These angles help define the evolving shape of the grain's surface as it regresses due to burning. The angles ω, χ, and β are particularly important as they capture the changes in the surface area of the grain's perforations.

Surface Area Calculation

The module calculates the burning surface area through a series of conditional computations based on the regression distance relative to the web thickness:

For regression distances less than half the web thickness ($r < 0.5w$):

$$S = n \cdot \pi \cdot (L - u) \cdot (D - u + N \cdot (d + u)) + 0.5 \cdot \pi \cdot ((D - u)^2 - N \cdot (d + u)^2) \quad (3.69)$$

This formula accounts for the surface area reduction due to the burning regression. The term $(L - u)$ reduces the length of the grain by the regression distance, while $(D - u)$ and $(d + u)$ adjust the diameters accordingly. The factor *N* multiplies the inner surface area by the number of perforations.

For regression distances greater than or equal to half the web thickness ($r \geq 0.5w$) and where $\beta_1 > 0$:

The area of lateral surfaces of $N - 1$ large, outer slivers S_L is:

$$S_L = (N - 1)(L - u)(\beta \cdot OQ + 2\chi \cdot AQ) \quad (3.70)$$

The area of lateral surfaces of $N - 1$ small, inner slivers S_l is:

$$S_l = (N - 1)(L - u)(3 \cdot OZ \cdot \beta_1) \quad (3.71)$$

The area of two end surfaces of $N - 1$ large, outer slivers S_E is:

$$S_E = 2(N-1)\{OQ \cdot sin(0.5\beta)[(2AQ \cdot \sin(0.5 * \chi))^2 - (OQ \cdot \sin(0.5 \cdot \beta))^2]^{1/2} + 0.5OQ^2(\beta - sin(\beta)) - AQ^2(\chi - sin(\chi))\} \quad (3.72)$$

And the area of two end surfaces of $N - 1$ small, inner slivers

$$S_e = 2(N-1)OZ^2\{sin^2(0.5\beta_1) \cdot 1.73206 - 1.5 \cdot [\beta_1 - sin(\beta_1)]\} \quad (3.73)$$

The total area of the slivers is the:

$$S = n \cdot (S_L + S_l + S_E + S_e) \tag{3.74}$$

The calculation involves summing linear and exponential terms to capture the complex surface area changes as the regression progresses beyond half the web thickness.

For $\beta_1 \leq 0$ and $\beta > 0$:

$$S_l = 0$$

$$S_L = (N-1)(L-u)(\beta \cdot OQ + 2\chi \cdot AQ) \tag{3.75}$$

$$S_e = 0$$

$$S_E = 2(N-1)\{OQ \cdot sin(0.5\beta)[(2AQ \cdot \sin(0.5 * \chi))^2 - (OQ \cdot \sin(0.5 \cdot \beta))^2]^{1/2} + 0.5OQ^2(\beta - sin(\beta)) - AQ^2(\chi - sin(\chi))\} \tag{3.76}$$

And the total area is:

$$S = n \cdot (S_L + S_l + S_E + S_e) \tag{3.77}$$

For cases where regression has progressed beyond critical dimensions:

$$S = 0$$

This indicates that the grain has fully burned out and the surface area is effectively zero.

Accurately modelling the burning surface area is essential for predicting the gas generation rate and the overall performance of the gas generator in the PDD. This module's computations provide the foundation for understanding how the propellant grains contribute to the system's dynamics during operation.

3.3.2.6 Nozzle Flow

The `MDT_Nozzleflow` module is responsible for calculating the mass flow rate through the nozzles of the gas generator. This calculation is crucial for understanding how the generated gases are expelled from the system, affecting the overall dynamics and performance of the parachute deployment device.

The module first calculates the upstream gas density using the given pressures, temperatures, and the specific gas constant. It then determines if the flow is choked by comparing the pressure ratio $\frac{P_{PL}}{P_{GG}}$ with the choked flow criterion. Depending on whether the flow is choked or not, it calculates the mass flow rate using the appropriate formula.

For unchoked flow, the mass flow rate is derived from the pressure difference and the gas properties, incorporating the discharge coefficient and nozzle area. For choked flow, the mass flow rate depends on the upstream conditions and the van Kerckhoven function, reflecting the maximum flow rate the nozzle can handle when the gas velocity reaches the speed of sound.

Mass Flow Rate Calculation

The mass flow rate through the nozzle is determined based on the pressure difference between the upstream (inside the gas generator) and downstream (outside or another chamber) sides, as well as the properties of the gas and the nozzle. The flow can be either choked or unchoked, depending on the pressure ratio.

Upstream Density Calculation:

$$\rho_{GG} = \frac{P_{GG}}{R_{GG} \cdot T_{GG} - P_{GG} \cdot b} \tag{3.78}$$

Where:

- P_{GG} is the upstream pressure (gas generator).
- R_{GG} is the specific gas constant.
- T_{GG} is the upstream temperature.
- b is the co-volume of the gas.

This equation calculates the density of the gas upstream of the nozzle using the Nobel-Abel equation of state, which accounts for the compressibility effects at high pressures.

Choked Flow Criteria:

$$choked\_criteria = \left(\frac{2}{\gamma + 1}\right)^{\frac{\gamma}{\gamma - 1}} \tag{3.79}$$

Where:

- γ is the ratio of specific heats.

This criterion determines whether the flow is choked. Choked flow occurs when the pressure ratio between the upstream and downstream sides is high enough that the flow reaches the speed of sound at the nozzle throat.

Unchoked Flow Calculation:

When the flow is not choked, the mass flow rate is given by:

$$M = Cd \cdot no \cdot Ao \cdot \sqrt{2 \cdot P_{GG} \cdot \rho_{GG} \cdot \left(\frac{\gamma}{\gamma - 1}\right)\left[\left(\frac{P_{PL}}{P_{GG}}\right)^{\frac{2}{\gamma}} - \left(\frac{P_{PL}}{P_{GG}}\right)^{\frac{\gamma+1}{\gamma}}\right]} \tag{3.80}$$

Where:

- Cd is the orifice discharge coefficient.
- no is the number of orifices.
- Ao is the area of a single orifice.
- P_{PL} is the downstream pressure (mortar tube plenum)

Choked Flow Calculation:

When the flow is choked, the mass flow rate is calculated using the van Kerckhoven function:

$$Kerck = \sqrt{\gamma \cdot \left(\frac{2}{\gamma + 1}\right)^{\frac{\gamma+1}{\gamma-1}}} \tag{3.81}$$

$$M = Cd \cdot no \cdot Ao \cdot \sqrt{\rho_{GG} \cdot P_{GG} \cdot Kerck^2} \tag{3.82}$$

Zero Flow Condition:

If the upstream pressure is less than the downstream pressure $\left(\frac{P_{GG}}{P_{PL}} < 1\right)$, the mass flow rate is set to zero.

3.3.2.7 Compression

The `MDT_Compression` module calculates the forces acting on the piston and the parachute pack during different phases of the Parachute Deployment Device (PDD) operation. These phases include the compression phase, the ejection phase, and the decompression phase. The module accounts for various forces such as spring force, damping force, and frictional forces.

Compression Phase

In the compression phase, the parachute pack is compressed against the lid by the piston. The forces acting during this phase are:

- **Spring Force (F_{Comp})**: This force is exerted by the compressed parachute pack and is given by:

$$F_{Comp} = C_{pack} \cdot exp\ (x_{piston} \cdot k_{pack}) \quad (3.83)$$

  Where C_{pack} is the spring constant of the pack, x_1 is the displacement of the piston, and k_{pack} is the stiffness constant.

- **Damping Force (F_{Damper}):** This force accounts for the damping effect during compression and is given by:

$$F_{Damper} = c_{pack} \cdot u_{piston} \quad (3.84)$$

  Where c_{pack} is the damping coefficient and u_{piston} is the velocity of the piston.

- **Friction Force on Piston ($F_{Friction_{piston}}$)**: The friction force due to the piston seals is given by:

$$F_{Friction_{piston}} = 2 \cdot F_{n_{seal}} \cdot \mu_{seal} \quad (3.85)$$

  Where$F_{n_{seal}}$ is the normal compression force of the seals and μ_{seal} is the friction coefficient of the seals.

- **Friction Force on Parachute Pack ($F_{Friction_{pack}}$):** The friction force acting on the parachute pack is given by:

$$F_{Friction_{pack}} = (\mu_{pack} \cdot \nu_{pack} \cdot P_{PL} \cdot Ab_{pack} * (L_{pack} - x_{pack})/L_{pack} \quad (3.86)$$

Where μ_{pack} is the friction coefficient of the pack, ν_{pack} is the Poisson's ratio, P_{PL} is the pressure, Ab_{pack} is the base area of the pack, L_{pack} is the length of the pack, and x_{pack} is the displacement of the pack.

Ejection Phase

During the ejection phase, the piston and the parachute pack are pushed out of the mortar tube. The forces during this phase are adjusted based on the position of the piston and the state of the ejection process.

Initial Ejection Phase (before piston out):

The shear pins are broken, so the lid is away from the mortar tube, then the compression and damping forces are null:

$$F_{Comp} = 0$$

$$F_{Damper} = 0$$

If the top O-ring seal is still inside the mortar tube ($x_{piston} \leq l_2$):

$$F_{Friction_{piston}} = 2 \cdot F_{n_{seal}} \cdot \mu_{seal} \quad (3.87)$$

$$F_{Friction_{pack}} = (\mu_{pack} \cdot \nu_{pack} \cdot P_{PL} \cdot Ab_{pack} * (L_{pack} - x_{pack})/L_{pack} \quad (3.88)$$

If the top O-ring seal of the piston is out of the mortar tube, it means that the parachute pack is already out of the mortar tube and only one seal of the piston remains in contact with the walls of the mortar tube:

$$F_{Friction_{piston}} = F_{n_{seal}} \cdot \mu_{seal} \quad (3.89)$$

$$F_{Friction_{pack}} = 0$$

Decompression Phase (After the Piston is Out):

When x_{piston} exceeds the travel distance of the piston's bottom O-ring (l_1), the friction forces on the piston and the pack are set to zero.

Decompression Phase

In the decompression phase, the forces acting on the piston and pack change as they exit the mortar tube, and the decompression starts.

Spring Force and Damping Force: These forces are recalculated based on the decompression displacement, which depends on the decompression rate and the time elapsed since decompression started.

The decompression displacement represents the distance the parachute pack has moved since the decompression started. This value is calculated using the decompression rate and the time elapsed since the decompression began. The decompression displacement is given by:

$$decomp_{displ} = t_{decomp} \cdot decomp_{rate} \quad (3.90)$$

where:

t_{decomp} is the time elapsed since the decompression started and $decomp_{rate}$ is the rate at which decompression occurs, which is a constant value.

The decompression rate $decomp_{rate}$ is a predefined constant that represents the speed at which the parachute pack decompresses. This rate is determined based on experimental data or design specifications and reflects how quickly the parachute pack can decompress under the given conditions.

Updated Spring Force (F_{Comp}):

$$F_{Comp} = C_{pack} \cdot exp\,(decomp_{displ} \cdot k_{pack}) \quad (3.91)$$

Where $decomp_{displ}$ is the decompression displacement.

Updated Damping Force (F_{Damper}):

$$F_{Damper} = c_{pack} \cdot decomp_{rate} \quad (3.92)$$

This comprehensive approach ensures that the dynamics of the piston and the parachute pack are accurately modelled, taking into account the forces during different phases of the deployment process.

3.4 Post Processing

The post-processing of the simulation results is visualized through a series of plots generated by the `MDT_BasicFigures_PDD` module. These plots provide insights into the dynamic behaviour of the parachute deployment device by illustrating how various parameters evolve over time. The following sections describe each of these plots in detail.

3.4.1 Gas Densities

The first subplot displays the gas densities in both the gas generator and the plenum over time. The blue line represents the gas density in the gas generator, while the orange line shows the gas density in the plenum. Vertical dashed lines mark significant events during the simulation, such as the bursting of disks or the release of shear pins, providing context for changes in density.

3.4.2 Gas Pressures

The second subplot focuses on gas pressures within the system. It shows the pressure in the gas generator (blue line) and the pressure in the plenum (orange line). Dashed and dotted lines indicate the burst pressure of the gas generator and the shear pin burst pressure, respectively. This plot provides a clear view of how pressure builds up and is released during the simulation, with event markers helping to correlate pressure changes with specific events.

3.4.3 Gas Temperatures

The third subplot presents the temperatures in both the gas generator and the plenum. The blue line represents the gas temperature in the gas generator, and the red line shows the wall temperature of the gas generator. The green line indicates the gas temperature in the plenum, while the orange line shows the wall temperature of the plenum. Vertical event markers provide context for temperature changes, helping to understand the thermal dynamics within the system.

3.4.4 Pack Velocity

The fourth subplot illustrates the velocities of the piston and the parachute pack over time. The blue line represents the piston velocity, and the orange line shows the pack velocity. Horizontal dashed lines indicate measured velocities for reference. Event markers help to correlate velocity changes with specific events, providing insights into the dynamic response of the piston and pack.

3.4.5 Pack Displacement

The fifth subplot focuses on the displacements of the piston and parachute pack. The blue line represents the displacement of the piston, and the orange line shows the displacement of the pack. Vertical event markers provide context for displacement changes, illustrating how far the piston and pack travel during the simulation.

3.4.6 Reaction Force

The sixth subplot displays the reaction force on the PDD. It shows the reaction force over time, with vertical event markers indicating significant events.

3.5 Model Calibration

3.5.1 Closed Bomb Calibration

The gas generator calibration uses closed bomb tests to adjust and fine-tune the parameters of the gas generator model. The primary objective is to ensure that the predicted pressures, temperatures, and mass flow rates align closely with the measured values from these tests.

Closed Bomb Test Calibration

The closed bomb test is an experimental setup used to study the combustion characteristics of propellants in a controlled environment. For the gas generator calibration, two setups were utilized: the Setup A at ambient temperature and the setup B (QM PDD2) Setup at ambient temperature. These tests provide essential data for calibrating the burn law coefficients, convective heat transfer coefficients, and the discharge coefficient.

3.5.1.1 Method

1. **Data Collection**: The calibration process begins with collecting experimental data from closed bomb tests. These tests measure the pressure and temperature of the gas inside the gas generator and the closed tank as seen on Figure 25. The setup A and the setup B (QM PDD2), both conducted at ambient temperature, provide the necessary data for calibration. These two test setups have different propellant loading and tank volumes, the gas generator remain the same.

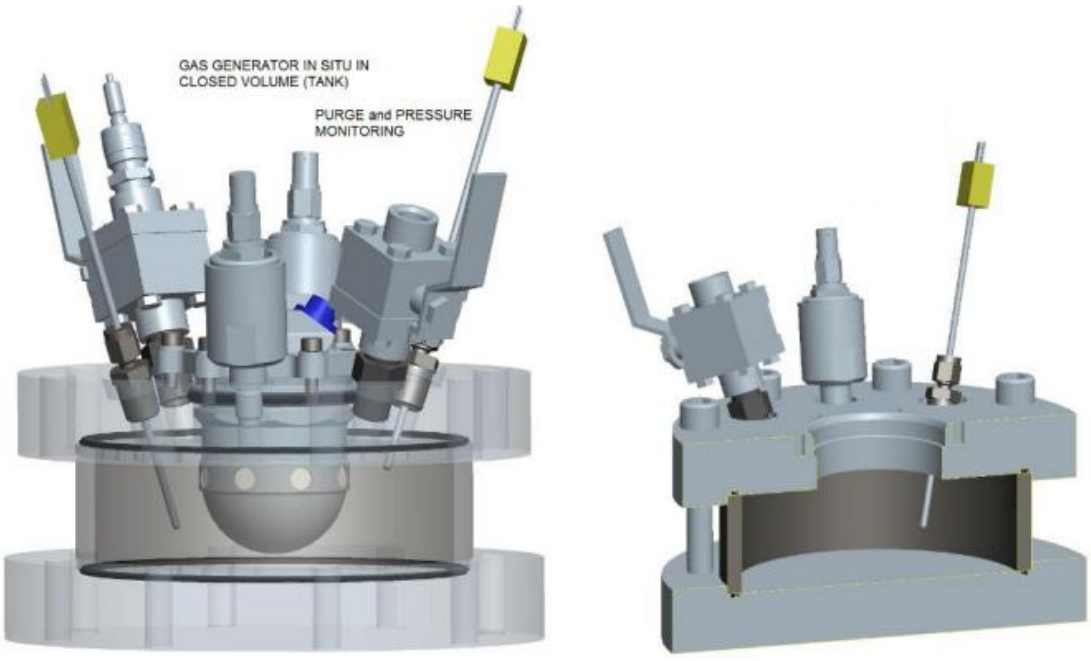

Figure 25: Closed Bomb Test Setup

2. **Initial Simulation**: An initial simulation is performed using estimated values for the gas generator parameters. This simulation serves as a baseline for comparison against the experimental data, highlighting any discrepancies between the predicted and observed values.

3. **Comparison and Adjustment**: The results of the initial simulation are compared with the experimental data. Differences between the simulated and measured values indicate the need for parameter adjustments. Parameters such as the burn law coefficients, convective heat transfer coefficients, and discharge coefficient are iteratively adjusted to minimize these differences.

4. **Convergence Check**: After each adjustment, the simulation is rerun, and the results are compared again with the experimental data. This iterative process continues until the differences between the simulated and measured values are within acceptable limits, indicating that the model has converted to a set of calibrated parameters.

3.5.1.2 Calibration Parameters

The parameters that are calibrated using the closed bomb test data include:

1. **Burn Law Coefficients:**

   - Burn Rate Coefficient (β_0): This parameter is adjusted to match the regression rate of the propellant as observed in the closed bomb tests.

   - Temperature Sensitivity Coefficient (σ): This coefficient is fine-tuned to account for the influence of temperature variations on the burn rate.

   - Burn Law Exponent (a): The exponent in the burn law equation is calibrated to ensure the burn rate aligns with experimental observations.

2. **Convective Heat Transfer Coefficients:**

   - Convective Heat Transfer Coefficient for Gas Generator (hc_{GG}): This coefficient is adjusted to match the heat transfer rates observed in the gas generator during the closed bomb tests.

   - Convective Heat Transfer Coefficient for Plenum (hc_{PL}): Similarly, this coefficient is fine-tuned to match the heat transfer rates in the plenum.

3. **Discharge Coefficient:**

   - Discharge Coefficient (C_d): This coefficient, which affects the mass flow rate through the orifices, is calibrated to ensure accurate prediction of the gas flow dynamics.

3.5.1.3 Results

3.5.1.3.1 Setup A

The graph below (Figure 26) depicts the pressure inside the Gas Generator over time for three different tests (GG-1, GG-2, GG-3) and the corresponding simulation (GG-Sim). Each of the test curves represents pressure readings from individual experimental runs, while the simulation curve (in red) is generated using the calibrated model parameters. The simulation results show a good match with the experimental data, with the pressure peak and the decay trends aligning closely with the experimental curves. This indicates that the calibrated parameters accurately capture the combustion dynamics and heat transfer characteristics of the GG. The alignment between the curves demonstrates the effectiveness of the calibration process in replicating real-world performance within the simulation model.

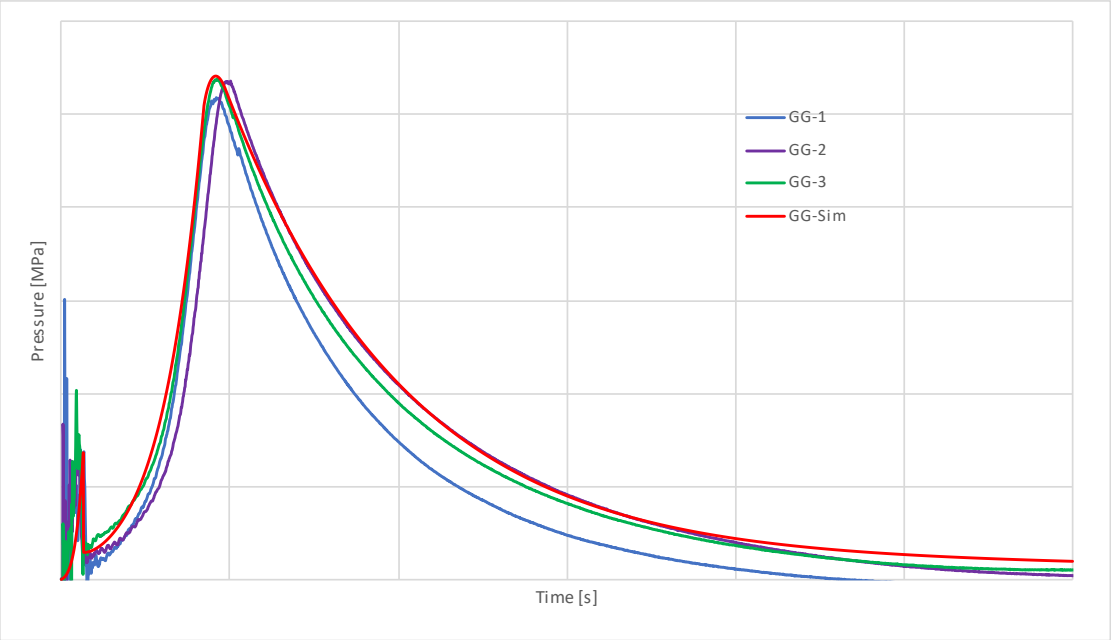

Figure 26: Setup A Closed Bomb Test - GG Pressure

The second graph on Figure 27 illustrates the pressure inside the closed bomb chamber for the same tests (PL-1, PL-2, PL-3) and the simulation (PL-Sim). Here, the pressure profiles within the closed bomb setup are shown, reflecting how the GG pressurizes a fixed volume over time. The experimental data from the three test runs are compared against the simulation results. The simulation curve (in red) closely follows the experimental data, particularly in capturing the initial rapid pressure rise and subsequent stabilization. This close alignment demonstrates the reliability of the calibration process, confirming that the model parameters not only predict the GG's internal pressure accurately but also its interaction with an external volume.

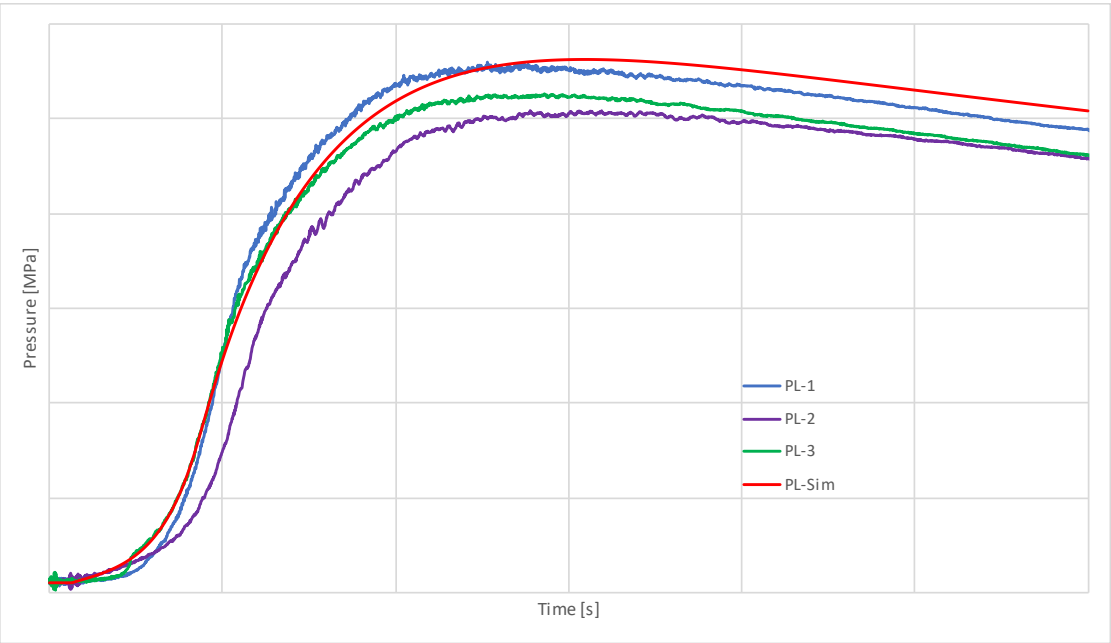

Figure 27: Setup A Closed Bomb Test - Tank Pressure

3.5.1.3.2 Setup B (PDD2)

The graph on Figure 28 shows the pressure inside the Gas Generator for three separate experimental runs (GG-1, GG-2, and GG-3), alongside the corresponding simulated results (GG-Sim). Each test used the setup B (QM PDD2), which was loaded with a pre-defined quantity of nitrocellulose propellant and conducted at ambient temperature.

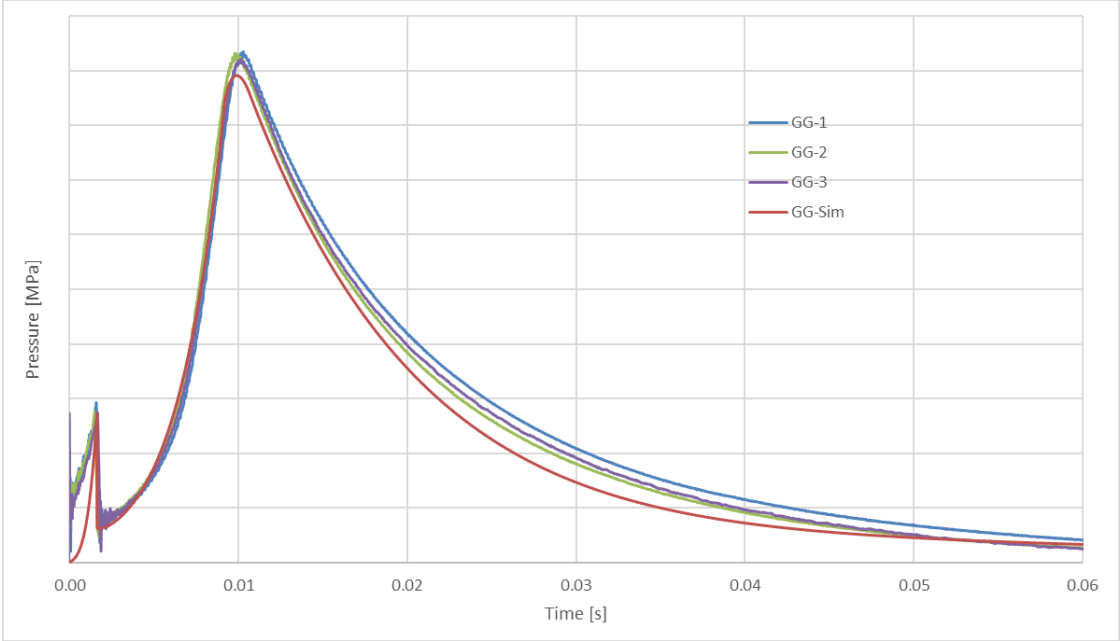

Figure 28: Setup B (QM PDD2) Closed Bomb Test - GG Pressure

In the experimental data, we observe a rapid rise in pressure during the initial milliseconds due to the combustion of the propellant within the closed combustion chamber. This leads to the first pressure peak, which corresponds to the gas generation rate before the burst disk ruptures. Once the burst disk reaches its designed threshold, the disk breaks, causing an expansion in the chamber volume. This expansion results in a pressure drop, followed by a second rise as the pressure builds up again in the larger post-combustion volume, reaching its maximum value. This two-stage pressure rise is a characteristic of the gas generator's behaviour in this setup.

The simulated data (GG-Sim) follows the experimental trends closely, successfully capturing the sharp pressure rise before the burst disk break and the subsequent increase in volume and pressure rise after the disk rupture. The small discrepancies between the simulated and experimental data could be due to factors such as slight variability in the experimental conditions, measurement uncertainties, or differences in the sensor placement and sensitivity. Nevertheless, the overall alignment between the GG-Sim curve and the test data suggests that the model has been well-calibrated for critical parameters, including the burn law coefficients (e.g., burn rate coefficient β_0, burn law exponent a), the discharge coefficient, and heat transfer coefficients. The calibration successfully replicates the rapid gas generation, the burst disk event, and the subsequent expansion dynamics of the gas generator, providing confidence in the model's ability to predict the pressure evolution accurately.

The second graph on Figure 29 shows the pressure inside the closed bomb chamber for the same three experimental runs (PL-1, PL-2, and PL-3) and the corresponding simulation results (PL-Sim). Here, the experimental data reveals a consistent pressure increase after the gas generated by the GG is transferred into the closed bomb chamber. The rise in pressure is rapid, and as the gas expands within the fixed tank volume, the pressure reaches a peak and then gradually starts to decrease.

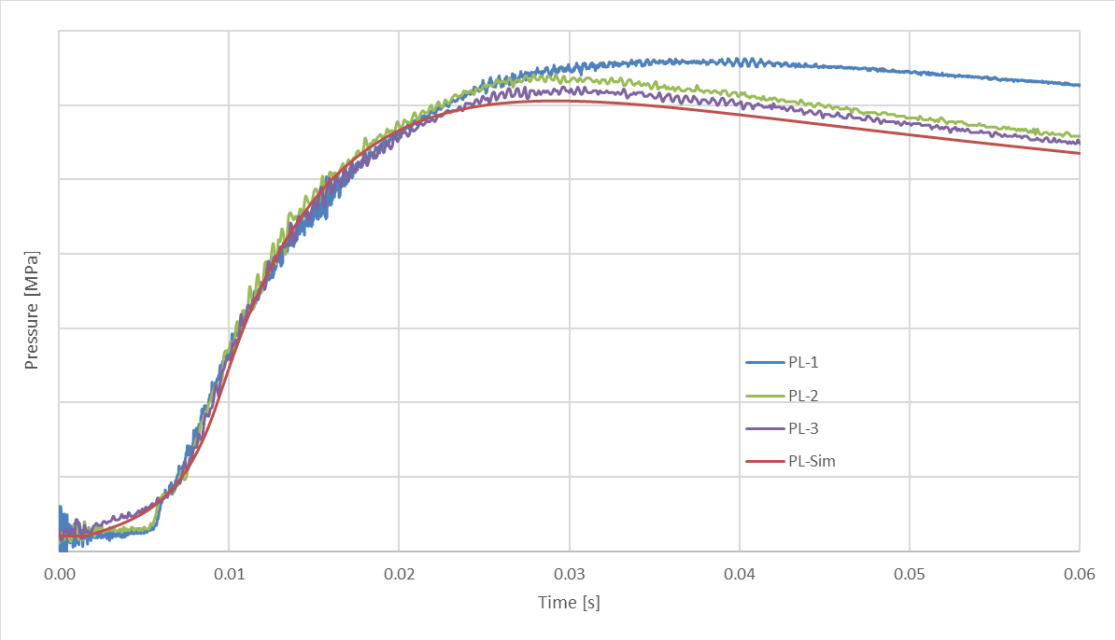

Figure 29:Setup B (QM PDD2) Closed Bomb Test - Tank Pressure at

In the PL-1 curve, we notice an unexpected behaviour where the pressure increases beyond what is observed in PL-2 and PL-3. This anomalous behaviour may result from experimental discrepancies or sensor errors during this particular test run. Despite this anomaly, the general pressure rise and decay trends for PL-2 and PL-3 remain consistent with each other, confirming the reproducibility of the test results under standard conditions.

The simulation results (PL-Sim) align closely with the experimental data, demonstrating that the model has been calibrated effectively for parameters such as the discharge coefficient (Cd) of the orifices between the gas generator and the closed bomb chamber. The close agreement between the simulated and experimental pressure curves confirms that the Cd value accurately reflects the gas transfer dynamics between the GG and the closed bomb chamber. The simulation also captures the plateau phase, validating the model's representation of the heat transfer dynamics (convection and radiation heat loss) between the hot gas and the chamber walls. These heat transfer effects are particularly important in capturing the gradual pressure decay post-peak, as the gas exchanges heat with the cooler walls of the tank.

3.5.2 Deployment Test Calibration

The deployment test was conducted to calibrate the gas generator pressure profile by comparing the experimental data against the simulation results. As seen in Figure 30, the simulation predicted a peak pressure with a percentage difference of only 1.26% compared to the experimental data. This close agreement indicates that the model accurately captures the rapid pressure rise and peak behavior of the gas generator. The close match between experimental and simulated peak pressures confirms that the calibrated parameters—such as the burn rate coefficient (β_0), burn law exponent (a), and discharge coefficient (C_d)—have been well adjusted to replicate the high-pressure combustion dynamics of the gas generator under deployment conditions.

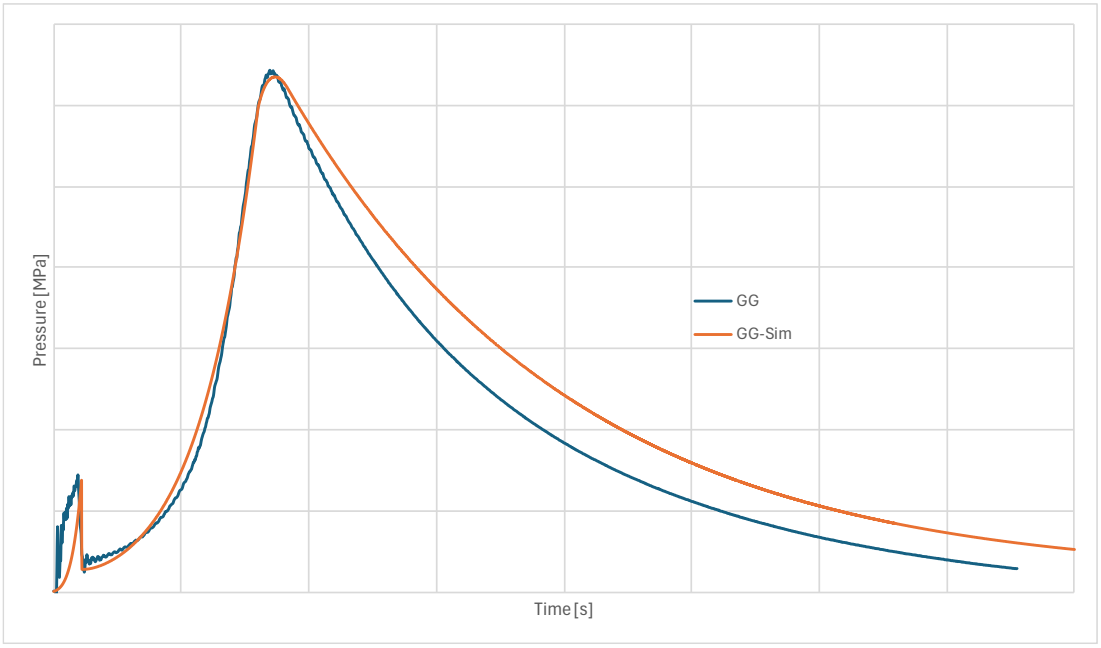

Figure 30: Setup A Deployment Test - Gas Generator Pressure at

However, despite the excellent agreement at the peak, the simulation slightly underestimates the pressure decay phase after the peak. The experimental data shows a faster pressure drop than the simulation, suggesting that the model might slightly underestimate the heat losses inside gas generator. This could be due to subtle discrepancies in the energy dissipation mechanisms or the specific gas dynamics modelled, such as heat transfer rates or the gas outflow rate through the orifices. Despite this small discrepancy, the overall percent error remains minimal, demonstrating that the model's gas generator pressure dynamics are highly accurate for calibration purposes.

In the plenum pressure analysis, experimental data from two test runs (Plenum 1 and Plenum 2) were compared against the simulation results (PL-Sim) to evaluate the model’s accuracy.

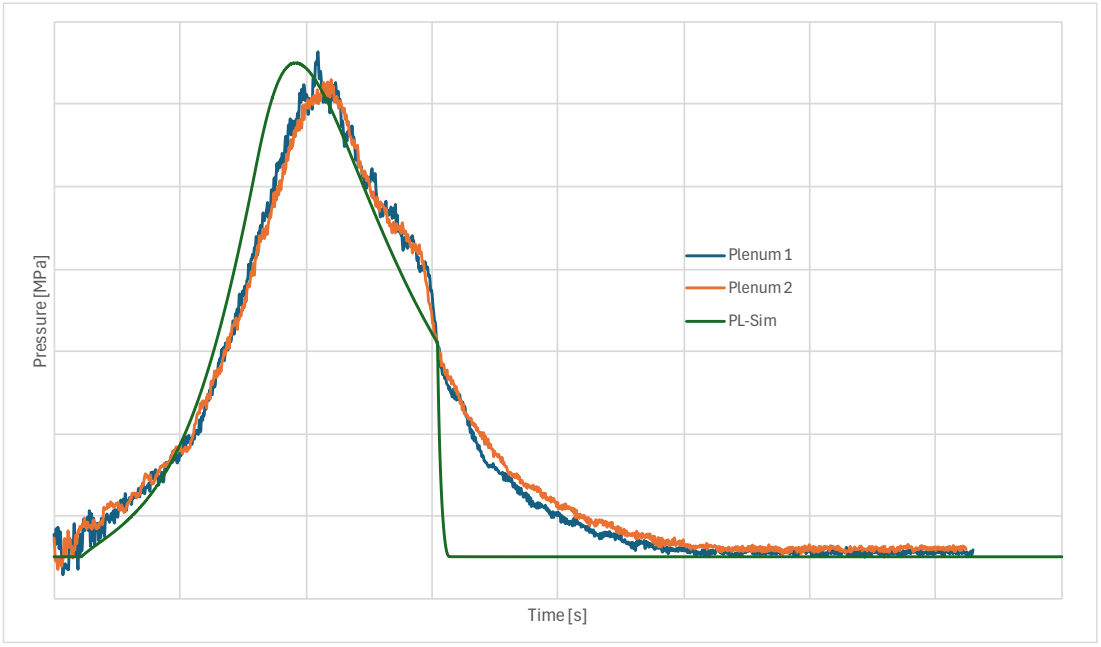

Figure 31: Setup A Deployment Test - Plenum Pressure at

The experimental tests recorded peak pressures with a percentage difference of 2.28% compared to the simulation results. This close alignment between experimental and simulated peaks validates the accuracy of the discharge coefficient (Cd) calibration, which controls the gas flow between the gas generator and the plenum. It also confirms the adequacy of the convective heat transfer coefficient (hc_PL) for representing the thermal exchanges inside the plenum.

3.5.3 Conclusion

The model calibration process, utilizing closed bomb tests and deployment tests, has demonstrated the effectiveness of the simulation in accurately capturing the dynamics of the gas generator and plenum across different experimental setups. Both Setup A and Setup B (QM PDD2) provided critical data for refining key parameters such as the burn rate coefficient (β_0), burn law exponent (a), discharge coefficient (Cd), and heat transfer coefficients (hc_GG and hc_PL). The close agreement between experimental data and simulation results across multiple test runs confirms that the model effectively replicates the pressure rise, peak behavior, and subsequent decay phases of the system.

While the model accurately captures gas generation, expansion dynamics, and the burst disk event, small discrepancies were observed during the pressure decay phase in both the gas generator and plenum simulations. These deviations likely arise from unmodeled energy dissipation mechanisms, gas dynamics complexities, or small environmental fluctuations during testing. Despite these differences, the overall low percent errors in peak pressures (e.g., 1.26% for the gas generator in Setup A test and 2.28% for the plenum) indicate that the model is robust and well-calibrated.

One of the key challenges in the calibration process was the limited number of experimental test results available for comparison, which constrained the ability to optimize all influencing parameters. Given the complexity of the system and the number of interdependent parameters requiring fine-tuning, a larger dataset would enhance the calibration robustness. Additionally, as observed in all test setups, even under identical conditions, notable variations in output pressures, loads, and temperatures were present—well beyond sensor accuracy limits. This lack of perfect repeatability highlights the inherent difficulty of precisely modelling the PDD system, as external factors such as material property variations, gas turbulence, and combustion inconsistencies likely contribute to these differences.

Despite these challenges, the calibration process successfully validated the key governing parameters of the model, ensuring its capability to predict gas generator combustion, pressure evolution, and energy transfer dynamics under different conditions. Future work should focus on expanding the experimental dataset, refining sub-models related to heat transfer and turbulence effects, and incorporating uncertainty quantification techniques to further improve the model’s accuracy and reliability.

Chapter 4

Verification & Validation

This chapter focuses on ensuring the accuracy and reliability of the Parachute Deployment Device simulation model. It aims to confirm that the model performs as intended and accurately represents real-world behaviour. The verification process checks the correctness of the model's implementation, while the validation process assesses its accuracy in replicating real-world phenomena.

The verification phase begins with Independent In-Depth Models Verification. This involves a detailed examination of specific components, such as the initiators ignition model, nitrocellulose grain surface and burning rate, nozzle mass flow, pack compression forces, heat flows, and burst disk failure. Each component is scrutinized to ensure it functions correctly and produces results consistent with empirical data and theoretical expectations.

Following the component-level verification, the focus shifts to Module Integration & Documentation Verification. This ensures that the integrated system functions correctly as a whole. It includes thorough testing of the integrated dynamics, simulation core, and events modules to verify their seamless interaction and accurate simulation of the PDD system’s behaviour. Additionally, the documentation is reviewed to ensure it is accurate, complete, and provides clear guidance on the model’s use, underlying assumptions, and limitations.

The validation process is divided into two main sections: Closed Bomb Test Validation and Ejection & Deployment Test Validation. The Closed Bomb Test Validation includes the validation of the ignition model, burning rate model, heat transfer model, and burst disk model. This involves comparing the simulation results against experimental data obtained from closed bomb tests to ensure the accuracy of these models. The Ejection & Deployment Test Validation focuses on the gas flow model, friction model, parachute compression model, parachute pack acceleration, ejection velocity validation, and reaction force. These validations ensure that the model accurately predicts the behaviour of the PDD during the ejection phase.

4.1 Verification

This section focuses on ensuring that each component of the Parachute Deployment Device (PDD) simulation model is correctly implemented and performs as expected. Verification is carried out in two main steps: independent verification of individual models and verification of the integrated modules and documentation.

4.1.1 Independent In-Depth Models

4.1.1.1 Initiators Model

This section details the verification process of the simplified initiators model to ensure it performs as expected and aligns with specified behaviour. The objective is to confirm that the simulation accurately replicates the ignition behaviour of the initiators under various simulated conditions.

The initiators model is parameterized based on specifications related to burning time, energy output, pressure output in a defined chamber volume, and propellant mass. These parameters were reviewed to ensure they reflect realistic values obtained from the initiators' specifications.

To verify the model, multiple simulations were conducted with varying input parameters to observe and analyse the model's response. The input variations considered were changes in the combustion chamber volume, number of initiators, and burning time. The following scenarios were simulated:

Initial Scenario: Combustion chamber volume of 18.8 cm^3 with 2 initiators.

Small Volume: Combustion chamber volume of 12 cm^3 with 2 initiators.

Large Volume: Combustion chamber volume of 25 cm^3 with 2 initiators.

Fewer Initiators: Combustion chamber volume of 18.8 cm^3 with 1 initiator.

More Initiators: Combustion chamber volume of 18.8 cm^3 with 3 initiators.

Short Burn Time: Combustion chamber volume of 18.8 cm^3 with 2 initiators and a burning time of 2 ms.

Long Burn Time: Combustion chamber volume of 18.8 cm^3 with 2 initiators and a burning time of 4 ms.

Extreme conditions were also tested to evaluate the model's robustness:

Extreme Maximum: Combustion chamber volume of 12 cm^3 with 3 initiators and a burning time of 2 ms.

Extreme Minimum: Combustion chamber volume of 25 cm^3 with 1 initiator and a burning time of 4 ms.

The outputs of these simulations were analysed through graphical representations. Pressure and enthalpy outputs were plotted over time for each scenario to visualize the model's response under different conditions.

Here are the results from the graphical analysis:

Pressure Outputs for Different Combustion Chamber Volumes:

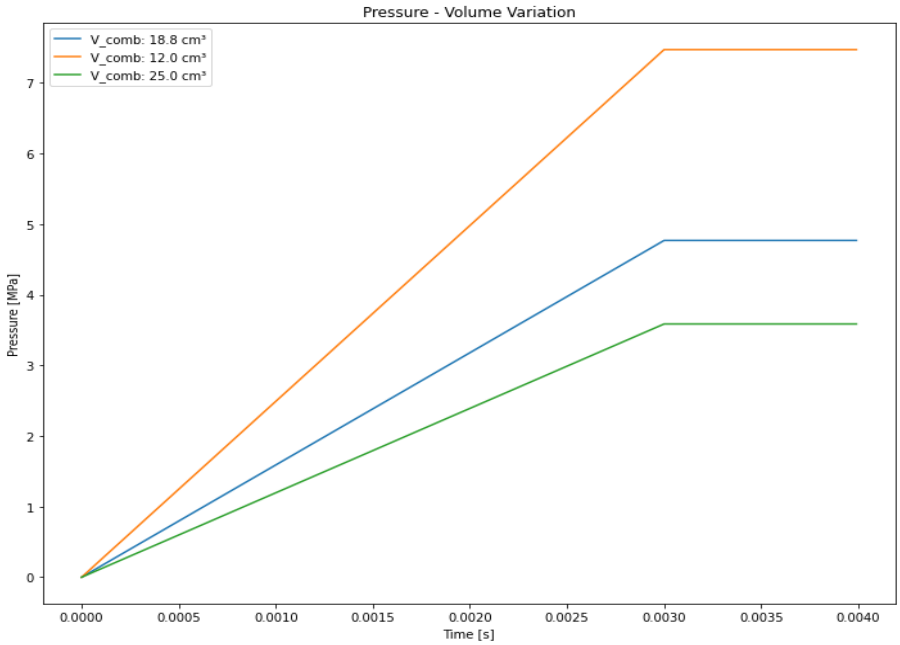

Figure 32: Pressure Outputs Vs. Volume

The pressure profiles scaled logically with changes in combustion chamber volume. Smaller volumes resulted in higher pressure outputs, while larger volumes resulted in lower pressure outputs.

Energy Outputs for Different Combustion Chamber Volumes:

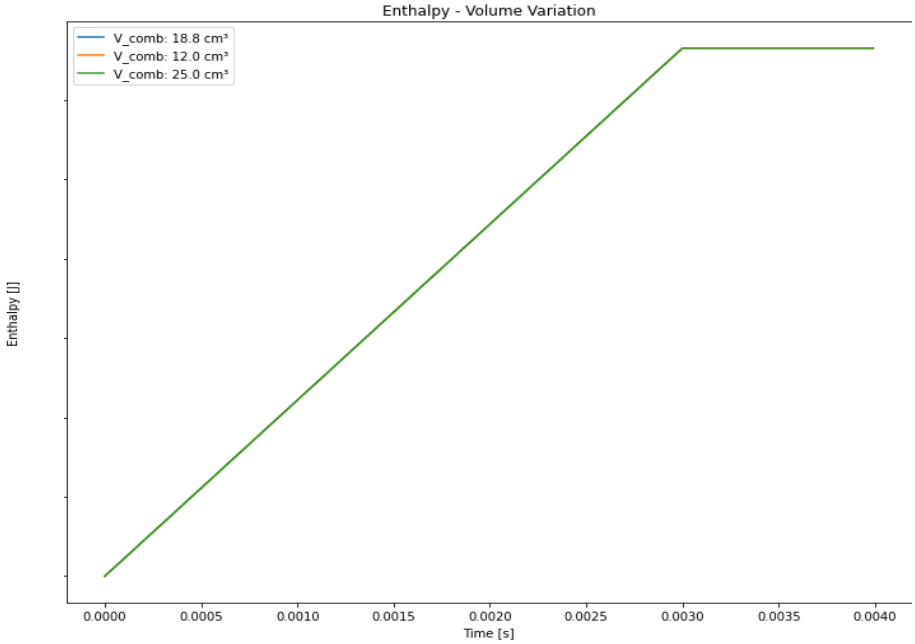

Figure 33: Energy Outputs Vs. Volume

The enthalpy outputs remained consistent across different combustion chamber volumes, reflecting the same total energy output, as the energy released in the system is independent of the volume of the chamber.

Pressure Outputs for Different Numbers of Initiators:

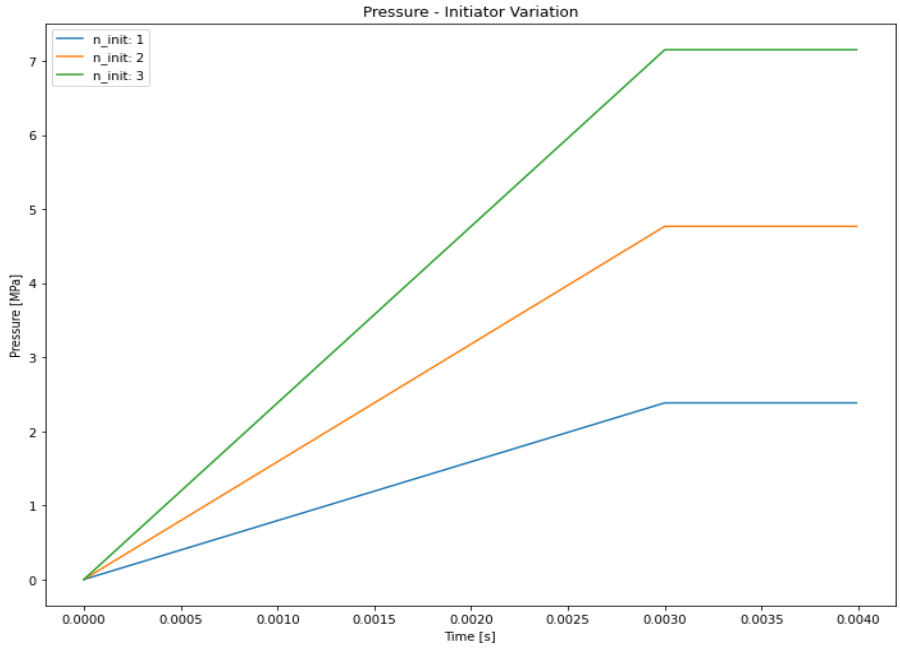

Figure 34: Pressure Outputs Vs. Number of Initiators

The pressure outputs increased with the number of initiators, demonstrating the model's consistency and logical response to parameter changes. More initiators means more propellant burning, so higher quantity of gas generated inside the combustion chamber.

Energy Outputs for Different Numbers of Initiators:

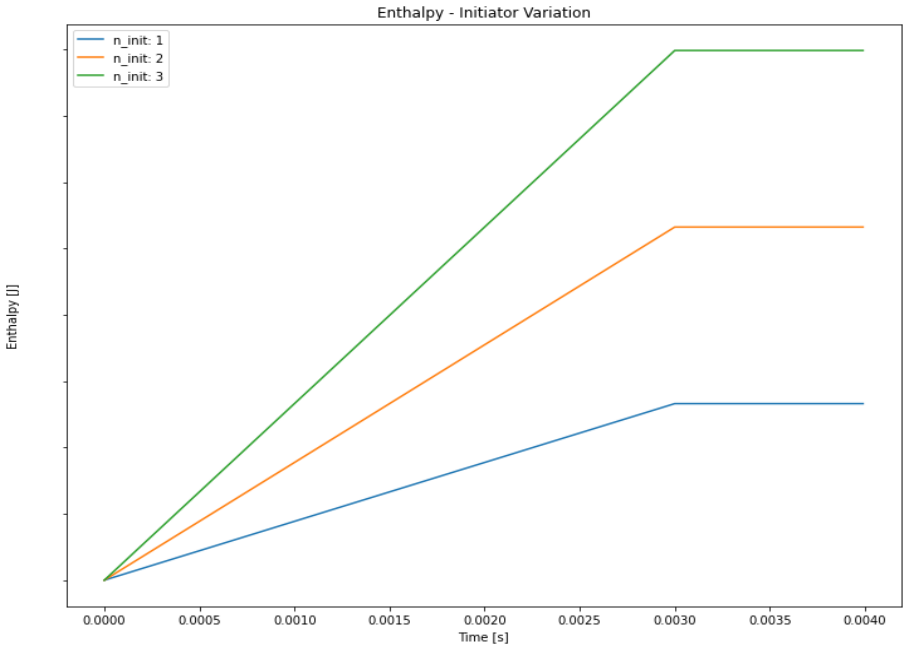

Figure 35: Energy Outputs Vs. Number of Initiators

Similar to the pressure outputs, the enthalpy outputs increased with the number of initiators, as more propellant is present in the system, resulting in higher energy released.

Pressure Outputs for Different Burning Times:

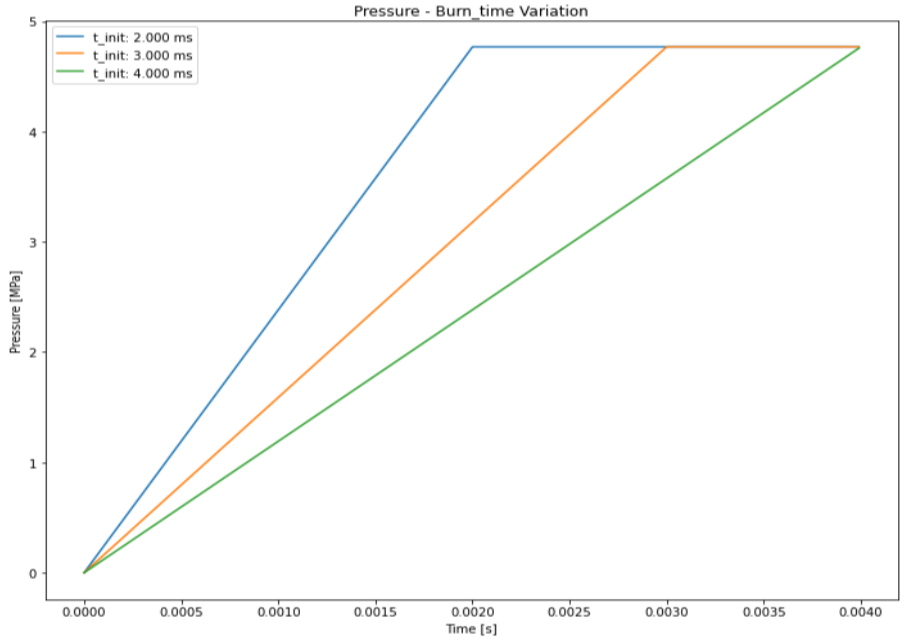

Figure 36: Pressure Outputs Vs. Burning Time Change

Shorter burning times resulted in higher instantaneous pressure outputs, while longer burning times spread the pressure increase over a longer duration. However, this does not impact the total final pressure as expected.

Energy Outputs for Different Burning Times:

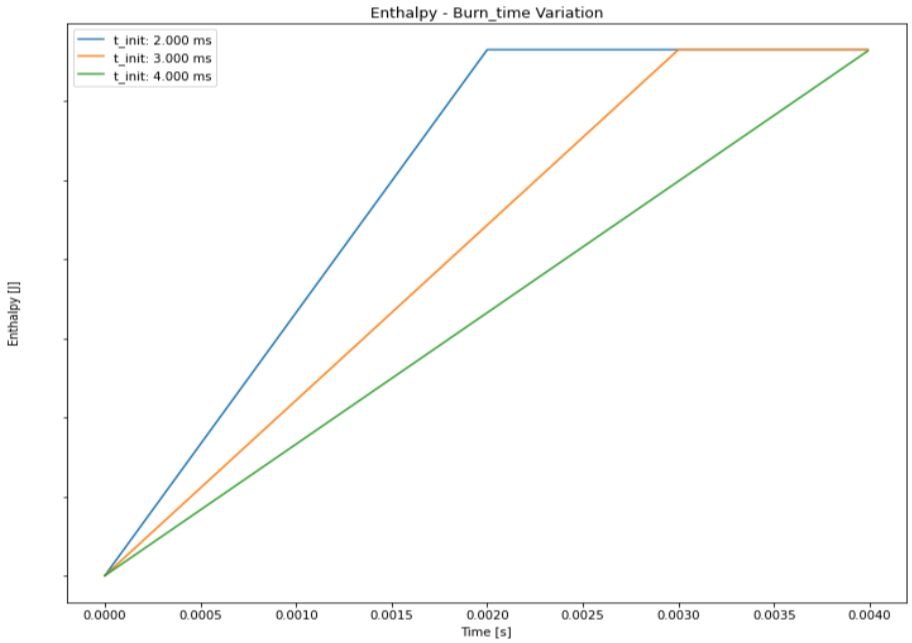

Figure 37: Energy Outputs Vs. Burning Time Change

Shorter burning times led to a quicker rise in enthalpy, while longer burning times spread the energy release over a longer period. Similarly, as the pressure outputs, the total energy remains the same in all cases.

Pressure Outputs for Extreme Conditions:

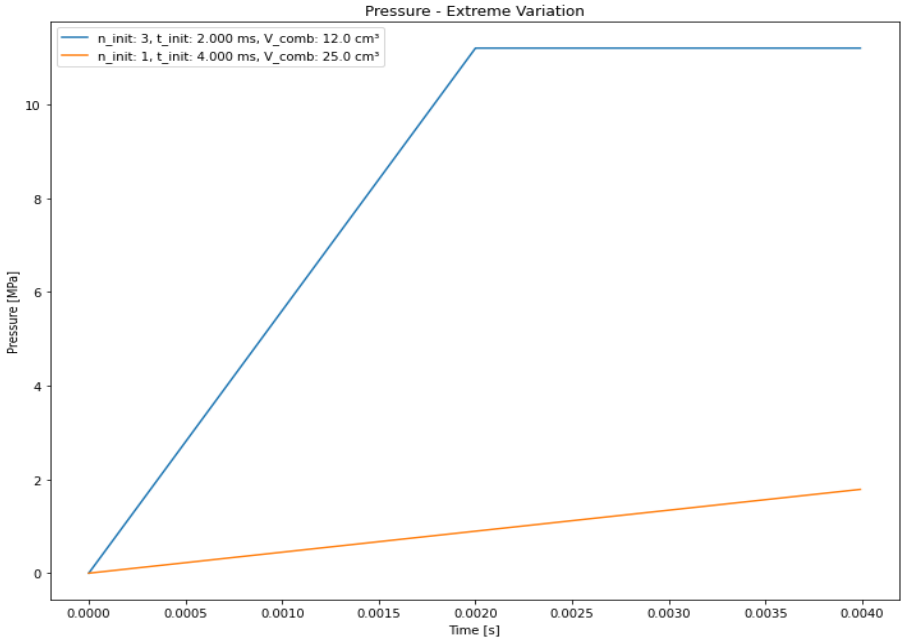

Figure 38: Pressure Outputs Vs. Extreme Conditions

The extreme maximum scenario resulted in significantly higher pressure outputs, while the extreme minimum scenario showed the lowest pressure outputs. This demonstrates that the model is robust for a very wide range of inputs and can handle both high-stress and low-stress conditions effectively.

Energy Outputs for Extreme Conditions:

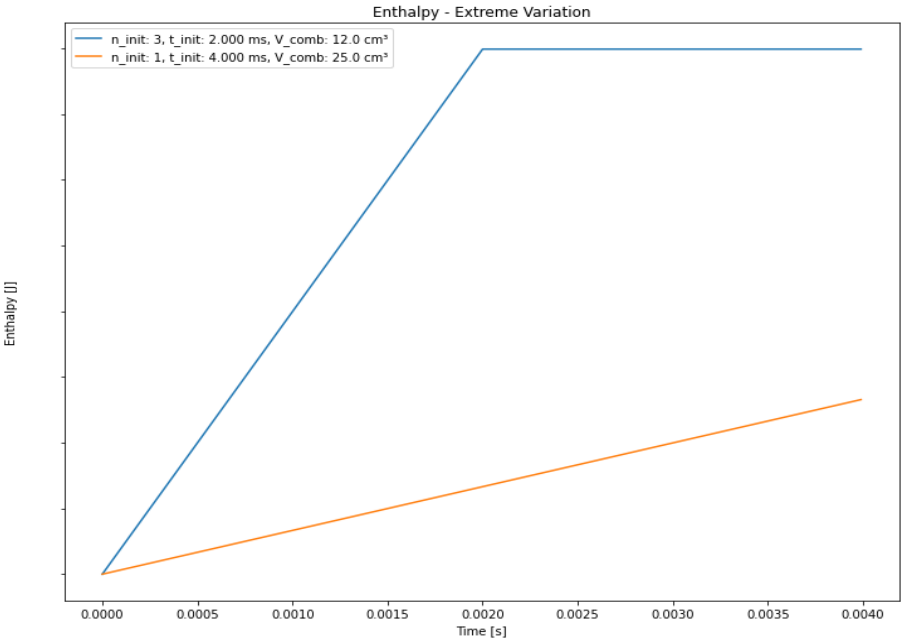

Figure 39: Energy Outputs Vs. Extreme Conditions

Similarly to the pressure outputs, the extreme maximum scenario resulted in the highest enthalpy outputs, while the extreme minimum scenario showed the lowest enthalpy outputs. This consistency across a wide range of scenarios ensures the reliability and accuracy of the initiators model.

The consistency of the model's outputs was verified by comparing the graphs across different scenarios. Sensitivity analysis was also conducted to understand how variations in key parameters affect the model's outputs. The analysis confirmed that the model is robust and performs reliably under different conditions. For example, adjusting the combustion chamber volume and the number of initiators showed logical and consistent changes in pressure and enthalpy outputs.

The verification of the initiators model indicates that the model accurately simulates pressure profiles and energy outputs under varying conditions. The responses are consistent and logical across different simulations, demonstrating robustness and reliability. The specifications of the initiators, including burning time, energy output, and pressure output, are accurately represented in the model.

In conclusion, the initiators model has been thoroughly verified through parameter review, simulation testing, consistency checks, and sensitivity analysis. The model accurately represents the ignition process and performs reliably under various simulated conditions. This verification process ensures that the initiators model is a robust component of the PDD simulation, providing confidence in its use for further analysis and simulation of the PDD system.

4.1.1.2 Grain Surface Regression & Burning Rate Models

This section details the verification process of the grain surface regression and burning rate models. The objective is to confirm that the simulation accurately represents the behaviour of the propellant under various conditions of pressure and temperature.

4.1.1.2.1 Verification of the Bruning Rate Model

This section details the verification process of the grain surface regression and burning rate models. The objective is to confirm that the simulation accurately represents the behaviour of the propellant under various conditions of pressure and temperature.

The burning rate model is parameterized based on the following specifications: burn law coefficient (β_0), temperature sensitivity (σ), rate constant reference temperature (T_0) of 294.15 K, auto-ignition temperature (T_{ig}) of 463.15 K, activation energy (Ea) of 197 J/mol, specific gas constant (R) of 8.314 J/(mol·K), and burn law exponent (a).

The burning rate equation reflects that below T_{ig}, the rate is influenced by temperature through an exponential term, while above T_{ig}, the rate depends only on pressure.

$$r = \begin{cases} \beta \left(\frac{P}{P_{ref}}\right)^{a} exp\left(\frac{-Ea}{R}\left(\frac{1}{T_{ig}} - \frac{1}{T}\right)\right) if\ T < T_{ig} & (4.1) \\ \beta \left(\frac{P}{P_{ref}}\right)^{a} \qquad if\ T \geq T_{ig} & (4.2) \end{cases}$$

Where:

- $\beta = \beta_0\left(1 + \sigma(T_{ENV} - T_0)\right)$
- P is the pressure.
- T is the temperature.
- P_{ref} is the reference pressure.
- Ea is the activation energy.
- R is the specific gas constant.
- a is the burn law exponent.

To verify the model, multiple simulations were conducted with varying input parameters to observe and analyse the model's response. The inputs considered were changes in pressure and temperature. The following scenarios were simulated with a pressure range from 1 MPa to 100 MPa and a temperature range from -150°C to 1000°C. The burning rate model's verification process involves examining its behaviour under different pressures and temperatures to ensure consistency with theoretical expectations and known physical behaviours.

Detailed Analysis of the Burning Rate Behaviour

1. Temperature Dependency Below T_{ig}:

For temperatures below the auto-ignition temperature ($T_{ig} = 463.15$ K) the burning rate shows a strong dependence on temperature. As the temperature increases, the burning rate increases due to the exponential term in the equation:

$$r = \beta \left(\frac{P}{P_{ref}}\right)^{a} exp\left(\frac{-Ea}{R}\left(\frac{1}{T_{ig}} - \frac{1}{T}\right)\right) \quad (4.3)$$

This exponential term accounts for the activation energy required for combustion. As temperature increases, the term $\frac{1}{T}$ decreases, making the exponent less negative, hence increasing the burning rate.

2. Temperature Dependency Above T_{ig}:

For temperatures above T_{ig}, the burning rate is primarily influenced by pressure, as the exponential temperature dependence is no longer active:

$$\mathrm{r} = \beta \left(\frac{P}{P_{ref}}\right)^{a} \quad (4.4)$$

This indicates that once the propellant has reached its auto-ignition temperature, the burning rate stabilizes with respect to temperature and becomes more sensitive to changes in pressure.

3. Pressure Dependency:

Across all temperatures, the burning rate increases significantly with pressure. This is consistent with the burn law where the burning rate is proportional to P^{a}. Higher pressures enhance the combustion process by increasing the rate at which the propellant burns, leading to higher burning rates.

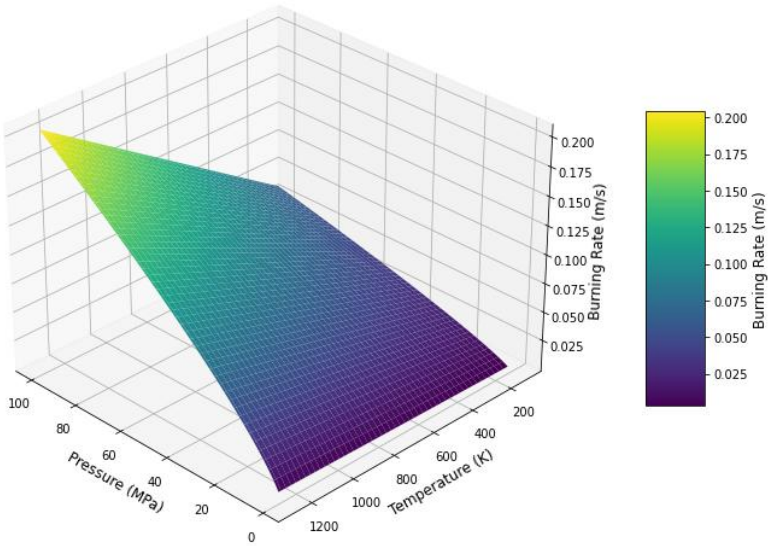

Figure 40: Burning Rate Dependency

The 3D plot provides several key observations regarding the burning rate behaviour under different conditions. At low temperatures and low pressures, the burning rate is minimal, representing conditions where the propellant burns slowly due to insufficient thermal and pressure energy to sustain high combustion rates. As the temperature increases, even at low pressures, the burning rate rises significantly until it reaches the auto-ignition temperature (T_{ig}), indicating the strong influence of temperature on the burning process in this region. Conversely, at high pressures, even low temperatures result in relatively higher burning rates, highlighting the impact of pressure on the combustion process. The highest burning rates are observed in regions of high temperature and high pressure, demonstrating the combined effect of these factors in enhancing the combustion process.

Conclusion

The burning rate model verification confirms that it accurately represents the physical behaviour of the propellant, showing strong sensitivity to both pressure and temperature, with a clear transition in temperature dependency around the auto-ignition temperature T_{ig}. The 3D plot provides a comprehensive visualization of these effects, validating the model's consistency with theoretical expectations.

This thorough verification process ensures that the burning rate model is a reliable component of the PDD simulation, providing confidence in its use for further analysis and simulation of the PDD system.

4.1.1.2.2 Verification of the Grain Surface Regression Model

The grain surface regression model was verified by calculating and analysing the surface area of the grain at various regression distances. The objective of this verification was to ensure that the model accurately reflects the changing surface area of the propellant grain as it burns.

Grain Surface Regression Model

The grain surface regression model calculates the surface area (S) of the propellant grain based on its geometrical dimensions and the regression distance (r). The dimensions used in the model include the length of the grain (L), the outer diameter (D), the perforation diameter (d), the number of perforations (N), the web thickness (w), and the number of grains (n).

Verification Process

To verify the model, multiple simulations were conducted with varying regression distances ranging from 0 to the web thickness (0.5 mm). The surface area was calculated at each regression distance using the MDT_NTC_Surface function. The results were plotted to visualize the changes in surface area as the grain burns.

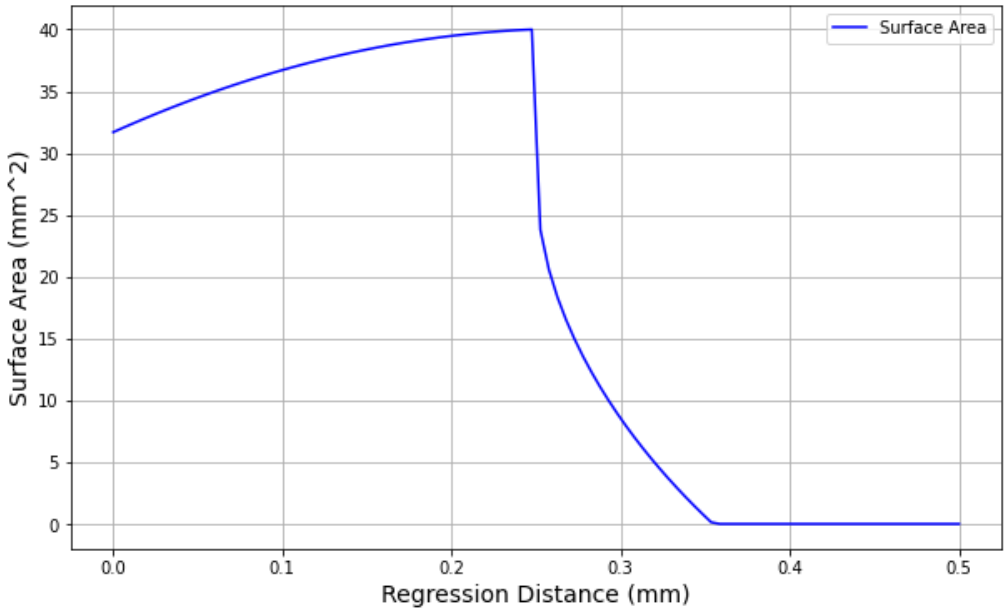

s

Figure 41: Burning Grain Surface Area Vs. Regression Rate

Observations

The plot of grain surface area versus regression distance shows several important trends. At the beginning (regression distance = 0 mm), the grain has its initial surface area available for burning. As the regression distance increases, the surface area initially increases, reflecting the exposure of more burning surfaces due to the regression of the grain material. This initial phase corresponds to the first stage of the grain burn, which continues until the regression distance reaches half the web thickness (0.25 mm). This is prior to web burn-through.

As the regression distance increases beyond this point, the surface area decreases significantly. This phase represents the slivers burning, where the burning surface area is significantly reduced as the grain is consumed. This rapid reduction continues until the majority of the grain material has been burned.

Finally, as the regression distance approaches the web thickness (0.5 mm), the surface area decreases less rapidly. This third phase corresponds to the burning of small residues of the initial grain. The remaining surface area at this stage is minimal, indicating that most of the grain has been consumed.

Conclusion

The verification process confirms that the grain surface regression model accurately calculates the changing surface area of the propellant grain as it regresses. The plot provides a clear visual representation of the changing surface area with increasing regression distance, consistent with theoretical expectations.

Initially, the surface area increases as more of the grain's burning surface is exposed. This continues until a maximum is reached at half the web thickness, after which the surface area decreases rapidly during the slivers burning phase. Finally, as the grain is nearly fully consumed, the surface area decreases less rapidly, corresponding to the burning of small residues.

This thorough verification ensures that the grain surface regression model is a reliable component of the PDD simulation, providing confidence in its use for further analysis and simulation of the PDD system. The model's ability to accurately represent the changing surface area of the propellant grain is crucial for predicting the burning behaviour and overall performance of the propellant.

Vivacity for Nitrocellulose

In addition to verifying the grain surface regression and burning rate models, we analyse the vivacity behaviour of the propellant to further confirm the simulation's consistency with known characteristics of nitrocellulose combustion. Vivacity, defined as $L = \frac{dP/dt}{P \cdot P_{max}}$, provides an indicator of the energy release rate relative to the peak pressure P_{max}. Proper vivacity modelling reflects the pressure buildup dynamics and energy output characteristics of nitrocellulose.

From the calibrated model parameters, we generate the vivacity curve. This model-based vivacity curve was compared against empirical vivacity data provided by the manufacturer. The results demonstrate a rise in vivacity with increasing pressure ratios (P/P_{max}), showing rapid energy release during the early combustion phase, peaking near 0.6–0.8 P/P_{max}, and then sharply tapering off as combustion concludes.

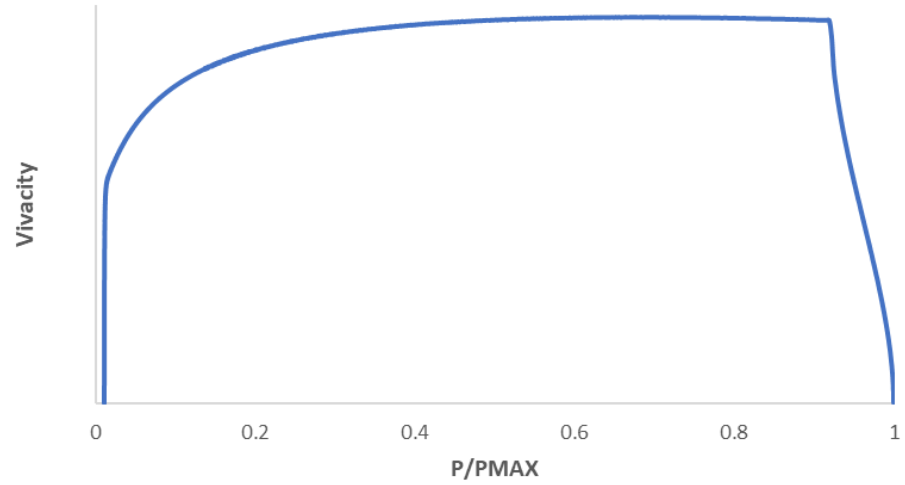

Figure 42: Vivacity from Model

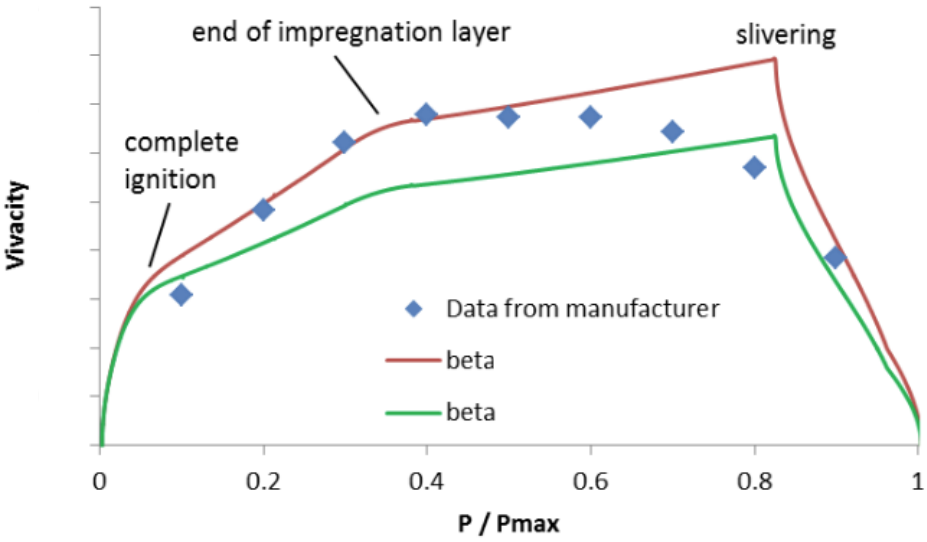

Figure 43: Vivacity from Manufacturer

The comparison reveals strong alignment between the modelled and empirical vivacity, validating the model's ability to represent the energy release dynamics of nitrocellulose accurately.

4.1.1.3 Nozzle Mass Flow

The verification of the nozzle mass flow model is conducted through a series of simulations that vary key parameters to ensure the model behaves as expected under different conditions. These simulations help in understanding the behaviour of the model and in validating its consistency with theoretical expectations.

The mass flow rate through a nozzle can be calculated using the following equations:

Unchoked Flow Condition: $M = Cd \cdot n \cdot A_o \cdot \sqrt{2 \cdot \rho \cdot P_1 \cdot \frac{\gamma+1}{\gamma-1}\left(\left(\frac{P_2}{P_1}\right)^{\frac{2}{\gamma}} - \left(\frac{P_2}{P_1}\right)^{\frac{\gamma+1}{\gamma}}\right)}$ *(4.5)*

Choked Flow Condition: $M = Cd \cdot n \cdot A_o \cdot \sqrt{\rho \cdot P_1 \cdot Kerck^2}$ *(4.6)*

Where: $\rho = \frac{P_1}{RT - P_1 \cdot b}$ and $Kerck = \sqrt{\gamma \left(\frac{2}{\gamma+1}\right)^{\frac{\gamma+1}{\gamma-1}}}$ *(4.7)*

where:

- M is the mass flow rate (kg/s)
- Cd is the discharge coefficient
- n is the number of nozzles
- A_o is the nozzle area (m²)
- ρ is the upstream density (kg/m³)
- P_1 is the upstream pressure (Pa)
- P_2 is the downstream pressure (Pa)
- γ is the specific heat ratio
- R is the specific gas constant (J/(kg·K))
- T is the temperature (K)
- b is the co-volume reaction products (m³/kg)

Nozzle Mass Flow Rate vs. P1/P2 Ratio

The mass flow rate as a function of the P1/P2 ratio is shown in the graph below. The red dashed line represents the choking ratio. The graph indicates that as the P1/P2 ratio increases, the mass flow rate initially increases sharply and then stabilizes when the flow becomes choked. This behaviour is consistent with theoretical expectations, where the mass flow rate remains constant once the flow is choked.

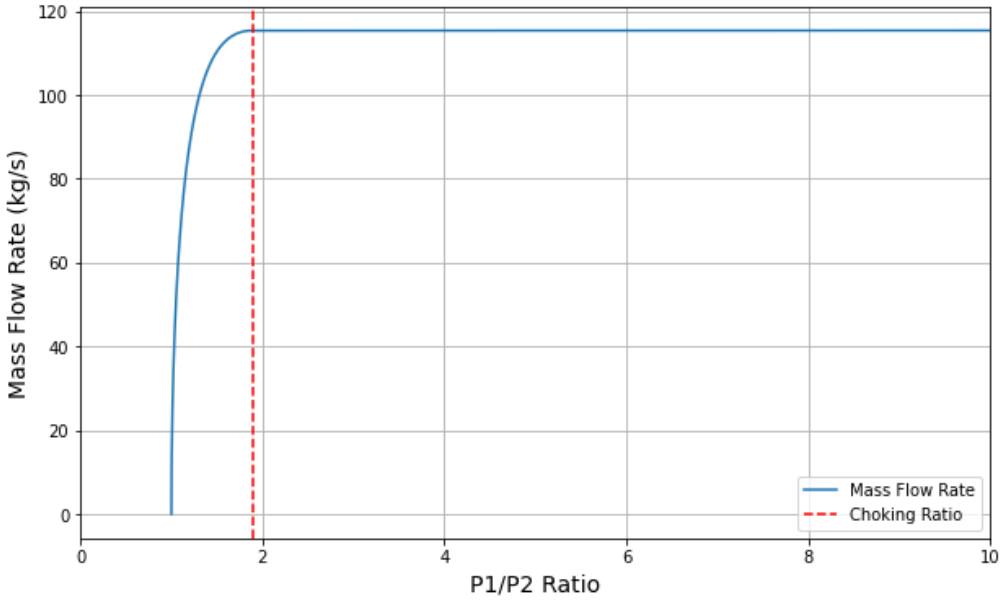

Figure 44: Nozzle Mass Flow Rate Vs. P1/P2 Ratio

Nozzle Mass Flow Rate vs. Discharge Coefficient

The graph below shows the relationship between the mass flow rate and the discharge coefficient. As expected, the mass flow rate increases linearly with the discharge coefficient. This is because the discharge coefficient directly affects the flow efficiency, with a higher coefficient indicating a more efficient flow and thus a higher mass flow rate.

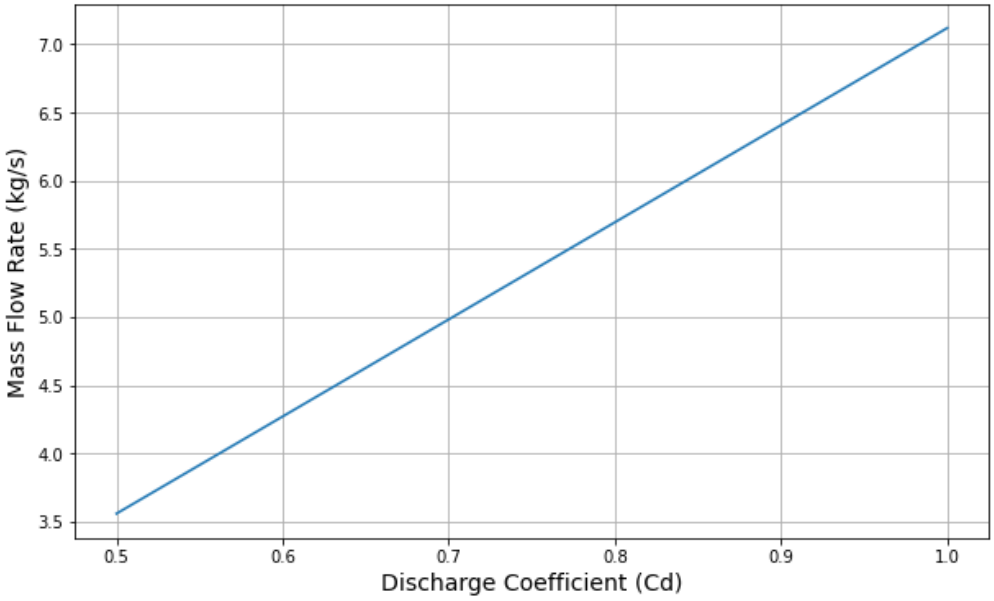

Figure 45: Nozzle Mass Flow Rate Vs. Discharge Coefficient

Nozzle Mass Flow Rate vs. Temperature

The effect of temperature on the mass flow rate is illustrated in the graph below. As the temperature increases, the mass flow rate decreases. This inverse relationship is expected as higher temperatures reduce the gas density, resulting in a lower mass flow rate.

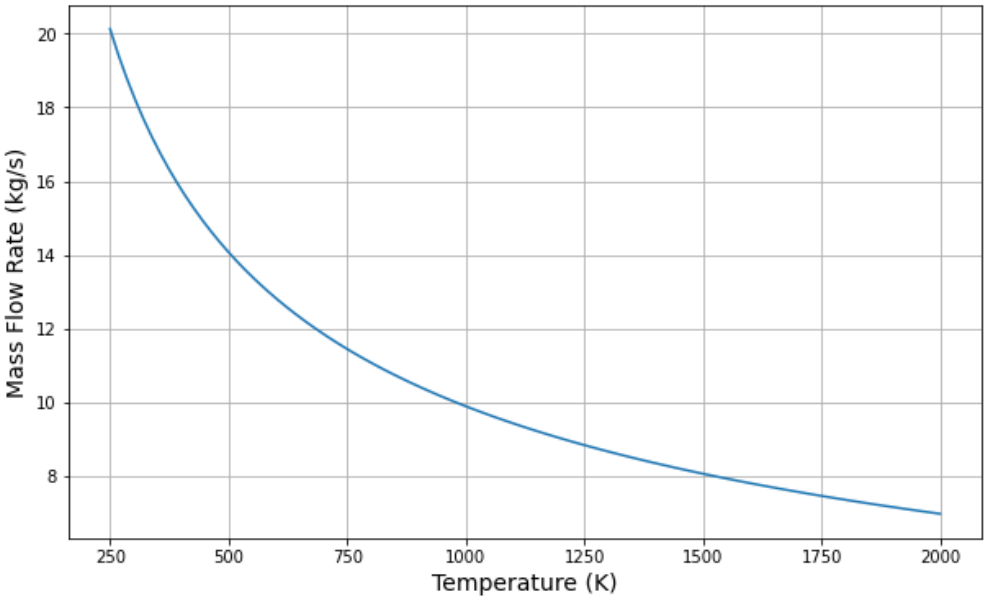

Figure 46: Nozzle Mass Flow Rate Vs. Temperature

Nozzle Mass Flow Rate vs. Number of Orifices

The graph below depicts the mass flow rate as a function of the number of orifices. The mass flow rate increases linearly with the number of orifices. This is logical as more orifices provide a greater total flow area, allowing more mass to flow through the nozzle.

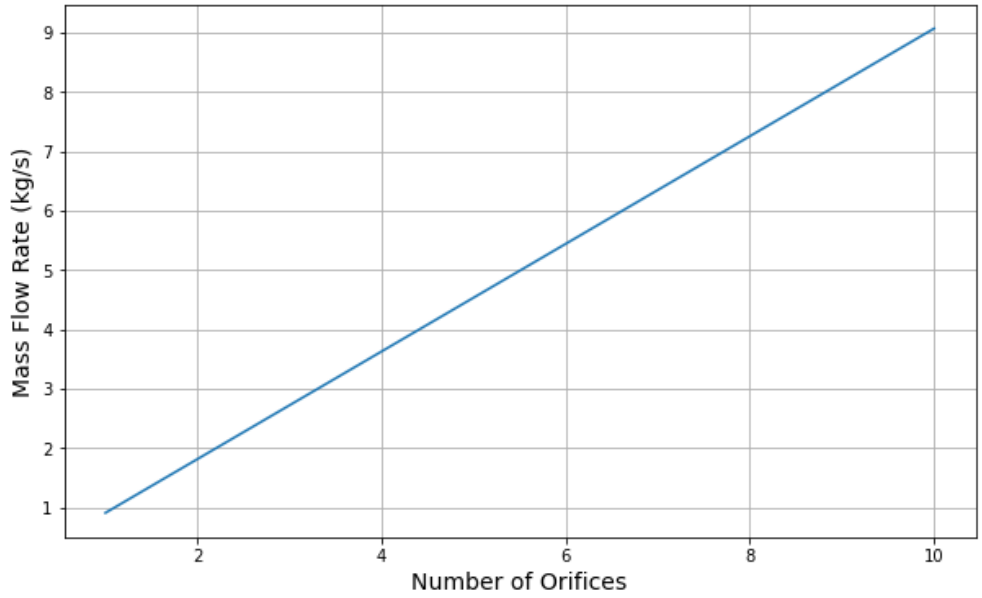

Figure 47: Nozzle Mass Flow Rate Vs. Number of Orifices

Nozzle Mass Flow Rate vs. Orifice Diameter

The final graph shows the relationship between the mass flow rate and the orifice diameter. As the orifice diameter increases, the mass flow rate also increases. This is because a larger orifice diameter provides a greater flow area, facilitating a higher mass flow rate.

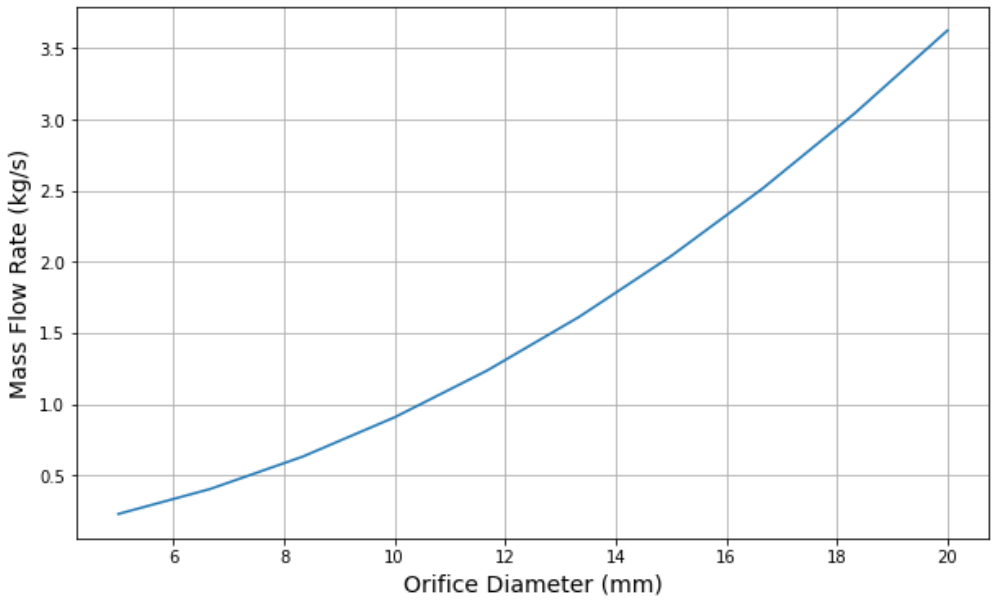

Figure 48: Nozzle Mass Flow Rate Vs. Orifice Diameter

To conclude, the series of simulations conducted for the nozzle mass flow model verification demonstrate that the model behaves consistently with theoretical expectations. The mass flow rate varies logically with changes in key parameters such as P1/P2 ratio, discharge coefficient, temperature, number of orifices, and orifice diameter. This verification process ensures the reliability and accuracy of the nozzle mass flow model, confirming its suitability for use in further analysis and simulation of the Parachute Deployment Device system.

4.1.1.4 Parachute Pack Compression

The parachute pack compression module is designed to model the forces involved during the compression and ejection phases of the parachute deployment system. This verification process ensures that the model accurately reflects the physical behaviour expected in each phase, particularly focusing on the different forces acting on the parachute pack, piston, and other components.

During the compression phase, the parachute pack is forced against the lid of the mortar tube by the piston, which is driven by the pressure behind it. This process compresses the parachute pack and generates several forces, including the compression force, damping force, piston friction, and pack friction. The compression force represents the resistance of the parachute pack as it is being compressed. This force is modelled by an exponential function based on the displacement of the pack. The graph of F_Comp on Figure 49 shows a rapid increase as the pack is compressed, peaking just before the shear pins break. The vertical orange dashed line on the graph indicates the moment the shear pins break, allowing the pack to start exiting the tube, at which point the compression force drops to zero.

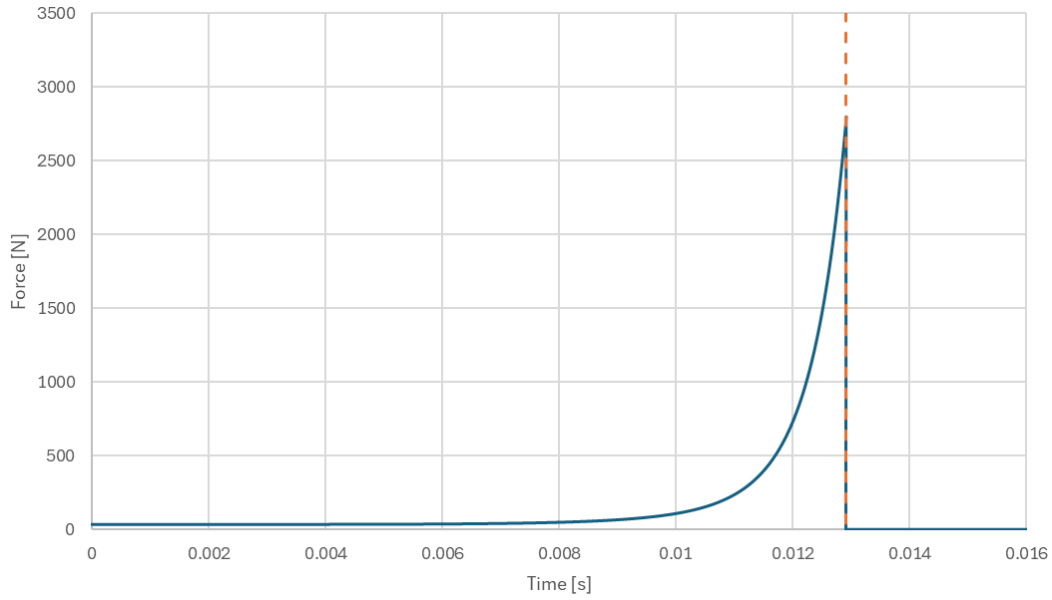

Figure 49: Parachute Pack Compression Force

The damping force is proportional to the velocity of the piston as it compresses the parachute pack. This force increases gradually as the velocity of the piston increases, reaching a maximum value just before the shear pins break, as seen on Figure 50. Once the pins break, as indicated by the vertical orange dashed line, the damping force rapidly decreases to zero since the piston is no longer compressed.

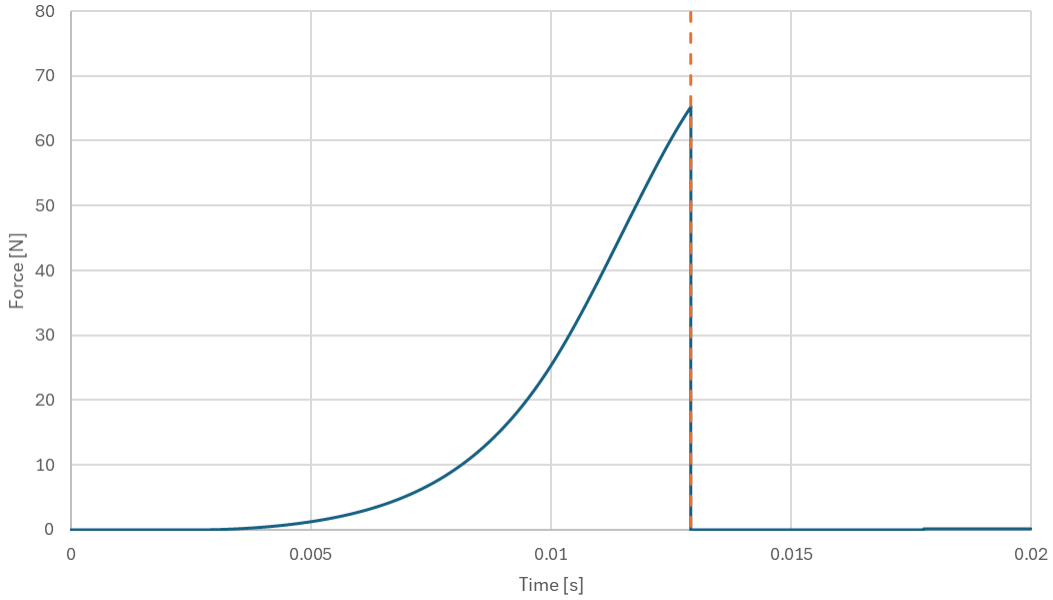

Figure 50: Parachute Pack Damping Force

The friction force generated by the piston depends on the contact between the O-rings and the walls of the mortar tube. Initially, both O-rings are in contact, resulting in a constant friction force. As the piston moves and the first O-ring exits the mortar tube (marked by the first green dashed line), the friction force decreases because only one O-ring remains in contact. When the piston is completely out of the tube, as indicated by the second orange dashed line, the friction force drops to zero, as it can be observed on Figure 51.

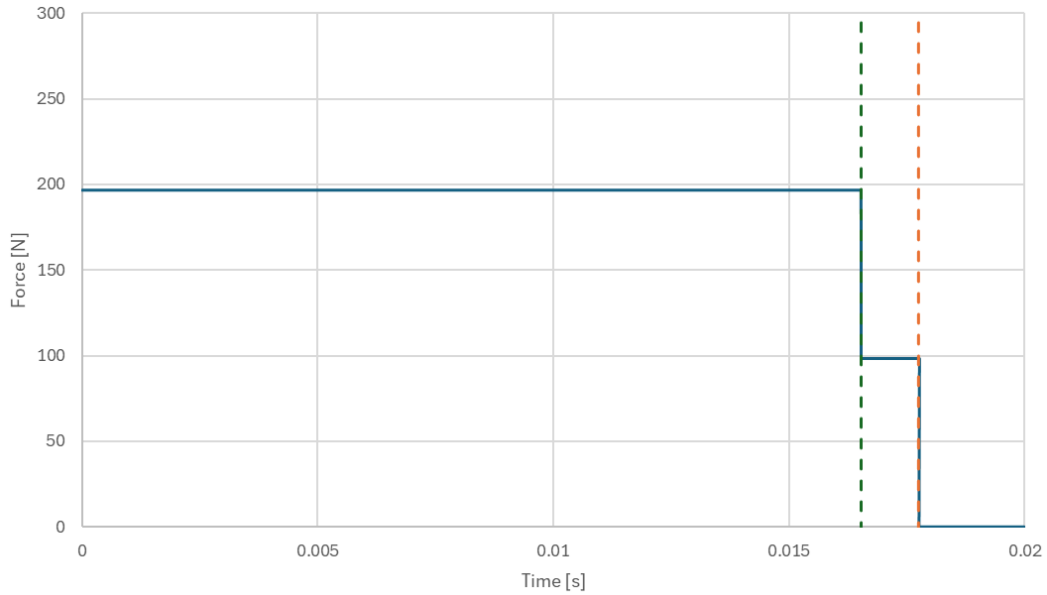

Figure 51: Piston Friction Force

The friction force of the parachute pack is a function of the pack's compression and displacement within the tube. This force increases as the pack becomes more compressed, reaching a maximum when the pack is at its most compressed state. The first orange dashed line represents the moment when this maximum friction occurs. As the pack begins to exit the tube and decompress, the friction force decreases, eventually reaching zero when the pack is fully out, as shown by the green dashed line on the Figure 52 below.

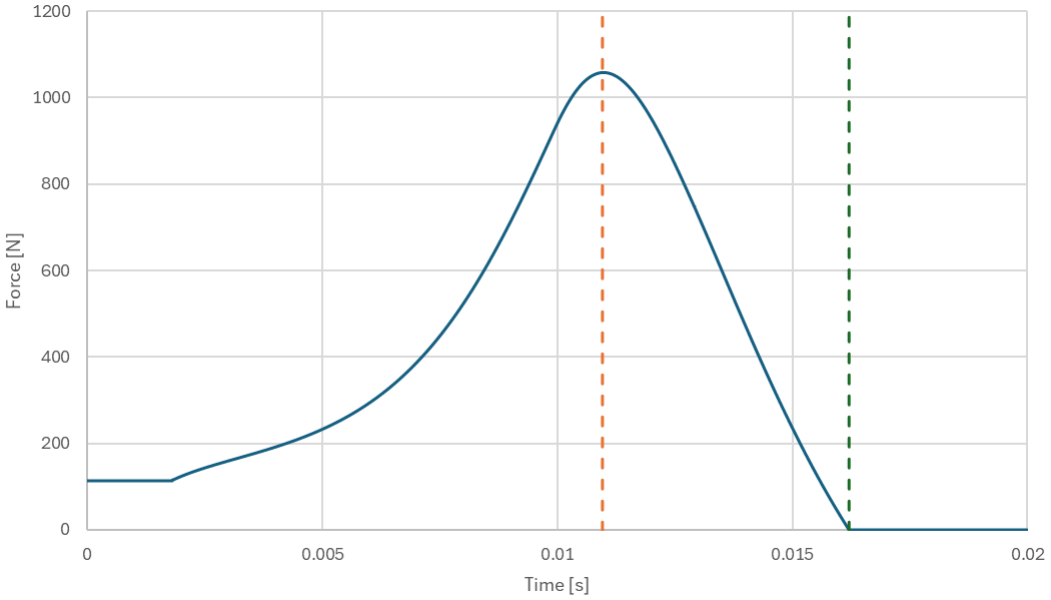

Figure 52: Parachute Pack Friction Force

In the ejection phase, once the shear pins break, the piston and parachute pack begin to move out of the tube. This phase is characterized by the following forces: as the piston moves, the friction force generated by the remaining O-ring continues to act until it too exits the tube, reducing the friction force to zero. As the parachute pack begins to decompress, the pack friction force decreases steadily until it reaches zero when the pack is fully ejected. Both the compression and damping forces drop to zero immediately after the shear pins break, as there is no longer any compression or relative motion

generating these forces.

The verification of the parachute pack compression module was conducted by analysing the output graphs of the various forces over time. These graphs clearly illustrate the expected physical behaviour of the system. The graph of the compression force shows a sharp increase in force as the parachute pack is compressed, peaking just before the shear pins break, after which the force rapidly drops to zero. This behaviour is consistent with the expected response of a compressed spring-like object being released. The graph of the damping force indicates a smooth increase in damping force, correlated with the velocity of the piston. The force reaches its peak just before the pins break, after which it falls to zero, aligning with the expected behaviour of damping in a system where motion is suddenly halted.

The graph of the piston friction force shows the friction force remaining constant until the first O-ring exits the tube, after which it decreases, reflecting the reduced friction from only one O-ring. The force then drops to zero as the piston fully exits the tube, confirming the model's accuracy in simulating the contact forces. The graph for the parachute pack friction force shows an initial increase as the pack is compressed, peaking when the compression is at its maximum. This force then decreases as the pack decompresses and exits the tube, eventually reaching zero. This behaviour accurately reflects the physical process of friction during compression and decompression.

The verification process of the parachute pack compression module has shown that the model accurately represents the expected physical behaviour during both the compression and ejection phases. The forces involved — compression, damping, piston friction, and pack friction — were analysed through their respective graphs, which showed consistent and correct behaviour throughout the process. The model effectively captures the dynamics of the parachute pack's interaction with the piston and mortar tube, confirming the module's reliability in simulating these critical aspects of the system.

4.1.1.5 Heat Flows

The verification of the heat flow models in the Parachute Deployment Device (PDD) simulation aims to ensure that the simulation accurately reflects the thermal dynamics within the system. The objective is to assess how variations in key parameters influence the heat flow components and to verify that the model behaves as expected based on theoretical principles. Since direct comparison with empirical data is not feasible for these particular heat flow components, the verification relies on a systematic approach involving multiple simulations where key parameters are varied.

The heat flow within the system is primarily influenced by several key parameters: the convective heat transfer coefficients hc_{PL} and hc_{GG}) and the emissivity values (ε_{gas}, ε_{PL}, and ε_{GG}). These parameters, initially calibrated using a combination of literature values and empirical data, play a crucial role in determining the accuracy of the model. To verify the model's robustness, these parameters were varied to observe their impact on the heat flow components, specifically the convective and radiative heat losses in both the gas generator and the plenum chamber.

To comprehensively verify the heat flow models, five distinct scenarios were designed. In each scenario, one or more key parameters were varied while keeping the others at their baseline values. The baseline scenario utilized default values for all parameters:

- $hc_{PL} = 3.5 \times 103\ W/m^2K$
- $hc_{GG} = 3.5 \times 104\ W/m^2K$
- $\varepsilon_{gas} = 0.7\ W/m^2$
- $\varepsilon_{PL} = 0.0525\ W/m^2$
- $\varepsilon_{GG} = 0.1\ W/m^2$

The variations in each scenario tested the model's sensitivity to increases and decreases in these parameters. For instance, hc_{PL} and hc_{GG} were both increased and decreased by 20% and 50% in separate scenarios. Similarly, the emissivity values ε_{gas}, ε_{PL}, and ε_{GG} were adjusted by 20% in various scenarios to assess their impact on the heat flow components.

During each simulation, several heat flow components are tracked and recorded over time. These included the convective heat loss in the gas generator ($Q_{GG_{\text{conv}}}$), the radiative heat loss in the gas generator ($Q_{GG_{\text{rad}}}$), the convective heat loss in the plenum volume ($Q_{PL_{\text{conv}}}$), the radiative heat loss in the plenum volume ($Q_{PL_{\text{rad}}}$), the gas temperature in the gas generator ($T_{g_{GG}}$), the walls temperature in the gas generator ($T_{w_{GG}}$), the gas temperature in the plenum chamber ($T_{g_{PL}}$), and the walls temperature in the plenum chamber ($T_{w_{PL}}$) ,. These values were stored in a CSV file, providing a detailed dataset for analysing how the heat flows evolve over time and how they are affected by the different parameter variations.

The analysis involves comparing the results from each scenario against the baseline scenario. This comparison highlights the sensitivity of the heat flow models to changes in convective heat transfer coefficients and emissivity values. The analysis focuses on overall trends in heat losses, particularly the distinction between convective and radiative components, the response of gas generator and plenum chamber temperatures to changes in heat transfer dynamics, and the consistency of the model's behaviour with theoretical expectations, such as the relationship between increased convective coefficients and faster temperature decreases.

First Scenario (hc_{PL})

The results of the first scenario, where the heat transfer coefficient of the plenum (hc_{PL}) is varied, demonstrate a clear relationship between the convective heat transfer and the temperatures within the system. In this scenario, hc_{PL} was increased and decreased by 20% and 50% from the baseline value of 3.5×10^3 W/m²·K. The graphs show the impact of these variations on the convective heat loss from the plenum ($Q_{PL_{\text{conv}}}$), the gas temperature in the plenum ($T_{g_{PL}}$), and the wall temperature of the plenum ($T_{w_{PL}}$).

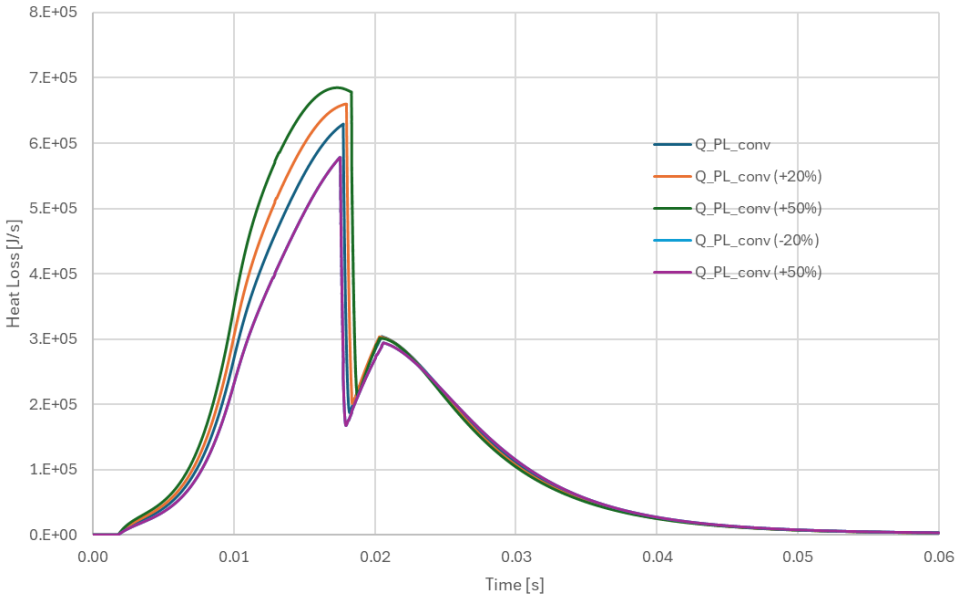

Figure 53: Scenario 1 - $Q_{PL_{conv}}$ Vs Time

As expected, increasing hc_{PL} leads to higher convective heat loss, as seen on Figure 53. The heat loss increases more rapidly with higher hc_{PL} values, peaking earlier and at a higher magnitude compared to

the baseline. Conversely, reducing hc_{PL} results in a lower and more gradual increase in heat loss, with the peak occurring later and at a reduced magnitude. This behavior directly influences the gas temperature in the plenum, $T_{g_{PL}}$. When hc_{PL} is higher, $T_{g_{PL}}$ decreases more rapidly after reaching its peak because more heat is being transferred out of the gas, as seen on Figure 54. On the other hand, with lower hc_{PL} values, $T_{g_{PL}}$ remains higher for a longer period as less heat is transferred away from the gas.

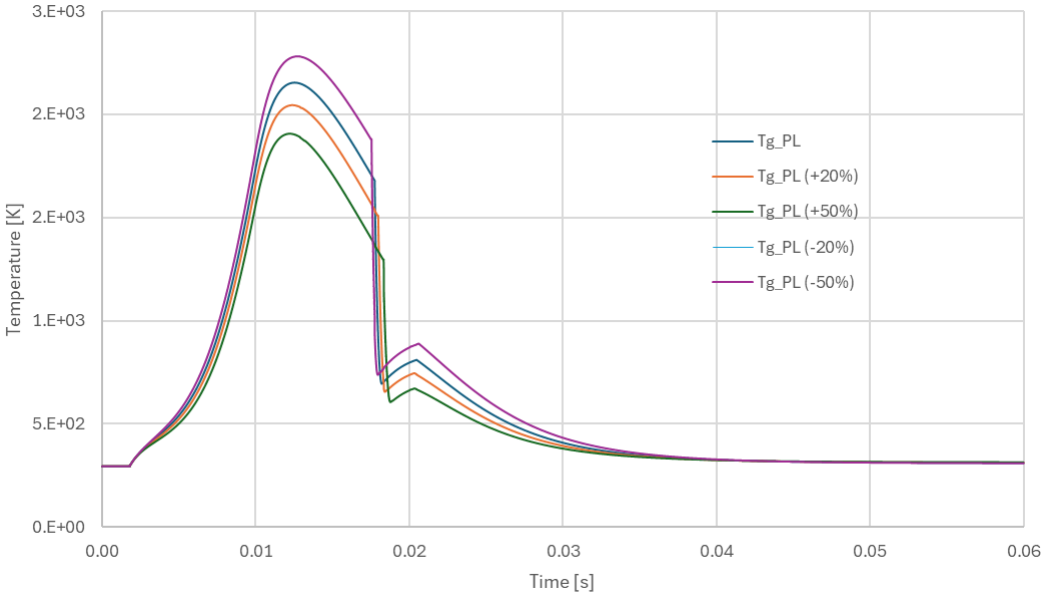

Figure 54: Scenario 1 - $T_{g_{PL}}$ Vs Time

The plenum wall temperature, $T_{w_{PL}}$, also reflects this trend as observed on Figure 55. With higher hc_{PL}, the wall temperature increases more quickly as more heat is transferred to the wall from the gas. This is especially evident in the $T_{w_{PL}}$ graph, where the highest hc_{PL} scenario results in the greatest and quickest rise in wall temperature. In contrast, when hc_{PL} is reduced, the wall temperature increases more slowly and reaches a lower maximum value.

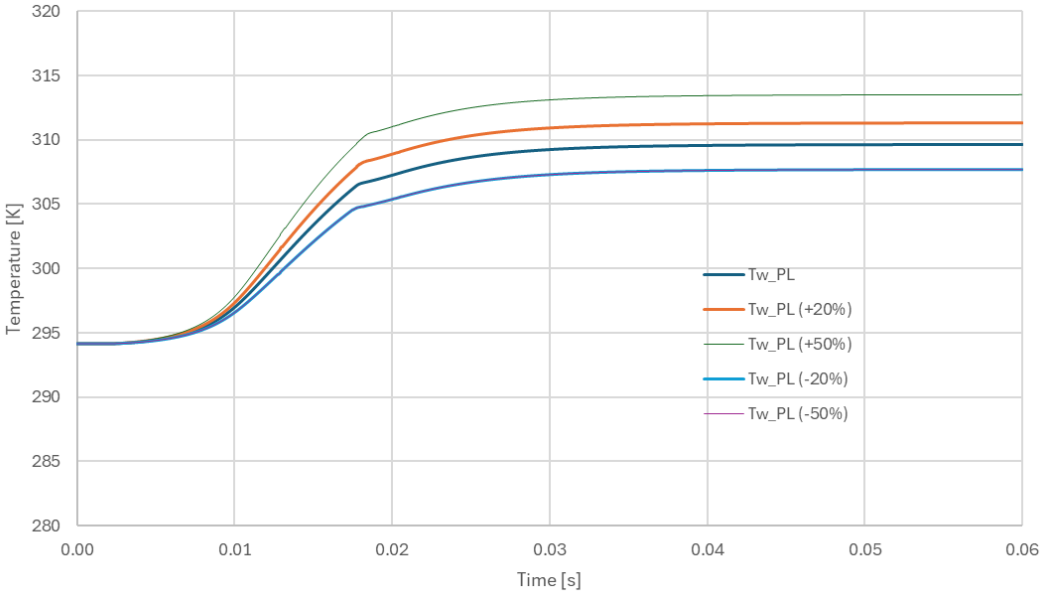

Figure 55: Scenario 1 - $T_{w_{PL}}$ Vs Time

These results are consistent with the principles of heat transfer, where the rate of heat transfer is directly proportional to the heat transfer coefficient. The simulations confirm that the model behaves as expected under varying heat transfer coefficients, indicating that the heat flow model is functioning correctly for these conditions.

Second Scenario (hc_{GG})

In analysing the second scenario, which involves varying the convective heat transfer coefficient (hc_{GG}) for the gas generator, the focus is on understanding the impact of these variations on the heat losses and temperature profiles within the gas generator system. The provided graphs offer insights into how the convective heat losses and corresponding temperatures evolve over time under different values of hc_{GG}, with increments and decrements of 20% and 50%.

The first graph (Figure 56), depicting $Q_{GG_{\text{conv}}}$, clearly demonstrates that an increase in hc_{GG} results in a higher peak of convective heat loss. This behavior is consistent with theoretical expectations, as a higher heat transfer coefficient enhances the rate of heat transfer from the gas generator to its surroundings. Consequently, the system experiences more pronounced convective heat losses, which peak earlier and decline more rapidly as the generator cools. The correlation between the increased hc_{GG} and the rising convective heat loss is evident, indicating that as the coefficient increases, the system's ability to dissipate heat improves substantially.

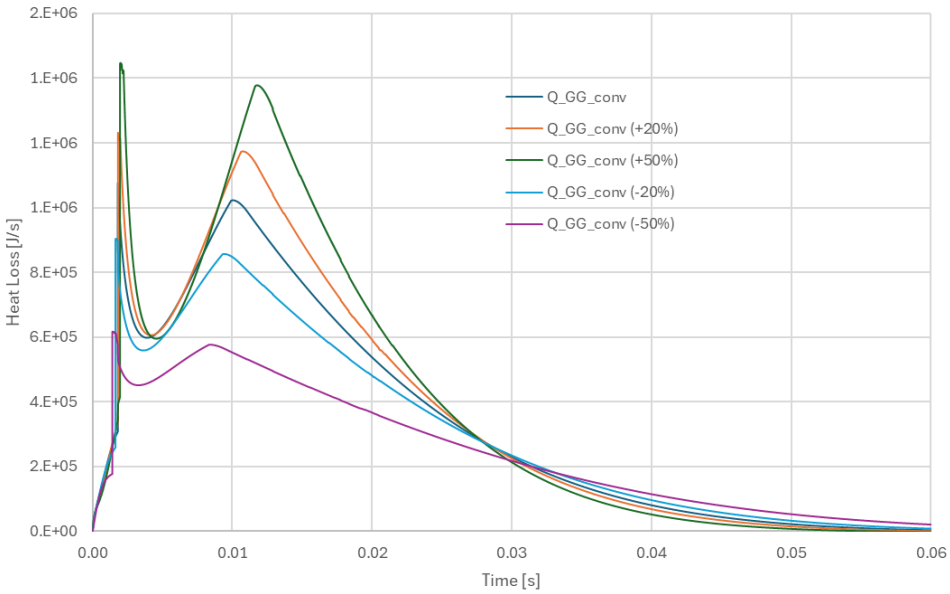

Figure 56: Scenario 2 - $Q_{GG_{conv}}$ Vs Time

The second graph, illustrating the gas temperature within the gas generator ($T_{g_{GG}}$), shows a marked decrease in the maximum gas temperature with increasing hc_{GG}. This outcome is anticipated, as a higher hc_{GG} facilitates more efficient heat dissipation, thereby preventing the gas temperature from reaching higher levels. The temperature curve also exhibits a more rapid decline post-peak, suggesting that the system cools down at an accelerated rate when the heat transfer is more efficient.

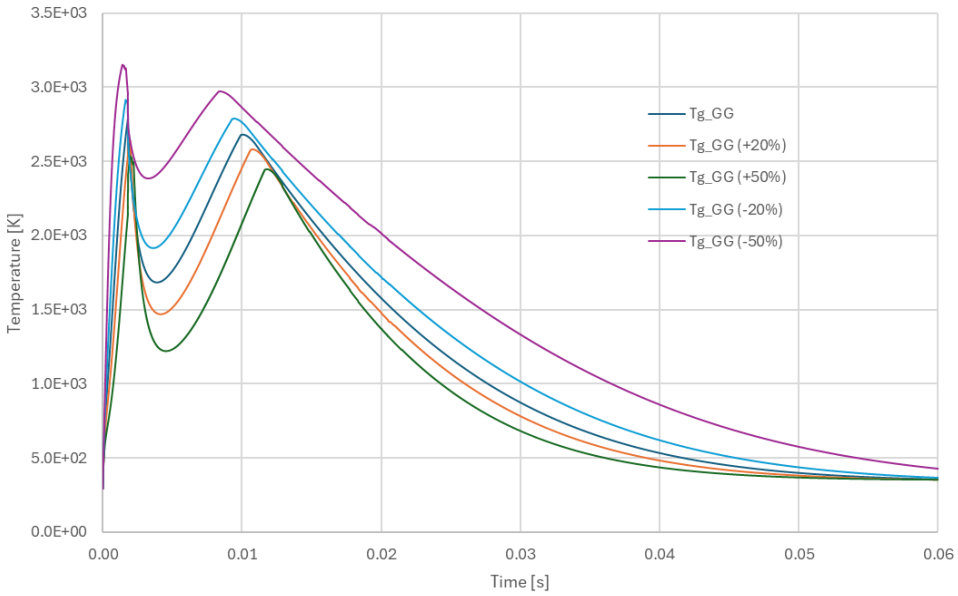

Figure 57: Scenario 2 - $T_{g_{GG}}$ Vs Time

In Figure 58, which presents the wall temperature of the gas generator ($T_{w_{GG}}$), it is observed that lower values of hc_{GG} lead to a slower increase in wall temperature. This trend is due to the reduced heat transfers from the wall surface and the gases, resulting in lower wall temperatures over time. The scenario with the largest increase in hc_{GG} (+50%) corresponds to the highest wall temperature, underscoring the significant influence of the heat transfer coefficient on the thermal management of the system.

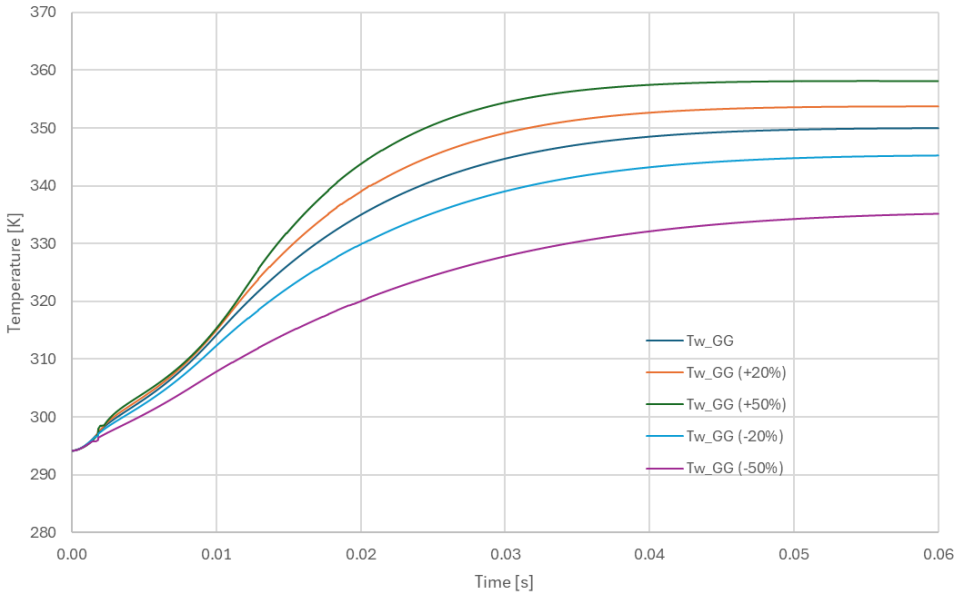

Figure 58: Scenario 2 - $T_{w_{GG}}$ Vs Time

The plenum volume is indirectly influenced by the heat transfer occurring within the gas generator, as reflected in the gas temperature ($T_{g_{PL}}$) and wall temperature ($T_{w_{PL}}$) of the plenum. When the convective heat transfer coefficient in the gas generator (hc_{GG}) is increased, the temperature of the gas in the gas generator decreases more quickly, which in turn slows down the rate at which the gas temperature in the plenum ($T_{g_{PL}}$) increases. This is because the gas entering the plenum is cooler, resulting in a less rapid rise in $T_{g_{PL}}$ compared to scenarios where hc_{GG} is lower. Consequently, the maximum temperature

achieved in the plenum gas is also lower.

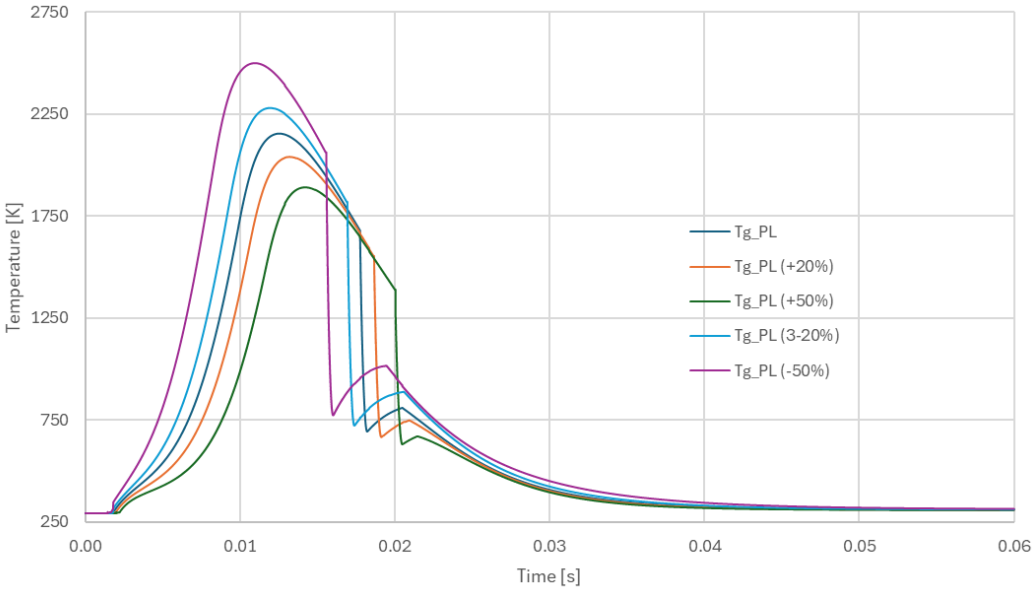

Figure 59: Scenario 2 - $T_{g_{PL}}$ Vs Time

Similarly, the wall temperature of the plenum ($T_{w_{PL}}$) rises more slowly when hc_{GG} is higher. This slower increase in $T_{w_{PL}}$ is due to the reduced heat input into the plenum, as the enhanced cooling in the gas generator lowers the overall temperature of the gas flowing into the plenum. As a result, the maximum wall temperature in the plenum is lower when hc_{GG} is higher, indicating that the system experiences less thermal stress under these conditions.

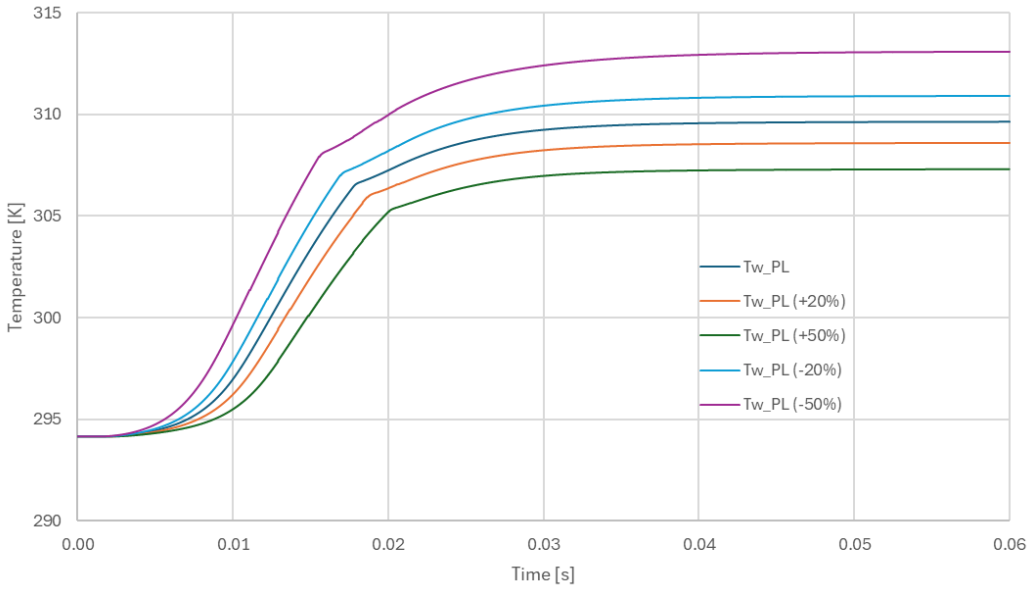

Figure 60: Scenario 2 -$T_{w_{PL}}$ Vs Time

The model's response to the variation of the hc_{GG} parameter behaves consistently with the expected trends, showing that as hc_{GG} varies, the gas and wall temperatures adjust accordingly, indicating the model is functioning as intended for this parameter.

Third Scenario (ϵ_{gas})

In this third scenario, where we vary the gas emissivity parameter, ϵ_{gas}, by +20% and -20%, the primary goal is to verify the model's behavior concerning radiative heat losses within the system. The emissivity of the gas directly influences the radiative heat transfer from the gas to the surrounding surfaces, particularly within the gas generator and the plenum volume.

Upon increasing ϵ_{gas} by 20%, there is a corresponding increase in both $Q_{GG_{\mathrm{rad}}}$ and $Q_{PL_{\mathrm{rad}}}$, which represent the radiative heat losses from the gas generator and plenum, respectively. The graphs of Figure 61 and Figure 62 indicate that with a higher emissivity, the peak values of radiative heat loss increase, signifying more energy is radiated away from the gas due to the enhanced capacity for radiation emission. Conversely, when ϵ_{gas} is decreased by 20%, the radiative heat losses diminish, resulting in lower peaks for $Q_{GG_{\mathrm{rad}}}$ and $Q_{PL_{\mathrm{rad}}}$.

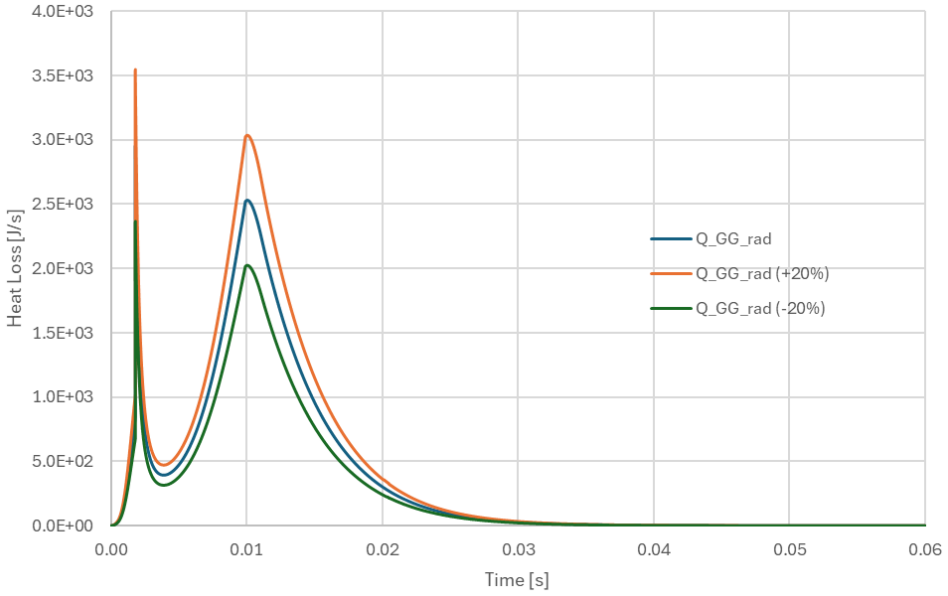

Figure 61: Scenario 3 -$Q_{GG_{rad}}$ Vs Time

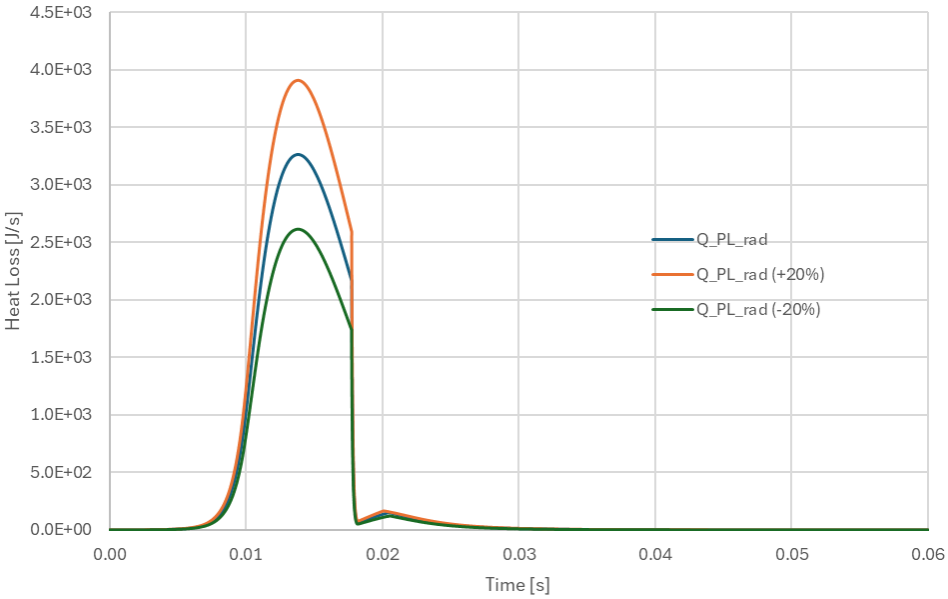

Figure 62: Scenario 3 - $Q_{PL_{rad}}$ Vs Time

Despite these adjustments in radiative heat losses, the overall temperature profiles within the gas generator and plenum volume exhibit only minor variations, as seen on Figure 63 and Figure 64. The

gas temperature in the gas generator ($T_{g_{GG}}$) and in the plenum volume ($T_{g_{PL}}$) show negligible fluctuations, remaining largely consistent across the different values of ϵ_{gas}. Similarly, the wall temperature of the gas generator ($T_{w_{GG}}$) and the plenum ($T_{w_{PL}}$) are only slightly impacted by the variations in radiative heat loss.

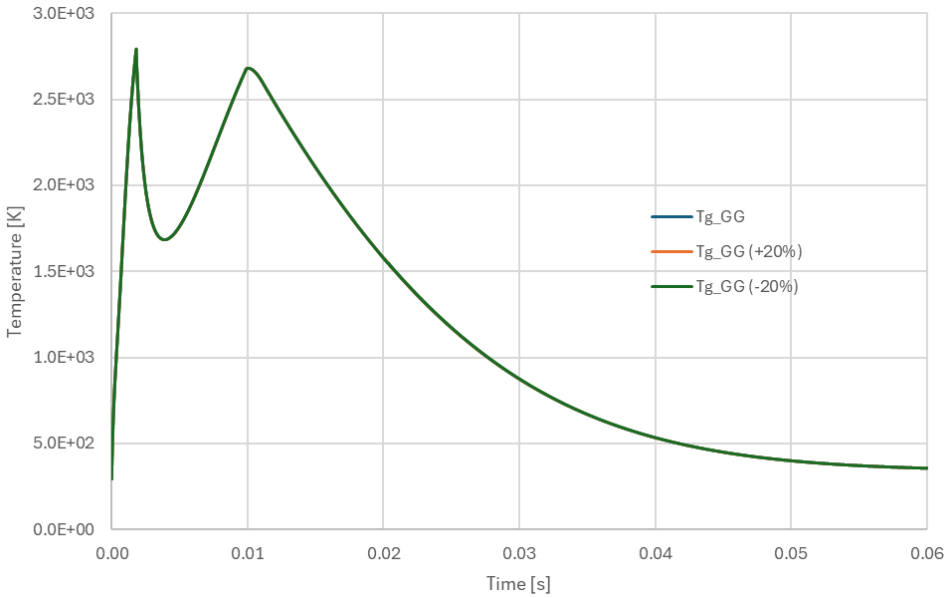

Figure 63: Scenario 3 - $T_{g_{GG}}$ Vs Time

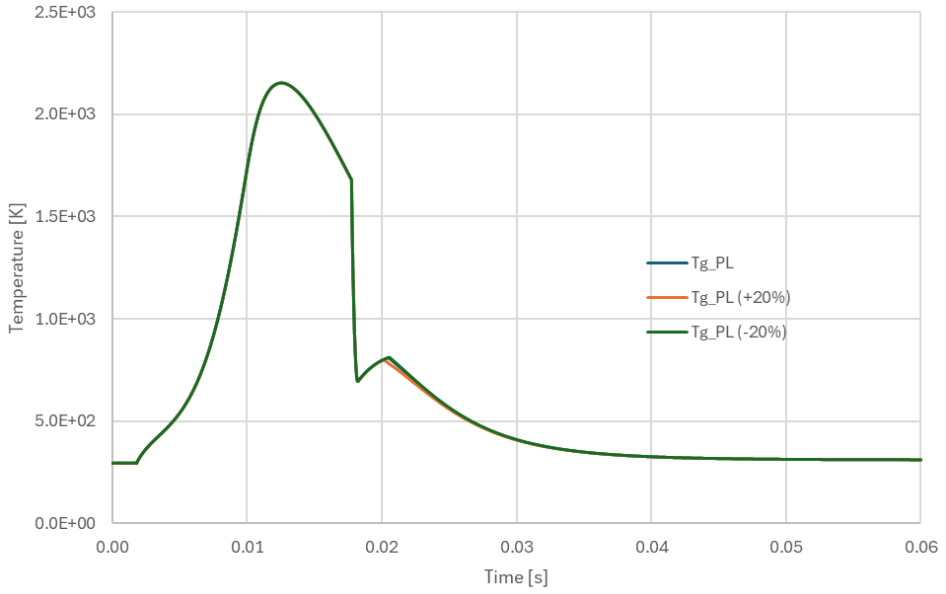

Figure 64: Scenario 3 - $T_{g_{PL}}$ Vs Time

This outcome aligns with the understanding that, within this system, convective heat transfer is the dominant mode of heat loss, contributing significantly more to the overall energy balance than radiative losses. The convective heat losses are substantially higher in magnitude compared to radiative losses, as evidenced by the previous scenarios involving variations in the convective heat transfer coefficients (hc_{GPL} and hc_{GG}). Consequently, changes in radiative heat transfer, while present, do not exert a strong influence on the gas and wall temperatures, which are predominantly governed by convective processes.

Therefore, the model's response to variations in ϵ_{gas} behaves as expected, confirming that radiative heat

losses, though affected by changes in gas emissivity, have a limited impact on the overall thermal behavior due to the dominant convective heat transfer. This consistency in the model's response further validates the accuracy and reliability of the heat transfer mechanisms as implemented in the model.

Scenarios 4 & 5 (ϵ_{PL} & ϵ_{GG})

In scenarios 4 and 5, we varied the values of ϵ_{PL} and ϵ_{GG} by +20% and -20%. Both scenarios resulted in changes in the radiative heat losses within the plenum volume ($Q_{\mathrm{PL}_{rad}}$) and the gas generator ($Q_{\mathrm{GG}_{rad}}$), respectively, as seen on Figure 65 and Figure 66. However, despite these changes in radiative heat loss, the temperatures of the gas and the walls in both the plenum volume and the gas generator remained largely unaffected. This is consistent with the fact that radiative heat loss is relatively minor compared to the dominant convective heat losses in the system. Therefore, these two scenarios can be merged, as they both demonstrate that variations in emissivity, while affecting radiative heat loss, do not significantly influence the overall thermal behaviour of the model.

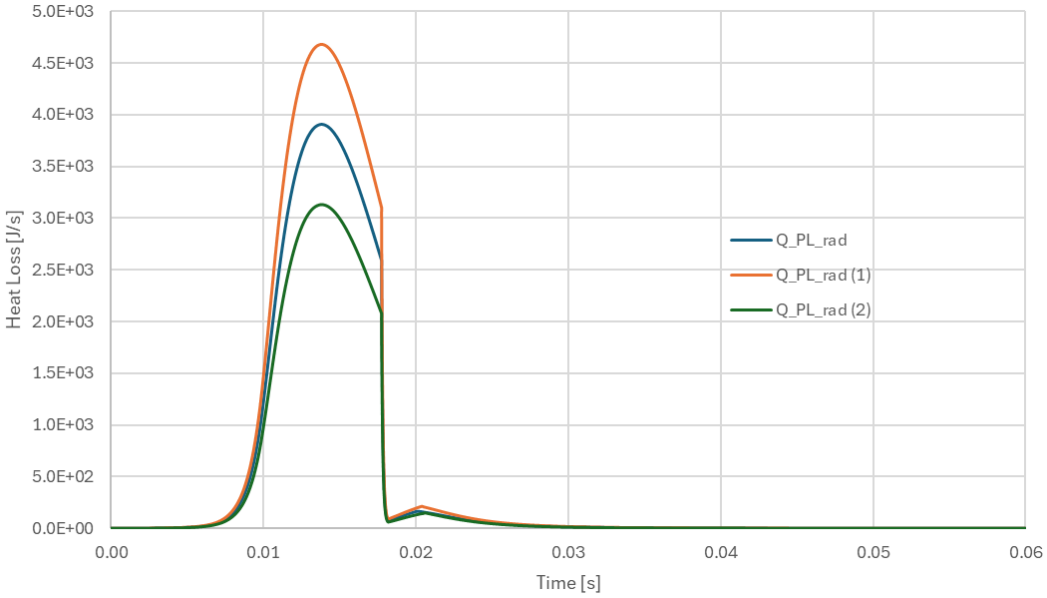

Figure 65: Scenario 4 - $Q_{PL_{rad}}$ Vs Time

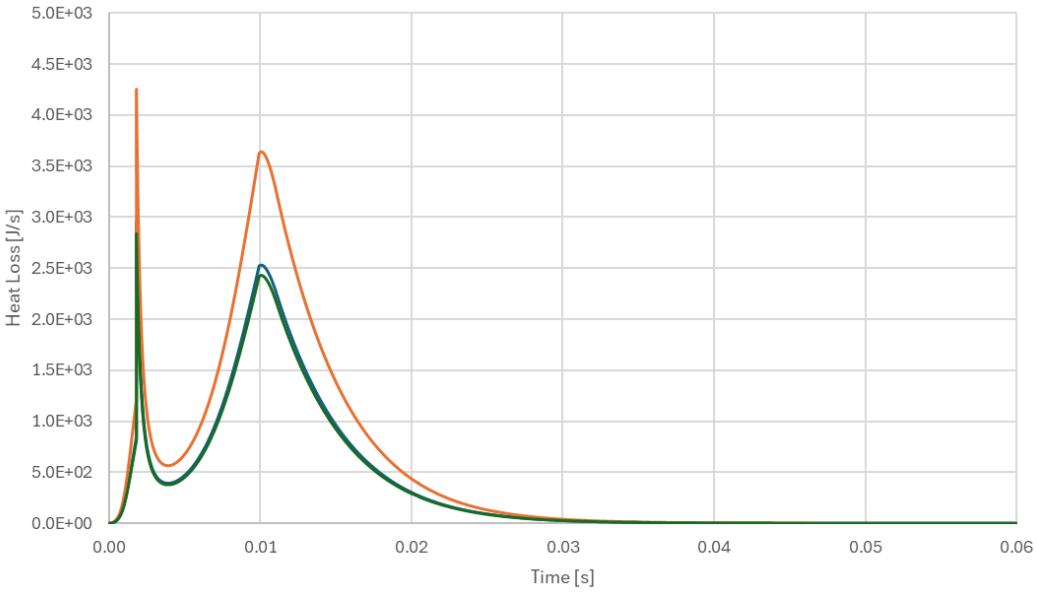

Figure 66: Scenario 5 - $Q_{GG_{rad}}$ Vs Time

4.1.1.6 Burst Disk

The burst disk module is designed to rupture at a specified pressure, regulating the release of gas generated from the combustion of solid propellant within the gas generator system. To ensure that the module performs as expected, its behaviour was tested by varying the burst disk pressure from its initial value of *Pb* by ±50%.

Simulations were conducted at three different burst disk pressures: 50% lower, initial value and 50% higher. The purpose was to observe whether the burst disk ruptured at the specified pressure and to analyse the resulting pressure dynamics within the system.

At the initial burst disk pressure, the model performed as expected, with the burst disk rupturing precisely at this threshold. The pressure curve (Figure 67) displayed a sharp increase followed by a gradual decrease, indicating the release of gas into the larger combustion chamber.

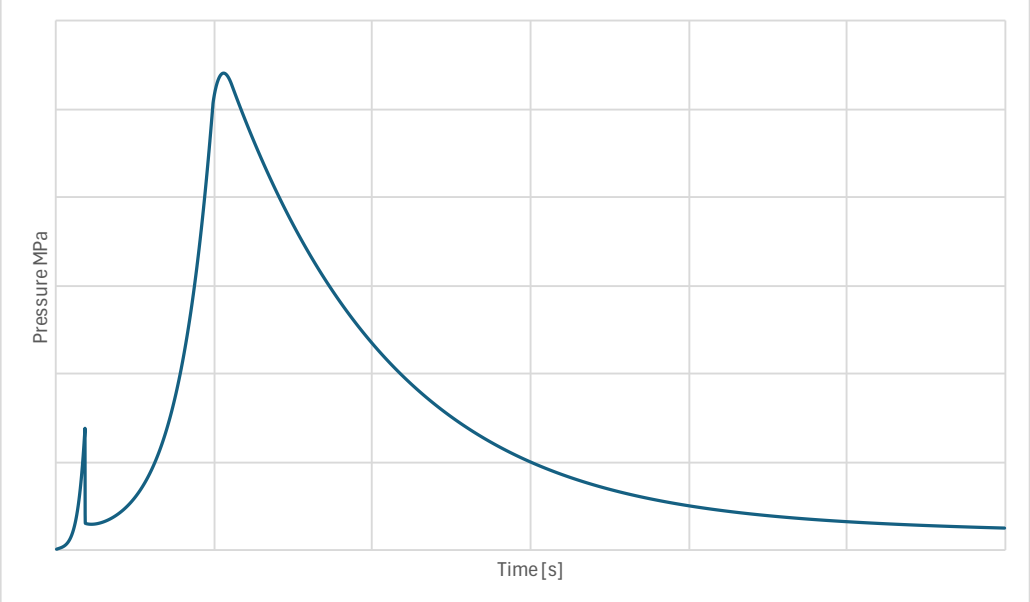

Figure 67: Gas Generator Pressure Vs Time for Pb initial

When the burst disk pressure was reduced by 50%, the disk ruptured earlier, as reflected in the pressure curve (Figure 2). This earlier rupture is consistent with the lower threshold, demonstrating the model's accuracy in responding to decreased burst disk pressures.

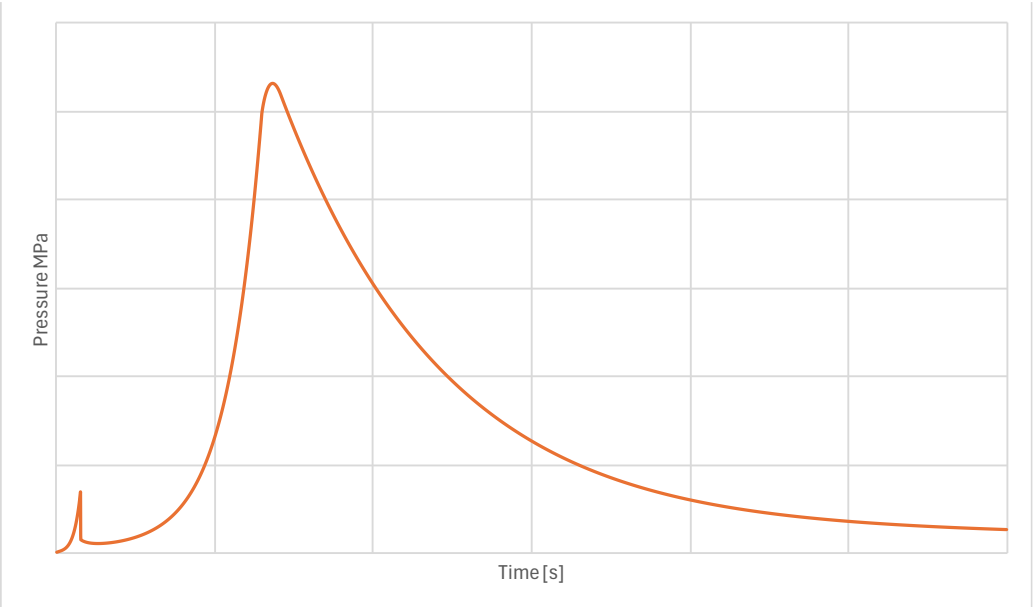

Figure 68: Gas Generator Pressure Vs Time for Pb -50%

At a higher burst disk pressure (+50%), the disk ruptured at a higher pressure, as expected. The pressure curve (Figure 3) showed a faster increase in pressure after the disk ruptured, with the peak pressure inside the gas generator being higher and occurring earlier than in the other cases. This behavior confirms that the model accurately captures the faster pressure dynamics associated with higher burst disk pressures.

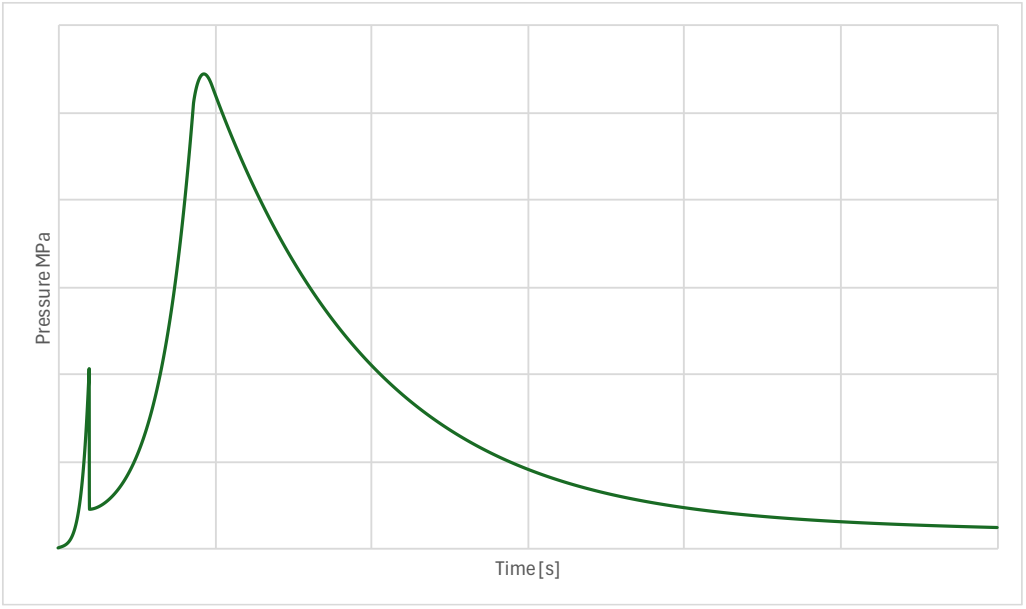

Figure 69: Gas Generator Pressure Vs Time for Pb +50%

These results, illustrated in the pressure curves, confirm that the burst disk module reliably ruptures at the specified pressures and accurately models the subsequent gas expansion and pressure dynamics. The consistency across different burst disk pressures validates the robustness of the module, ensuring it operates as intended within the gas generator system.

4.1.2 Module Integration & Documentation Verification

4.1.2.1 Dynamics, Simulation Core and Events Modules Verification

The verification process for the mathematical model extended beyond the validation of individual modules to ensure the cohesive functioning of the entire system. This involved the integration of all key components—dynamics, simulation core, events, and others—into a unified model. The primary goal was to verify that these modules interact seamlessly, producing accurate and reliable results across various operational scenarios.

Once the modules were integrated, the complete system underwent a series of comprehensive simulations. These simulations were designed to replicate a diverse range of scenarios, including both standard operating conditions and edge cases. The purpose was to assess how well the modules communicated with one another, processed data inputs, and responded to changing conditions within the model.

Key aspects of the verification included:

- **Inter-Module Communication:** The verification began with ensuring that data flows between modules were consistent and error-free. For example, the dynamics and events modules needed to accurately receive and process inputs from the simulation core. Particular attention was given to modules with critical triggering events, such as the burst disk module, whose behaviour could significantly impact other parts of the system. The verification confirmed that these inter-module communications occurred without delay or data loss, maintaining the integrity of the simulation.

- **System-Wide Dynamics:** The next step was to verify that the integrated model accurately represented the intended physical and chemical processes. This included ensuring correct pressure build-ups, flow rates, and the triggering of events at the appropriate times. The verification process demonstrated that the system-wide dynamics were consistent with both the theoretical predictions and the individual behaviours observed in module-specific simulations. For example, pressure responses and flow dynamics were accurately simulated, reflecting the correct operation of the overall system.

- **Robustness Under Stress Conditions:** To further ensure the reliability of the model, the integrated system was subjected to stress testing. This involved running simulations under extreme and boundary conditions, such as maximum expected pressures, temperatures, or unexpected module failures. The purpose was to confirm that the model could handle these conditions without experiencing errors, crashes, or unrealistic outputs. The stress tests were successful, with all modules continuing to function as intended, thus validating the robustness of the entire system.

The results of these simulations confirmed that the modules were well-integrated, with no significant discrepancies observed in the outputs. The system's response across various scenarios was consistent with theoretical expectations and the behaviours observed in individual modules. This indicated that the integration process was successful, and the entire model could reliably simulate the complex interactions within the gas generator system.

4.1.2.2 Documentation Accuracy and Completeness

In parallel with the technical verification of the mathematical model, a comprehensive review of the associated documentation was conducted. This review was essential to ensure that the documentation accurately reflects the model’s design, functionality, and operational procedures, thereby enabling correct understanding, usage, and maintenance by future users.

The documentation review focused on several critical aspects:

- **Accuracy of Descriptions:** The first step was to verify that the documentation accurately describes the mathematical formulations, assumptions, and algorithms used within each module. This involved a detailed cross-referencing of the documentation with the actual code and simulation outputs to ensure consistency. The goal was to confirm that all theoretical underpinnings and implementation details were correctly captured in the documentation.

- **Completeness:** Next, the review ensured that the documentation comprehensively covers all relevant aspects of the model. This includes not only the core functionalities but also the model's limitations, potential sources of error, and troubleshooting guidance. The completeness of the documentation is crucial for making it a reliable reference for both current and future users, ensuring that they can fully understand and apply the model as intended.

- **User Guidance:** Special attention was given to the clarity and practicality of the instructions provided for setting up, running, and interpreting simulations. The documentation was reviewed to ensure that it offers clear, concise, and actionable guidance, which is particularly important for users who may not be intimately familiar with the model's development. This user-focused approach helps to bridge any gaps between the model's complexity and the user's expertise, facilitating effective use of the tool.

The review process concluded that the documentation was both accurate and complete. It effectively serves as a solid foundation for the model's future use and potential updates. The clear and detailed explanations included in the documentation will support users in applying the model correctly, understanding its capabilities and limitations, and making informed decisions during its operation.

4.2 Validation

The validation of the Parachute Deployment Device (PDD) mathematical model is a critical step to ensure that the simulations accurately reflect the physical behaviour of the system. The PDD is composed of two primary components: a gas generator and a mortar tube. The validation process compares the simulation results with experimental data to establish the model's accuracy and reliability.

In the PDD, the ignition of the solid propellant inside the gas generator generates high-pressure gas. This gas flows into the mortar tube, where it drives a piston that compresses the parachute pack against the lid of the tube. When the shear pins retaining the lid break, the parachute pack is expelled from the mortar tube, deploying the parachute.

The validation is conducted using two types of experimental tests:

- **Closed Bomb Test:** In this test, the gas generator is connected to a closed tank. The data obtained from this test allow us to validate the ignition, combustion, and heat transfer models by comparing the simulation results with the actual pressure, temperature, and combustion characteristics observed in the closed environment.

- **Deployment Test:** This test involves the complete PDD system, where the gas generator and mortar tube are fully operational. The data from this test provide a basis for validating the full model, including the dynamics of the parachute pack being expelled from the mortar tube. The comparison between the simulated and observed behaviour of the parachute pack during deployment is crucial for confirming the model's accuracy.

This validation process aims to ensure that the mathematical model not only functions correctly within the simulation but also accurately predicts the physical outcomes observed in real-world scenarios. The following sections detail the validation efforts for each component of the PDD model, focusing on how well the simulations align with the experimental data.

4.2.1 Closed Bomb Test Validation

The Closed Bomb Test is an essential experimental procedure used to validate the gas generator model within the Parachute Deployment Device. This test allows for an accurate assessment of the combustion and heat transfer models, providing a controlled environment where key parameters such as pressure, temperature, and gas generation rate can be observed and measured. By comparing these experimental results with simulation outputs, the validation process confirms that the model accurately replicates the physical processes involved in the PDD's gas generation system.

4.2.1.1 Test Setup and Parameters

In the Closed Bomb Test, the gas generator is connected to a sealed tank, ensuring no gas escapes during the combustion process. The combustion of the solid propellant produces high-pressure gas, which is contained within the tank, allowing for precise measurements of pressure, temperature, and energy release. The test tank has a known volume and is instrumented with pressure transducers and thermocouples to monitor the dynamic behaviour of the system throughout the burn.

The key parameters measured during the test include:

- **Pressure inside the gas generator (GG)**: This provides insight into the combustion process and how the gas pressure evolves over time.
- **Pressure inside the tank (PL)**: This reflects the total gas production, and the expansion of the gas generated from combustion.
- **Ambient temperature**: This is recorded to account for environmental effects on the combustion process.

The simulation parameters for the gas generator model are configured to match the experimental setup, including the volume of the test tank, the propellant properties, and the initial conditions. The following key aspects of the gas generator model are validated against the Closed Bomb Test data: pressure dynamics, energy release, gas generation rate, and heat transfer.

4.2.1.2 Test Campaigns Overview

Three key testing campaigns provided data for this validation process: the Setup A Qualifying Tests, the Setup B Development Tests and the Setup B Qualifying Tests. These campaigns were conducted to test the PDD systems in preparation for their respective space missions, and the data obtained from these tests is now used to validate our gas generator model.

Each of these campaigns involved different setups, which varied in terms of tank volume and the amount of propellant used:

- **PDD1 Setup:** This setup features a small tank volume. It was used in both the Setup A Qualifying Tests and the Setup B campaigns (Development and Qualifying).
- **PDD2 Setup:** This setup involves a much larger tank volume, allowing for greater gas expansion and lower pressures. It was used in the Setup B Development and Qualifying campaigns only.

Each test campaign utilised different amounts of propellant, tailored to the specific mission requirements. The data from these campaigns allows us to validate the robustness of the gas generator model across a wide range of operating conditions.

4.2.1.3 Setup B Development Tests

4.2.1.3.1 Setup B (DevM PDD1)

The Setup B (DevM PDD1) tests utilized a pre-defined charge of propellant and a fixed tank volume. Tests were conducted under three main temperature conditions: ambient, high, and low. For each test, both gas generator and tank pressures were measured. We begin by analysing the results from the ambient temperature tests.

Ambient Temperature Test

Five experimental tests were conducted at ambient temperature, alongside simulated outputs. Below, we analyse the gas generator pressure and tank pressure results. The graph below (Figure 70) shows the gas generator pressure for five experimental tests (GG-1 to GG-5) and the corresponding simulation (GG-Sim).

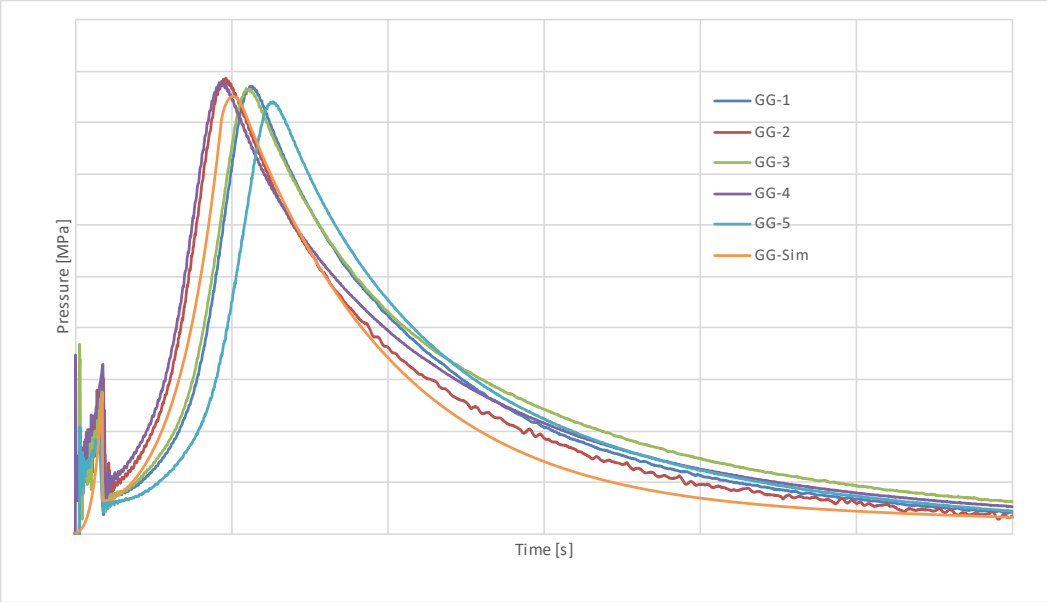

Figure 70: Setup B (DevM PDD1) Gas Generator Pressure at ambient temperature

The gas generator pressure analysis shows a maximum difference of 5.3% between the peak values recorded across the experimental tests, with GG-2 exhibiting the highest peak and GG-5 the lowest. The simulation peak pressure is 1.6% lower than the average experimental peak values, indicating strong agreement between the model and test data. While the simulation curve demonstrates a slightly faster decay after the peak, the overall pressure profile remains well-aligned with the experimental results, effectively capturing the key dynamics of the gas generator with only minor deviations.

Figure 71 below illustrates the tank pressure for the five experimental tests (PL-1 to PL-5) and the corresponding simulation (PL-Sim).

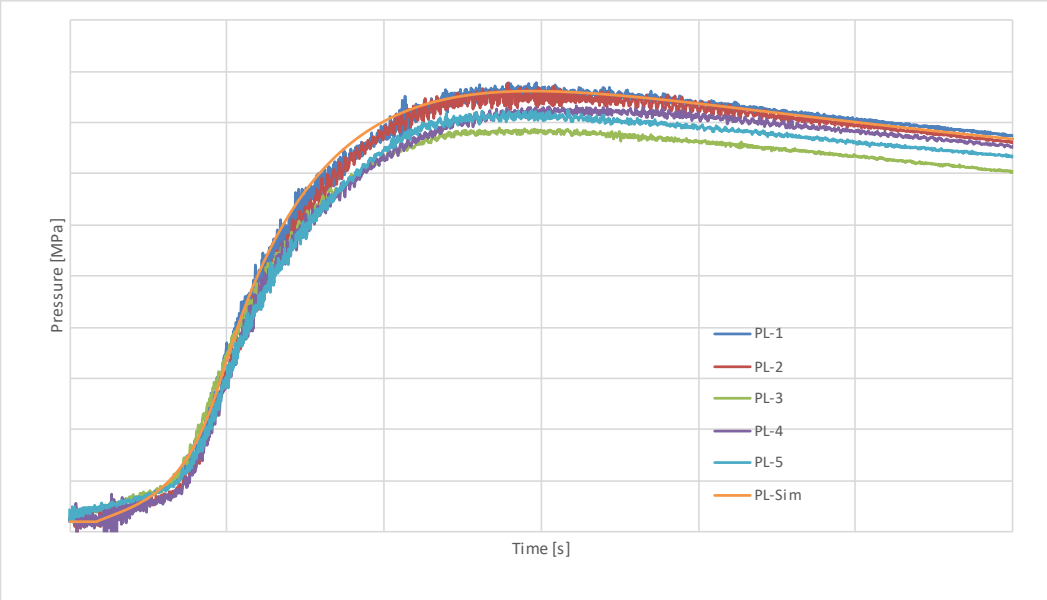

Figure 71: Setup B (DevM PDD1) Tank Pressure at ambient temperature

The simulation accurately captures the plenum pressure behaviour, with the simulated peak pressure closely aligning with the experimental values, which show a limited range of variation. The closest peak value between the test and the model differs by only 1.8%, demonstrating the model's strong predictive capability. This agreement confirms that the simulation effectively represents the overall pressure dynamics within the plenum. The minor differences observed fall within expected variability, reinforcing the model's reliability in predicting plenum pressure across multiple tests.

The analysis of the Setup B (DevM PDD1) at ambient temperature shows a strong correlation between the simulation and the experimental results for both gas generator and tank pressures. The gas generator pressure was slightly underestimated in the simulation but followed the correct trend, while the tank pressure was well-predicted. The slight variability across the five experimental runs is likely due to real-world test variations but does not significantly impact the overall trends.

Hot Temperature Test

In the hot test, the propellant's combustion characteristics are expected to change due to the increased initial temperature, leading to faster combustion and higher peak pressures. The graph below on Figure 72 shows the gas generator pressure from two experimental tests (GG-1, GG-2) and the simulation (GG-Sim).

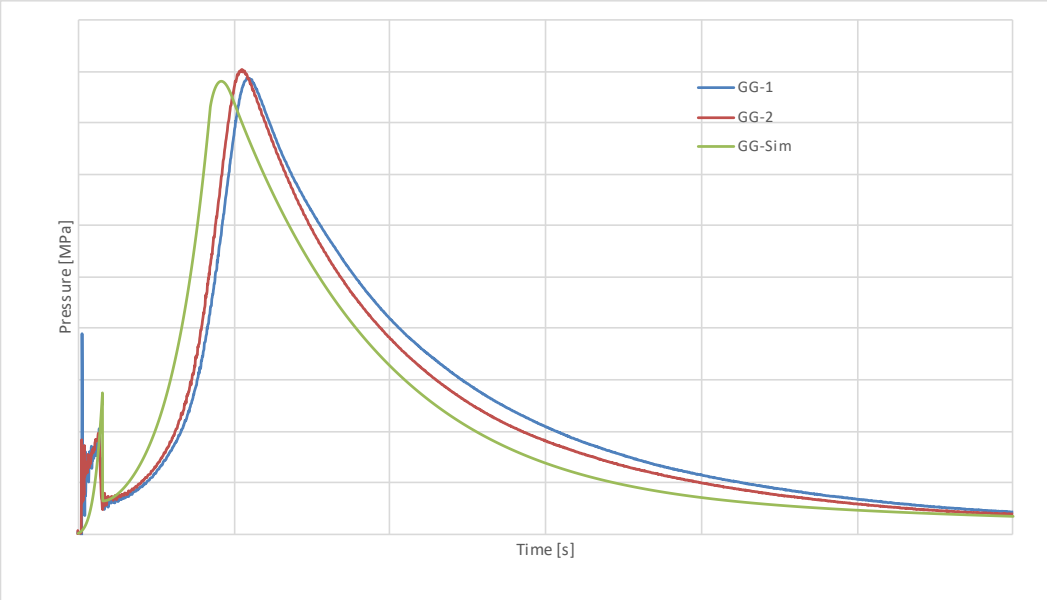

Figure 72: Setup B (DevM PDD1) Gas Generator Pressure at high temperature

At high temperature, the gas generator pressure rose more rapidly compared to the ambient temperature test, reflecting the faster combustion process. The simulation predicted a peak gas generator pressure with a percentage difference of 0.78% compared to the closest experimental test GG-1. The experimental tests showed peak pressures that were very close to the simulated value, with the highest percentage difference between the test and model being within a small range. The simulation effectively captured the overall trend of the experimental data, including the initial rapid pressure rise and subsequent decay, though the simulated peak occurred slightly earlier than observed in the tests.

The graph below (Figure 73) shows the tank pressure for the two experimental tests (PL-1, PL-2) and the simulation (PL-Sim).

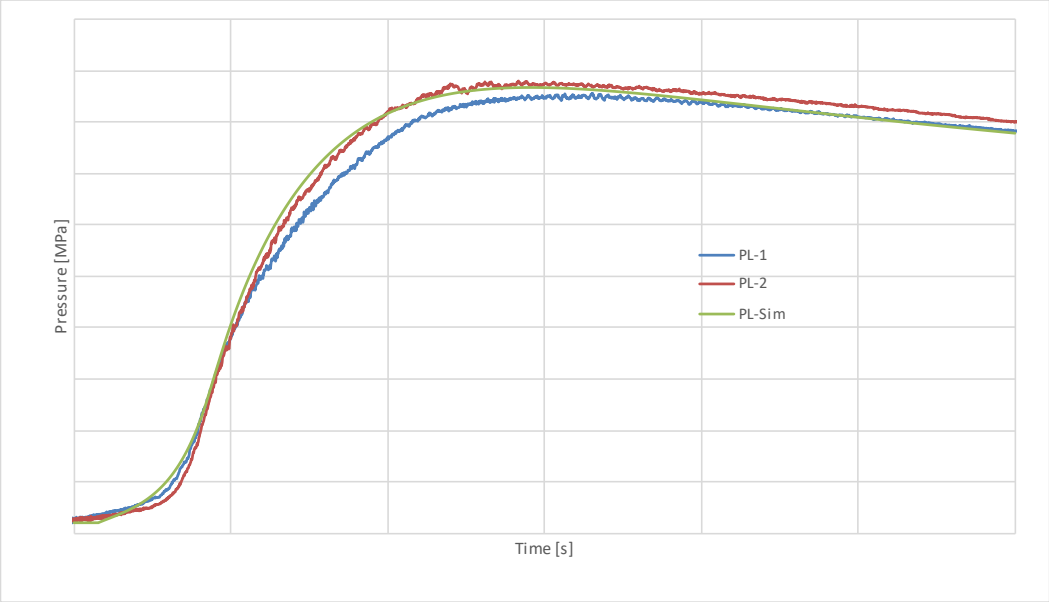

Figure 73: Setup B (DevM PDD1) Tank Pressure at high temperature

In the tank pressure results, the simulation predicted a peak pressure with a percentage difference of 1.37% compared to the closest experimental test PL-2. The experimental tests recorded peak pressures

that were very close to the simulated value, further validating the model's accuracy. The simulation followed the general trend of the experimental data closely, though there was a slight mismatch in the rate of pressure increase during the initial few milliseconds.

The hot test shows that the model can accurately simulate the faster combustion process expected at elevated temperatures. The gas generator and tank pressure profiles from the simulation were closely aligned with the experimental data, with minimal deviations in peak values and overall trends. Overall, the hot test validation demonstrates the robustness of the gas generator model in handling variations in ambient temperature, with reliable predictions of both gas generator and tank pressures.

Cold Temperature Test

The cold test at was conducted to assess the model's accuracy in simulating the combustion process at low temperatures, where combustion is expected to be slower due to the reduced thermal energy in the system. The Setup B (DevM PDD1) is tested in cold environment both one initiator and two initiator configurations being tested. The graph below on Figure 74 shows the gas generator pressure for three experimental tests (GG-1, GG-2, GG-3-1init) and the two simulations (GG-Sim, GG-Sim-1init), where the "1init" label indicates the tests and simulations that used only one initiator.

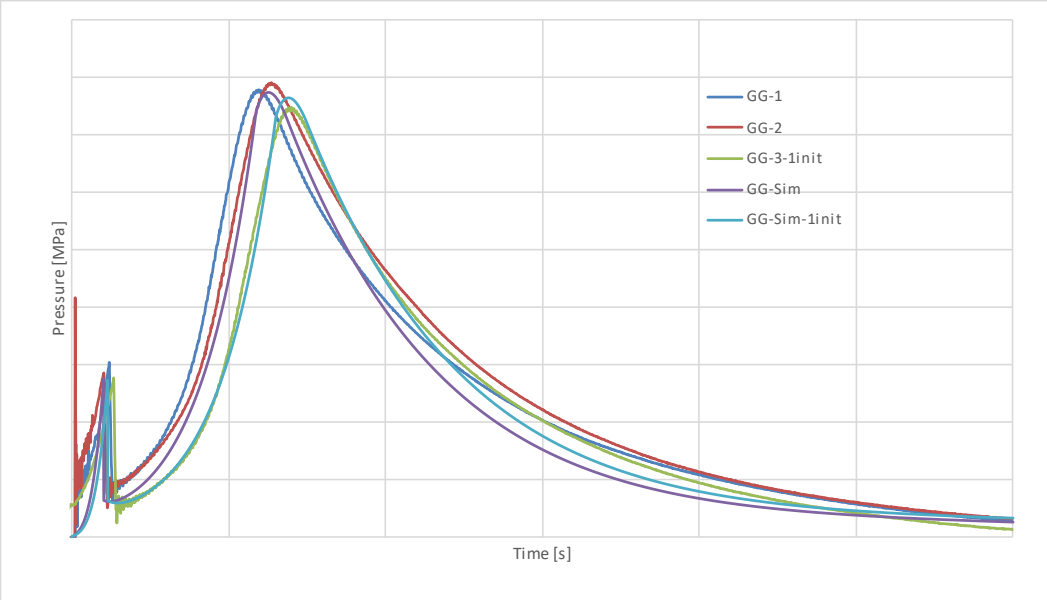

Figure 74: Setup B (DevM PDD1) Gas Generator Pressure at low temperature

For the gas generator pressure, the percent differences between the experimental tests and the simulation results are minimal: 0.61% for the two-initiator configuration (GG-1), 2.16% for the second two-initiator test (GG-2), and 2.15% for the one-initiator test (GG-3-1int). Additionally, a close match is observed between the experimental and simulated pressures throughout the entire test, confirming that the model accurately captures both the peak dynamics and the overall pressure behaviour of the gas generator system, including the effects of varying initiator configurations.

The graph below (Figure 75) shows the tank pressure for three experimental tests (PL-1, PL-2, PL-3-1init) and the two simulations (PL-Sim, PL-Sim-1init).

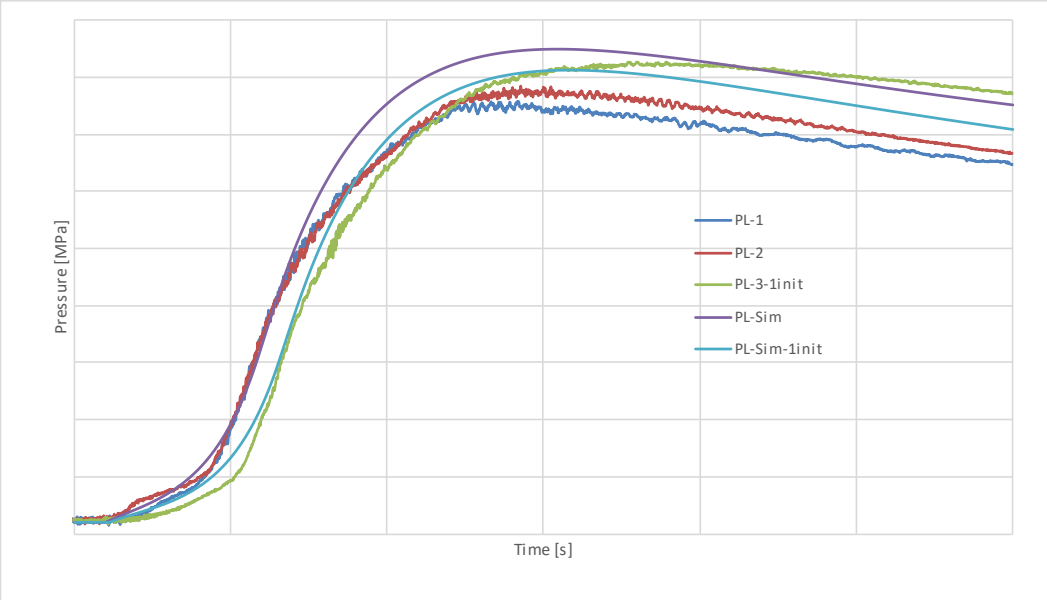

Figure 75: Setup B (DevM PDD1) Tank Pressure at low temperature

For the plenum pressure, the simulation slightly overestimates the peak pressures, with percent differences of 11.44% for the first two-initiator test (PL-1), 8.08% for the second two-initiator test (PL-2), and 1.7% for the one-initiator test (PL-3-1init). Despite these differences, the general trend and overall behaviour of the plenum pressure curve are well captured by the model, demonstrating that the simulation accurately follows the experimental pressure dynamics throughout the test.

Overall, the model shows a strong capability to replicate the experimental behaviour of both the gas generator and plenum pressures, validating its mathematical formulation. Minor discrepancies in the plenum pressure can be attributed to the inherent uncertainty and variability in the experimental system, as well as the simplifications in the simulation model.

4.2.1.3.2 Setup B (DevM PDD2)

The Setup B (DevM PDD2) was designed with a larger tank volume and a similar propellant charge. This setup differs from the PDD1 setup due to the increased tank size, which results in a slower pressure rise and lower peak pressures due to the larger volume available for gas expansion. Multiple tests were conducted to validate the gas generator model under various conditions, starting with the ambient temperature test.

Ambient Temperature Test

For the ambient temperature test, the gas generator pressure analysis shows that the experimental peak pressures vary slightly across the five tests (GG-1 to GG-5). The simulation (GG-Sim) predicted a peak pressure, which aligns well with the experimental data, showing a small deviation from the average. The pressure curves between the experimental tests and the simulation follow a consistent trend, with similar rise and decay behaviour, validating the model's ability to capture the gas generator dynamics under ambient conditions.

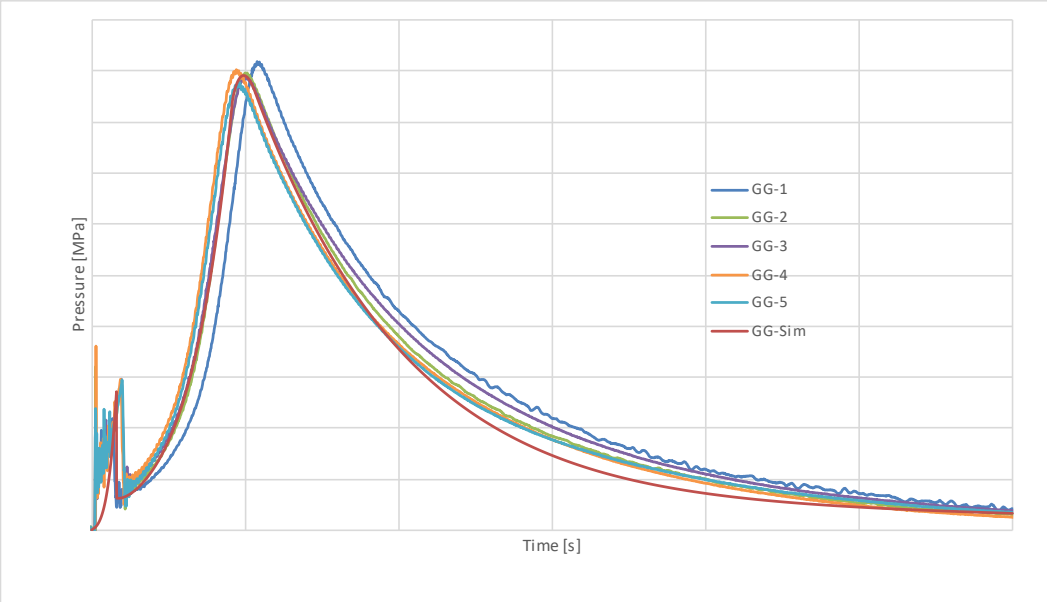

Figure 76: Setup B (DevM PDD2) Gas Generator Pressure at ambient temperature

For the hot temperature test, the gas generator pressure analysis reveals slight variations in the experimental peak pressures across the tests. The simulation predicted a peak pressure that aligns well with the experimental data, with the closest match occurring between the PL-3 test and PL-sim, showing a 2.6% difference. The pressure curves for both the experimental tests and the simulation follow a similar trend, capturing the rapid pressure rise and decay behaviour. This close match validates the model's ability to accurately represent the gas generator dynamics under hot temperature conditions.

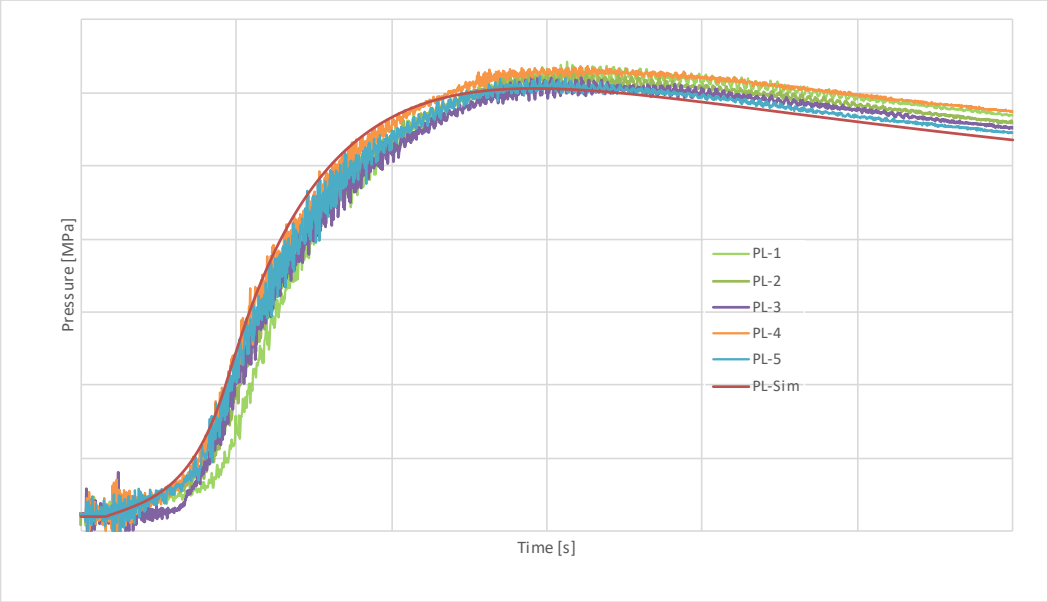

Figure 77: Setup B (DevM PDD2) Tank Pressure at ambient temperature

The ambient temperature test for the Setup B (DevM PDD2) demonstrated that the gas generator model accurately simulates the pressure dynamics in larger-volume systems. Both the gas generator and tank pressure profiles were well-represented in the simulation, with minimal deviations from the experimental data. The larger tank volume led to a slower pressure rise and lower peak pressures, as expected, and these dynamics were effectively captured by the model.

Hot Temperature Test

In the hot test, the higher temperature accelerates the combustion process, leading to faster gas generation and higher peak pressures compared to the ambient test. The Setup B (DevM PDD2), with a larger tank volume and a similar propellant charge, was subjected to these conditions to validate the model's response to elevated temperatures. The graph below shows the gas generator pressure from two experimental tests (GG-1 and GG-2) and the simulation (GG-Sim).

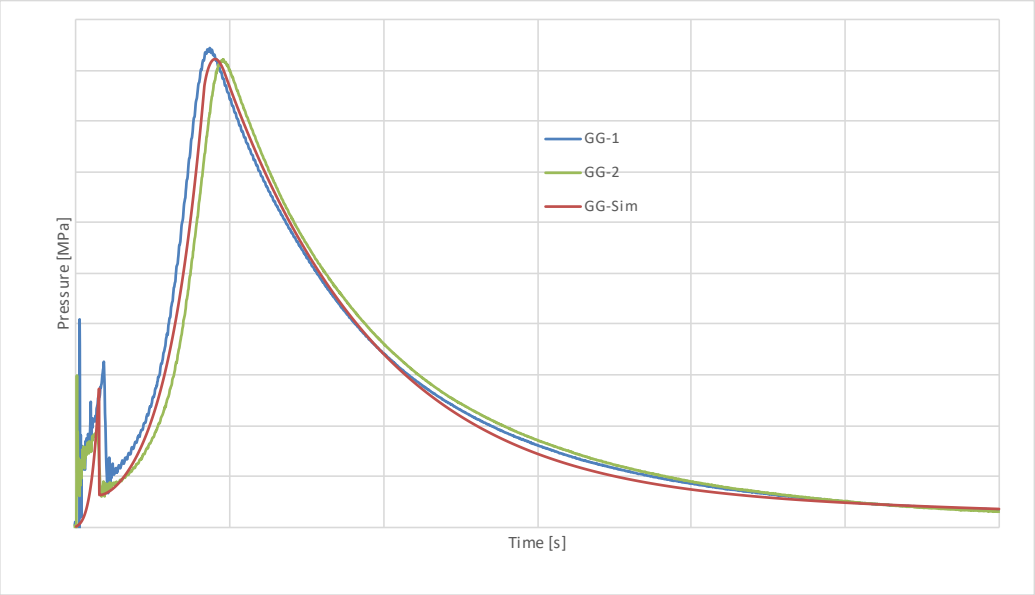

Figure 78: Setup B (DevM PDD2) Gas Generator Pressure at high temperature

The experimental data for the gas generator shows a 2.36% difference between the peak pressures of the two tests, GG-1 and GG-2, highlighting the natural variation between identical experiments. However, the simulation results show a remarkably close match with the experimental data, with only a 0.04% difference between the peak of GG-2 and the simulated peak. This demonstrates that while there is variability between the experiments, the model still accurately simulates the system's behaviour, capturing the rapid pressure rise and decay effectively.

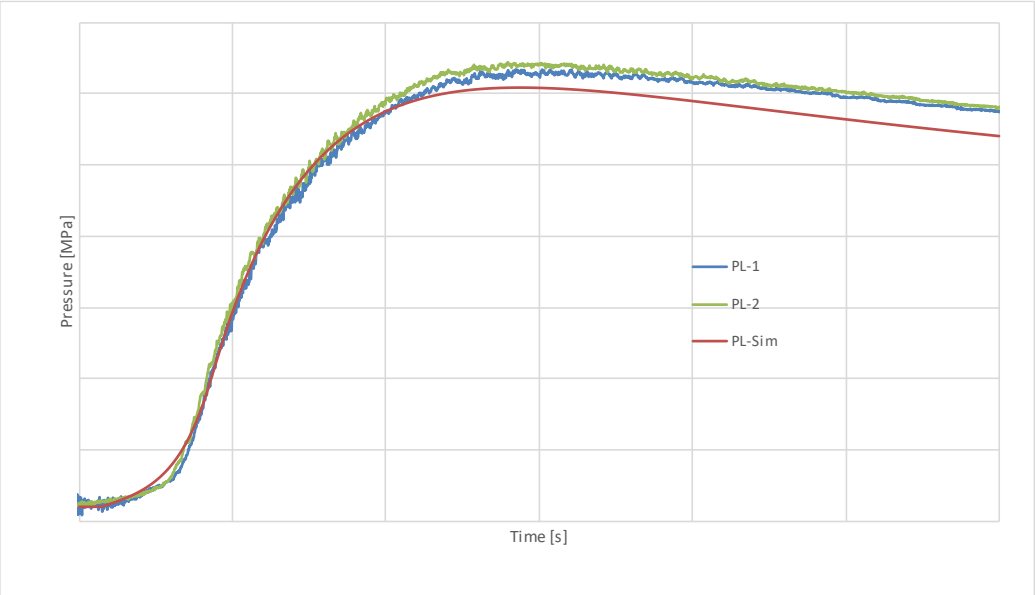

Figure 79: Setup B (DevM PDD2) Tank Pressure at high temperature

For the plenum pressure, the experimental tests show a difference of 4.18% between the simulation and PL-1, and a 5.75% difference between the simulation and PL-2. Despite these small differences in peak values, the simulation curve closely follows the experimental data, accurately reflecting the rise and decay in pressure. The minor discrepancies in peak values can likely be attributed to slight variations in the experimental conditions, such as the influence of temperature on gas expansion behaviour.

Overall, the hot test at validates the model's ability to predict the faster combustion and pressure dynamics that occur at elevated temperatures. The simulation captures the key features of both the gas generator and plenum pressures, with deviations well within acceptable margins, affirming the robustness of the model under these conditions.

Cold Temperature Test

In the cold test, the low temperature slows down the combustion process, resulting in a delayed gas generation and lower peak pressures compared to the ambient and hot tests. The Setup B (DevM PDD2) was subjected to these cold conditions to validate how the gas generator model performs under extremely low temperatures, with a configuration of 1 initiator and 2 initiators. The graph below shows the gas generator pressure from three experimental tests (GG-1 to GG-3, including one with only one initiator) and the simulation results (GG-Sim and GG-Sim-1init).

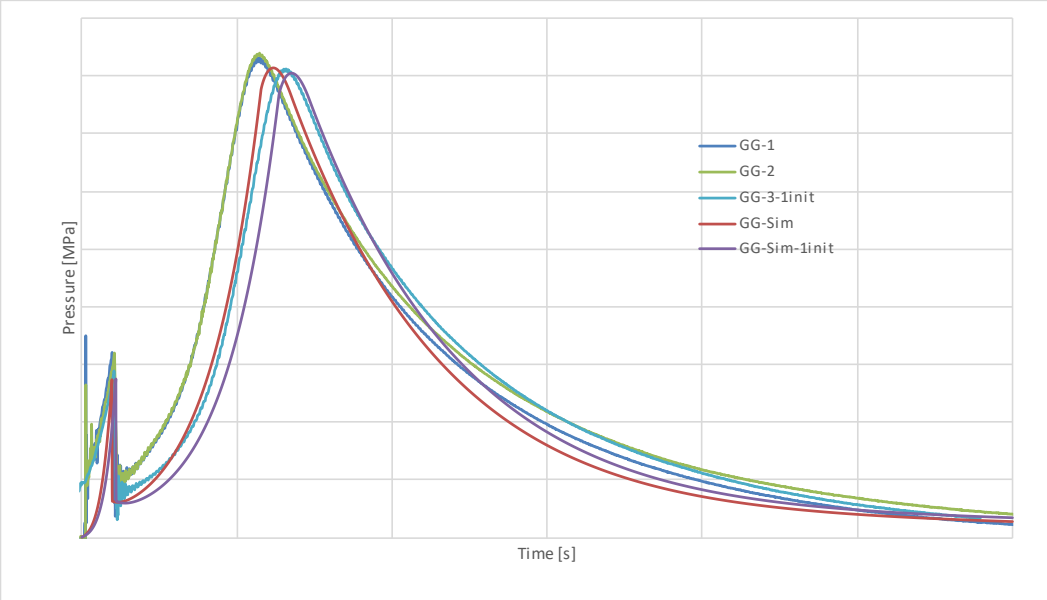

Figure 80: Setup B (DevM PDD2) Gas Generator Pressure at low temperature

The gas generator peak pressures in the experimental tests showed some variation, with the highest peak observed in GG-2 and the lowest in GG-3-1init. The simulations predicted peak pressures that closely align with these experimental values, with minimal differences. The model accurately captures both the overall trend and peak pressure behaviour, reflecting the slower combustion and delayed pressure rise in the cold environment. This effect is particularly noticeable in the one-initiator configuration, where the reduced initiator count further lowers the peak pressure.

The graph below shows the tank pressure from the three experimental tests (PL-1 to PL-3, with one using a single initiator) and the simulation results (PL-Sim and PL-Sim-1init).

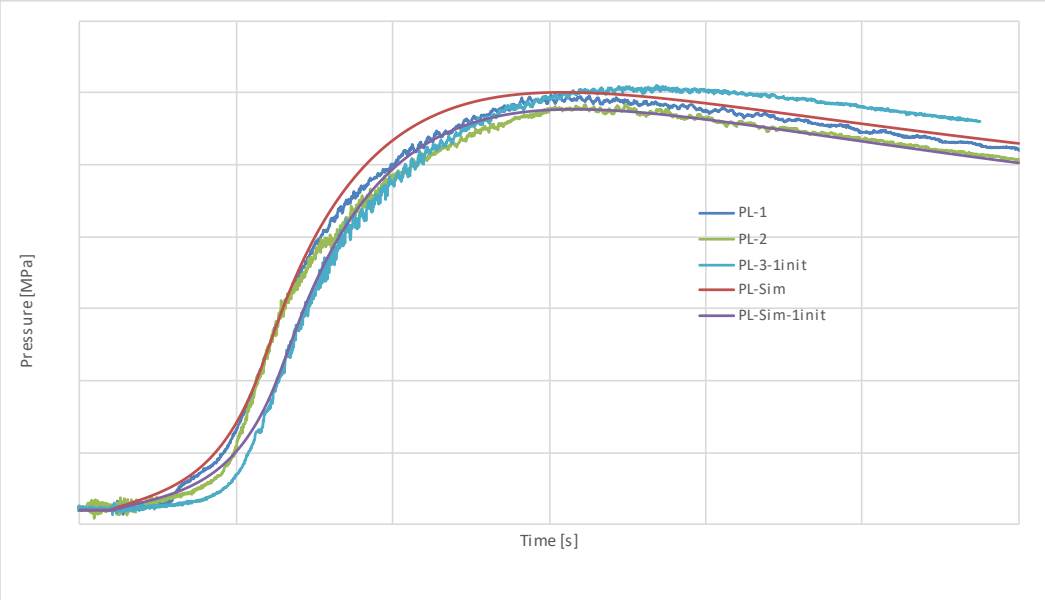

Figure 81: Setup B (DevM PDD2) Tank Pressure at low temperature

The plenum pressure experimental results showed slight variations between tests, with the highest and lowest peaks falling within a narrow range. The simulation closely aligns with the experimental values, with the highest accuracy for the two-initiator configuration showing a percent difference of 1.66%. The model effectively captures the overall pressure behaviour, including the slightly lower peak in the one-initiator configuration. The observed variability in experimental values remains within expected limits, reflecting inherent system uncertainties even under identical test conditions.

The cold test confirmed the model's ability to simulate slower combustion and lower pressure generation under extremely low temperatures. Both the gas generator and tank pressure results from the simulation closely matched the experimental data, validating the model's performance at low temperatures with this setup.

4.2.1.4 Setup B Qualifying Tests

4.2.1.4.1 Setup B (QM PDD1)

The Setup B (QM PDD1) used a small tank and a reduced propellant charge. The validation of the gas generator model was carried out by comparing the model's predictions against experimental results across various temperature conditions: ambient, hot, and cold. This allowed us to assess the accuracy and robustness of the model under different environmental scenarios. The following sections cover the results and analysis of each test condition, comparing the gas generator and tank pressure data between the experimental and simulated results.

Ambient Temperature Test

The gas generator pressure graph (Figure 82) presents three experimental tests (GG-1, GG-2, GG-3) compared to the simulated output (GG-Sim).

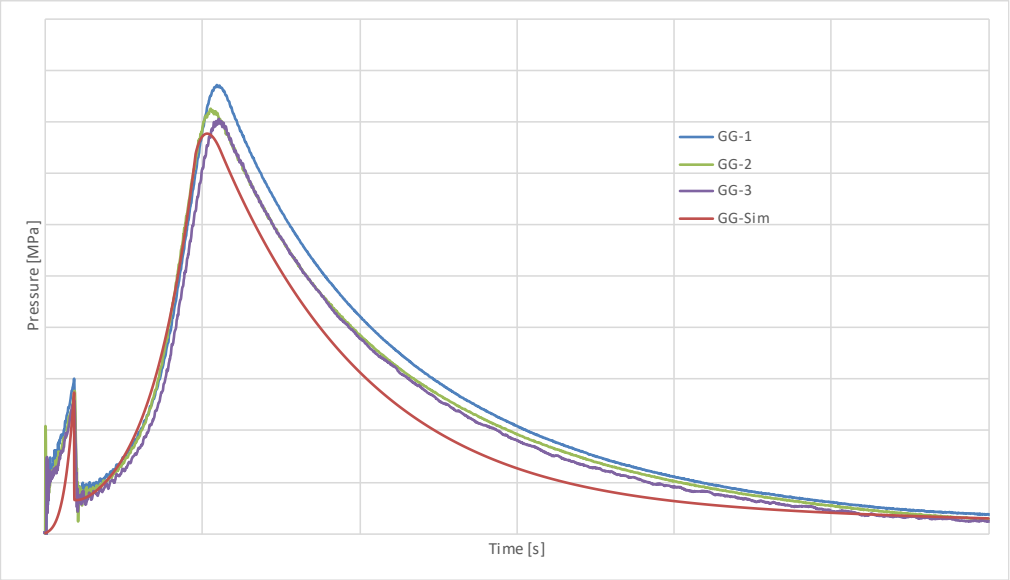

Figure 82: Setup B (QM PDD1) Gas Generator Pressure at ambient temperature

The experimental tests for gas generator pressure showed a peak variation of approximately 8% between the highest and lowest values, highlighting the natural variability in the combustion process. The simulation predicted a peak pressure that was between 5.1% and 10.8% lower than the experimental results. Despite this underestimation, the model accurately captures the overall trend, particularly the pressure rise and decay phases. The consistency in the decay phase indicates that the simulation effectively represents the key gas generator dynamics, though it slightly underestimates combustion intensity, leading to lower peak pressures.

For the plenum pressure, the experimental tests showed a variation of around 13% between the highest and lowest peak values. The simulation predicted a peak pressure that closely matched the experimental results, with the smallest difference being approximately 3%. This close alignment confirms the accuracy of the model in capturing the tank pressure dynamics. Additionally, the simulation effectively represents the pressure rise and decay phases, demonstrating its reliability in predicting the system's behaviour.

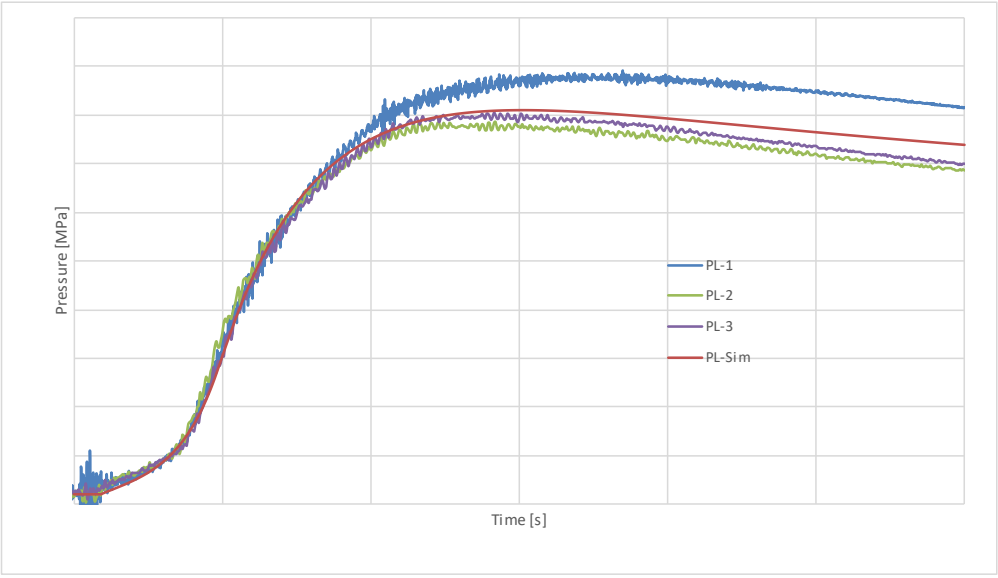

Figure 83: Setup B (QM PDD1) Tank Pressure at ambient temperature

Overall, while the simulation underpredicts the peak gas generator pressures, it provides a close match for the plenum pressure. The trends are well-captured in both cases, validating the model's effectiveness in simulating the pressure dynamics of the Setup B (QM PDD1) at ambient temperature. Minor calibration adjustments could improve the accuracy of peak pressure predictions, but the overall behaviour of the system is accurately reflected.

Hot Temperature Test

For the hot tests in the Setup B (QM PDD1), the results for the gas generator pressure and tank pressure are shown in the following two graphs.

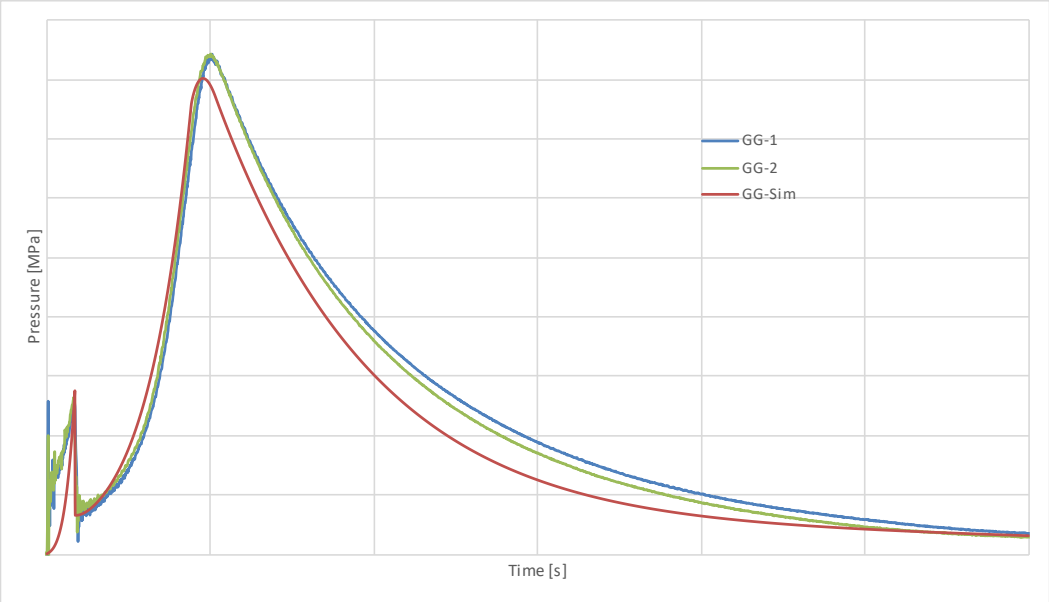

Figure 84: Setup B (QM PDD1) Gas Generator Pressure at high

In the gas generator pressure graph, the experimental peak pressures show a close match between tests, while the simulation predicts a slightly lower peak, with the closest difference being 4.97%. The simulation curve rises to the peak more quickly and exhibits a slightly faster decay. Despite this, the overall decay trend aligns well with the experimental results, indicating that the model captures the main combustion behaviour but slightly underestimates the peak pressure, possibly due to variations in the combustion rate at elevated temperatures or heat exchange effects.

The tank pressure graph below on Figure 85 shows a similar alignment between the experimental tests and the simulated curve.

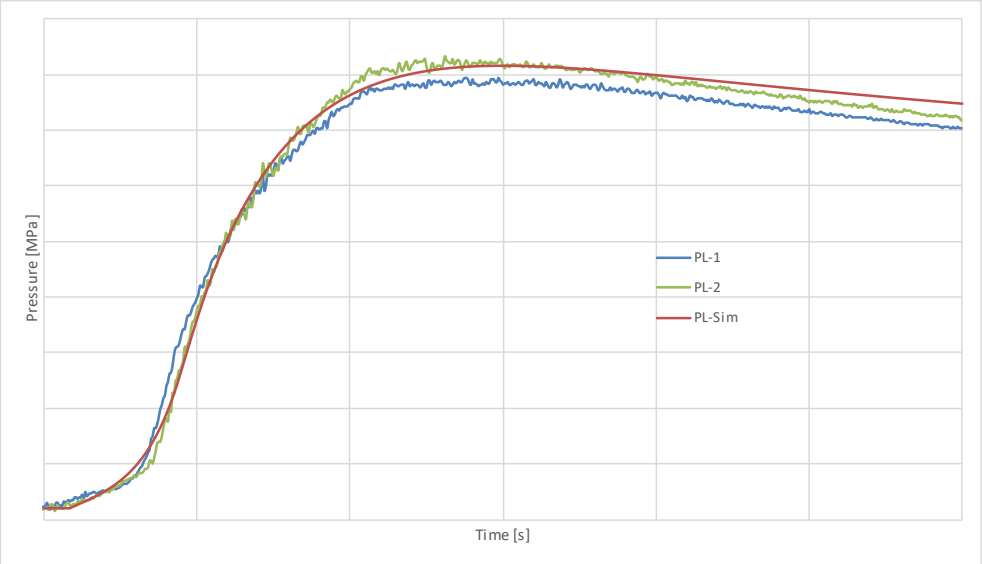

Figure 85: Setup B (QM PDD1) Tank Pressure at high temperature

For the plenum pressure, PL-1 and PL-2 reach peak values with a difference of 2.73% and 1.94% compared to PL-Sim, respectively. The simulation closely follows the experimental pressure rise, capturing the early-stage behaviour with minimal deviations. In the later stages, PL-Sim aligns very accurately with the experimental data, with only a minor difference in pressure decay.

The overall alignment between the experimental and simulated results confirms that the model provides a reliable representation of the physical process in both the gas generator and tank at elevated temperatures. Any small discrepancies are within acceptable limits and suggest that the model can be trusted to predict performance under these test conditions.

Cold Temperature Test

For the cold tests, we used the small tank with a reduced propellant charge, testing with both one and two initiators. The results show how the system behaves under low-temperature conditions.

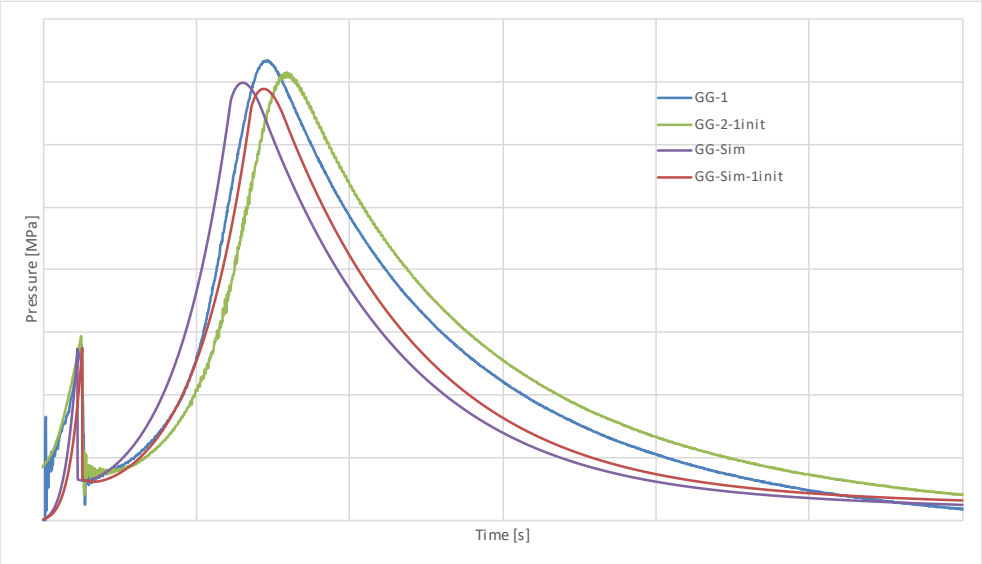

Figure 86: Setup B (QM PDD1) Gas Generator Pressure at low temperature

For the gas generator, the two-initiator test (GG-1) and the single-initiator test (GG-2-1init) showed a

small variation in peak pressure. The simulations (GG-Sim and GG-Sim-1init) followed the experimental trends well, with the single-initiator case achieving the closest match, showing only a slight difference in peak pressure. The two-initiator simulation slightly underestimated the experimental peak but still captured the overall pressure rise and decay behaviour accurately. The single-initiator case clearly demonstrated the expected delay in pressure rise, further validating the model's accuracy in representing different initiator configurations.

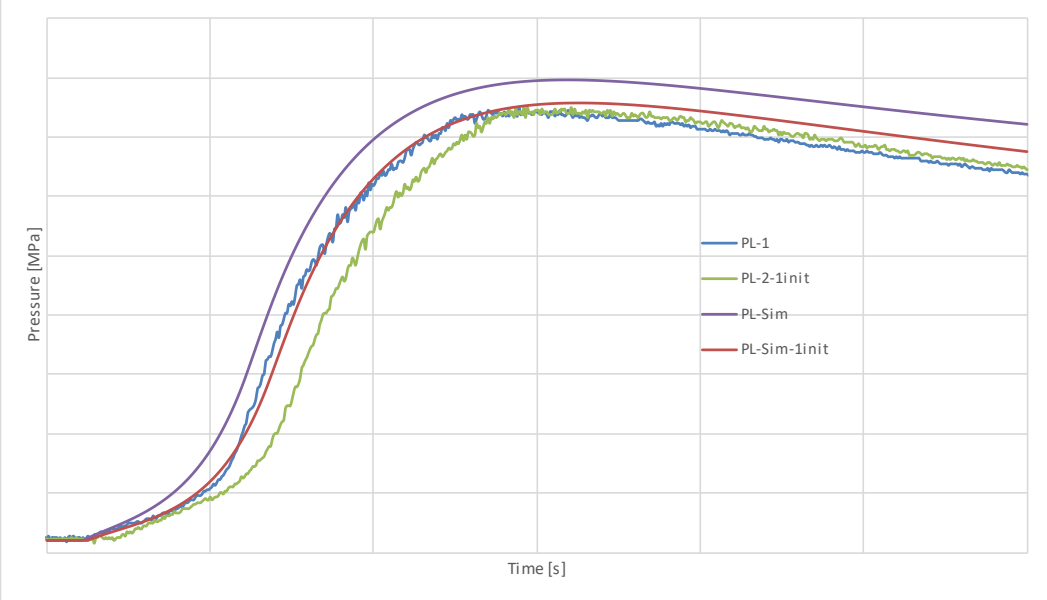

Figure 87: Setup B (QM PDD1) Tank Pressure at low temperature

In terms of tank pressure, the experimental results for both the two-initiator (PL-1) and single-initiator (PL-2-1init) tests exhibited nearly identical peak pressures, which contrasts with the expected difference observed in the simulation. The two-initiator simulation (PL-Sim) slightly overestimated the peak pressure, while the single-initiator simulation (PL-Sim-1init) closely followed the experimental trend. Although both simulations accurately captured the overall pressure profiles and behaviour, the unexpected similarity between PL-1 and PL-2-1init in the experimental data introduces uncertainty, preventing a full validation of the model.

4.2.1.4.2 Setup B (QM PDD2)

The Setup B (QM PDD2) is used as part of the validation process for the propellant combustion and gas generator model. This setup consists of a larger tank and a medium propellant charge. The test conditions include hot and cold tests with one and two initiators.

Hot Temperature Test

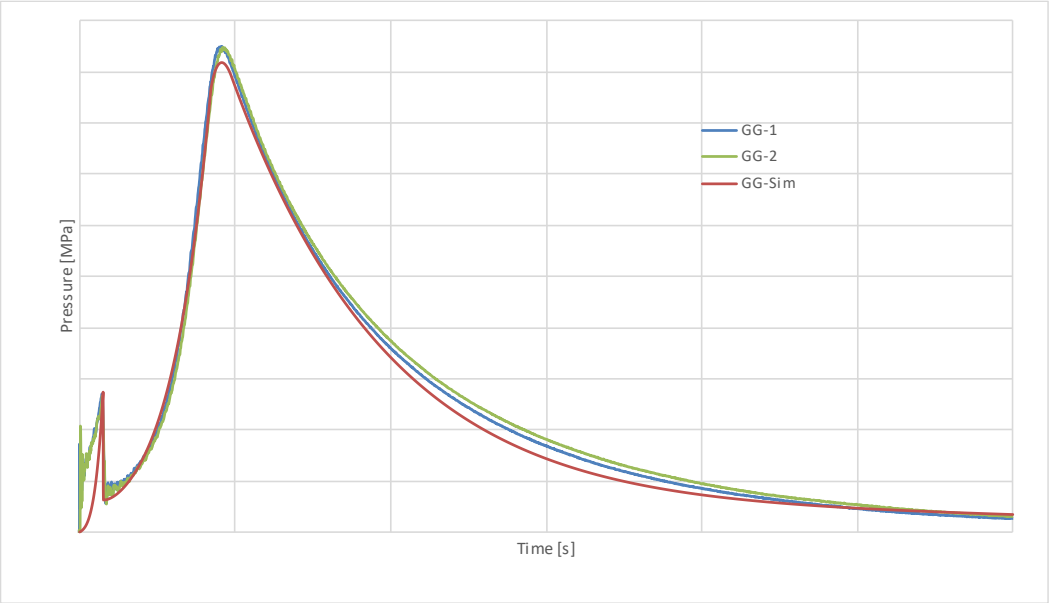

Figure 88: Setup B (QM PDD2) Gas Generator Pressure at high temperature

In the hot test, the experimental data shows a peak for GG-1 and GG-2, with a slight difference between them. The simulation (GG-Sim) follows the same trend but peaks slightly lower. The difference between the simulation and experimental results for both GG-1 and GG-2 is minimal, with percentage differences of 3.39% for GG-1 and 3.14% for GG-2. While there is a small underprediction of the peak pressure, the simulation closely aligns with the experimental results during the pressure decay phase. This indicates that the model is slightly conservative, but overall, it effectively captures the gas generator's behaviour at elevated temperatures.

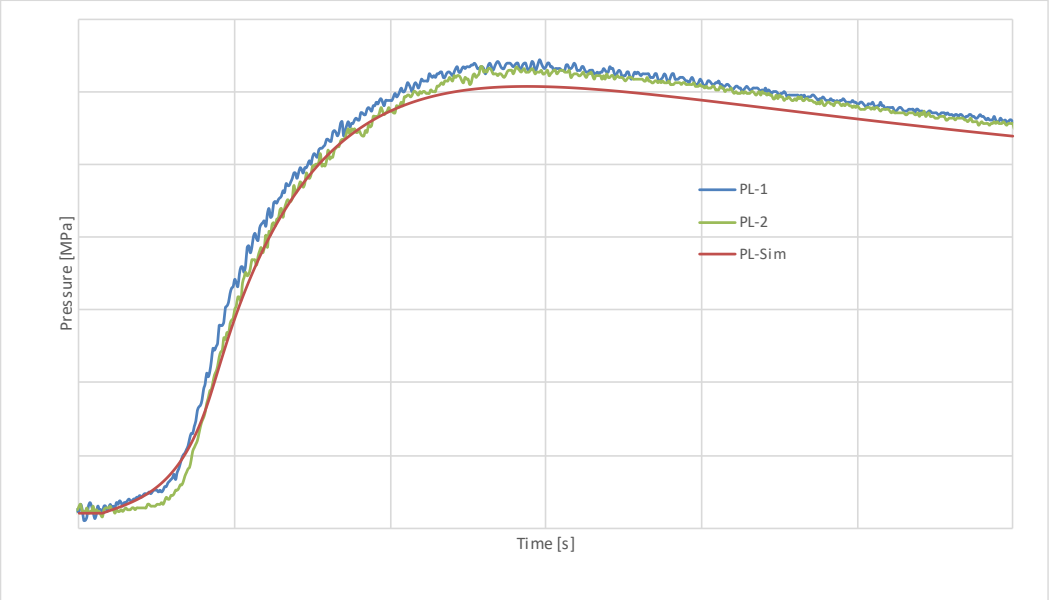

Figure 89: Setup B (QM PDD2) Tank Pressure at high temperature

For the tank pressure, the experimental data from PL-1 and PL-2 shows similar peak values. The simulated tank pressure (PL-Sim) peaks slightly lower, with a 5.75% difference for PL-1 and a 4.18% difference for PL-2. Despite these minor differences, the pressure curves for both experimental and

simulated data show strong agreement during the pressurization and decay phases. The simulation follows the same pattern as the experimental data, with a slight underprediction in peak values, reflecting a conservative estimate. Overall, the simulation accurately captures the tank pressure behaviour under hot test conditions.

Cold Temperature Test

For the gas generator pressure, GG-1 (with two initiators) peaks higher compared to GG-2-1init (with one initiator). The simulation (GG-Sim) follows the two-initiator results closely but shows a deviation in the one-initiator configuration (GG-Sim-1init), where it peaks at a lower value, indicating an anomaly in the simulation for that case. The experimental results demonstrate a more significant energy release with the two-initiator configuration, aligning with expectations, but the simulation struggles to replicate the behaviour of the one-initiator case accurately.

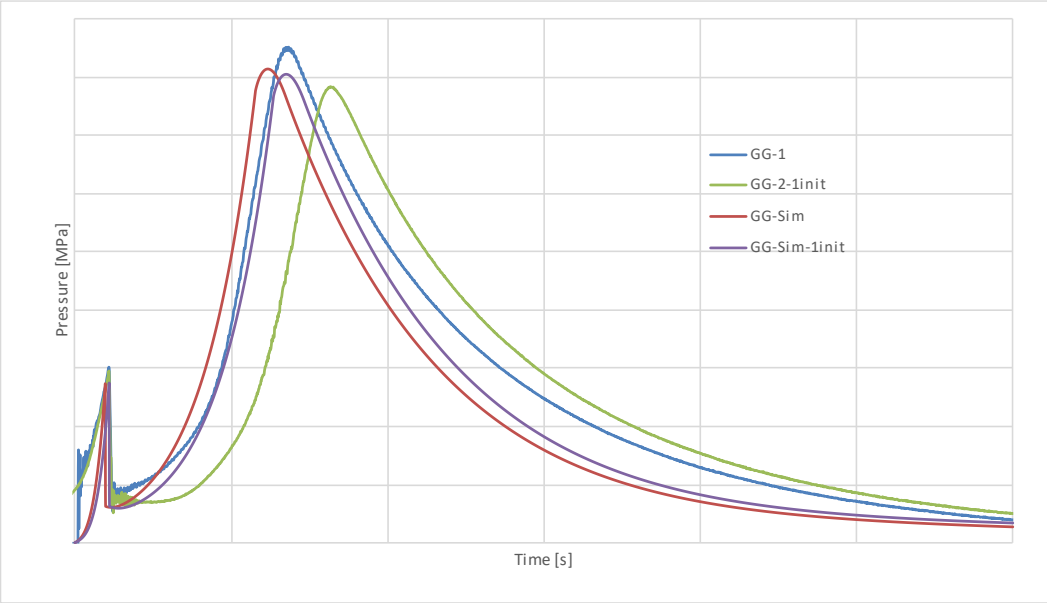

Figure 90: Setup B (QM PDD2) Gas Generator Pressure at low temperature

For the tank pressure, PL-1 (two initiators) and PL-2-1init (single initiator) show similar peak pressures, with PL-1 slightly higher than PL-2-1init. The simulation results (PL-Sim and PL-Sim-1init) follow the same trend, with minor deviations in peak pressures. These results demonstrate that the simulation accurately models the experimental behaviour, with both experimental and simulated pressure profiles closely matching each other. The model effectively captures the key dynamics of the system under cold test conditions, highlighting its reliability in replicating the pressure rise and decay patterns.

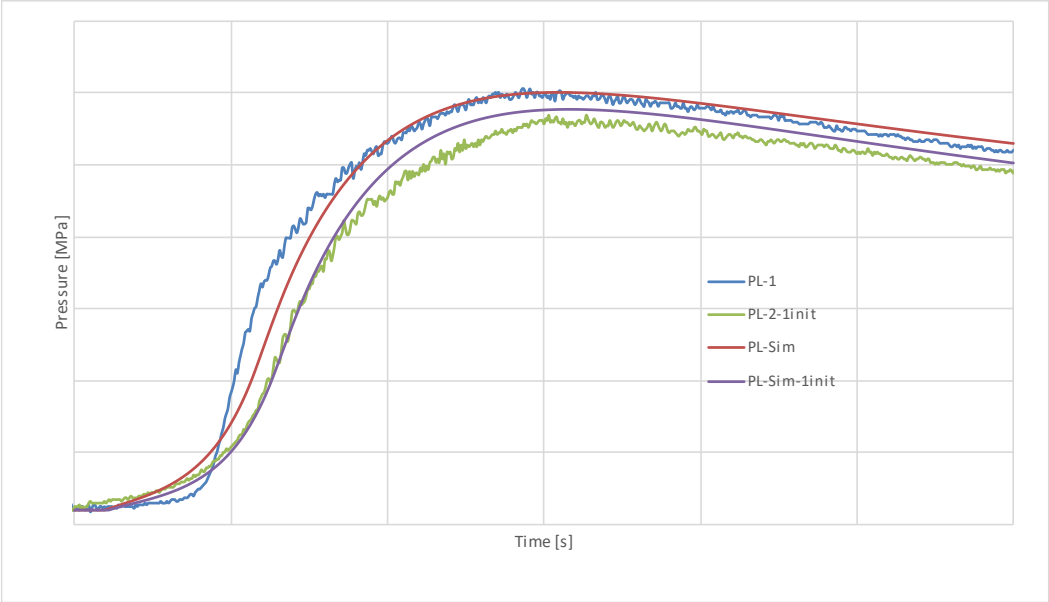

Figure 91: Setup B (QM PDD2) Tank Pressure at low temperature

The cold test results for the Setup B (QM PDD2) demonstrate a good correlation between experimental and simulated data for both the gas generator and tank pressures. The model successfully captures the pressure trends, particularly for the two-initiator setup, with minor deviations observed in the one-initiator case. Overall, the model provides reliable predictions of the system's behaviour under cold test conditions, validating its accuracy for further analyses.

4.2.1.5 Setup A Tests

For the Setup A tests, the setup involved a normal tank volume and a higher propellant charge. The tests were carried out under two different conditions: in a hot environment, and in a cold environment. These conditions provide a comprehensive validation across a range of operational environments to compare experimental data with model predictions.

Hot Temperature Test

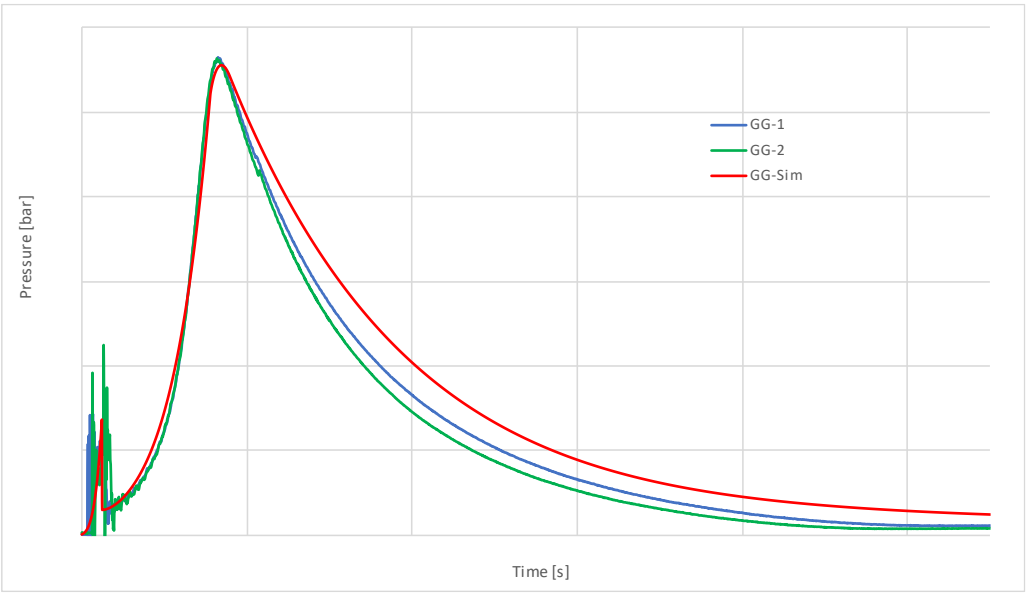

Figure 92: Setup A Gas Generator Pressure at high temperature

For the gas generator pressure, as shown in Figure 92, GG-1 and GG-2 peak at similar values, with the simulation (GG-Sim) showing a slight underestimation. The percentage differences between the experimental data and the simulation are minimal, with only a 1.67% difference for GG-1 and a 1.45% difference for GG-2. Despite these small variations, the overall agreement between the experimental data and the simulation is excellent, indicating that the model accurately captures the gas generator pressure dynamics.

The second graph shows the tank pressure behaviour, where PL1 and PL2 exhibit slight differences in peak pressures. The simulation (PL-Sim) closely aligns with both experimental data sets, with a 1.4% difference between PL-1 and PL-Sim and a 1.6% difference between PL-2 and PL-Sim. The simulation curve accurately follows the experimental trends, with minor deviations observed in the peak pressures. This indicates that the model is effective in capturing the dynamics of the tank pressurization, demonstrating reliable performance under hot test conditions.

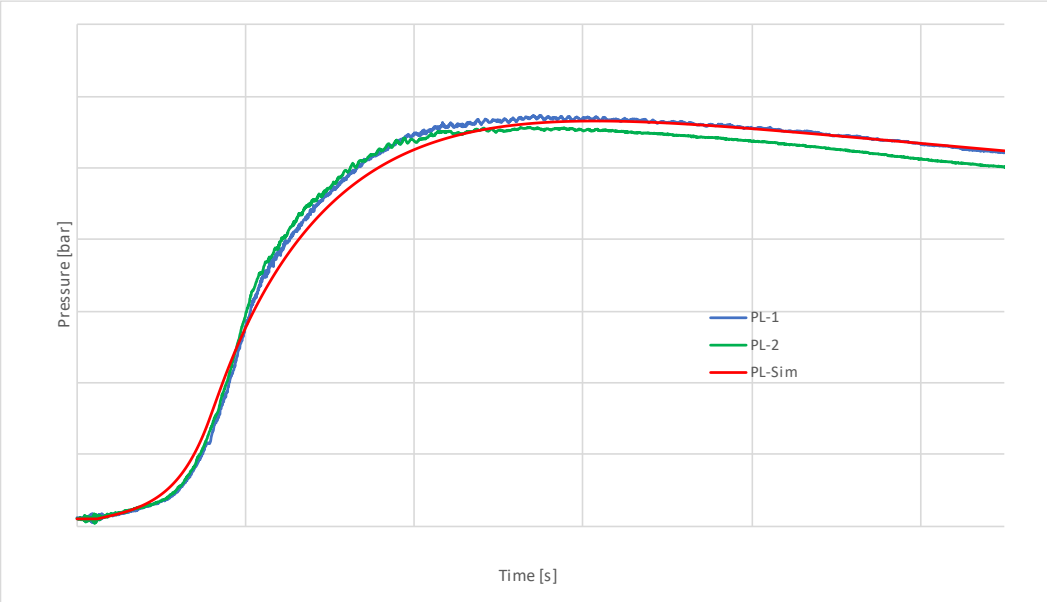

Figure 93: Setup A Tank Pressure at high temperature

In summary, the model shows a strong correlation with the experimental data for both the gas generator and tank pressure in the hot test.

Cold Temperature Test

For the gas generator pressure, the peak values are observed in the graph. GG1 reaches a peak, while GG-2-1init peaks slightly lower, both representing the experimental data. The simulated data, GG-Sim, peaks slightly lower than GG1 but is consistent with the overall trend. GG-Sim-1init peaks closer to the experimental values. The decay trends are similar between the experimental and simulated data, with the simulated curves showing a smoother decline compared to the experimental data. The model captures the general pressure behaviour well, though slight differences in the decay phase are present.

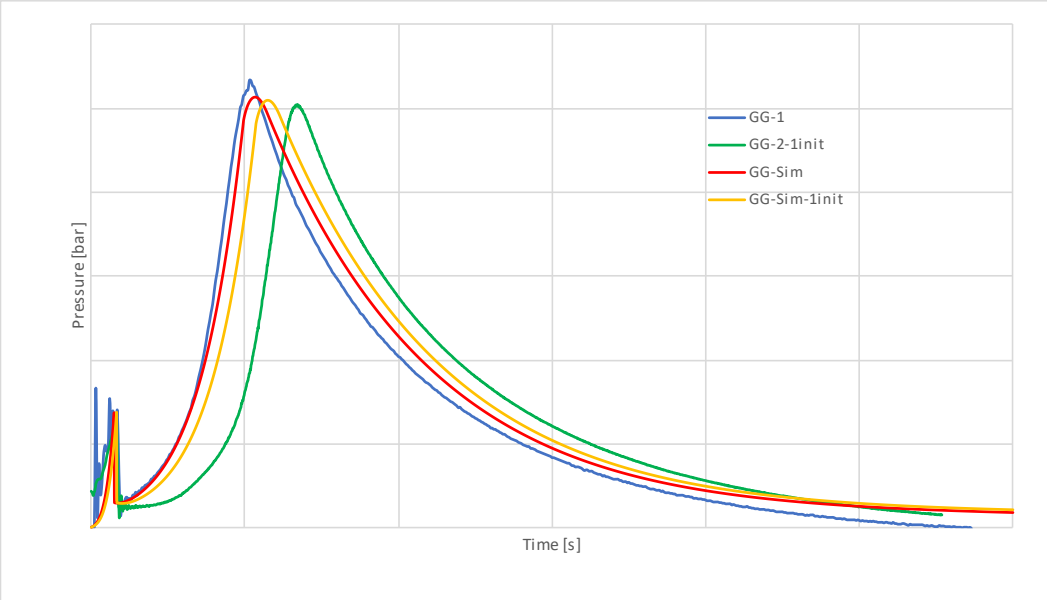

Figure 94: Setup A Generator Pressure at low temperature

For the tank pressure, PL1 and PL-2-1init represent the experimental tests, with PL1 slightly higher than PL-2-1init. The simulation results, PL-Sim and PL-Sim-1init, show slightly higher peak pressures than the experimental data. However, the overall trends in the tank pressure graph are consistent between the experimental and simulated results, with similar curves during the pressure rise and decay phases. The minor deviation in peak values reflects the simulation's conservative prediction, but the model effectively captures the general pressure behaviour and dynamics of the system.

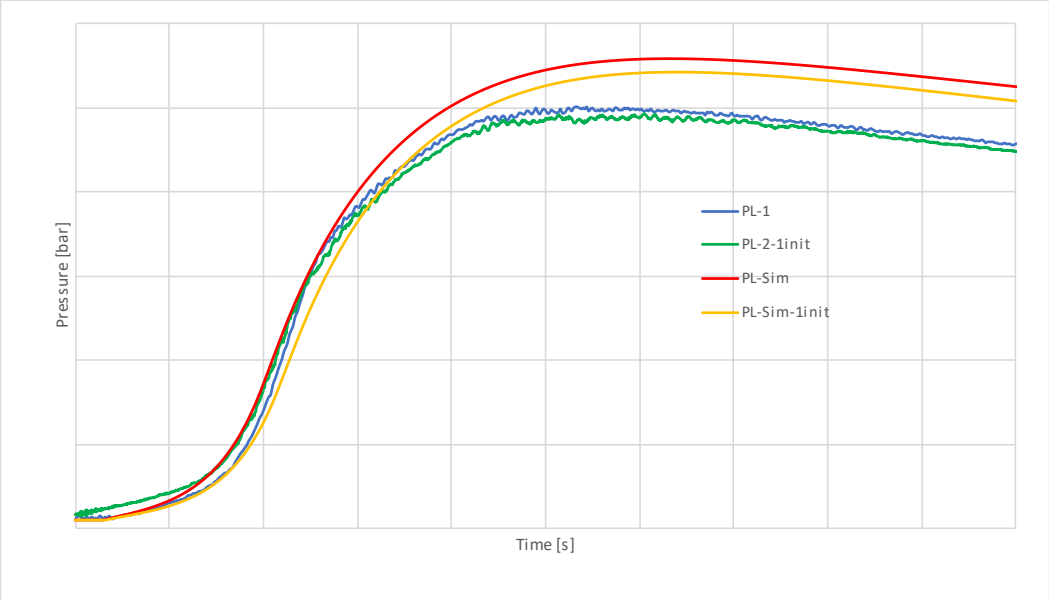

Figure 95: Setup A Tank Pressure at low temperature

The comparison shows a good correlation between the experimental and simulation data, with the simulations capturing the key features of the cold test performance, validating the model's capability to reproduce both gas generator and tank pressure behaviours.

4.2.2 Ejection & Deployment Test Validation

4.2.2.1 Deployment Test Validation (Temperature: ambient, Propellant Load: medium)

Gas Generator Pressure Analysis

In the deployment test, the experimental gas generator peak pressure was slightly higher than the simulated result, with a percent difference of 2.67%. As shown in Figure 96, the simulated pressure profile closely follows the experimental data, with the peak pressure occurring at nearly the same time.

Although the simulated peak pressure slightly underestimates the experimental value, the general shape and behaviour of the pressure profile are well captured. The minor differences can be attributed to idealized assumptions in the model regarding gas expansion dynamics, but overall, the model demonstrates strong accuracy in predicting gas generator behaviour.

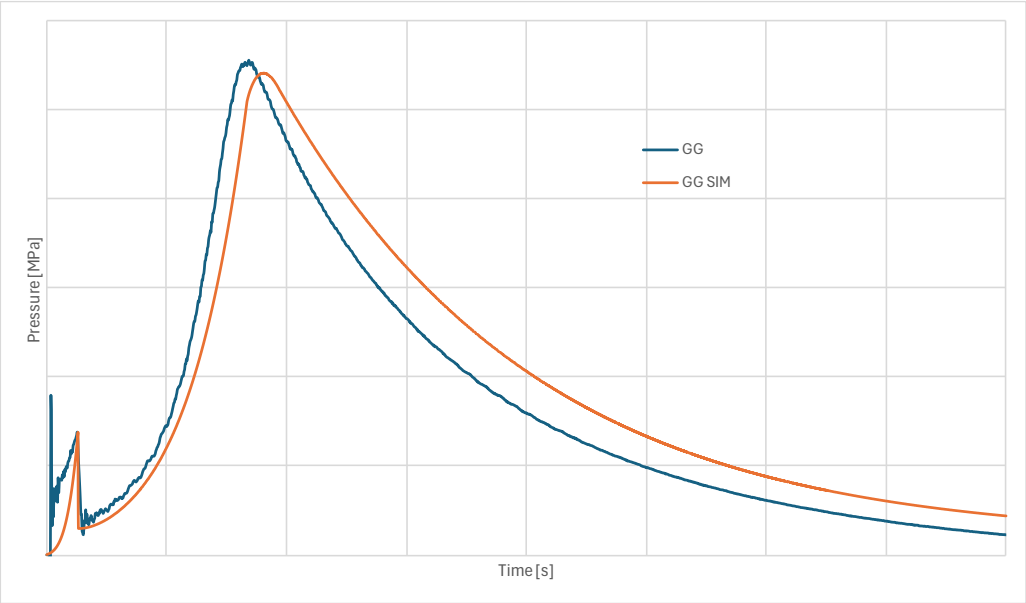

Figure 96: Setup A Deployment Test - Gas Generator Pressure at ambient temperature

Plenum Pressure Analysis

The comparison between the experimental and simulated plenum pressure for this test, shown in Figure 97 , reveals a slight discrepancy. The experimental data, representing both Plenum 1 and Plenum 2, shows a peak pressure slightly higher than the simulation (PL-Sim), resulting in a percent difference of 6.72%. Despite this difference, the overall pressure profile and trends in the simulation closely match the experimental data, reflecting the model's ability to capture the dynamics, though with a slight underprediction in the peak pressure.

As with the previous test, significant noise is present in the experimental data, especially around the peak pressure. This noise, likely due to sensor inaccuracies, which explain part of the discrepancy between the experimental and simulated peak pressures.

Despite the noise, the overall profile of the pressure rise, and decay phases is well captured by the simulation. The difference in peak pressure can reasonably be attributed to the noise in the experimental data and the simplifications inherent in the simulation model. However, the model provides a good approximation of the plenum pressure behaviour, and the differences remain within acceptable bounds for validation purposes.

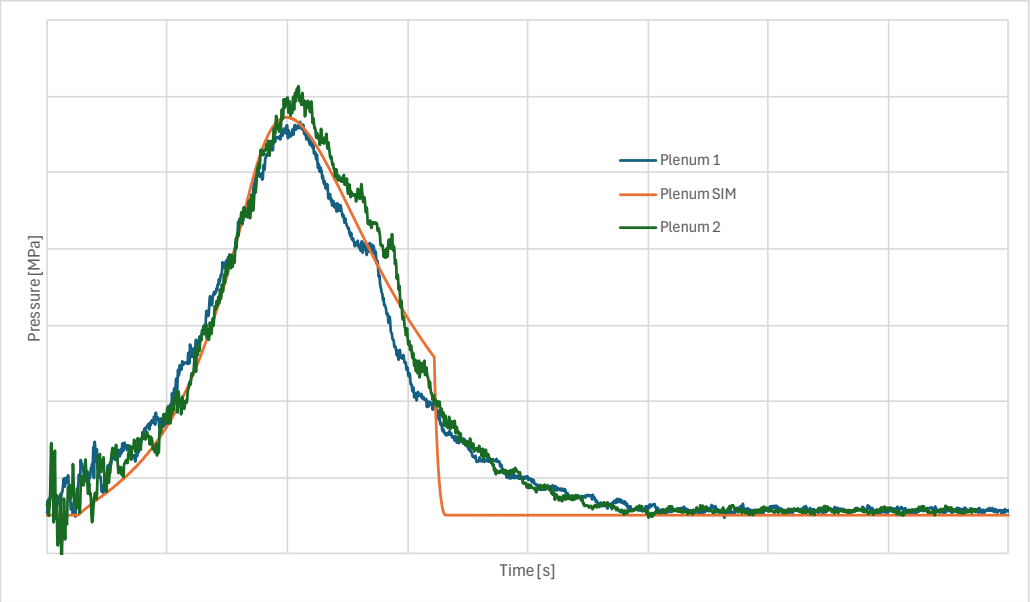

Figure 97: Setup A Deployment Test - Plenum Pressure at ambient temperature

Reaction Force Analysis

The maximum reaction force recorded during the experiment and the simulated force showed a percent difference of 16.65%. This discrepancy, shown in Figure 98, reflects an underestimation of the peak force by the model.

The general trend of the force profile is well captured by the simulation, but as with the first test, the model struggles to accurately capture the sharp peaks observed in the experimental data. These discrepancies may arise from assumptions in the mechanical modelling, such as idealized material properties or energy transfer dynamics. Further refinement of the force model could reduce the error and improve alignment with experimental data.

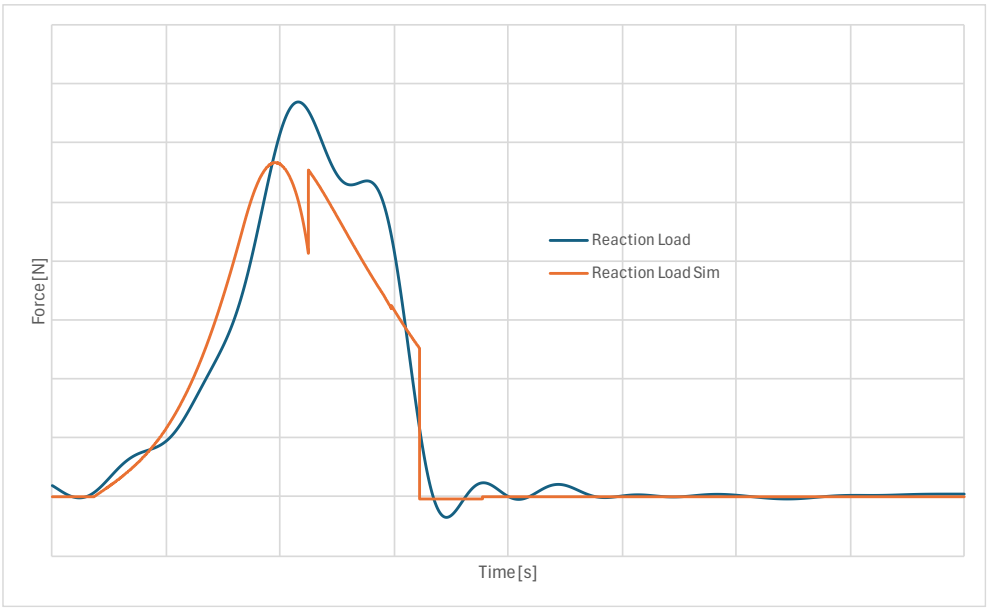

Figure 98: Setup A Deployment Test - Filtered Reaction Force at ambient temperature

Compressibility and Ejection Velocity Analysis

For this test, the percent difference in compressibility was 5.55%, indicating reasonable agreement between the experimental and simulated data. The slight difference is likely due to simplifications in the model's material properties. Similarly, the percent difference in ejection velocity was 1.5%, suggesting that the model is highly accurate in predicting the ejection dynamics, with only minor variations from the experimental results.

The combined results for compressibility and velocity indicate that the model effectively simulates the mechanical behaviour of the parachute system, with differences within acceptable limits.

Parameter	*Percent Difference*
GG Peak Pressure	2.67%
Plenum Peak Pressure	6.72%
Maximum Reaction Force	16.65%
Compressibility	5.55%
Ejection Velocity	1.5%

Table 16: Setup A Deployment Test - Key Parameters at ambient temperature

Conclusion

The second deployment test demonstrates that the model provides reasonably accurate predictions across key parameters, with particularly good performance in predicting gas generator pressure, compressibility, and ejection velocity. The plenum peak pressure was slightly underestimated, and the maximum reaction force showed a more significant deviation from the experimental data, similar to the first test.

While the overall model performance is satisfactory, improvements could be made to better capture the reaction force dynamics, possibly through more detailed mechanical modelling. Nonetheless, the model remains a valid tool for simulating parachute deployment behaviour under the tested conditions.

4.2.2.2 Ejection Test Validation (Temperature: ambient, Propellant Load: higher)

Gas Generator Peak Pressure Analysis

In the ejection test, the percent difference between the experimental and simulated gas generator peak pressure was 0.84%, showing excellent agreement between the two sets of data. This small discrepancy suggests that the simulation is highly accurate in predicting the peak pressure behaviour during the ejection process. Figure 99 shows the comparison between the experimental and simulated pressure profiles.

The general trend is well captured by the model, the simulation accurately estimates the peak pressure. The overall profile of the pressure decay after the peak is well aligned, indicating that the model reasonably approximates the pressure dynamics over time.

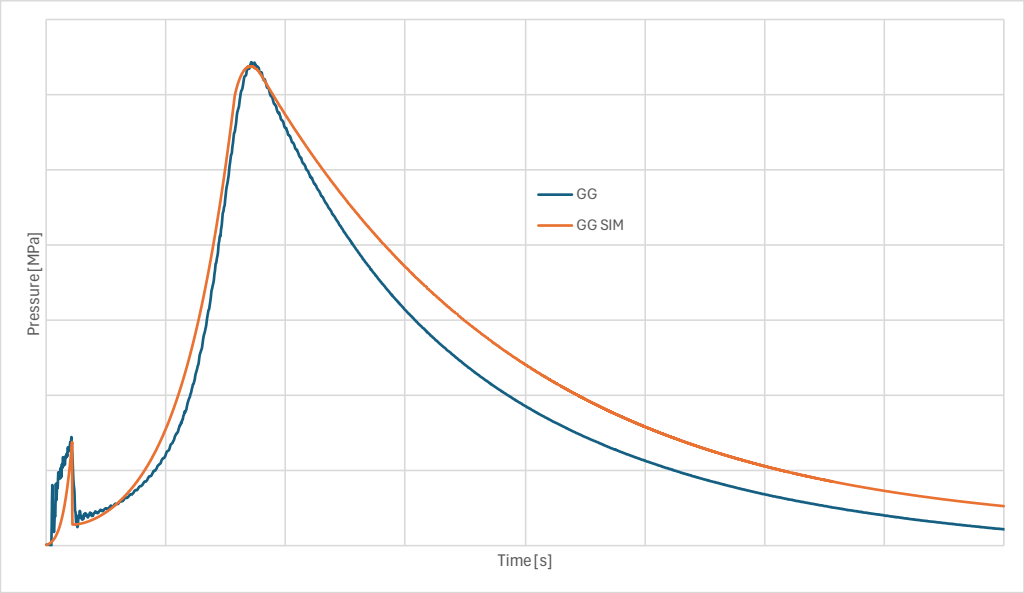

Figure 99: Setup A Ejection Test - Gas Generator Pressure at ambient temperature

Plenum Peak Pressure Analysis

The percent difference between the experimental and simulated plenum peak pressure was 1.52%. Figure 100 illustrates that, similar to the GG pressure, the simulation captures the general shape of the pressure profile with very high accuracy.

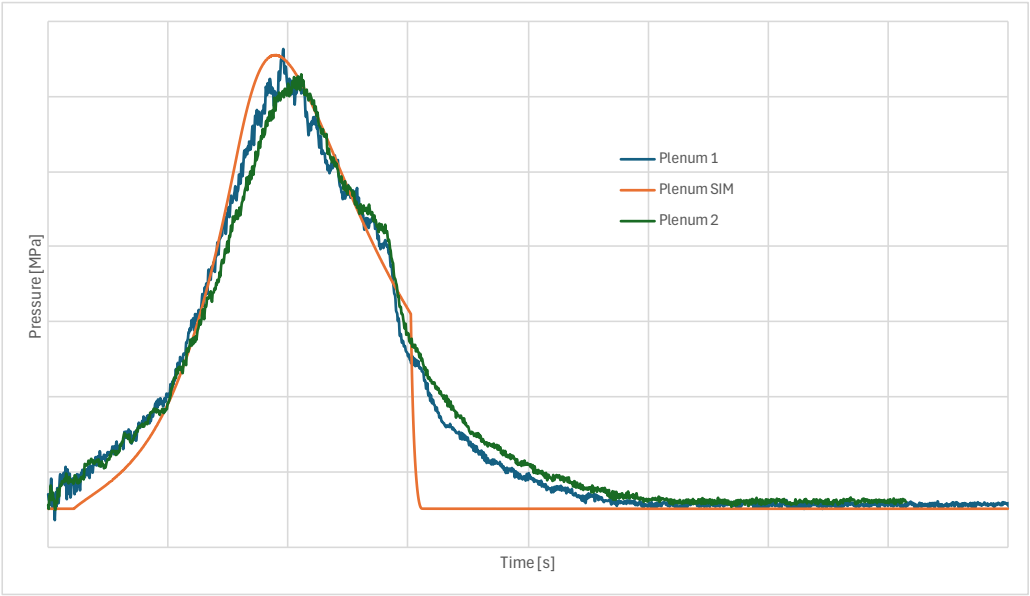

Figure 100: Setup Ejection Test - Tank Pressure at ambient temperature

Maximum Reaction Force Analysis

The percent difference between the experimental and simulated maximum reaction force was 3.26%. Figure 101 shows the comparison of the reaction force profiles.

While the overall force trend is captured, the model slightly overestimates the peak force. The deviations in peak force could result from the model's simplified treatment of mechanical interactions and the energy transfer between the gas and the parachute system. Additional modelling complexity might help

to capture these force dynamics more accurately.

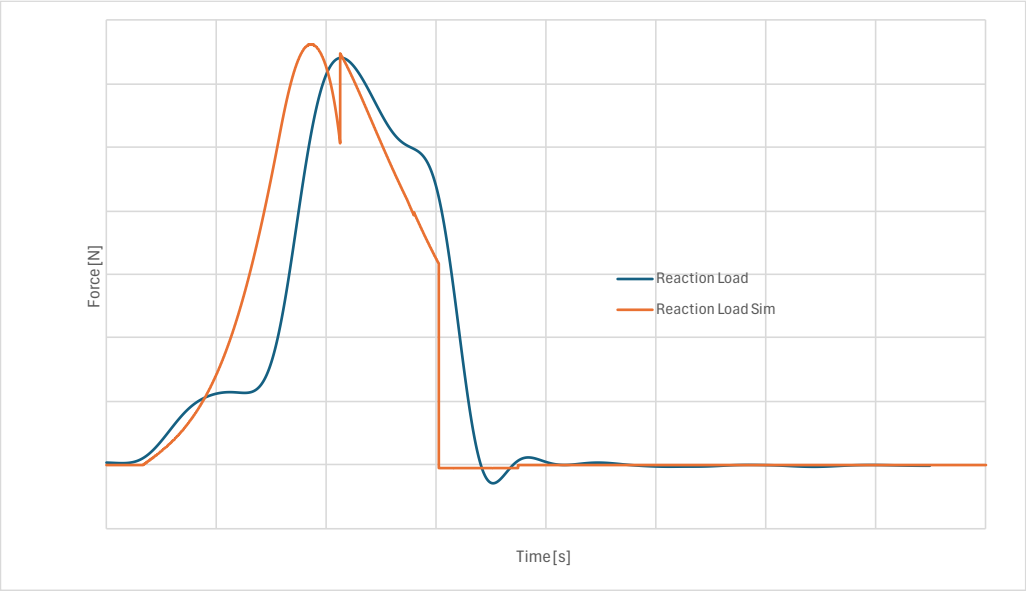

Figure 101: Setup A Ejection Test - Reaction Force at ambient temperature

Compressibility and Ejection Velocity Analysis

The percent difference in parachute pack compressibility between the experimental and simulated values was 8.03%. This slight overestimation in compressibility may stem from the model's treatment of the material properties of the parachute pack. Overall, the model reasonably approximates the compressibility value.

The percent difference in ejection velocity between the experimental and simulated values was 6.28%. This small discrepancy indicates that the model provides an accurate prediction of the ejection dynamics, with only a minor underestimation of velocity.

The combined results for compressibility and velocity show that the model performs well in simulating the parachute pack's mechanical behaviour during ejection, with differences that are acceptable for validation purposes.

Parameter	*Percent Difference*
GG Peak Pressure	0.84%
Plenum Peak Pressure	1.52%
Maximum Reaction Force	3.26%
Compressibility	8.03%
Ejection Velocity	6.28%

Figure 102: Setup A Ejection Test - Key Parameters at ambient temperature

Conclusion

In this ejection test, the model demonstrates reasonably accurate predictions for ejection velocity and compressibility, with minor discrepancies. However, the gas generator and plenum peak pressures are significantly underestimated by the model, and the reaction force also shows a moderate underestimation. These results suggest that while the model provides a good approximation of the system's overall behaviour, it could benefit from refinements in modelling gas dynamics and

mechanical interactions to improve the accuracy of peak predictions.

Despite these discrepancies, the model offers a valid approximation of the parachute deployment system's behaviour, particularly in simulating the ejection phase.

4.2.2.3 Hot Deployment Test Validation (Propellant Load: medium)

Gas Generator Pressure Analysis

In the hot test, the gas generator pressure rapidly rises and peaks, with the simulation predicting a slightly lower peak than the experimental result, resulting in a 3.66% difference. As shown in Figure 103**,** the initial pressure buildup is well captured by the simulation, but it slightly overestimates during the early phase.

The pressure decay phase is slower in the simulation compared to the experimental data, indicating potential oversimplifications in how the model accounts for heat dissipation or gas leakage at higher temperatures. Overall, the model captures the general trend well but slightly lags in decay dynamics, especially after the peak.

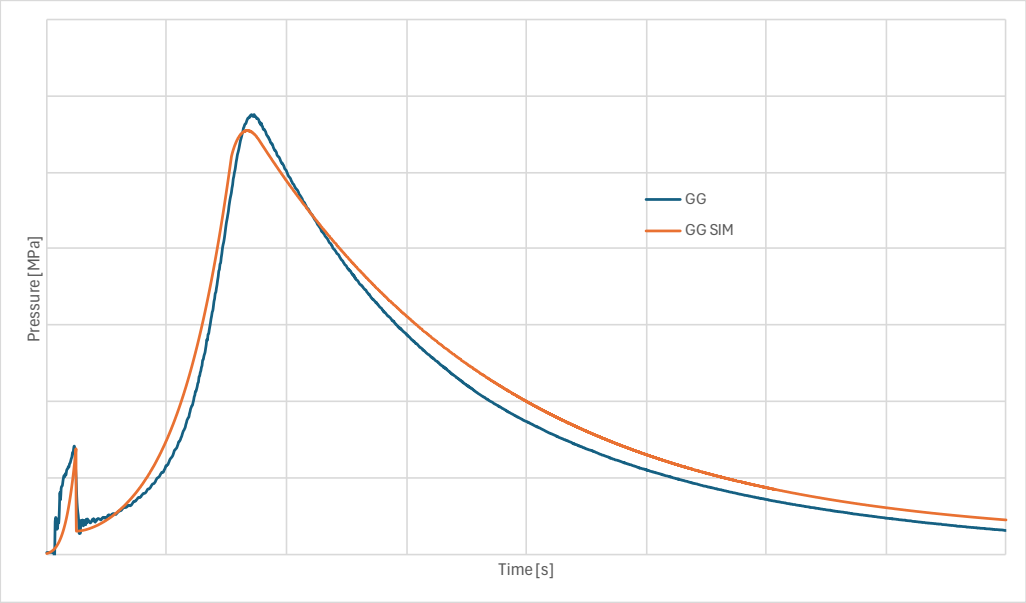

Figure 103: Setup A Deployment Test - Gas Generator Pressure at high temperature

Plenum Pressure Analysis

The plenum pressure peaked slightly lower in the simulation compared to the experimental result, with a percent difference of 2.06%. The simulation closely follows the experimental rise, though it peaks slightly earlier. The pressure decay is slower in the simulation, which indicates that the model may not fully capture gas dissipation rates at higher temperatures.

The timing differences in the rise and decay phases suggest that adjustments to the gas flow dynamics in the model, particularly under thermal influences, could improve accuracy. Still, the overall behaviour aligns reasonably well between the two.

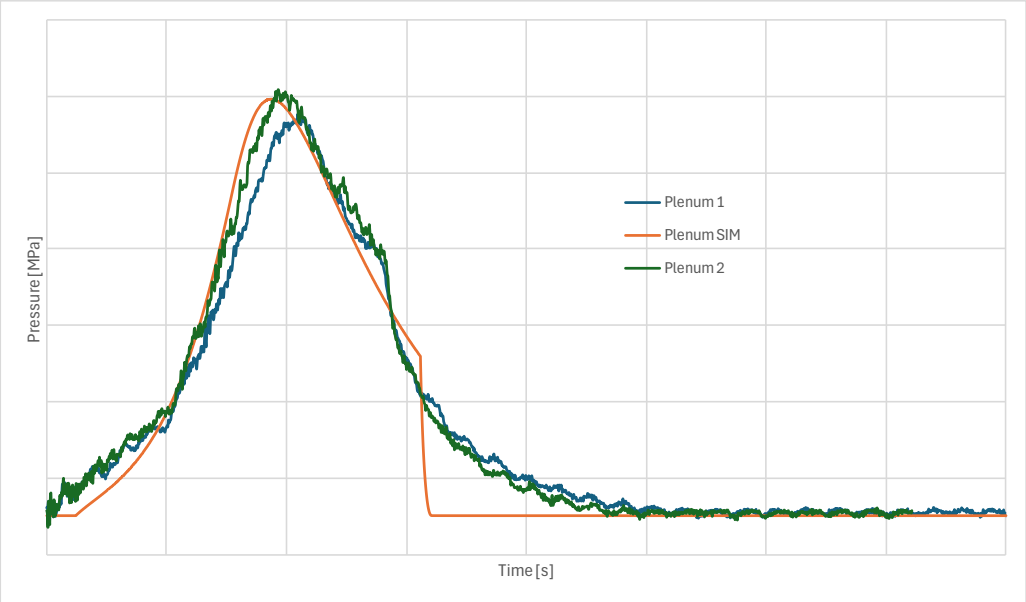

Figure 104: Setup A Deployment Test - Tank Pressure at high temperature

Reaction Force Analysis

The reaction force in the simulation was lower than the experimental peak, with a percent difference of 9.26%. Both the buildup and decay phases are well represented by the model, but the peak force is underestimated, likely due to simplified energy transfer modelling during parachute ejection.

The simulation also lacks the oscillations seen in the experimental data, indicating that the model doesn't fully capture dynamic effects like structural vibrations or aerodynamic forces. These dynamics are critical to understanding the force fluctuations, which are not well-represented in the current model.

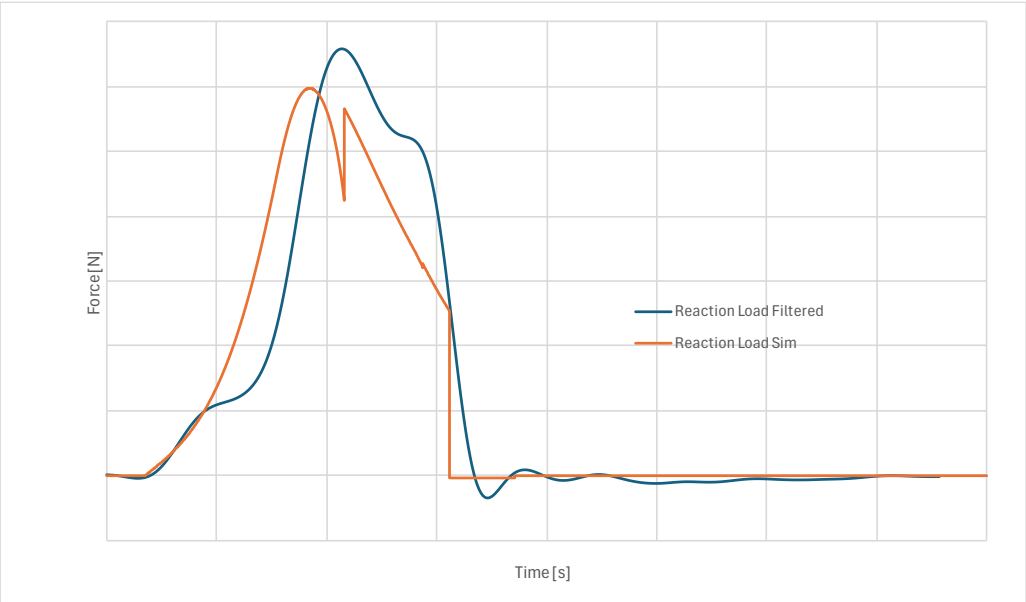

Figure 105: Setup A Deployment Test - Reaction Force at high temperature

Compressibility and Ejection Velocity Analysis

The simulation overestimated the compressibility by 8.36%, indicating a slight deviation in modelling the material properties or packing dynamics of the parachute pack. This suggests the model

overestimates the flexibility of the parachute pack, likely due to assumptions about material behaviour at higher temperatures.

The ejection velocity showed excellent agreement, with only a 0.8% difference between the experimental and simulated values. This indicates the model accurately captures the velocity dynamics during hot deployment, with only minor overestimations.

Parameter	*Percent Difference*
GG Peak Pressure	2.67%
Plenum Peak Pressure	6.72%
Maximum Reaction Force	16.65%
Compressibility	5.55%
Ejection Velocity	0.6%

Table 17: Setup A Deployment Test - Key Parameters at high temperature

Conclusion

In this hot deployment test, the model provides highly accurate predictions for most parameters, particularly for gas generator pressure, plenum pressure, and ejection velocity. The compressibility was slightly overestimated, and the reaction force was moderately underestimated, likely due to simplifications in the model related to material properties and energy transfer in hot conditions.

Overall, the model effectively simulates the parachute deployment dynamics at elevated temperatures, with small deviations that are acceptable for validation purposes. Further refinement of the mechanical and thermal modelling could improve accuracy for peak forces and compressibility, but the current model performs well for hot conditions.

This analysis includes the key observations and discrepancies from the hot deployment test. Let me know if you need further adjustments!

4.2.2.4 Cold Deployment Test Validation (Propellant Load: medium)

Gas Generator Pressure Analysis

In the cold deployment test, the gas generator pressure showed a percent difference of 3.34% between the experimental and simulated peak values. Figure 106 shows that both the experimental and simulated curves align well, particularly during the pressure rise and decay phases. Despite the cold conditions, the model accurately captures the GG pressure dynamics, with minor deviations likely attributable to environmental factors not fully captured by the simulation, such as thermal effects on the gas dynamics.

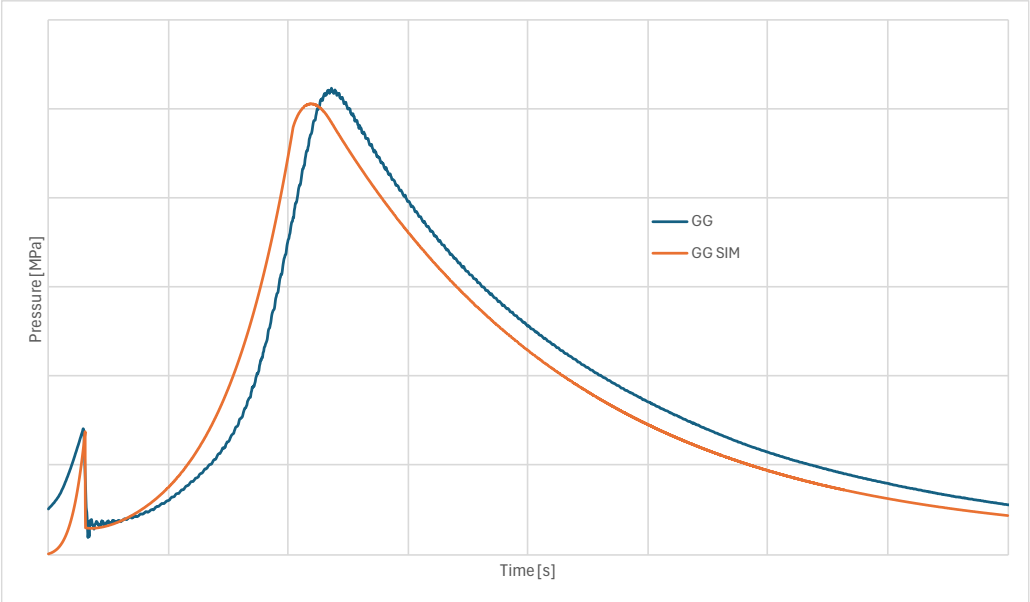

Figure 106: Setup A Deployment Test - Gas Generator Pressure at low temperature

Plenum Pressure Analysis

The plenum pressure exhibited a larger percent difference of 30.34% between the experimental and simulated peak values. This significant difference is primarily due to the effect of icing observed during the test. The icing restricted the movement of the piston and parachute pack, causing a buildup of pressure in the mortar tube that is not accounted for in the simulation model. As a result, the plenum pressure in the experimental setup exceeded the predicted values, contributing to a higher-than-expected acceleration of the parachute pack upon release.

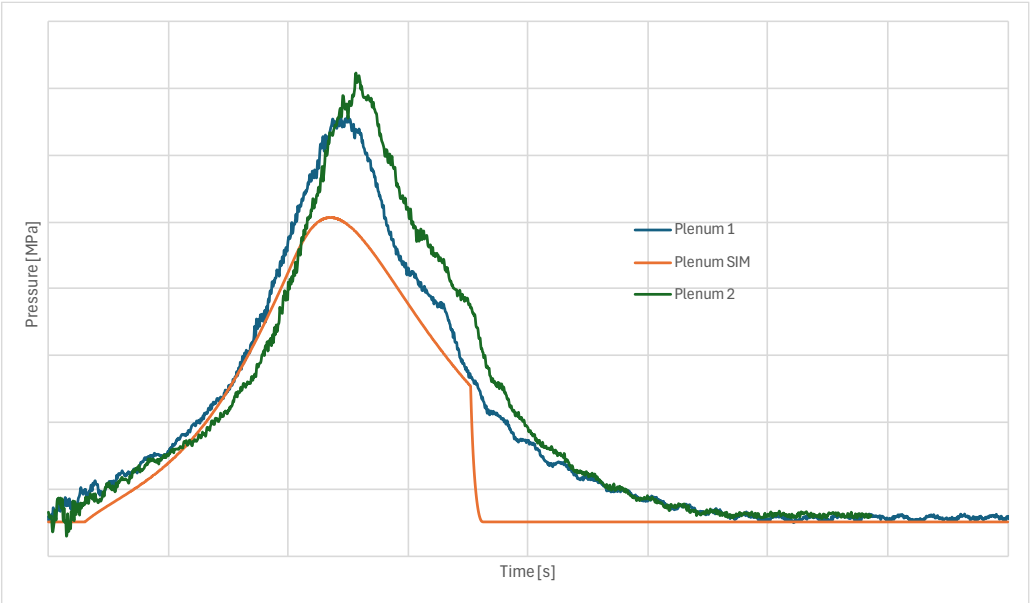

Figure 107: Setup A Deployment Test - Tank Pressure at low temperature

Reaction Force Analysis

The experimental and simulated maximum reaction loads differ by 35.57%. As with the plenum pressure, this large discrepancy is a result of the icing effect, which restricted the parachute pack's movement. The accumulated pressure led to a rapid release and higher acceleration, causing the measured reaction force to be significantly higher than the simulation predicted. The simulation curve, shown in Figure 108, underestimates the reaction force due to the idealized mechanical assumptions and the absence of the icing phenomenon in the model.

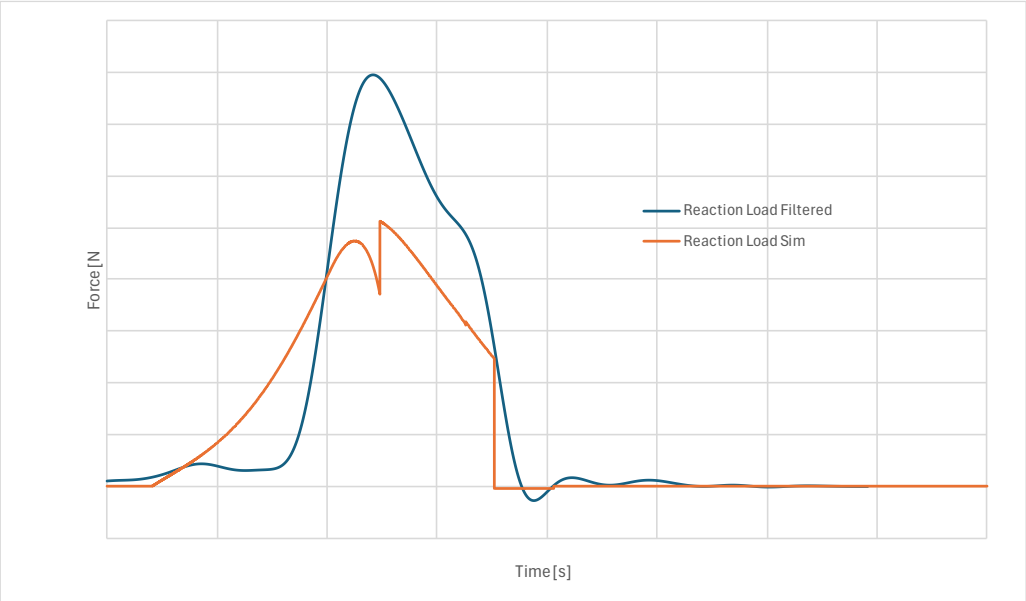

Figure 108: Setup A Deployment Test - Reaction Force at low temperature

Compressibility and Ejection Velocity Analysis

The compressibility of the parachute pack shows a significant difference of 41.34%. This discrepancy further highlights the effect of icing, which increased the resistance to compression before ejection, leading to a smaller measured compressibility.

The ejection velocity showed a notable difference of 13.19%, with the simulation underestimating the experimental value. The higher velocity observed in the experiment can be directly attributed to the increased acceleration caused by the pressure buildup from the restricted piston movement.

Parameter	*Percent Difference*
GG Peak Pressure	3.41%
Plenum Peak Pressure	35.77%
Maximum Reaction Force	43.33%
Compressibility	52%
Ejection Velocity	14.1%

Table 18: Setup A Deployment Test - Key Parameters at ambient temperature

Conclusion

The cold test demonstrates that the model successfully predicts the behaviour of the gas generator pressure, with the experimental and simulated peak pressures aligning closely, differing by only 3.34%. This validates the accuracy of the model in simulating gas generator dynamics under cold conditions.

However, due to the unexpected icing effect observed during the experiment, which restricted the movement of the piston and parachute pack, this test cannot be used to validate other parameters such as plenum pressure, reaction force, compressibility, and ejection velocity. The icing led to a significant pressure buildup in the mortar tube, causing higher acceleration and force than the simulation predicted. As a result, the discrepancies between the experimental and simulated data for these parameters are not reflective of model inaccuracies but rather the influence of external, uncontrolled factors during the test.

4.2.3 Conclusion

The validation of the Parachute Deployment Device model demonstrated its effectiveness in replicating key physical processes involved in parachute deployment, including gas generator combustion, plenum pressurization, and ejection dynamics. The model successfully captured pressure profiles, force evolution, and overall system behaviour in comparison with experimental data from both closed bomb and deployment tests. This confirms the robustness of the numerical approach employed in the simulation.

In the Closed Bomb Tests, the model closely matched the experimental trends in gas generator and plenum pressure, with minor deviations in peak pressures, particularly under extreme temperature conditions. These discrepancies, though within acceptable margins, may be attributed to environmental factors or minor experimental inaccuracies, reaffirming the model's reliability in simulating combustion and energy release mechanisms.

The Deployment Tests further validated the model's capability to predict parachute ejection performance. Key parameters such as gas generator pressure, plenum pressure, reaction force, parachute pack compressibility, and ejection velocity aligned with experimental results. However, slight underestimation of reaction forces and slight overestimation of compressibility suggest that improvements in energy transfer modelling and material properties could enhance model accuracy. Notably, the reaction force was almost always lower than the observed experimental values. This discrepancy can be explained by the simplified model used for parachute pack compression. As the parachute pack is manually packed, its behaviour under compression can vary, making it difficult to accurately model, thus contributing to the underestimation of the reaction force.

A significant observation from the validation process was the variability in experimental results across repeated tests under identical conditions. Despite consistent input parameters, variations in pressures, forces, and temperatures were noted, which cannot be fully explained by sensor limitations. This highlights the inherent complexity of the system, as even with tightly controlled conditions, repeatability remains challenging. These differences likely arise from factors such as material property variations, flow disturbances, and dynamic interactions within the system.

Nevertheless, the validated model offers a solid foundation for further analysis and optimization of PDD performance. While improvements in mechanical interactions and material modelling could refine predictions, the model provides valuable insights into parachute deployment dynamics. Future studies could benefit from additional statistical analysis and uncertainty quantification to better address the observed variability and improve the accuracy of system designs for planetary exploration missions.

Chapter 5

Model Performances

In this section, we assess the model's performance under a variety of scenarios that push the boundaries of the Parachute Deployment Device system. These scenarios are designed to evaluate the behaviour of the system across a range of operating conditions, testing both the nominal performance and the extremes of the system.

The input parameters include variations in propellant mass and temperature. The maximum propellant loading is 19.53g under normal atmospheric conditions (21°C), beyond which the simulation crashes due to excessive pressure (around 350 MPa), which would likely result in gas generator failure under real-life conditions. On the other hand, the minimum tested propellant mass is 2g, providing a lower operational boundary.

For temperature, the program can run with inputs as low as -272°C and well above 1500°C. However, these extremes far exceed the realistic operating temperature ranges for the actual hardware, so practical limits need to be considered. The chosen temperatures include -150°C and 300°C to assess the system under extreme cold and high-temperature conditions, respectively.

In terms of pressure, the simulation can handle a wide range from 4 Pa to 6 MPa. These limits again exceed realistic conditions, but for the purposes of this assessment, the scenarios focus on realistic operational pressures within the range where the hardware would function without catastrophic failure.

In addition to testing standard and elevated scenarios, two extreme cases are added: one with very low temperature and low propellant mass and the other with high temperature and high propellant mass. These extreme cases will help explore the limits of the model's robustness and dynamic responses under scenarios where the hardware would typically struggle or fail.

This wide variety of input scenarios, combined with an understanding of the system's upper and lower limits, enables a comprehensive evaluation of the model's robustness and dynamic performance. Each scenario helps highlight specific aspects of the PDD's response, such as event timings, pressure profiles, and the effects of varying input parameters on the system's overall behaviour.

Scenario	*Propellant Mass (g)*	*Ground Test Temperature (°C)*	*Assembly Temperature (°C)*
1. Nominal Scenario	Nominal	21	21
2. High Propellant Load	Nominal + 87.5%	21	21
3. Low Propellant Load	Nominal – 73.5%	21	21
4. Critical Propellant Load	Nominal +143.75%	21	21
5. Low Temperature	Nominal	-150	21
6. High Temperature	Nominal	300	21
7. Extreme Low	Nominal – 73.5%	-150	21
8. Extreme High	Nominal + 137.5%	300	21

Table 19: Model Performance Scenarios

5.1 Event Timing

This section evaluates the timing of key deployment events within the Parachute Deployment Device model under varied input conditions, with the aim of examining the sequence and timing of each event, including burst disk rupture, shear pin release, compressibility at break, and venting initiation and completion. By assessing these critical events across different scenarios, the model's responsiveness to changes in propellant mass and temperature becomes clear. This provides a robust assessment of its dynamic performance under both nominal and extreme conditions.

The following table summarizes the event timings across scenarios, highlighting how variations in temperature and propellant mass impact event sequencing. Observing these timing changes reveals trends in response times across scenarios, especially under high-load or extreme temperature conditions.

Scenario	*E1: Burst Disk Open (s)*	*E2: Shear Pins Break (s)*	*E3: Vent Start (s)*	*E4: Vent Complete (s)*
Nominal	nominal	nominal	nominal	nominal
High Propellant Load	-79%	-28%	-30%	-2.4%
Critical Propellant Load	-99%	-31%	-35%	-3.9%
Low Temperature	+90%	+37%	+39%	+34%
High Temperature	-47%	-24%	-20%	-9.4%
Low Propellant Load	+423%	+106%	+180%	+69%
Extreme Low Temperature & Load	+985%	+184%	-	+111%
Extreme High Temperature & Load	-99%	-50%	-47%	2.1%

In analysing the influence of temperature, it is clear that higher temperatures lead to earlier occurrences of burst disk and shear pin release events. This trend reflects the accelerated pressure rise in the gas generator under elevated thermal conditions, as demonstrated in both high-temperature and extreme high-temperature scenarios. Conversely, low temperatures delay these events significantly, indicating that propellant combustion and gas expansion proceed more slowly under colder conditions. The model's accurate response to these temperature-induced shifts aligns with physical expectations. With

increased thermal energy, the propellant combustion accelerates; with reduced thermal energy, it decelerates. These findings suggest that real PDD systems operating in extreme cold would require additional safeguards or heating mechanisms to ensure timely deployment, while high-temperature conditions might necessitate material reinforcements to withstand rapid pressure increases.

The impact of propellant mass is similarly clear, as higher propellant loads consistently lead to faster event sequences. Increased gas production speeds up the pressure buildup, leading to earlier occurrences of burst disk opening and venting. Conversely, low propellant loads delay the entire event sequence, illustrating how reduced gas generation slows down deployment dynamics. Real-world applications of this observation suggest that propellant mass can be strategically controlled to adjust deployment timing. The model's stability at high propellant loads is evident, particularly as the critical load scenario, which approaches the maximum operational load, shows only slightly earlier event timings, indicating that the model can accurately simulate behaviour close to operational thresholds.

Scenarios that combine extreme temperatures with high or low propellant loads further demonstrate the model's limits. The extreme high-temperature and high-load scenario yields rapid events nearing the model's upper operational threshold, showcasing the model's capacity to simulate fast event sequences in high-stress conditions. This scenario underscores how amplified pressure buildup can occur under compounded high-temperature and high-load conditions, posing challenges to material and structural endurance. In contrast, the extreme low-temperature and low-load scenario emphasizes the model's ability to simulate deployment under challenging conditions for gas generation, as delayed events reflect the combined physical impacts of low thermal energy and reduced propellant mass. These results reveal areas for further improvement in model performance, particularly in enhancing predictive accuracy for slow-response scenarios in cold environments.

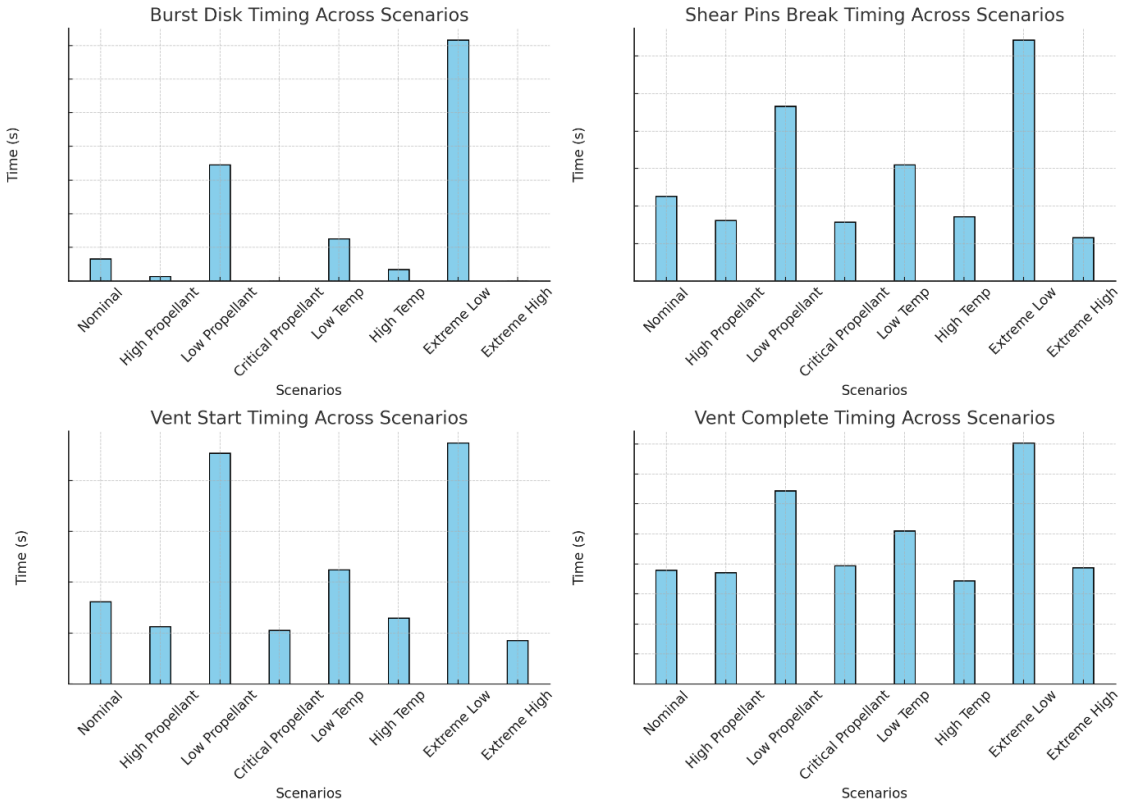

Figure 109: Scenarios Events Timing

The accompanying graphical analysis of each scenario further clarifies these findings by illustrating event sequences and pressure profiles. Each graph visually represents how variations in input conditions impact the timing and dynamics of key events. These plots confirm trends observed in the table, emphasizing the model's consistent and predictable behaviour across a range of input conditions. For

practical deployment applications, this comprehensive understanding of model performance under varied conditions can inform recommendations for design and testing protocols, as well as improvements in calibration for extreme operational scenarios.

5.2 Pressure Profiles and Temperature Responses

This section assesses the model's performance by examining the pressure and temperature profiles in the Gas Generator and Plenum chambers across various scenarios. By comparing these profiles, we can understand how changes in propellant mass and operating temperature affect system behaviour, and we can evaluate the robustness of the model in simulating these dynamic conditions.

5.2.1 Gas Generator Pressure Analysis

High and Critical Propellant Loads: In the high and critical load scenarios, the GG pressure reaches impressive peaks of approximately +137% and +233% of the nominal scenario peak value, respectively. The critical load scenario approaches the system's operational pressure limit, and the rapid initial pressure rise reflects the substantial energy release from increased gas generation. This confirms the model's accuracy in simulating high-pressure conditions and capturing rapid combustion, followed by a gradual decay as gas transfers into the PL chamber.

Low Propellant Load: The low propellant load scenario exhibits a much gentler pressure rise, peaking at -74% of the nominal peak. This illustrates the model's ability to accurately depict slower pressure dynamics, and a more gradual pressure decay associated with lower energy output, demonstrating its effectiveness at simulating minimal loading conditions.

Temperature Extremes: The low (-150°C) and high (300°C) temperature scenarios reveal significant differences in the GG pressure response. At -150°C, the GG pressure builds up more slowly, with a delayed peak of around 24% of the nominal peak, reflecting the impact of reduced combustion efficiency. Conversely, at 300°C, the model predicts a faster pressure rise, reaching approximately +17% of the nominal peak, which aligns with improved combustion dynamics under higher temperatures. These variations illustrate the model's sensitivity to initial temperature effects on pressure dynamics and combustion efficiency.

These trends confirm that the model accurately simulates the effects of both propellant mass and temperature on pressure dynamics, aligning well with expected physical responses across different conditions.

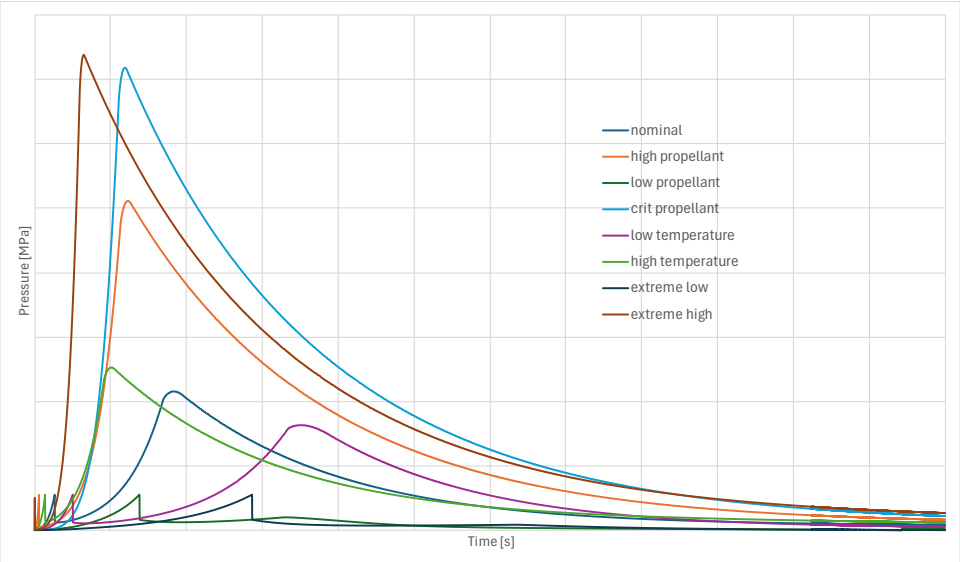

Figure 110: Gas Generator Pressures

5.2.2 Plenum Pressure Analysis

The PL pressure curves reveal the dynamics of gas transmission from the GG to the PL chamber, illustrating the model's ability to handle gas flow and pressure equalization.

High and Critical Loads: In the high and critical load scenarios, PL pressure peaks increase by approximately +108% and +176%, respectively, soon after the initial GG peak. This rapid pressure increase in the PL is consistent with the large gas volume transferring from the GG, demonstrating that the model accurately depicts gas transfer dynamics under elevated energy conditions.

Low Load and Low Temperature Sensitivity: The low propellant and low-temperature scenarios show a more gradual rise in PL pressure, with a peak pressure decreased by around -76% and -41% to the nominal value, respectively. These moderate pressure levels indicate limited gas transfer and lower combustion intensity, aligning with expectations for low-energy scenarios. This confirms the model's capacity to handle gradual pressure changes and reduced flow dynamics.

Extremes: At 300°C and critical propellant load, the PL pressure peak increases by 185% , aligning closely with the higher GG pressure from rapid gas generation. Meanwhile, in the -150°C and low propellant scenario, the PL pressure peak decrease by -77% compared to the nominal value, highlighting reduced energy transfer under cold conditions. These values confirm that the model effectively adapts to the different gas transfer rates and pressures expected from temperature variations.

The PL pressure trends across scenarios verify that the model captures the complexities of gas transfer and pressure equalization, maintaining accuracy across a wide range of conditions.

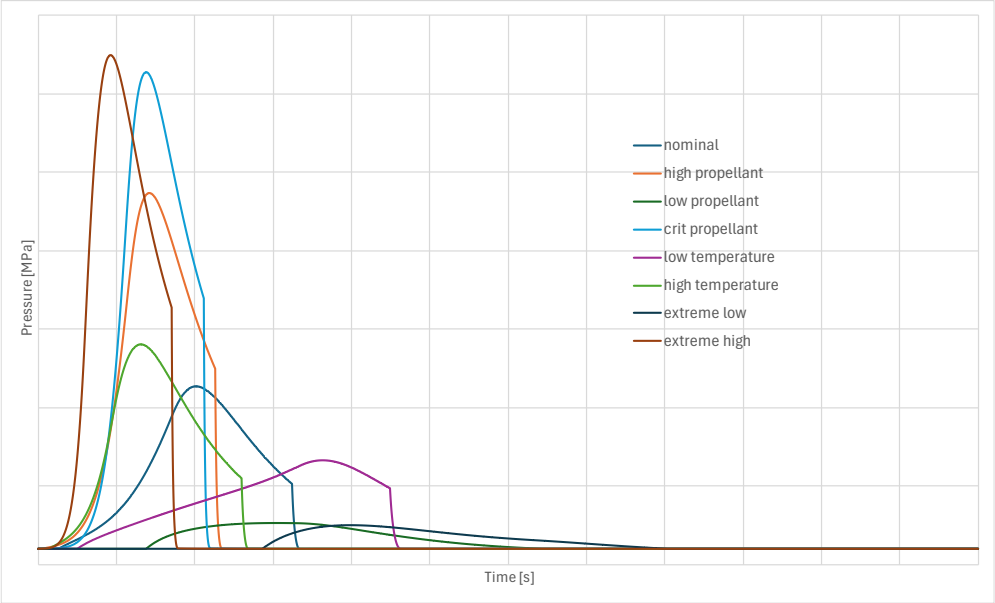

Figure 111: Plenum Pressures

5.2.3 Gas Generator Temperature Analysis

The GG gas temperature profiles provide insights into combustion dynamics and the thermal response under various propellant loads and temperature settings.

High and Critical Propellant Loads: The high and critical load scenarios reach GG temperature peaks of around 3200 K and 3600 K, respectively. These elevated temperatures reflect the intense combustion processes associated with larger propellant masses. The model's accurate representation of peak temperature and decay phases demonstrates effective calibration of heat transfer rates, simulating rapid

cooling post-combustion.

Low Propellant Load: In the low propellant load scenario, the GG temperature rises slowly, peaking around 1000 K, indicative of reduced combustion intensity. This confirms the model's ability to simulate the thermal behaviour associated with minimal propellant, validating its applicability for low-energy cases.

Temperature Extremes: Temperature extremes show distinct effects on GG temperature profiles. At -150°C, the temperature rise is sluggish, reaching only about 1500 K, while at 300°C, the GG temperature reaches a peak of 2800 K. These differences reflect the influence of initial temperatures on combustion efficiency and thermal response, confirming that the model can simulate a range of thermal dynamics effectively.

These temperature profiles affirm the model's adaptability to variations in initial conditions, ensuring accurate representation of combustion dynamics under both moderate and extreme settings.

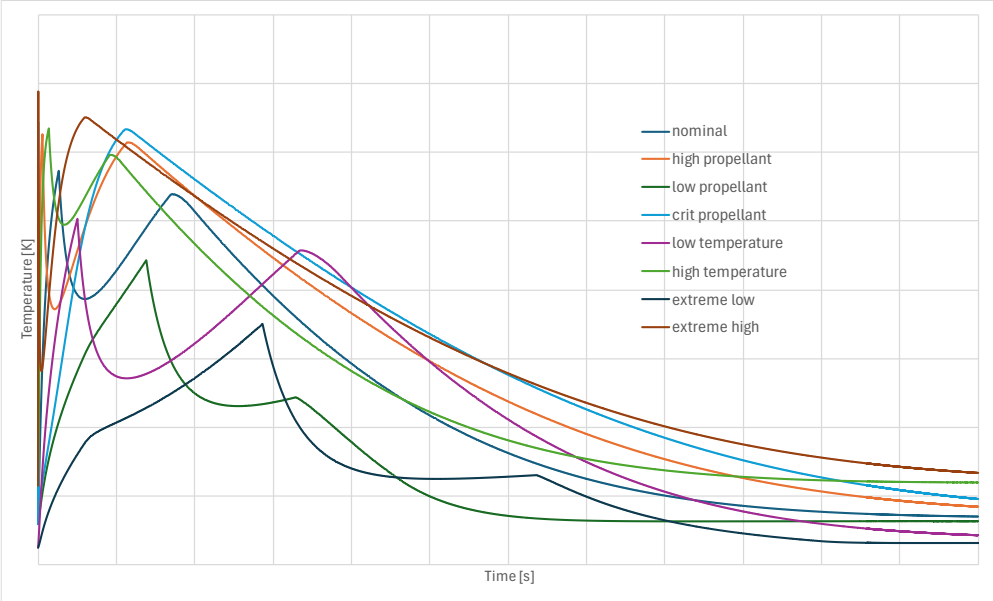

Figure 112: Gas Generator Temperatures

5.2.4 Plenum Temperature Analysis

The PL gas temperature profiles complement the pressure data by showing the thermal characteristics of the gas as it moves from the GG to the PL chamber.

High and Critical Loads: With higher propellant masses, PL temperatures reach approximately 2500 K and 3000 K, respectively, shortly after the GG peak. This rapid temperature rise confirms that the model effectively handles thermal transfer dynamics from the GG, simulating appropriate thermal behaviour for elevated energy conditions.

Low Load and Low Temperature: In the low propellant and low-temperature scenarios, the PL temperature peaks are more modest, reaching only around 600 K and 800 K, respectively. This aligns with a lower transfer of thermal energy, validating the model's representation of moderate heat propagation under low-energy conditions.

Temperature Impact: The high-temperature scenario (300°C) sees PL temperatures peak at around

2800 K, reflecting rapid and efficient thermal transfer from the GG to the PL chamber. In contrast, the -150°C scenario results in a subdued temperature peak around 800 K. These values highlight the model's sensitivity to temperature effects, capturing efficient thermal transfer under high-temperature conditions and reduced dynamics under extreme cold.

The PL temperature profiles provide a comprehensive view of the model's capability to simulate thermal transfer across different scenarios, accurately depicting temperature propagation from the GG to the PL chamber under varying conditions.

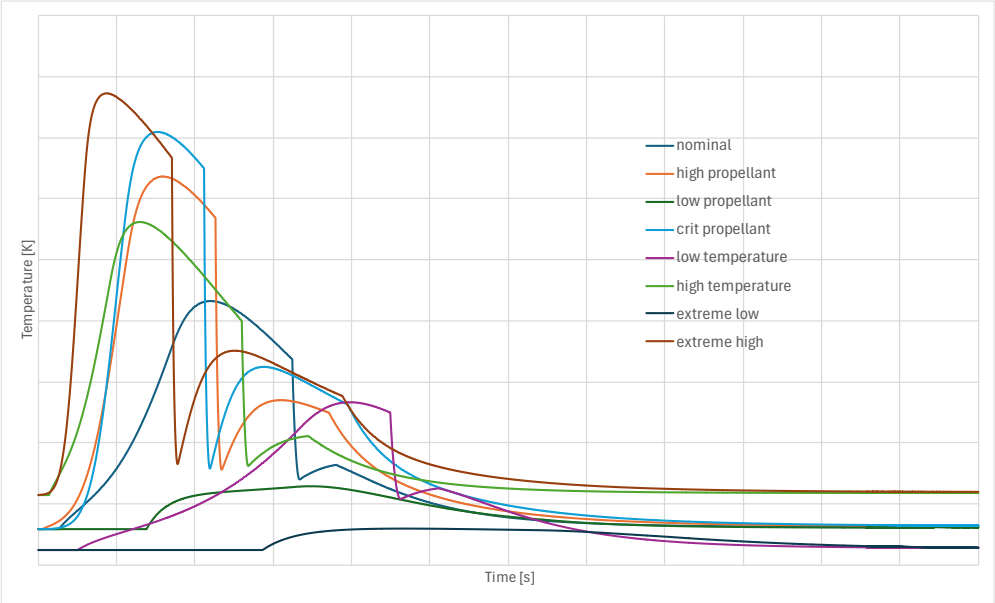

Figure 113: Plenum Temperatures

Conclusion

This analysis of pressure and temperature results across the Gas Generator and Plenum chambers demonstrates the model's robustness in handling diverse operating conditions. With high accuracy in simulating pressure and thermal dynamics across scenarios ranging from minimal to near-failure levels, the model shows adaptability to different propellant masses and temperatures. These results confirm the model's predictive accuracy and reliability for analysing the Parachute Deployment Device under a broad spectrum of operational conditions, providing a solid foundation for further applications and assessments.

5.3 Dynamic Behaviour

5.3.1 Piston and Parachute Pack Displacement

The piston and parachute pack displacement graphs illustrate the cumulative effect of different input conditions on the displacement response of both components. For scenarios with higher propellant mass, such as Scenarios 2 and 8, we observe a significantly higher maximum displacement for both the piston and parachute pack, which indicates that an increase in propellant mass directly correlates with the force exerted on these components, pushing them further along the tube. This greater displacement reflects the elevated gas generation and increased pressure exerted by a larger propellant load, as these conditions amplify the energy available to drive the piston and parachute pack.

In contrast, scenarios with minimal propellant loading, including Scenarios 3 and 7, show limited displacement due to lower gas generation and consequently lower pressure. Here, the reduced propellant

mass yields insufficient force to drive the piston and parachute pack to comparable levels as higher mass scenarios, indicating the model's sensitivity to propellant load variations.

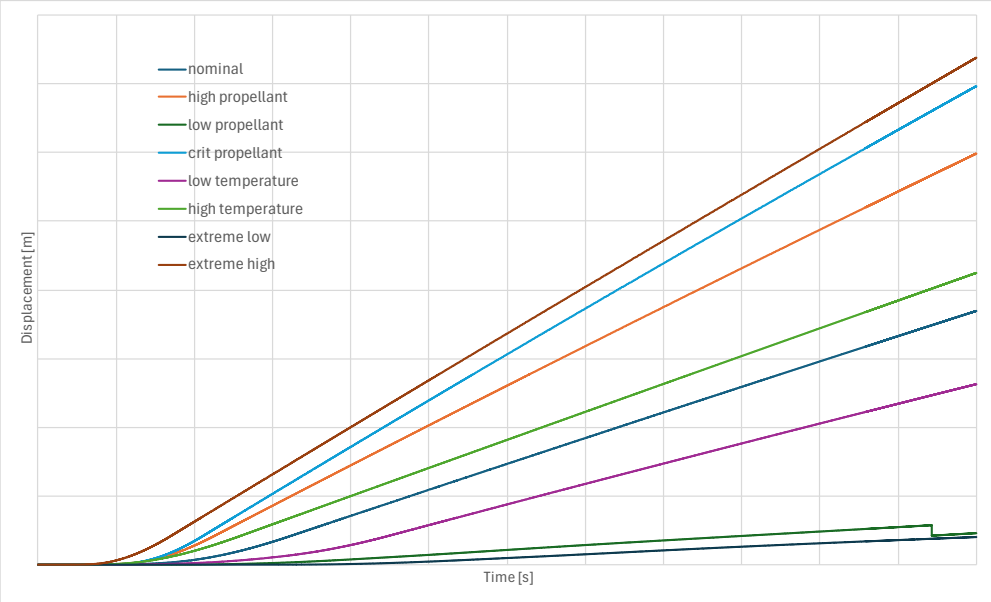

Figure 114: Piston Displacements

The parachute pack displacement shows a similar trend as the piston displacement, emphasizing how closely the two components interact during deployment. In scenarios with high propellant loads, the pack reaches a further displacement due to the higher energy transfer from the gas generator. This behaviour underscores that the pack's motion is directly influenced by the force applied by the piston, which itself depends on the initial gas expansion within the combustion chamber. Conversely, in scenarios with minimal propellant, the pack displacement remains subdued, highlighting that under these conditions, the PDD may not achieve the necessary deployment range.

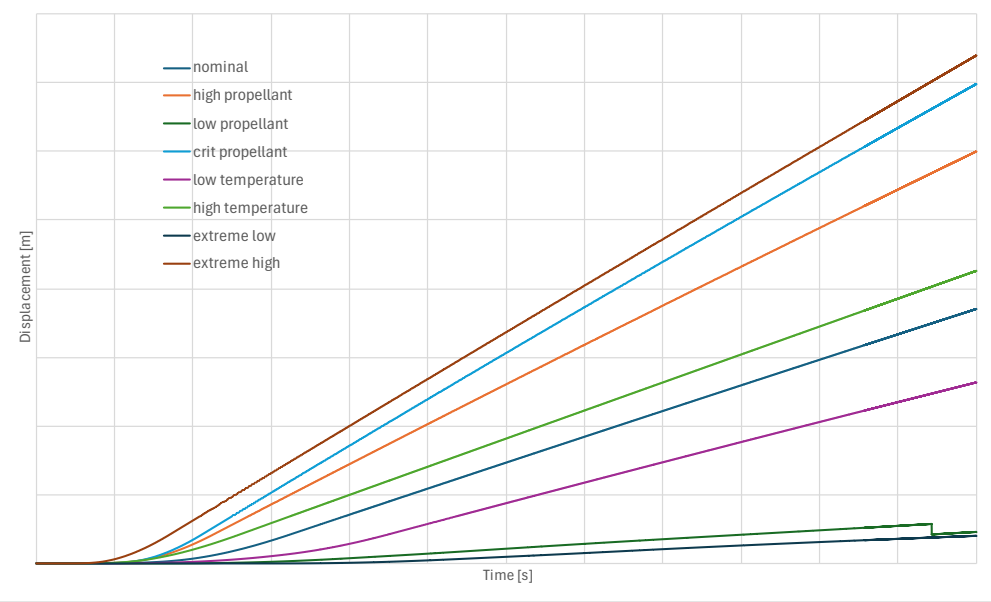

Figure 115: Parachute Pack Displacements

5.3.2 Piston and Parachute Pack Velocity

The piston and parachute pack velocity graphs provide insight into the system's dynamic response by showing distinct velocity peaks across scenarios. In Scenario 8, where both high temperature and high propellant mass are combined, the velocity peak for the piston surpasses all other scenarios, underscoring how these combined factors intensify the model's kinematic response. This high velocity is driven by the rapid gas generation and expansion, pushing the piston and parachute pack at accelerated rates. Such behaviour illustrates the model's effective response under demanding conditions, simulating robust deployment speeds.

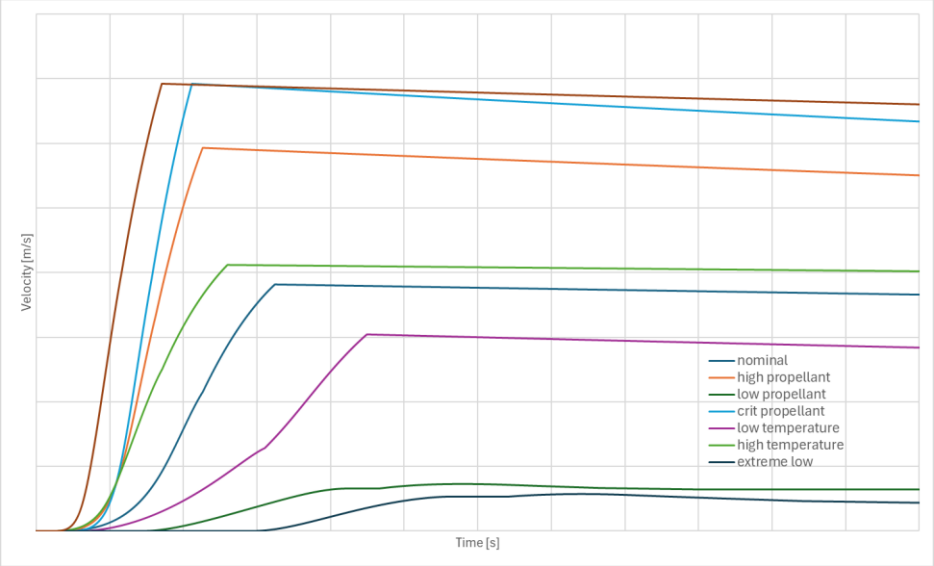

Figure 116: Piston Velocities

In examining the parachute pack velocity, we see a similar pattern, with high-mass and high-temperature scenarios leading to pronounced velocity peaks. The increased force from the gas generator and subsequent energy transfer causes the parachute pack to achieve maximum speed, indicating that the model effectively simulates the combined impact of temperature and propellant load on the pack's kinematics. Lower propellant and low-temperature scenarios, in contrast, yield a reduced pack velocity, signalling potential challenges in achieving adequate ejection speed under these minimal input conditions.

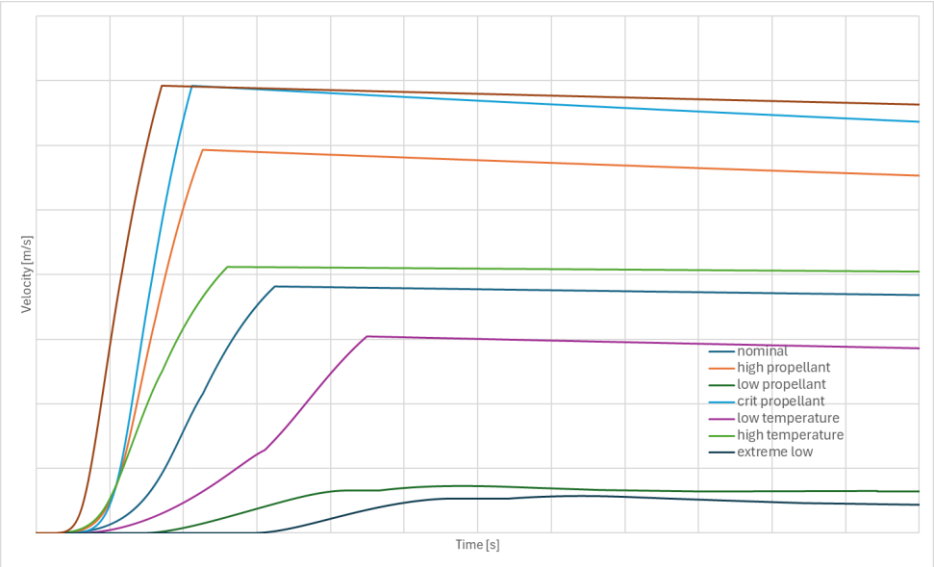

Figure 117: Parachute Pack Velocities

5.3.3 Reaction Force

The reaction force graph captures the force exerted by the gas generator on the piston during the ejection process. High propellant scenarios (2 and 8) lead to significantly higher reaction forces, with peak forces reaching above 35,000 N, especially in Scenario 8. In comparison, low-propellant scenarios exhibit much lower reaction forces, barely reaching 5,000 N, due to the limited gas expansion and energy generation.

Temperature impacts are also visible, with Scenario 6 (high temperature) showing a heightened reaction force due to faster combustion rates and energy transfer, leading to more rapid expansion. Conversely, the reaction force in low-temperature scenarios is more gradual, and lower peaks are observed. This confirms that lower temperatures inhibit the rapid force generation required for effective piston movement.

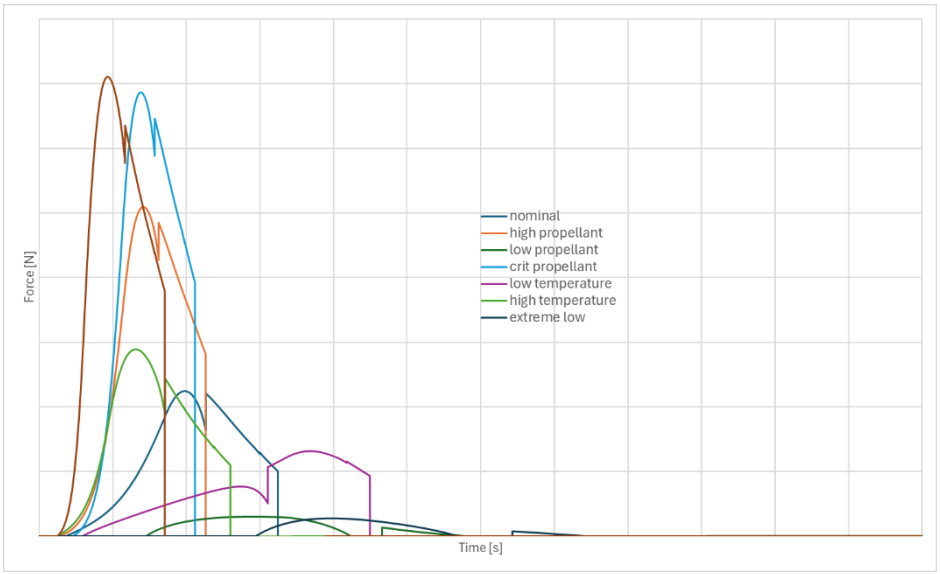

Figure 118: Reaction Forces

5.3.4 Observations and Insights

The graphs collectively indicate that the PDD model's response varies noticeably with changes in temperature and propellant mass. Increased propellant loads and higher temperatures lead to heightened displacement, velocity, and reaction force, which collectively enhance the deployment performance by generating greater force and faster movement. These conditions suggest that the model performs optimally under high-performance scenarios where both temperature and propellant mass are elevated, aligning with the anticipated deployment requirements.

In contrast, scenarios with lower temperatures and reduced propellant mass significantly diminish deployment effectiveness. These conditions limit force generation, reduce movement speed, and decrease travel distance, which could potentially compromise the system's ability to meet the necessary deployment parameters.

These results underscore the limitations of the mathematical simulation model, particularly when tested at the extremes of its input range. Although these test conditions lie well beyond the actual physical operating parameters of the PDD, they demonstrate the boundary of the model's predictive capacity rather than limitations within the PDD system itself. For the nominal and high-performance operating conditions, the model shows strong accuracy and consistent reliability, underscoring its suitability for simulating real-world scenarios within realistic operational parameters.

5.4 Sensitivity

In this section, we conduct a detailed sensitivity analysis to evaluate how variations in key model parameters impact the Parachute Deployment Device (PDD) system's performance. Sensitivity analysis is essential for identifying which parameters significantly influence the model's outputs, particularly in terms of timing events, pressure and temperature profiles, and force generation.

The analysis considers both core and additional parameters selected based on their relevance to the PDD's operational dynamics. Key parameters include the discharge coefficient, which directly affect gas generation and flow rates. Additionally, parameters such as burst disk pressure threshold and post-combustion chamber volume are included to capture their influence on gas expansion dynamics, while the shear pins force threshold relates to the mechanical breakpoints that define the system's deployment phases. The plenum properties, including diameter and length, influence gas dynamics post-combustion and are critical to understanding pressure propagation and venting behaviour.

This sensitivity analysis will help delineate the range within which each parameter can vary without compromising performance, clarifying both the robustness and potential adjustment needs of the PDD model under diverse operating conditions.

5.4.1 Individual Parameter Analysis

To conduct a comprehensive sensitivity analysis, we will adjust a set of key parameters that define the behaviour of the PDD model. Each parameter plays a distinct role in determining specific aspects of the deployment process, such as pressure dynamics, energy transfer, structural response, and gas flow. The sensitivity of the model to these parameters will highlight which factors most significantly affect the system's performance and identify areas where precision is paramount for reliable deployment across different conditions.

The following parameters will be examined, with adjustments based on the criticality and potential variability of each parameter. Standard parameters, such as the discharge coefficient and convective heat transfer coefficients, will be varied by ±10%, allowing us to assess their impact within realistic operational tolerances. For critical thresholds, such as the burst disk pressure and shear pin force, we will apply a variation between ±5% and ±15%, reflecting their essential role in system integrity. Dimensional parameters, like plenum diameter and length, may be varied up to ±20% to simulate design adjustments.

1. **Discharge Coefficient (Cd)**: This parameter governs the rate of gas flow from the gas generator to the plenum. Adjusting Cd will show how flow restrictions impact the pressure rise in the plenum and the timing of events like piston displacement and venting.

2. **Convective Heat Transfer Coefficients (hc_GG and hc_PL)**: These coefficients control the rate of heat transfer from the gas to the walls in both the gas generator and the plenum. Sensitivity analysis on hc_GG and hc_PL will clarify their influence on temperature regulation within the chambers, particularly under scenarios of high or low ambient temperatures.

3. **Burst Disk Pressure Threshold**: This threshold is the pressure at which the burst disk ruptures, allowing gas to flow into the plenum. By varying this threshold, we can assess its impact on event timing, specifically the delay or acceleration of the disk rupture event, and consequently, the entire deployment sequence.

4. **Combustion Chamber Volume**: The initial volume of the combustion chamber directly affects the pressure generation rate. An increase in volume should theoretically delay the pressure peak, affecting all downstream events. This parameter's sensitivity highlights how changes in chamber size could alter the PDD's dynamic response.

5. **Post-Combustion Chamber Volume**: This additional volume becomes active once the burst disk ruptures, allowing gas expansion. Adjusting this parameter allows us to observe its effect on pressure redistribution and how it influences the venting timing and overall energy transfer.

6. **Number of Orifices**: The number of orifices between the combustion chamber and the plenum affects the rate of gas transfer. By increasing or decreasing the number of orifices, we can observe variations in the plenum pressure buildup and changes in the force applied to the piston and parachute pack.

7. **Shear Pins Force Threshold**: This parameter represents the force required to break the shear pins and initiate piston and parachute movement. Sensitivity to this threshold will indicate its role in deployment timing and the system's ability to overcome initial resistance.

8. **Plenum Diameter and Length**: The dimensions of the plenum directly affect its volume, impacting how gas pressure accumulates and influences the deployment force. Varying the diameter and length will provide insights into how changes in plenum design could optimize or hinder deployment dynamics.

Each parameter will be varied incrementally, within ranges reflecting practical and theoretical operational limits. This approach allows for a precise understanding of the model's responsiveness to parameter changes, facilitating identification of critical thresholds that could impact deployment success. Additionally, the insights from this analysis will guide recommendations for parameter adjustments and potential areas for further model refinement to ensure optimal performance across a spectrum of operating conditions.

5.4.2 Comparative Sensitivity Analysis

The comparative sensitivity charts provide a visual analysis of the PDD model's response to variations in critical parameters. Key metrics—including event timings, maximum pressures, exit velocity, maximum reaction force, and piston displacement—are assessed to determine the sensitivity of the model to each parameter change. These metrics are essential indicators of deployment performance, capturing both the temporal and dynamic behaviours of the PDD system.

5.4.2.1 Metrics

The analysis is organized by metric, with each metric's response shown across a range of parameter variations. This approach highlights the degree to which each parameter influences overall system dynamics.

Event Timings: By tracking timings for events such as burst disk rupture, shear pin breakage, vent start, and vent completion, we capture the sensitivity of the deployment sequence to each parameter. For example, the burst disk pressure threshold influences the exact moment of rupture, while the discharge coefficient affects the timing of subsequent events as gas flows between the combustion chamber and plenum. Adjusting the combustion chamber volume can also shift these events, as it directly influences pressure build-up. These timing variations highlight how closely each parameter is tied to the PDD's precise sequential operation.

Maximum Gas Generator and Plenum Pressures: Maximum pressures within the GG and PL directly affect the system's structural integrity and deployment efficacy. The GG's pressure is influenced by the burn rate and gas generation rate, while the discharge coefficient (Cd) affects how pressure is transferred between the GG and PL. The combustion and post-combustion chamber volumes also play significant roles, as increasing volume generally leads to a delayed pressure peak. Analysing these variations provides insights into achieving optimal pressure levels without risking damage to the PDD.

Parachute Pack Velocity: The exit velocity of the parachute pack is a mission-critical metric, as it must fall within a specified range for successful deployment. This velocity depends on parameters like the discharge coefficient, the number of orifices, and the shear pin force threshold, which affect the force applied to the parachute pack and the timing of release. Adjusting the plenum's diameter and length will impact the pressurization and, thus, the exit velocity. For the PDD's performance requirements, this exit velocity metric is essential for assessing whether the device meets mission deployment criteria.

Maximum Reaction Force: The maximum reaction force generated during ejection is a critical metric due to the upper limit required by mission-specific PDD performance requirements. Exceeding this force could compromise the system's integrity or deployment sequence. Therefore, tracking the sensitivity of this metric to parameter variations is essential for assessing how changes affect the model's adherence to these limits. Analysing the sensitivity of the maximum reaction force helps identify the parameters with the most significant impact on deployment force, supporting design adjustments to meet required thresholds.

5.4.2.2 Event Timings

In this sensitivity analysis, we examine how variations in key parameters impact the timings of significant events during the deployment sequence: burst disk rupture (Event 1), shear pin breakage (Event 2), vent start (Event 3), and vent completion (Event 4). Each of these events is crucial to the controlled sequence of deployment, as any variation in timing can influence subsequent phases and potentially alter the overall deployment outcome.

Parameters	***Variation***	***Event 1 (s)***	***Event 2 (s)***	***Event 3 (s)***	***Event 4 (s)***
Cd	-10%	0.00%	1.94%	2.34%	0.94%
	0%	-	-	-	-
	10%	0.00%	-1.68%	-1.99%	-0.22%
hc_GG	-10%	-2.73%	-1.74%	-1.65%	0.69%
	0%	-	-	-	-
	10%	2.57%	1.72%	1.63%	0.19%
hc_PL	-10%	0.00%	-0.62%	-0.80%	0.53%
	0%	-	-	-	-
	10%	0.00%	0.60%	0.78%	-1.76%
P_Burst	-10%	-1.82%	0.84%	0.62%	0.52%
	0%	-	-	-	-
	10%	3.26%	-1.49%	-1.10%	-0.27%
F_shear	-10%	0.00%	-0.65%	-0.06%	-0.16%
	0%	-	-	-	-
	-10%	0.00%	0.57%	0.06%	-0.22%
V_cc	-20%	-31.42%	0.87%	-0.22%	0.40%
	0%	-	-	-	-
	20%	30.66%	0.76%	1.28%	0.20%
V_pcc	-20%	0.00%	-8.28%	-8.34%	-7.54%
	0%	-	-	-	-
	20%	0.00%	8.05%	8.20%	6.91%
n_orifices	-2	0.00%	5.51%	6.84%	1.52%
	0	-	-	-	-
	2	0.00%	-3.83%	-4.44%	-1.26%
L_pl	-20%	0.00%	-8.65%	-9.65%	-1.72%
	0%	-	-	-	-
	20%	0.00%	6.82%	9.96%	4.49%
D_pl	-15%	0.00%	-13.33%	-4.91%	1.50%
	0%	-	-	-	-
	20%	0.00%	14.97%	12.97%	7.18%

Table 20: Event Timings Sensitivity Analysis

Table 20 captures the timing data for each event across different parameter variations, providing a detailed look at how adjustments to parameters like discharge coefficient, heat transfer coefficients, burst disk pressure, and plenum dimensions affect the deployment process.

Event Timing Analysis
The sensitivity results illustrate how each parameter affects the sequence timing of events.

- **Discharge Coefficient (Cd):** Altering the Cd value influences the timing of shear pin breakage and vent start. With a 10% increase in Cd, Event 3 initiates slightly earlier, likely due to faster pressure buildup in the plenum. This change in event timing underscores the influence of Cd on the rate of gas transfer from the gas generator to the plenum, thus affecting the sequence of deployment.

- **Heat Transfer Coefficients (hc_GG and hc_PL):** Both hc_GG and hc_PL demonstrate modest impacts on event timings, though these effects are most noticeable in the vent start and completion events. Higher heat transfer rates slow down the progression slightly, as seen by later timings in Event 3 and Event 4 with an increased hc_GG or hc_PL. This indicates that increased heat dissipation modulates the pressure development rate, highlighting the role of heat transfer dynamics within the PDD system.

- **Burst Disk Pressure Threshold:** Variations in the burst disk pressure threshold result in predictable shifts in the timing of Event 1 (disk rupture). A lower threshold accelerates rupture, subsequently affecting all downstream events by advancing their timings slightly. This sensitivity confirms the burst disk threshold's role in pacing the initial gas release and subsequent deployment phases.

- **Combustion Chamber Volume (V_cc):** The combustion chamber volume exerts a pronounced effect on the timing of the burst disk rupture and shear pin breakage. A larger V_cc delays Events 1 and 2, as the increased volume results in slower pressure buildup. This parameter's sensitivity is essential for understanding how chamber sizing influences deployment initiation.

- **Post-Combustion Chamber Volume (V_pcc):** This parameter significantly affects the vent start and completion events. A 20% increase in V_pcc causes Event 3 and Event 4 to occur later due to delayed pressure redistribution. This illustrates the role of post-combustion volume in defining the venting phase dynamics and ensuring that sufficient pressure is maintained throughout deployment.

- **Number of Orifices:** Changing the orifice count impacts the shear pin breakage and venting events. A higher number of orifices promotes faster gas transfer, which speeds up the entire sequence by reducing pressure bottlenecks. This parameter is thus crucial for adjusting the deployment speed without compromising pressure levels.

- **Plenum Length (L_pl) and Diameter (D_pl):** Both plenum dimensions show sensitivity across the timing of all events. Notably, a smaller plenum length and diameter accelerate event timing by creating higher pressure peaks within a confined space. The adjustments to plenum size underscore its importance in optimizing gas distribution for timely and controlled deployment.

Overall, these findings emphasize the nuanced relationships between each parameter and the PDD's sequential events, illustrating where precision is necessary to meet mission timing requirements.

5.4.2.3 Peak Pressures

The sensitivity of peak pressures in the Gas Generator and Plenum highlights how adjustments to core parameters impact the maximum internal pressures achieved during the deployment sequence. Peak pressures are essential to the PDD's structural integrity and deployment efficacy, as excessive pressure could risk damage to the components, while insufficient pressure may impair deployment performance.

The Table 21 below presents the maximum GG and PL pressures for each parameter variation. These pressures provide insight into how parameter adjustments affect the overall pressurization dynamics within the PDD.

Parameters	***Variation***	***Max GG Pressure (MPa)***	***Max PL Pressure (MPa)***
Cd	-10%	1.45%	-4.46%
	0%	-	-
	10%	-1.42%	3.99%
hc_GG	-10%	2.11%	2.08%
	0%	-	-
	10%	-2.04%	-2.00%
hc_PL	-10%	0.00%	1.44%
	0%	-	-
	10%	0.00%	-1.36%
P_Burst	-10%	-0.04%	-0.24%
	0%	-	-
	10%	0.05%	0.27%
F_shear	-10%	0.00%	0.00%
	0%	-	-
	-10%	0.00%	0.00%
V_cc	-20%	6.32%	4.93%
	0%	-	-
	20%	-5.57%	-4.12%
V_pcc	-20%	18.93%	16.28%
	0%	-	-
	20%	-14.36%	-12.67%
n_orifices	-2	3.71%	-12.18%
	0	-	-
	2	-3.54%	9.20%
L_pl	-20%	-3.54%	9.20%
	0%	-	-
	20%	0.00%	-4.87%
D_pl	-15%	0.00%	-19.34%
	0%	-	-
	20%	0.00%	-16.83%

Table 21: Peak Pressure Sensitivity Analysis

Peak Pressure Analysis

The sensitivity results for peak pressures in the GG and PL demonstrate that certain parameters directly impact the pressurization dynamics of the PDD system.

- **Discharge Coefficient (Cd):** Adjustments to Cd have a moderate effect on GG and PL peak pressures. A 10% increase in Cd reduces GG peak pressure slightly, as the increased gas flow reduces pressure buildup in the GG while accelerating pressurization in the PL. This highlights

the Cd's role in balancing the pressure distribution across the system.

- **Convective Heat Transfer Coefficients (hc_GG and hc_PL):** Increases in hc_GG and hc_PL moderately reduce GG and PL pressures. This effect is more pronounced in hc_GG, indicating that increased heat dissipation from the gas to the GG walls slightly dampens the peak pressures, as the gas loses energy more quickly. These coefficients illustrate the role of thermal dynamics in controlling the pressurization rate and peak pressure within the system.

- **Burst Disk Pressure Threshold (P_Burst):** Changes in the burst disk pressure threshold result in minimal effects on both GG and PL peak pressures. Although the timing of the burst disk rupture is sensitive to P_Burst, the overall pressure peaks remain stable, indicating that the initial threshold does not significantly alter the cumulative pressurization effects.

- **Combustion Chamber Volume (V_cc):** Varying the combustion chamber volume significantly impacts the GG peak pressure. Reducing V_cc by 20% increases GG peak pressure due to the reduced volume for gas expansion. Conversely, a 20% increase in V_cc lowers the peak pressure in both the GG and PL, indicating that an increase in chamber volume provides more space for gas expansion, thus reducing peak pressures.

- **Post-Combustion Chamber Volume (V_pcc):** Adjustments to V_pcc have a marked effect on both GG and PL pressures. Increasing V_pcc by 20% results in the lowest observed pressures, while decreasing it by 20% yields a substantial increase in both GG and PL peak pressures. This suggests that the post-combustion volume serves as a critical moderator for gas expansion, providing additional capacity to prevent excessive pressure buildup.

- **Number of Orifices (N_orifices):** Increasing the number of orifices significantly lowers GG peak pressure and raises PL peak pressure, as the increased flow capacity allows pressure to transfer more readily from the GG to the PL. Reducing the orifice count limits this flow, keeping more pressure within the GG and resulting in lower pressures in the PL.

- **Plenum Dimensions (L_pl and D_pl):** Changes in plenum length and diameter impact PL pressure primarily, as they determine the plenum's total volume. A smaller diameter (-15%) results in lower PL peak pressure, reflecting reduced gas volume capacity and, hence, lower pressurization. Similarly, a 20% increase in length decreases PL pressure due to an expanded plenum volume. These variations indicate that the plenum's design directly affects pressure buildup and helps modulate the pressure profile experienced by the parachute pack.

The results from this sensitivity analysis illustrate the importance of balancing pressure generation and dissipation within the PDD. Parameters like chamber volumes and orifice counts demonstrate considerable influence over pressure distribution and intensity, highlighting their relevance in achieving desired deployment forces while preventing structural overloading. These insights are essential for refining design choices in future PDD systems, ensuring that pressures remain within safe operating limits under varied conditions.

5.4.2.4 Reaction Force

The reaction force exerted during the ejection process is a critical indicator of the deployment effectiveness in the PDD system. This force directly influences the acceleration of both the piston and parachute pack, impacting the velocity at which these components are propelled. Examining the sensitivity of the reaction force to variations in key parameters offers insight into how different design aspects can enhance or diminish the deployment's force profile.

Parameters	***Variation***	***Max Reaction Force (N)***
Cd	-10%	-4.75%
	0%	-
	10%	4.59%
hc_GG	-10%	2.39%
	0%	-
	10%	-2.30%
hc_PL	-10%	1.49%
	0%	-
	10%	-1.42%
P_Burst	-10%	-0.31%
	0%	-
	10%	0.36%
F_shear	-10%	0.00%
	0%	-
	-10%	0.00%
V_cc	-20%	5.80%
	0%	-
	20%	-4.78%
V_pcc	-20%	19.33%
	0%	-
	20%	-14.83%
n_orifices	-2	-13.20%
	0	-
	2	12.72%
L_pl	-20%	12.72%
	0%	-
	20%	-5.28%
D_pl	-15%	-16.92%
	0%	-
	20%	-18.36%

Table 22: Reaction Force Sensitivity Analysis

Reaction Force Analysis

The results for reaction force across parameter variations reveal several notable sensitivities:

- **Discharge Coefficient (Cd):** The reaction force is directly influenced by Cd variations, with a 10% increase in Cd resulting in the highest reaction force observed in this analysis (+4.59%). Conversely, a 10% decrease in Cd lowers the reaction force by -4.75%. This sensitivity indicates that controlling the rate of gas flow through the orifices significantly affects the force exerted on the piston and parachute pack.
- **Convective Heat Transfer Coefficients (hc_GG and hc_PL):** Variations in hc_GG and

hc_PL both impact reaction force, though the effect is relatively moderate. A 10% increase in hc_GG results in a slight reduction of reaction force, suggesting that increased heat transfer from the gas generator walls dissipates energy that would otherwise contribute to force generation. This implies that material properties, such as surface texture and coating, could play a role in optimizing the force profile.

- **Burst Disk Pressure Threshold (P_Burst):** Adjustments to P_Burst have minimal influence on the maximum reaction force, which remains relatively consistent across the threshold's variations. This finding suggests that while P_Burst impacts event timing, it does not significantly alter the peak reaction force achieved during deployment, as gas expansion dynamics take precedence once the burst disk ruptures.

- **Combustion Chamber Volume (V_cc):** A smaller combustion chamber volume increases the reaction force by 5.80% due to faster gas compression within the confined space. On the other hand, a 20% increase in volume reduces the reaction force by -4.78%, as the larger chamber allows for a slower pressure buildup. These results demonstrate that V_cc is a critical parameter for fine-tuning the force profile in the early stages of deployment.

- **Post-Combustion Chamber Volume (V_pcc):** The impact of V_pcc on reaction force is substantial. Decreasing V_pcc by 20% results in a reaction force increase of 19.33%, the highest recorded in this analysis, while a 20% increase in V_pcc lowers the reaction force by -14.83%. This variation indicates that the volume available for gas expansion after the burst disk rupture significantly influences the deployment force, underscoring the importance of carefully calibrating this parameter.

- **Number of Orifices (N_orifices):** Increasing the orifice count yields higher reaction forces, with two additional orifices increasing the reaction force by 12.72%. Reducing the orifice count has the opposite effect, lowering the reaction force by 13.20%. This sensitivity highlights the role of gas transfer rate in sustaining adequate force for deployment, suggesting that a larger number of orifices facilitates a more rapid energy transfer and reaction force buildup.

- **Plenum Dimensions (L_pl and D_pl):** Both plenum length and diameter affect the reaction force generated during deployment. Reducing the plenum length by 20% produces a reaction force higher by 12.7%, while a 20% increase in length decreases the force by -5.28%. Similarly, reducing the plenum diameter by 15% leads to an increased reaction force by -16.92%, the lowest observed in this section. This suggests that plenum geometry significantly influences force generation, with smaller plenum volumes promoting higher reaction forces due to restricted gas expansion.

Overall, the reaction force results emphasize the influence of gas transfer dynamics, chamber volumes, and plenum geometry on force generation within the PDD. Parameters like V_cc, V_pcc, and N_orifices demonstrate a high degree of sensitivity, with changes in these parameters substantially affecting the maximum reaction force. These findings highlight the importance of optimizing these parameters to achieve the necessary force for reliable deployment, especially in high-performance or constrained environments.

5.4.2.5 Parachute Pack Velocity

The exit velocity of the parachute pack is a critical metric for evaluating the deployment efficacy of the PDD, as it must meet mission requirements for safe and reliable parachute release. This analysis examines how variations in selected parameters affect the exit velocity, providing insight into design considerations for achieving optimal deployment speed.

Parameters	***Variation***	***Parachute Pack Exit Velocity (m/s)***
Cd	-10%	-3.86%
	0%	-
	10%	3.40%
hc_GG	-10%	1.62%
	0%	-
	10%	-1.58%
hc_PL	-10%	1.66%
	0%	-
	10%	-1.60%
P_Burst	-10%	-0.13%
	0%	-
	10%	0.14%
F_shear	-10%	0.11%
	0%	-
	-10%	-0.11%
V_cc	-20%	2.90%
	0%	-
	20%	-2.58%
V_pcc	-20%	9.13%
	0%	-
	20%	-7.82%
n_orifices	-2	-10.72%
	0	-
	2	7.80%
L_pl	-20%	7.80%
	0%	-
	20%	4.35%
D_pl	-15%	-9.98%
	0%	-
	20%	-6.58%

Table 23: Parachute Pack Velocity Sensitivity Analysis

Parachute Pack Velocity Analysis

The results for the parachute pack exit velocity highlight the following sensitivities:

- **Discharge Coefficient (Cd):** Variations in Cd produce noticeable changes in exit velocity, with a 10% increase in Cd raising the velocity by 3.4% and a 10% decrease lowering it by 3.86%. This sensitivity suggests that a higher discharge coefficient promotes faster gas flow into the plenum, thus enhancing the force applied to the parachute pack. Precise control of Cd is essential to meet the required exit velocity range for effective deployment.

- **Convective Heat Transfer Coefficients (hc_GG and hc_PL):** The convective heat transfer coefficients influence exit velocity moderately, with hc_GG and hc_PL variations each

showing slight impacts. Increasing these coefficients by 10% reduces the exit velocity marginally (-1.58% for hc_GG and -1.6% for hc_PL), as more heat is lost to the chamber walls, slowing gas expansion. Although these parameters do not drastically affect exit velocity, optimizing hc_GG and hc_PL contributes to consistent deployment performance across temperature variations.

- **Burst Disk Pressure Threshold (P_Burst):** Changes in P_Burst have minimal effect on exit velocity, suggesting that, while this parameter influences initial event timing, it does not significantly alter the final deployment speed of the parachute pack. This result implies that focusing on other parameters might yield more substantial improvements in deployment speed.

- **Combustion Chamber Volume (V_cc):** A smaller combustion chamber volume increases exit velocity by 2.9% due to the faster gas buildup in a confined space, whereas a 20% increase in V_cc results in a lower exit velocity (-2.58%). This outcome confirms that reducing the combustion chamber volume can enhance deployment speed, offering a design consideration for applications requiring rapid deployment.

- **Post-Combustion Chamber Volume (V_pcc):** The exit velocity shows high sensitivity to V_pcc variations, with a 20% decrease leading to an exit velocity of +9.13%, the highest recorded in this section, and a 20% increase reducing it by 7.82%. The post-combustion volume plays a pivotal role in the acceleration phase, as it determines the gas expansion area after burst disk rupture. Minimizing V_pcc thus results in a more concentrated force transfer, accelerating the parachute pack more effectively.

- **Number of Orifices (N_orifices):** Increasing the number of orifices between the combustion chamber and the plenum enhances exit velocity, with two additional orifices yielding a velocity increase of 7.80%. Reducing orifices lowers the velocity by 10.72%, indicating that gas flow restrictions can significantly affect exit speed. Adjusting the number of orifices is therefore a key factor in achieving mission-specific deployment velocities.

- **Plenum Dimensions (L_pl and D_pl):** Plenum length and diameter significantly influence exit velocity, with reduced plenum dimensions generating higher exit velocities. A 20% reduction in plenum length results in a velocity increase of 7.80%, while a 15% decrease in diameter yields to a decrease of -9.98%. This result shows that reducing the plenum's internal volume amplifies force transfer to the parachute pack, which is beneficial for missions requiring high exit speeds.

In summary, parameters such as the discharge coefficient, post-combustion chamber volume, number of orifices, and plenum dimensions exhibit the highest sensitivity regarding parachute pack exit velocity. Adjusting these parameters allows for precise tuning of deployment speed to meet mission requirements. By identifying these influential parameters, this analysis provides design insights for optimizing the PDD model's performance across varying operational scenarios.

5.4.3 Findings and Implications

The sensitivity analysis conducted on the PDD model reveals valuable insights into how variations in different parameters affect deployment performance, providing guidance for both model refinement and design adjustments in future PDD systems. Each parameter exhibited unique influences on key metrics, such as event timings, peak pressures, reaction force, and exit velocity, highlighting where precise control is necessary to meet performance objectives.

The discharge coefficient showed a strong effect on reaction force and exit velocity, with changes impacting gas flow rates, force buildup, and deployment speed. A higher discharge coefficient allows quicker pressure buildup in the plenum, which accelerates key deployment events and improves exit velocity, indicating that controlling this parameter is essential for optimizing deployment speed and

energy transfer.

Convective heat transfer coefficients in the gas generator and plenum affected temperature regulation, reaction force, and exit velocity. Although these coefficients had a more modest impact on direct force or speed metrics, their role in managing heat dissipation from gas to chamber walls highlights their importance in maintaining deployment consistency across varying thermal environments. Properly tuning these coefficients ensures the PDD performs reliably under temperature fluctuations.

Thresholds like the burst disk pressure and shear pin force proved critical in event timing control. Lower thresholds caused earlier ruptures and pin breakage, which sped up the deployment sequence overall. These thresholds directly impact timing precision, underscoring the need to maintain them within tight tolerances to achieve predictable deployment timings.

Chamber volumes in the combustion and post-combustion phases exerted significant influence over peak pressures, reaction force, and exit velocity. Reducing these volumes resulted in increased pressures and faster deployment speeds, while increased volumes reduced peak pressures. This finding indicates that proper chamber sizing plays an important role in balancing deployment force and structural integrity, allowing teams to tailor PDDs for specific mission needs while ensuring durability.

Plenum dimensions, including diameter and length, affected maximum pressures and reaction force. Smaller plenum volumes promoted higher pressures and enhanced exit velocity, underscoring the relevance of these parameters for achieving rapid deployment when needed. By carefully adjusting plenum dimensions, designers can optimize deployment dynamics, balancing speed requirements with structural safety considerations.

The insights gained from this analysis suggest several implications for future PDD designs. For exit velocity control, focusing on parameters like discharge coefficient, number of orifices, and post-combustion volume will help meet mission-specific speed requirements. Structural integrity management can benefit from carefully adjusting chamber volumes and orifice counts to control peak pressures, ensuring that PDDs remain within safe operating limits. Heat transfer coefficients provide further control over temperature stability, which is essential for ensuring reliable performance across various environmental conditions.

By balancing deployment speed with reliability, parameters such as discharge coefficient and plenum dimensions provide flexible design options for rapid deployment while safeguarding system durability. Overall, the analysis emphasizes that key parameters, especially those influencing pressure and gas dynamics, are instrumental in achieving optimal performance. Future model refinements can focus on these critical parameters, supporting the development of PDD systems tailored to diverse operational requirements and mission objectives.

5.5 Computational Efficiency

The computational efficiency of the PDD model was observed to be exceptionally high, with all scenarios, including those involving maximum propellant loads and extreme temperatures, completing within approximately one second. Given this swift execution across a variety of input conditions, further computational efficiency testing was deemed unnecessary. The model's current performance is more than adequate for iterative testing and scenario-based analysis, supporting its usability in design optimization and sensitivity analysis without requiring additional resource management or solver adjustments.

Chapter 6

Conclusion & Recommendations

6.1 Conclusion

In conclusion, this study successfully developed and validated a high-fidelity numerical model for simulating the dynamics of a Parachute Deployment Device used in planetary Entry, Descent, and Landing applications. The model accurately captures the key physical processes, including gas generation, pressure dynamics, and parachute ejection, providing a strong foundation for analyzing and improving PDD designs.

The validation process demonstrated that the model effectively replicates the system's behavior under various conditions. The gas generator peak pressure showed an excellent match with experimental results, with differences as low as 0.8%, confirming the model's accuracy in capturing internal flow dynamics. The ejection velocity followed the experimental trends closely, further validating the model's predictive capability. Variations in reaction force, particularly in the cold test, were within the range of experimental repeatability, highlighting both the inherent uncertainties in testing and the model's robustness in representing real-world behavior. These results confirm that the model provides reliable performance predictions, making it a valuable tool for design evaluation and system optimization.

The sensitivity analysis revealed that key parameters significantly influence the PDD's deployment sequence and performance. The discharge coefficient was found to be a critical factor affecting reaction force and ejection velocity, as it governs the rate of gas expansion and pressure buildup. Chamber volumes, particularly in the combustion and post-combustion phases, had a strong effect on peak pressures and deployment speed, emphasizing the importance of optimizing these dimensions for both efficiency and structural integrity. The propellant loading played a direct role in energy release and deployment force, confirming its central role in performance tuning. Plenum dimensions were also identified as a major contributor to peak pressures and reaction forces, making them essential considerations in achieving mission-specific deployment requirements. Parameters related to event sequencing, such as burst disk pressure and shear pin force, were shown to control deployment timing, reinforcing the need for precise calibration to maintain predictable and reliable ejection behavior.

These insights enable targeted optimization strategies for future PDD designs. By adjusting parameters such as discharge coefficient, chamber volumes, and plenum dimensions, deployment dynamics can be tailored to mission-specific constraints, ensuring both rapid ejection and system durability. The findings also highlight the trade-offs between deployment speed and structural loads, providing a clear framework for balancing performance and reliability.

This work directly answers the research question by demonstrating how a high-fidelity numerical model can be developed and validated to accurately simulate PDD dynamics. By integrating critical physical and operational parameters, leveraging experimental validation, and identifying optimization strategies, the study establishes a strong foundation for advancing PDD technology.

6.2 Recommendations

This chapter outlines recommendations for enhancing the accuracy and reliability of the Parachute Deployment Device model developed in this study. While the model has demonstrated satisfactory performance across various scenarios, certain limitations have emerged, primarily due to incomplete data on some physical behaviours and material properties. These limitations necessitated the calibration of several parameters, as a lack of precise experimental data prevented a fully predictive approach.

The following recommendations aim to address these limitations by proposing areas for further study and refinement. Enhancing data accuracy and modelling techniques—such as examining the thermal emissivity of gases, improving understanding of the propellant behaviour at high temperatures, and investigating the thermal and mechanical interactions within the PDD system—would collectively improve the model's accuracy and predictive power. By implementing these recommendations, future work could refine the model to more closely align with physical behaviour, thereby providing a stronger foundation for design and testing of parachute deployment devices.

6.2.1 Determine the Emissivity of Gases

A precise understanding of gas emissivity within the Parachute Deployment Device system is crucial for enhancing the model's accuracy, particularly regarding thermal behaviour and heat transfer within the gas generator and plenum volume. Given the high temperatures and pressures generated in these environments, it is necessary to establish an accurate emissivity measurement to ensure the thermal model effectively predicts the influence of heat radiation on pressure and temperature dynamics.

To determine the emissivity of the hot gases within the PDD, a controlled high-temperature, high-pressure gas cell setup can be adapted, following methodologies outlined in (Christiansen, Stolberg-Rohr, Fateev, & Clausen, 2016). For example, Christiansen et al. describe a high-temperature, high-pressure gas cell designed for quantitative spectroscopic measurements, which could be directly relevant here. Their experimental design allows for the assessment of gas emissivity at temperatures up to 1300 K and pressures up to 200 bar, making it suitable for environments similar to those in the PDD.

In this setup, gases flow through a cell constructed with sapphire windows, which permit the passage of thermal radiation without significant absorption. The emissivity is measured by analysing the absorption spectra captured by a Fourier Transform Infrared (FTIR) spectrometer, which provides data on gas radiative properties under controlled thermal conditions. The data are then processed according to Beer-Lambert's law, which enables the derivation of emissivity based on gas absorption at specific wavelengths.

For the PDD system, this methodology would involve testing combustion gases from the combustion of nitrocellulose. The derived emissivity values could then be applied to the PDD model, helping to refine its thermal accuracy and improve its predictive reliability. By implementing these values, the model would better account for radiative heat transfer effects, allowing for more precise simulations and ultimately supporting more robust system design and operational performance across varied thermal

scenarios.

This process of determining gas emissivity, while complex, represents a critical step toward ensuring the PDD's thermal behaviour aligns closely with actual physical conditions, reducing reliance on assumptions and approximations in future modelling efforts.

6.2.2 Conduct Further Analysis of Propellant Behaviour at Elevated and Low Temperatures

To increase the PDD model's accuracy and reliability, it is advisable to conduct comprehensive testing of the propellant's behaviour across both elevated and low-temperature conditions. The current model relies on a baseline operational range, and while effective, it is likely that the propellant's combustion characteristics vary significantly under extreme temperatures, affecting pressure dynamics, gas generation rates, and reaction forces. Incorporating data from these conditions would refine the model's predictive capabilities, replacing assumptions with experimentally validated inputs.

A recommended approach involves conducting closed bomb tests across an expanded temperature spectrum. Closed bomb tests, which measure the rate of gas generation under controlled conditions, offer detailed insights into how burning rates, thermal decomposition, and heat release vary with temperature. Capturing data across a range from very low to elevated temperatures would reveal the full profile of the propellant's performance, enabling a more precise integration of temperature-dependent behaviour in the model. These tests would allow us to observe and define burning rate fluctuations and heat generation specific to extreme thermal conditions, critical for modelling the PDD's response in all potential operating scenarios.

Further testing would ultimately eliminate the need for calibration-based inputs in the model, enabling the construction of an accurate burning rate model rooted solely in experimental data. This model would better represent the propellant's combustion dynamics by capturing the exact rates of gas and heat generation without relying on estimated adjustments. Incorporating this precise burning behaviour into the simulation framework would substantially enhance the model's overall accuracy and predictability, yielding a tool that more closely mirrors real-world performance requirements.

6.2.3 Development of an Initiator Model

In the current model, the initiators are represented simplistically, with their contributions to gas generation and pressure dynamics embedded as assumptions rather than derived from detailed empirical data. A more accurate approach would involve developing a specific model for the initiators, grounded in the unique burning behaviour of the propellant charge inside them. Such a model would enable us to predict the initiator's output with greater fidelity, including the rate at which it contributes to pressure buildup, gas flow, and thermal effects in the system.

To achieve this, experimental data on the initiator's propellant burn rate, ignition characteristics, and combustion dynamics under varying conditions could be collected. Closed-bomb tests or other controlled combustion tests could be used to establish a detailed burn profile of the propellant in the confined space of the initiator. This would allow us to characterize the initiator's impact on the PDD's overall dynamics, taking into account parameters such as burn rate variability, ignition delay, and gas output rate.

By integrating a dedicated initiator model that reflects this empirical data, the PDD simulation could better capture the early phases of pressure development and provide more accurate predictions of timing and force for deployment. This enhancement would be particularly useful for mission scenarios requiring precise deployment profiles, as it would allow for improved synchronization of gas generation and deployment timing.

6.2.4 Investigation of Wall Surface Effects on Heat Transfer

The heat transfer dynamics between the gases and the walls of the gas generator and the mortar tube significantly affect the thermal profile and pressure buildup within the PDD. The surface condition of the walls, including factors such as smoothness, coating, or any residual debris, directly influences the rate of heat transfer. For instance, polished surfaces typically have lower emissivity and can result in reduced heat loss, while rougher or unclean surfaces might increase heat dissipation rates, thereby altering the pressure and temperature dynamics in the system.

To improve the accuracy of the heat transfer model, it would be beneficial to investigate the impact of different wall surface conditions on thermal behaviour. This investigation could include experimental studies with varying surface treatments and roughness levels to establish a correlation between wall condition and heat transfer efficiency. Additionally, adjusting the convective heat transfer coefficients in the model to reflect different surface types could allow for more precise control over simulated temperature and pressure profiles.

Such a study would offer valuable insights into the range of possible thermal variations and allow for adjustments in the model to account for specific wall conditions in real-world deployments.

6.2.5 Conduct Detailed Analysis of the Parachute Pack's Mechanical Behaviour

To enhance the model's accuracy, a detailed analysis of the parachute pack's mechanical behaviour is recommended. Key aspects of this analysis should include the pack's spring and damping properties, which influence how it responds to applied forces, as well as its frictional behaviour, which affects movement speed and resistance within the mortar tube. Currently, these characteristics may rely on approximations or calibration adjustments, adding uncertainty to the model. Experimental data on these mechanical properties would allow the model to more accurately represent the physical behaviour of the parachute pack, minimizing reliance on calibration and providing a more precise simulation of the deployment process.

Improving the characterization of the parachute pack's behaviour would yield insights into how it interacts with the piston and responds to various deployment forces, leading to more reliable predictions under diverse conditions. By incorporating these refined data points, the model would better capture the dynamics of the pack's motion, timing, and response, ultimately enhancing the overall fidelity and robustness of the PDD system simulation.

References

Anderson, J. D. (1999). *Modern Compressible Flow With Historical Perspective.* New York: McGraw Hill Publishing Company.

Arpad, J., & Channon, P. (1979). The Closed Bomb Technique for Burning Rate Measurementat High Pressure. *Progress in Astronautics and Aeronautics*.

Beckstead, M., Puduppakkam, K., Thakre, P., & Yang, V. (2007). Modeling of combustion and ignition of solid-propellant ingredients. *Progress in Energy and Combustion Science*, 33:498-551.

Brecht, J., Pleasants, J., & Mehring, R. (1973). *The Viking mortar - Design, development, and flight qualification.* Palm Springs: American Institute of Aeronautics and Astronautics.

Christiansen, C., Stolberg-Rohr, T., Fateev, A., & Clausen, S. (2016). High temperature and high pressure gas cell for quantitative spectroscopic measurements. *Journal of Quantitative Spectroscopy & Radiative Transfer*, 96-103.

E. Vasas, R., & Styner, J. (2003). *Mars exploration rover parachute mortar deployer development.* Monterey: AIAA Aerodynamic Decelerator Systems Technology.

Gusachenko, L., & Zarko, V. (2008). *Analysis of Unsteady Solid-PropellantCombustion Models.* Springer Science + Business Media, Inc.

Harrland, A., & Johnston, I. (2012). *Review of Solid Propellant Ignition Models Relative to the Interior Ballistic Modelling of Gun Systems.* Edinburgh: Defence Science and Technology Organisation.

Hohmann, C., Tipton, B. J., & Dutton, M. (2000). *Propellant for the NASA Standard Initiator.* Houston: NASA.

Johnston, I. A. (2005). *The Noble-Abel Equation of State: Thermodynamic Derivations for Ballistics Modelling.* Edinburgh: Defence Science and Technology Organisation.

Knacke, T. W. (1991). *Parachute Recovery Systems Design Manual.* China Lake: U.S. Navy Edition.

Koster, S., Wells, J., & Sinclair, R. (2011). *Pneumatic Mortar DEvelopment for the NASA/Orion Capsule Drogue Parachute System.* Santa Ana: Amercian Institute of Aeronautics and Astronautics.

Novozhilov, B. V., & Novozhilov, V. B. (2021). *Theory of Solid-Propellant Nonsteady.* John Wiley & Sons Ltd.

Pawlikowski, T. P. (1986). *Drogue Mortar System Simulation Development and Performance Evaluations.* St. Louis: American Institute of Aeronautics and Astronautics.

Pleasants, J. E. (1974). *Parachute Mortar Design.* Hampton: NASA Langley Research Center.

Powell, E. Z., Wilmot, G., Haar, L., & Klein, M. (1979). Equations of State and Thermodynamic Data for Interior Ballistics Calculations. *Interior Ballistics of Guns, Vol. 66 of Progress in Astronautics and Aeronautics*, 325–348.

Price, C., & Juhasz, A. (1977). *A Versatile User-Oriented Closed Bomb Data Reduction Program (CBRED).* USA Bllistic Research Laboratory.

Rowan, J., Moran, J., & S. Adams, D. (2009). *Development and Qualification of the Mars Science Laboratory Mortar Deployment System.* Washington DC: AIAA Aerodynamic Decelerator Systems Technology.

Stals, J. (1975). *Form-Functions For Multi-Component Propellant Charges Including Inhibited Grains and Sliver Burn.* Maribyrnong: Australian Defence Scientific Service Materials Research Laboratories.

Sutton, G., & Biblarz, o. (2001). *Rocket propulsion elements.* New York / Chichester / Weinheim / Brisbane / Singapore / Toronto: John Wiley & Sons.

Varghese, P. L. (1988). *Investigation of Energy Transfer in The Ignition Mechanism of a NASA Standard Initiator.* Austin: The University of Texas at Austin.

Whalley, I. A., & Churchill, J. (2003). *Development of a parachute mortar cartridge for the Galileo Jupiter Probe.* Huntsville: AIAA/ASME/SAE/ASEE Joint Propulsion.